# Deflagration to Detonation Transition with Increased Reactivity of Iso-octane and Ethane Mixtures

By

**Jinzhou Li**

MSc (Eng)

BEng

Submitted in accordance with the requirements for the degree of Doctor of Philosophy

**Institute of Thermofluids**

**School of Mechanical Engineering**

**The University of Leeds**

Feb 2024

## Intellectual Property and Publication Statements

The candidate confirms that the work submitted is his own, except where work which has formed part of jointly authored publications has been included. The contribution of the candidate and the other authors to this work has been explicitly indicated below. The candidate confirms that appropriate credit has been given within the thesis where reference has been made to the work of others

- Chapter 4 of this thesis is based on a jointly-authored journal paper: Bradley, D., Li, J. Reaction Propagation Prior to Developing Detonation in a Rapid Compression Machine. *Combustion and Flame*. 2024, **262**, article no: 113331. The candidate conducted the primary experimental work, methodology, analyzed the results, and prepared the initial draft. Prof. Derek Bradley provided supervision, enhanced the manuscript's writing, and offered invaluable technical discussions, insight and guidance.
- Section 5.2 of this thesis is based on a jointly-authored journal paper: Li, J., Xie Y., Morsy, Mohamed., Yang, J. Laminar Burning Velocities, Markstein Numbers and Cellular Instability of Spherically Propagation Ethane/Hydrogen/Air Premixed Flames at Elevated Pressures. *Fuel*. 2024, **364**, article no: 131078. The candidate conducted the primary experimental work, analyzed the results, and prepared the initial draft. Dr. Junfeng Yang provided supervision, enhanced the manuscript’s writing, and offered invaluable technical insights and guidance. Other authors contributed experimental support and valuable discussions
- Section 5.3 of this thesis is based on a jointly-authored journal paper: Li, J., Yang J. Turbulent burning velocity of pure ethane and blends with hydrogen at elevated pressure. Submitted to Combustion and Flame journal. The candidate conducted the primary experimental work, analyzed the results, and prepared the initial draft. Dr. Junfeng Yang provided supervision, enhanced the manuscript's writing, and offered invaluable technical insights and guidance.

"*My words fly up, my thoughts remain below: Words without thoughts never to heaven go*." - William Shakespeare, Hamlet, Act 3, Scene 3.

## Acknowledgements

My deepest appreciation goes to my supervisory team: Dr. Junfeng Yang, Prof. Derek Bradley, Dr. Sven van Loo, and Prof. Samual Falle and Dr. Andrzej Pekalski. Each member played a pivotal role in shaping the trajectory and success of this research. I would like to acknowledge Shell Global Solutions Ltd. (UK) for their generous partial financial support for my PhD study.

I extend my gratitude to the technicians at the combustion lab: Peter Grieve, Samuel Flint, and Max Peper. Their expertise was indispensable in maintaining the Leeds Rapid Compression Machine and MK-II Combustion Vessel. A special mention goes to Dr. Mohamed Morsy and Ahmed Pervez for their comprehensive training on the MK-II combustion vessel, and to Christian Michelbach for his demonstration and guidance on the Rapid Compression Machine.

I am fortunate to have been surrounded by a supportive community of fellow PhD students and researchers. My sincere thanks to Yu Xie, An Lu, Chengpei Wu, Marwaan Al Khafaji, Rawan Alkandari, Olayinka Ramonu, Adebayo Fakeye and Junior Achumu for their camaraderie and collaboration.

Lastly, I am profoundly thankful for the unwavering encouragement, support, and love I received from my family throughout my PhD research journey. Special thanks go to my parents, Shiyong Li and Xiaoling Jia, and my grandparents, Xicai Li and Xiying Cui, for their understanding, consistent support, and encouragement. Their belief in me has been the foundation upon which this research was built. I am also indebted to my girlfriend, Rong Huang, for her unconditional love and steadfast support.

## Abstract

The deflagration to detonation transition (DDT) represents the most catastrophic explosion scenario, characterized by supersonic flame propagation, overpressure, and shock waves. This phenomenon poses significant safety risks to human safety and property damage particularly in fuel storage facilities. In combustion engines, DDT events are abnormal occurrences that can damage engine components, obstructing the progression toward engines with higher compression ratios and thermal efficiency. In the face of pressing demands for energy conservation and carbon emission reductions, a thorough understanding of DDT, especially within combustion engine environments, is essential for the innovation of advanced engines. Furthermore, the increasing reliance on ethane, both as an essential feedstock for ethylene production in the petrochemical industry and as a potential source for power generation, underscores the need to understand its combustion characteristics. This includes a particular focus on the risks of explosion associated with DDT in open environments. Such understanding is crucial for mitigating DDT-related risks and for the advancement of safer and more efficient combustion technologies.

This research firstly investigates and analyze the different ignition modes including deflagration, autoignition and transition to detonation inside an optical Rapid Compression Machine (RCM), aiming to have a comprehensive understanding of the DDT mechanism and the phenomenon of super-knock in compressed engine conditions. Concurrently, to understand the laminar and turbulent characteristics of ethane-air flames and effects of hydrogen on laminar ethane flames, measurements were taken in a fan-stirred spherical combustion vessel, and specific correlations were proposed to align with the measured data. These measurements are valuable for the application of ethane-hydrogen-air mixtures in engines, gas turbines, burners, and serve as a critical database for simulation purposes. Additionally, the specialized finite volume computational fluid dynamics (CFD) code, MG, incorporates the compressible Navier-Stokes equation, progress variable and $k$-$\varepsilon$ turbulence model, along with a correlation of measured

turbulent burning velocities, to enable simulations of large-scale ethane-air DDT.

The experiments conducted in the RCM indicated that the transition to detonation occurs when the velocity of the autoignitive reaction wave matches the acoustic velocity, coupled with rapid heat release from a hot spot. This phenomenon was analysed by monitoring changes in two dimensionless parameters $\xi$ the ratio of autoignition velocity to acoustic velocity, and $\varepsilon$, representing the rate of heat release in hot spots. In terms of ethane-air combustion characteristics, the knowledge gap of the Markstein length/number, flame instability, and the effects of hydrogen addition on ethane-air laminar flame characteristics and turbulent flame characteristics of ethane-air are filled. The large-scale ethane-air DDT simulation demonstrated that the process unfolds in four phases: laminar propagation, turbulent flame acceleration, transition to detonation, and detonation propagation. The simulation highlighted that turbulence generated from the flame's interaction with baffles plays a crucial role in accelerating the flame, thereby facilitating the DDT.

# Table of Contents

# List of Figures

# List of Tables

# Nomenclature

| | |
|---|---|
| $a$ | Acoustic velocity (m/s) |
| $A$ | Laminar flame surface area ($m^2$) |
| c | Progress variable |
| $c_p$ | Specific heat at constant pressure (J/kg.k) |
| $c_v$ | Specific heat at constant volume (J/kg.k) |
| $D_a$ | Turbulent Dankohler number |
| $D_T$ | Thermal diffusivity coefficient |
| $D_M$ | Mass diffusivity coefficient |
| $\tilde{E}$ | Density-weighted average total energy |
| $\tilde{e}$ | Internal energy |
| $f$ | Fan speed (rpm) |
| $K_a$ | Turbulent Karlovitz number |
| $K_B$ | Boltzmann constant |
| $K$ | Karlovitz number |
| $k$ | Thermal conductivity (W/(m·K)) |
| $\bar{k}_\eta$ | Dimensionless wave number |
| $R_{et}$ | Turbulent Reynolds number |
| $L$ | Intergral length scale (m) |
| $L_b$ | Markstein length on the burned side of the flame (m) |
| $Le$ | Lewis number |
| $Le_{eff}$ | Effective Lewis number |
| $\bar{M}$ | Mean molar mass (kg) |
| $m_a$ | Atomic mass (kg) |
| $Ma_b$ | Burned gas Markstein number |
| $Ma_{sr}$ | Strain rate Markstein number |

| | |
|---|---|
| $Ma_{cr}$ | Markstein number associated to flame curvature |
| $Pe_{cl}$ | Critical Peclet number |
| $\Delta P$ | Pressure oscillation amplitude (MPa) |
| $P$ | Pressure (MPa) |
| $P_0$ | Datum atmospheric pressure (MPa) |
| $Pr$ | Prandtl number |
| $r_{cl}$ | Critical flame radius (m) |
| $r_u$ | Cold flame radius (m) |
| $r_v$ | Reference flame radius based on the volume (m) |
| $r_{sch}$ | flame front radius obtained by Schlieren ciné-photography (m) |
| $r_0$ | Hot spot radius (m) |
| $R_{uu}$ | autocorrelation function of the velocity fluctuation |
| $Re_t$ | turbulent Reynolds number |
| $S_a$ | Computed autoignitive speed (m/s) |
| $S_l$ | laminar propagation speed (m/s) |
| $S_m$ | Measured propagation speed (m/s) |
| $S_{sch}$ | Turbulent flame propagation speed based on Schlieren flame radius (m/s) |
| $S_n$ | Stretched flame speed (m/s) |
| $S_s$ | Flame speed at zero stretch rate (m/s) |
| $S_g$ | Mean gas velocity ahead of flame (m/s) |
| $T$ | Temperature (K) |
| $T_{ad}$ | adiabatic flame temperature (K) |
| $T_0$ | Datum atmospheric temperature (K) |
| $T_c$ | End of compression temperature (K) |
| t | Time (s) |

| | |
|---|---|
| $U$ | Dimensionless parameter with the ratio of $\frac{u_t}{u_k{}'}$ |
| $u'$ | RMS turbulent velocity (m/s) |
| $u_k{}'$ | Effective rms turbulent velocity (m/s) |
| $u_a$ | Autoignitive velocity (m/s) |
| $u_l$ | Unstretched laminar burning velocity (m/s) |
| $u_n$ | Stretched lamianr burning velocity (m/s) |
| $u_t$ | Turbulent burning velocity (m/s) |
| $u_{tv}$ | Turbulent burning velocity based on $r_v$ (m/s) |
| $u_{l,0}$ | Datum unstretched laminar burning velocity at $T_0$ and $P_0$ |
| $u_\eta$ | Velocity on Kolmogorov scale (m/s) |
| $V_{H_2}$ | Hydrogen volume fraction |
| $V_{C_2H_6}$ | Ethane volume fraction |
| $X_{H_2}$ | Percentage of hydrogen based on volume |

**Greek Symbols**

| | |
|---|---|
| $\alpha$ | Flame stretch rate (1/s), Numerical constant, Thermal diffusivity ($m^2/s$) |
| $\alpha_c$ | Stretch rate for curvature |
| $\alpha_s$ | Stretch rate for strain |
| $\alpha_T$ | Temperature coefficients for $u_l$ |
| $\beta$ | Numerical constant |
| $\beta_P$ | Pressure coefficients for $u_l$ |
| $\beta^*$ | Numerical constant, equal to 0.09 |
| $\gamma$ | Ratio of specific heats |
| $\delta_l$ | laminar flame thickness (m), = $\nu/u_l$ |
| $\delta_k$ | Preheat zone flame thickness (m) |
| $\varepsilon$ | Ratio of $\frac{r_0}{a\tau_e}$, excitation factor and turbulent |

| | |
|---|---|
| | dissipation rate |
| $(\varepsilon/\xi)$ | Detonation parameter |
| $\eta$ | Kolmogorov length scale (m) |
| $\lambda$ | Taylor length scale (m) |
| $\nu$ | unburned gas kinematic viscosity ($m^2/s$) |
| $\xi$ | Ratio of $u_a/a$, autoignitive parameter |
| $\xi_l$ | Lower limits of detonation peninsula |
| $\xi_u$ | Upper limits of detonation peninsula |
| $\rho$ | Density ($kg/m^3$) |
| $\rho_b$ | burned gas density ($kg/m^3$) |
| $\rho_u$ | unburned gas density ($kg/m^3$) |
| $\sigma$ | Closure terms, equal to 1/1.3 |
| $\sigma^*$ | Numerical constant, equal to 0.8 |
| $\tau_e$ | Chemical excitation time (s) |
| $\tau_i$ | Ignition delay time (s) |
| $\tau$ | Stress tensor |
| $\mu$ | Molecular viscosity (kg/(m.s)) |
| $\phi$ | Equivalence ratio |
| $\omega$ | Turbulent dissipation rate |
| $\Lambda$ | Eigenvalue value |

**Subscripts, Superscripts and Notation**

| | |
|---|---|
| a | Autoignitive |
| b | Burned |
| c | End of compression |
| cl | Critical value |
| cr | Curvature |
| e | Excitation |

| | |
|---|---|
| g | Gas |
| i | Ignition |
| k | effective |
| l | Laminar |
| m | Measured; mass |
| n | Stretched |
| o | Datum |
| s | Unstretched |
| sr | Strain rate |
| sch | Schlieren |
| p | Pressure |
| t | Turbulent; thermal |
| T | Temperature |
| u | Unburned |
| v | Volume |
| u,v,w | Velocity at x,y,z direction respectively |
| x,y,z | x,y,z direction, coordinate |

**Abbreviations**

| | |
|---|---|
| AI | Autoignition |
| ARC | Advance Research Computing |
| AMR | Adaptive Mesh Refinement |
| BMF | Burned Mass Fraction |
| CJ | Chapman-Jouguet |
| CFD | Computational Fluid Dynamic |
| CGS | Centimeter-Gram-Second |
| DL | Darrieus-Landau Instability |
| DDT | Deflagration to Detonation Transition |

| | |
|---|---|
| DME | Dimethyl Ether |
| EOC | End of Compression |
| FPS | Frame Per Second |
| HPC | High Performance Computing |
| IDT | Ignition Delay Time |
| L | Laminar Flame Propgation |
| LES | Large Eddy Simulation |
| LLNL | Lawrance Livermore National Laboratory |
| MPI | Message Passing Interface |
| NTC | Negative Temperature Coefficient |
| P | Pressure Pulse |
| PIV | Particle Image Velocimetry |
| RCM | Rapid Compression Machine |
| RON | Research Octane Number |
| RMS | Root Mean Square |
| TD | Thermal-Diffusivity Instability |

# 1. Introduction and Thesis Scope

## 1.1 Motivation of the Research

The accidental explosion of a fuel-air mixture in the oil and gas industries is a danger to both life and property. Such explosions can escalate into severe detonations through DDT, a process where detonations, once initiated, rapidly consume the entire detonable mixture. The detonation wave is characterized by a high propagation speed, typically supersonic, and exerts an overpressure several times greater than atmospheric pressure [1]. Such intense overpressure not only poses severe threats to life but also results in substantial property damage. Detonation occurs not only in open spaces but also within combustion engines, leading to super-knock. This phenomenon is characterized by significant pressure oscillations inside the engine and is a well-known challenge to the enhancement of advanced engines designed for high thermal efficiency [2].

Understanding the mechanisms of transition to detonation, both in open spaces and confined engine conditions, is crucial for several reasons. Firstly, understanding DDT in industrial fuel gas storage facilities enables a better prediction and mitigation of explosion risks, thereby enhancing the design of safer facilities. Secondly, understanding the transition to detonation in combustion engines is essential for avoiding unwanted detonations that lead to engine super-knock. Such understanding is pivotal for designing advanced engines with high thermal efficiency, which, in turn, reduces fuel consumption and $CO_2$ emissions.

Numerous explosion incidents throughout history have been linked to DDT. A review of these events offers insights into their severity and implications. The accidental explosion at Buncefield in 2005 is a typical DDT explosion. This disaster resulted in a staggering financial cost of approximately 1.5 billion GBP, coupled with 43 minor injuries, marking it as one of the most catastrophic explosion accidents in British history [1]. The explosion accident at the Fukushima Daiichi nuclear power plant in 2011 was one of the biggest environmental disasters in recent years. Post-disaster investigations revealed that the

explosion resulted from a hydrogen-air DDT, where a large amount of hydrogen was produced by a redox reaction between zirconium and water [3,4]. More recently, in 2020, a devastating explosion occurred at the Port of Beirut when nearly 3,000 tons of stored ammonium nitrate detonated. This event stands as one of the most severe non-nuclear man-made explosions in history. Figure 1.1 presents a visual documentation of the Beirut explosion, capturing the moment of a vast explosion characterized by a significant mushroom cloud formation. A robust shock wave, evident from the concentric blast patterns, radiated from the epicenter, leading to extensive destruction of nearby facilities and buildings. The aftermath witnessed over 6,500 injuries and the tragic loss of 220 lives, including two children. The destruction extended beyond residential areas, with damages estimated at a staggering 4.6 billion dollars [5]. Through the incident review, it is noticed that DDT is a significant threat to life and facilities. Therefore, DDT is an important topic in the safety and handling of energetic fuels. Oran and Gamezo [6] mentioned that a deep understanding of DDT can help mitigate and avoid DDT. Upon reviewing these incidents, it became evident that DDT poses a significant threat to both life and infrastructure.

Figure 1.1. Explosion at the port of Beirut [7].

Ethane is an important petrochemical product, primarily used as a feedstock in the petrochemical industry to produce ethylene, which is further processed into various chemicals and plastics [8]. Ethane is the second-largest component in natural gas, with its concentration ranging between 0.5% and 13.3% by volume [8]. Over recent years, there has been a surge in ethane storage worldwide. As specifically shown in Figure 1.2, ethane

production in the U.S. increased from $3\times10^8$ barrels to $7.5\times10^8$ barrels between 2010 and 2022, marking a 250% increase. As a testament to ethane's rising importance, Shell launched a $6 billion facility in Pennsylvania, USA, in November 2022. Known as an ethane cracker, this plant is designed to process ethane from regional fracking operations, producing up to 1.6 million metric tons of plastic annually [10]. Ethane has recently garnered attention as a potential fuel for power generation and as a diesel additive in large marine vessels and engines [11, 12]. Its comparative advantages over methane include a shorter combustion duration, reduced ignition delay time, enhanced heat release, and more stable combustion under lean conditions, positioning it as an attractive alternative [13, 14]. Furthermore, the strategic addition of hydrogen to hydrocarbon fuels like ethane can facilitate ignition and enhance combustion systems, leading to reduced $CO_2$ emissions and improved performance [15].

The increasing production, storage, and utilization of ethane, particularly in power generation, have highlighted the importance of a thorough understanding of safety measures and combustion characteristics. This is crucial, especially considering the potential risks associated with DDT, underscoring the need for advanced knowledge in managing and harnessing ethane as a reliable and safe energy source. Numerous studies concur that a precise characterization of ethane-air combustion, which includes the analysis of both laminar and turbulent premixed flames as well as autoignition, is essential for accurately predicting DDT. This detailed understanding is also vital for its application as a power source in combustion systems [1, 6, 16-21] Furthermore, since this project is funded by Shell Global Solutions, and ethane is their target fuel, the goal is to understand the combustion characteristics and DDT.

This research poses several critical questions: (i) Is the mechanism of DDT fully understood? (ii) How well is the combustion characteristics of the ethane-air mixture understood? If gaps in knowledge exist, can they be addressed through direct measurement (iii) Under what conditions does the ethane-air mixture transition to DDT? (iv) Can a CFD code be developed to simulate the DDT of an ethane-air mixture in open spaces?

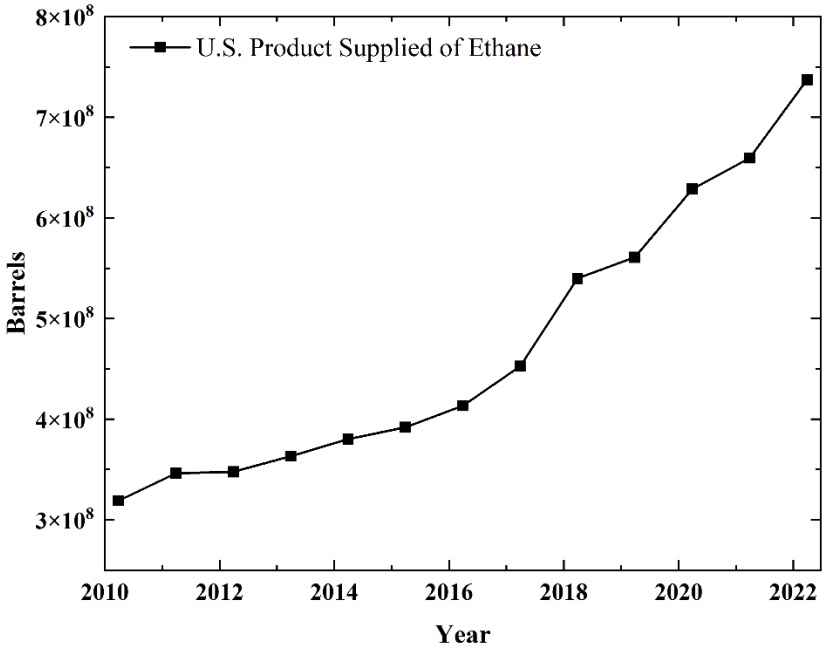


Figure 1.2 Ethane product supply in the U.S. (2010-2022). Data sourced from [9].

## 1.2 Aim and Objective

Considering the motivations outlined above, it is crucial to comprehend the mechanism of transition to detonation across both engine conditions and open spaces. Moreover, the rising production, storage, and utilization of ethane, especially in power generation, underscore the significance of deeply understanding its combustion characteristics. Despite this, current literature scarcely addresses the turbulent characteristics of ethane-air flames and the impact of adding hydrogen to laminar ethane-air mixtures, which can enhance the combustion process and decrease $CO_2$ emissions. The project aim is threefold:

- Investigate and analyze the different ignition modes including deflagration, autoignition and detonation inside an optical RCM, and develop a detonation peninsula diagram aiming to understand the mechanism of DDT and super-knock in engine conditions.
- To quantify the laminar and turbulent characteristics of premixed ethane-air flames with hydrogen additions, aiming to establish correlations for burning velocities as functions of dimensionless groups.
- To implement the afore-developed detonation diagram and burning velocity correlation into the in-house CFD code, MG, for simulating large scale DDT of

ethane-air mixtures.

In order to achieve the aims above, it is essential to undertake the following objectives:

1. Develop the Leeds RCM by integrating optical access and a high-speed camera system to enable observation of autoignition wave propagation and detonation formation.
2. Iso-octane is chosen as the target fuel for RCM experiments, attributed to its designation as a primary reference fuel and its Research Octane Number (RON) of 100, closely approximating the RON of commercial gasoline, typically around 95. Additionally, its unique Negative Temperature Coefficient (NTC) behavior facilitates the investigation of NTC effects on autoignition wave propagation.
3. Analyzing autoignition, detonation and super-knock through experimental monochrome images, pressure traces, and ignition delay time data sourced from the Leeds optical RCM. This analysis will be integrated with predicted ignition delay times and chemical excitation durations from chemical kinetics studies to deepen the understanding of the DDT and super-knock mechanisms in engine conditions.
4. Conduct measurements of laminar burning velocities, Markstein length/number, critical flame radius, and Peclet number and examine the effects of hydrogen additions on the ethane-air premixed flame in the Leeds MK-II combustion vessel.
5. Formulate a generalized correlation that defines the stable regime for the propagation of flames.
6. Perform measurements to investigate the turbulence effects with root-mean-square (RMS) turbulent velocity up to 5 m/s on the ethane-air premixed flame in Leeds MK-II combustion vessel.
7. Propose a turbulent burning velocity correlation based on two dimensionless parameters $U$ and $K$, ensuring it aligns well with the measured data.
8. Develop the finite volume MG code that incorporates a source term of progress variable and $k$-$\varepsilon$ turbulence model.
9. Incorporate the measured turbulent burning velocity correlation into the MG code, facilitating precise simulations of turbulent ethane-air flame propagation and its

eventual transition to detonation.

10. The simulation results of large-scale flame propagation and DDT of ethane-air mixtures, utilizing the previously mentioned MG code within a congested rig setup, are presented and compared with Shell's large-scale experimental work.
11. Implement the detonation peninsula method to determine the specific temperature and pressure conditions under which the DDT of ethane-air occurs.

### 1.3 Thesis Outline

This thesis is divided into seven chapters, including this introductory chapter. A brief outline and description of each chapter are as follows:

Chapter 2 delves into the principles of combustion, covering laminar premixed flames, turbulent premixed flames, and autoignition/DDT.

Chapter 3 provides an overview of the experimental apparatus, simulation methodologies, and data processing techniques employed in this study.

Chapter 4 presents the results of ignition modes of *i*-octane-oxygen mixtures over a range of temperatures obtained from RCM study.

Chapter 5 presents measured laminar/turbulent combustion characteristics data for ethane-hydrogen-air over various conditions and includes correlations for stable flame propagation and the effects of turbulence.

Chapter 6 discusses turbulent flame acceleration and DDT in ethane-air mixtures, comparing simulations with experimental data and presenting a detonation peninsula.

Chapter 7 summarizes the research findings and contributions, offering suggestions for future research.

## 2. Background and Literature Review

### 2.1 Laminar Premixed Flames

Laminar premixed flame is the simplest form of flame propagation. There are multiple

parameters to describe the laminar premixed flames including laminar burning velocity, Markstein length and number, Lewis number, Zel'dovich number and instability parameter such as critical radius, Peclet number [22]. Among these, the laminar burning velocity stands out as the most fundamental characteristic of premixed combustion. It not only aids in validating detailed chemical kinetics but also serves as a benchmark in both laminar and turbulent analyses. Practically, its significance extends to applications such as the design of internal combustion engines, gas turbines, and rockets [23-27].

Several experimental methods have been developed to study laminar premixed flames, including the constant pressure or volume spherical flame method [28-31], the counterflow burner method [32-35], and the heat-flux method [36-39]. In this study, the constant volume spherical flame method is employed utilizing the Leeds MK-II fan-stirred combustion vessel, chosen for its capacity to conduct experiments at the maximum pressures up to 1 MPa and temperatures up to 450 K. This apparatus uniquely enables the observation of flame cellular instability, a capability not offered by other methods. Employing Schlieren imaging, the study investigates laminar ethane-hydrogen-air premixed flames across a broad spectrum of equivalence ratios, temperatures, and pressures. This combustion vessel offers several advantages, allowing us to study laminar premixed flames at elevated pressures and temperatures, closely resembling the working conditions of internal combustion engines. Subsequent from 2.1.1 to 2.1.7 will provide a comprehensive overview of laminar premixed flame fundamentals.

### 2.1.1 Laminar Flame Structure and Thickness

Figure 2.1 depicts the one-dimensional profile of a premixed adiabatic flame, including the variations in concentrations of reactants, intermediates, products, and temperature. A typical laminar premixed flame can be divided into four zones, cold reactants, pre-flame zone, reaction zone and products zone [40]. In the cold reactants zone, reactants begin at an initial temperature of $T_0$. The temperature of the mixtures then rises within the pre-flame zone due to conductive heat transfer from the subsequent reaction zone. Within the reaction zone, dominated by chemical reactions and mass diffusion, a rapid temperature rise occurs due to chain reactions involving radicals, creating a sharp density gradient

across the flame front. This zone is the locus of both visible and invisible flame regions; the former is characterized by light emission from soot particles or excited molecules, while the latter persists without visible light despite the intense chemical activity [40]. Ultimately, the products zone reaches the adiabatic burned gas temperature, $T_b$.

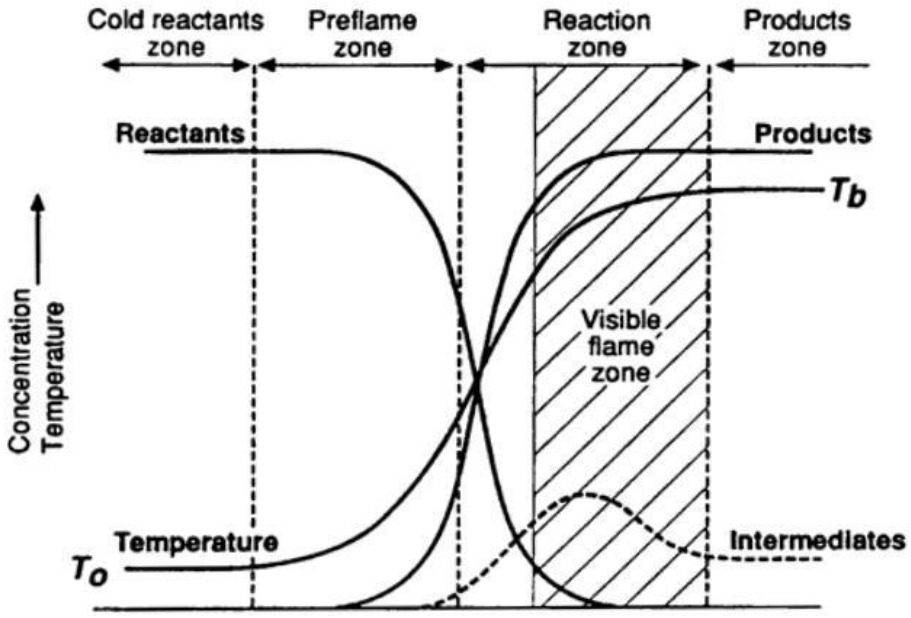


Figure 2.1. Reactants and products concentration and temperature profiles associated with one-dimensional, premixed adiabatic flame [40].

The laminar flame thickness, represented by $\delta_l$, is defined as the width of the flame preheat zone, which is the region where the unburned mixture is heated to its ignition temperature prior to the onset of actual combustion reactions [40]. There are many different definitions of the laminar flame thickness, $\delta_l$. Göttgens et al. [41] defined the laminar flame thickness of the preheat zone using the temperature gradient, formulated as:

$$\delta_k = \frac{(k/c_p)_{T^0}}{\rho_u u_l}, \tag{2.1}$$

where $(k/c_p)_{T^0}$ is the ratio of thermal conductivity and specific heat at a certain inner layer temperature, $T^0$, which represents the critical temperature at which chemical reactions commence [41]. $\rho_u$ is the unburned density and $u_l$ is the lamianr burning velocity. This definition echoes the sentiments of Clavin [42], who also proposed a similar description of laminar flame thickness grounded on the temperature gradient. For

hydrocarbons, the most widely used definition of laminar flame thickness is grounded on the hydrodynamic length [43-47], described as:

$$\delta_l = \frac{v}{u_l Pr}, \tag{2.2}$$

where, $v$ is the kinematic viscosity, $P_r$ is the Prandtl number $P_r = \frac{v}{\alpha}$ where here $\alpha$ is the thermal diffusivity. The units for these parameters are detailed in the provided nomenclature. The kinematic viscosity and thermal diffusivity of ethane-hydrogen-air mixtures were all derived from GASEQ code [48]. Following the previous works in [43-47] This definition of the laminar flame thickness is used in Chapter 5.

### 2.1.2 Laminar Flame Radius and Speed

In this study, the laminar flame radius and speed were measured from the Leeds MK-II combustion vessel in conjunction with the Schlieren ciné photography technique. A comprehensive description of the Leeds MK-II combustion vessel and the Schlieren cine photography can be found in Section 3.1. This study utilizes the constant volume spherical flame method due to its capability to perform experiments under high pressures and temperatures, closely mirroring real-world conditions in gas turbines and engine operations, enabling the observation of flame instability. As depicted in Fig. 2.2, the Schlieren images illustrate the progression of laminar ethane-air with $\phi$ = 1.1 under varying pressures and temperatures. The distinctive cellular flame instability observed at 0.5 MPa is detailed as a unique phenomenon in Section 2.1.5.

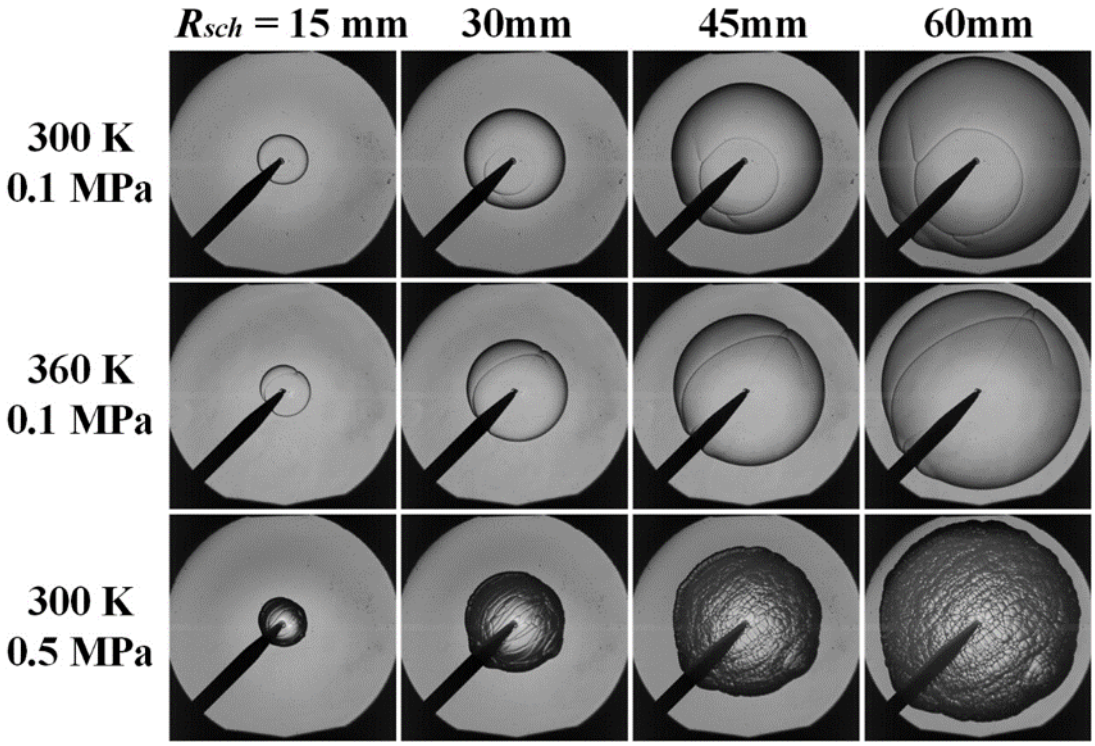


Figure 2.2. Schlieren images showing the effects of initial temperature and pressure on the developments of laminar ethane-air flame at $\phi$ = 1.1.

Through post-processing of the Schlieren images, as detailed in Section 3.1.6, the Schlieren flame radius, $r_{sch}$, can be derived. The cold flame radius is defined as the 5 K temperature above the reactants' temperature [49]. A computational study of spherical flame propagation [44] reported that a correlation between the cold flame radius and the Schlieren-detected flame radius, which is expressed as:

$$r_u = r_{sch} + 1.95\delta_l(\frac{\rho_u}{\rho_b})^{0.5}, \quad (2.3)$$

where, $\frac{\rho_u}{\rho_b}$ is ratio of the unburned to burned density of mixtures and the its value is derived from the GASEQ code [48]. Once the cold flame radius is established, the stretched flame speed is described by the time derivative of the radius:

$$S_n = \frac{dr_u}{dt}. \quad (2.4)$$

The observed flame radius and the computed stretched flame speed are utilized to determine the flame stretch rate, laminar burning velocity, Markstein length, and Markstein number.

### 2.1.3 Flame Stretch Rate

The propagation of spherical laminar flames is influenced by transverse and tangential velocity gradient. Coupled with flame curvature, these components contribute to stretching the flame surface. The flame stretch rate, $\alpha$, changes the total flame surface area, $A$, and alters the spatial distributions of temperature, species concentrations and laminar burning velocity. For the spherical flame measurements, the total stretch rate acting on the flame with surface area, $A = 4\pi r^2$, is formulated as [50]:

$$\alpha = \frac{1}{A}\frac{dA}{dt} = \frac{2}{r_u}\frac{dr_u}{dt} = \frac{2}{r_u}S_n \tag{2.5}$$

Here $S_n$ represents the stretched laminar flame speed, with its expression provided in Eq. 2.4. The study of Candel and Poinsot [51], and Bradley et al. [22] reported that the total stretch rate can be split into two components, due to the aerodynamic strain rate, $\alpha_s$, and curvature strain rate, $\alpha_c$:

$$\alpha = \alpha_s + \alpha_c. \tag{2.6}$$

The spherical flame stretch due to aerodynamic strain rate is given by:

$$\alpha_s = \frac{2u_g}{r_u}. \tag{2.7}$$

The aerodynamic strain rate describes the influence of gas flow dynamics on the flame, with faster gas velocities leading to increased stretching of the flame surface due to aerodynamic forces [44]. The spherical flame stretch due to curvature strain rate is given by:

$$\alpha_c = \frac{2u_n}{r_u}. \tag{2.8}$$

Where, $u_g$ is the gas velocity ahead of propagation spherical flame at $r_u$ and $u_n$ is the stretched laminar burning velocity. The curvature strain rate quantifies the influence of a flame's convex or concave shape on the rate at which its surface area stretches, directly linking flame geometry to its dynamic stretching behavior [44].

### 2.1.4 Laminar Burning Velocities and Markstein Length/Number

The laminar burning velocity, $u_l$ ,often termed as the “unstretched laminar burning velocity”, represents the burning rate in the absence of flame stretch effects [28]. The laminar burning velocity provides a measure of the overall reactivity of fuel-air mixtures,

describing the rate at which the unburned mixture is consumed by the flame. As a key parameter, it plays a crucial role in understanding various combustion phenomena, including flame stabilization, flame flashback, flame blowout, and flame extinction [52]. Beyond its significance in academic research, the laminar burning velocity is a fundamental physical property that is critical in practical combustion applications. It informs the design of gas turbines, burners, and spark ignition engines, and is essential in developing chemical kinetics mechanisms.

Numerous experimental studies have been conducted to investigate how pressure, temperature, and equivalence ratio influence the laminar burning velocity across various fuels. Specifically, Hu et al. [53], Verhelst et al. [54], and Xie et al. [55] focused on measuring the laminar burning velocity for hydrogen-air mixtures, varying temperature and equivalence ratio. In parallel, Takizawa et al. [56] and Halter et al. [57] explored these variables for methane-air mixtures. The investigation into ethane-air mixtures, particularly relevant to our current work, has seen extensive research. Notable contributions by Lowry et al. [58], Mitu et al. [59], Nilsson et al. [60], Goswami et al. [61], Ravi et al. [62], and Zuo et al. [63, 64] have thoroughly examined the effects of pressure and equivalence ratio on ethane-air flames. However, there remains a significant knowledge gap regarding the impact of temperature on the laminar burning velocity of ethane-air mixtures. This oversight is critical, especially considering the elevated temperatures typical of real-world applications in engines and gas turbines. Additionally, research on propane-air mixtures by Hassan et al. [65] and Jomaas et al. [66] contributes further to the breadth of knowledge in this domain.

From the principle of mass conservation and considering a one-dimensional planar flame, the volume flow rate of unburned mixture into the flame is given by $u_l\rho_u$ and the volume flow rate of burned gases away from the flame is represented as $S_s\rho_b$. This relationship can be expressed as:

$$u_l\rho_u = S_s\rho_b. \tag{2.9}$$

Thus, the laminar burning velocity is expressed as:

$$u_l = S_s \frac{\rho_b}{\rho_u}. \quad (2.10)$$

From Eq. 2.10, the $S_s$ is the key to determine $u_l$. The unstretched laminar flame speed, $S_s$, refers to the speed at which a flame propagates under conditions of zero stretch. However, the unstretched flame speed is only observed with an infinity flame radius. Consequently, extrapolation becomes necessary to determine $S_s$. Two methodologies have been employed to extrapolate $S_s$. The first one is the linear extrapolation method, which is extensively used in [22, 44, 46, 47, 49] and expressed as:

$$S_s - S_n = L_b \alpha. \quad (2.11)$$

The second method is the nonlinear extrapolation method emphasis on nonlinear variation of $S_n$ to $\alpha$ proposed by Kelley and Law [67] and this nonlinear extrapolation expressed as:

$$(\frac{S_n}{S_s})^2 ln(\frac{S_n}{S_s})^2 = -2\frac{L_b \alpha}{S_S}. \quad (2.12)$$

To better understand the effect of stretch rate on flame speed and the extrapolation method for $S_s$, variations of flame speed against the stretch rate were illustrated for different initial pressures and temperatures of the ethane-air mixture in Fig. 2.3. The $S_s$ is extrapolated flame speed at zero stretch rate. This is derived from a stable flame, utilizing either a linear or nonlinear relationship between $S_n$ and α. As show in Fig. 2.3, the # symbol shows the start of self-sustained propagation with free of spark energy and the critical radius $r_{cl}$ marks the onset of cellular instability for the condition 0.5 MPa, 300 K (details on laminar flame instability are explored in Section 2.1.5). Both linear (represented by a black solid line from Eq. 2.11) and nonlinear (denoted by a red dashed line from Eq. 2.12) extrapolations were employed to determine $S_s$. A comparison of the two methods reveals that they yield identical results for the unstretched flame speed.

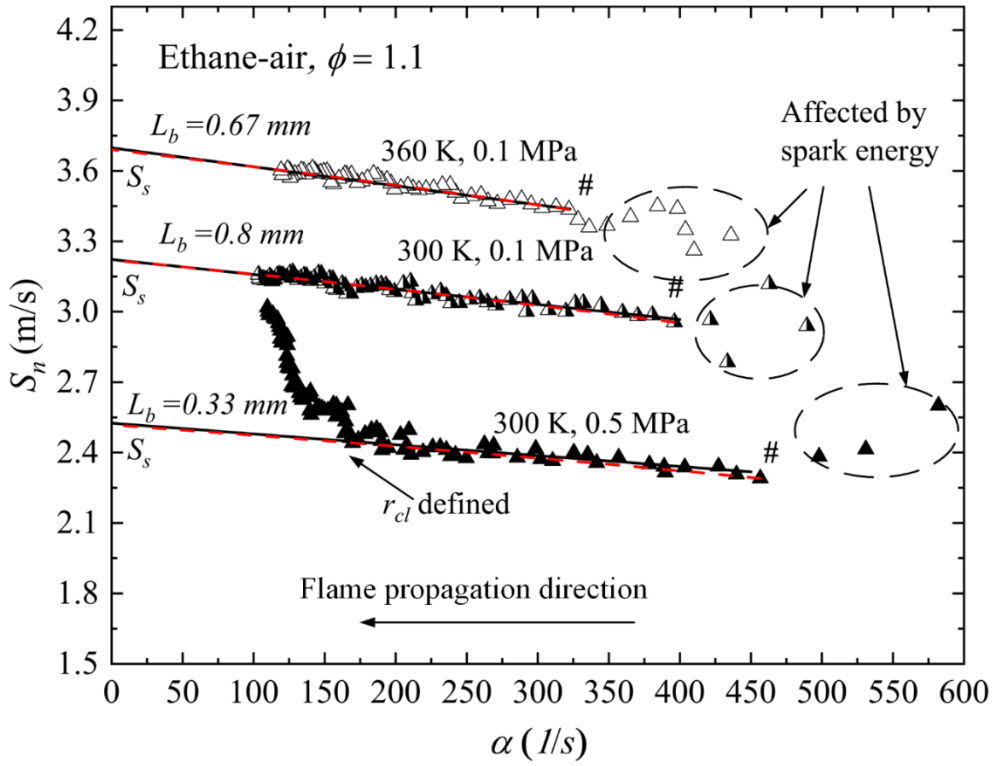


Figure 2.3. Variations of measured flame speeds, $S_n$, with stretch rate, $\alpha$, for the conditions of Figure 2.1.

The burned gas Markstein length, $L_b$, is derived from the gradient of straight solid lines in Fig.2.3 fit to the experimental data in the $S_n/\alpha$ relationship and is adopted here to present the effects of stretch rate on the flame speed. The burned gas Markstein number, $Ma_b$, is the dimensionless parameter and defined as the ratio of the Markstein length divided by the laminar flame thickness:

$$Ma_b = \frac{L_b}{\delta_l}. \tag{2.13}$$

The Markstein number is employed to characterize the influence of stretch on flame speed and the Markstein number also plays a pivotal role as a parameter in correlating with flame instability parameters [55,64,67,68].

### 2.1.5 Flame Instabilities

Flame instability in laminar conditions becomes evident when the flame is subjected to perturbations, resulting in the formation of cellular structures, as depicted in the third row of Fig. 2.2 at $r_{sch}$= 45 mm, the flame becomes unstable to perturbation and form cellular structures. These cellular structures enhance the flame's surface area, thereby increasing

the speed of flame propagation. As illustrated in Fig. 2.3, beyond the critical radius, $r_{cl}$, the flame displays instability and a notable jump in flame speed accompanied by cellular formations. The hydrodynamic theory of these laminar flame instabilities was first probed by Darrieus [69] in 1938 and subsequently by Landau [70] in 1944. Often referred to as the Darrieus-Landau instability, this hydrodynamic phenomenon arises from density discontinuities when the flame interacts with hydrodynamic disturbances. The effect of wave-like perturbation of a planar flame front is illustrated in Fig. 2.4. Within the flame reaction zone, disturbances arise due to the expansion of hot products and the formation of vortices. These disturbances cause the streamlines of incoming unburned gas to converge and diverge, leading to a wrinkled flame front. Should the flame front experience positive stretching, it could counterbalance the emerging instability. The Darrieus-Landau instability is governed by two parameters thermal expansion coefficient, $\sigma$, across the flame front and laminar flame thickness, $\delta_l$, where the $\sigma = \frac{\rho_u}{\rho_b}$ is the ratio of burned to unburned gas density.

Thermo-diffusive transport methods, which encompass both heat and mass fluxes as shown in Fig. 2.4, can also help in moderating this instability. Within Fig. 2.4, a solid arrow illustrates the heat flux moving from the burned mixture to the unburned one, whereas a dashed line represents the mass diffusive flux of the primary reactant transitioning from unburned to burned gas.

The Lewis number, $Le$, is introduced to represent the ratio of these heat and mass fluxes to show thermal-diffusive instability on a flames surface [44]:

$$Le = \frac{D_T}{D_M} = \frac{\lambda}{\rho_u c_p D_M}, \tag{2.14}$$

where, $\lambda$ is the thermal conductivity, $c_p$ is the specific heat at constant pressure, $D_m$ is the mass diffusive coefficient. The unity Lewis number indicated that the rates of thermal and mass diffusion are equal, leading to a flame that's considered diffusion-neutral. When $Le < 1$, mass diffusion of the fuel-air mixtures outpaces thermal diffusion, creating an unstable flame. This leads to a concentration of energy at the flame peak, amplifying the local burning velocity, whereas the opposite effect a reduction in burning

velocity and local temperature is seen in the trough due to the spreading gas flow. This makes the flame increasingly unstable. Conversely, when $Le > 1$, thermal diffusion of the fuel-air mixtures surpasses mass diffusion, representing a stable flame. In the trough, the flame front experiences a spreading effect, resulting in a decelerated burning velocity that steadies and evens out the flame surface.

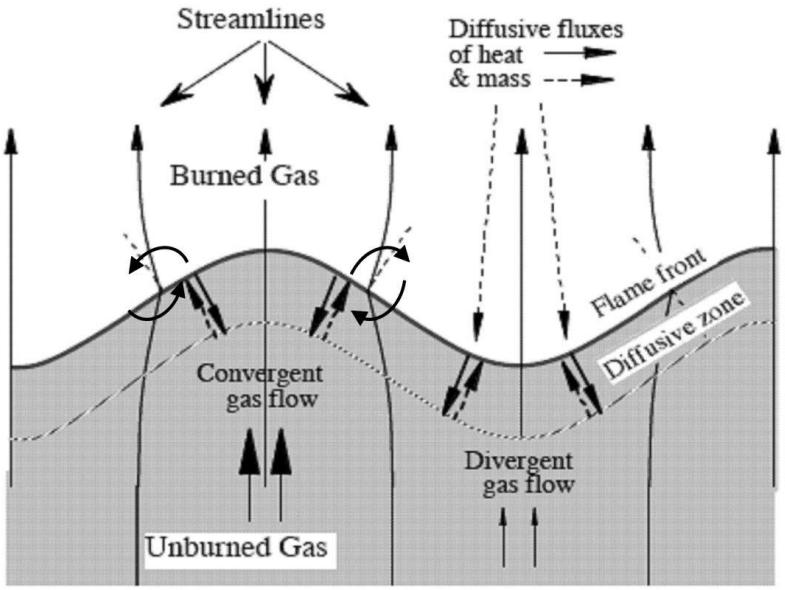


Figure 2.4. Structure of a wrinkled flame front, showing the hydrodynamic streamlines and the diffusive fluxes of heat and mass [71].

In the early stages of laminar premixed flame propagation, the flame endures a high stretch rate and this stretch rate diminishes as the flame propagates. Despite the high stretch rate, the laminar flame maintains a smooth spherical surface until its radius reaches a critical value, $r_{cl}$, where the flame instability creates a cellular flame structure [72]. As shown in Fig. 2.3 the of $S_n/\alpha$ relationship for ethane-air flame at 300 K, 0.5 MPa, this critical radius signifies the onset of cellular instability, marked by a notable increase in flame speed corresponding to the stretch rate. The Peclet number, $Pe_{cl}$, is applied here as the critical dimensionless group to quantify the onset of cellular instability and it expressed as the critical radius normalized with laminar flame thickness [44]:

$$Pe_{cl} = \frac{r_{cl}}{\delta_l}. \tag{2.15}$$

## 2.2 Turbulent Premixed Flames

Turbulent premixed flames have been a subject of intense research and practical interest ever since their first investigation by Mallard and Chaterlier in 1883 [73]. Later, Damkohler [74] reported that turbulent eddies significantly wrinkle the flame front, thereby augmenting the flame surface area and, consequently, the flame propagation speed. Turbulent premixed flames are highly relevant to various real-world applications, including gas turbines, internal combustion engines, and explosion hazards, e.g. DDT.

Serval studies have been conducted to report the turbulent flame characteristics of different fuels including hydrogen [75-79], methane [79-82], *i*-octane [79, 81, 82], ethanol [83], hydrogen-methane mixtures [80, 83], and ammonia-hydrogen mixture [84]. These studies aim to examine the impact of root mean square (r.m.s.) turbulent velocity, equivalence ratio, temperature, and pressure on the behavior of turbulent premixed flames. Despite the breadth of research, there appears to be a gap in the literature regarding the turbulent characteristics of ethane-air flames, to the best of our current knowledge.

In this study, the Leeds MK-II fan stirred combustion vessel with high speed Schlieren system was implemented to study the turbulence effect on the ethane-air premixed flame over a wide range of equivalence ratio, and effects of temperature and pressure. This aims to understand the temperature and pressure effects on the turbulent ethane-air flame and enable to predict the turbulent burning velocity at high temperature and pressure. Additionally, the conditions of relatively higher temperature and pressure examined closely resemble the operational environments of combustion engines and gas turbines. This section aims to explain the key aspects of turbulent premixed flames including turbulent length scales, turbulent combustion regime, turbulent flame reference radius, burning velocity, and the correlation for turbulent burning velocity.

### 2.2.1 Turbulent Length Scales and Root-Mean-Square Turbulent Velocity

Tennekes and Lumley [85] identified the characteristic of turbulent flow irregularity, diffusivity, large Reynolds numbers, three-dimensional, dissipation and continuum. As depicted in Fig. 2.5, a turbulent flow is inherently irregular and can be characterized by a

spectrum of three length scales, integral scale, $l$, Taylor micro scale, $\lambda$ and Kolmogorov scale, $\eta$, listed in descending order of size. A cascade process occurs wherein shear forces break down large eddies into intermediate-sized eddies, which then further disintegrate into the smallest eddies. Through the cascade process, the kinetic energy is transferred from largest scale to smallest scale through the interaction, and the kinetic energy of smallest scales eventually transformed into the thermal energy due to frictional forces [87].

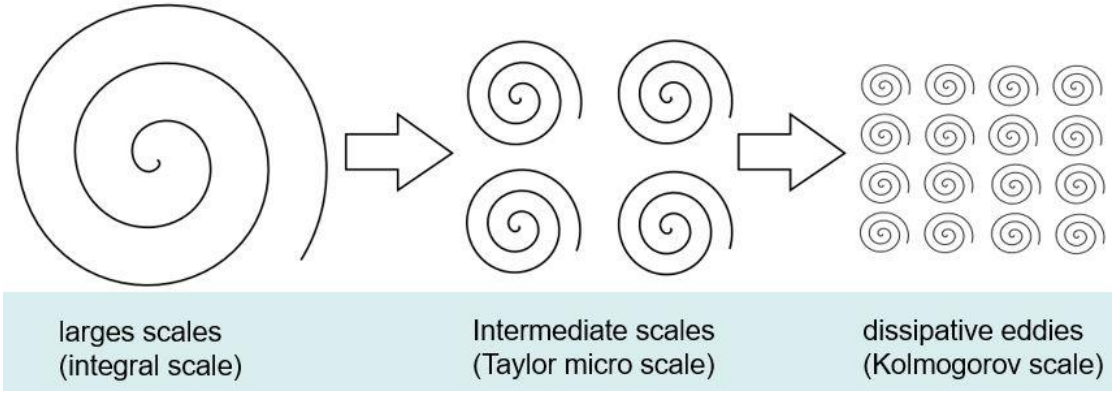


Figure 2.5. Cascade process with a spectrum of eddies [86].

The Kolmogorov scale is the smallest length scale where the turbulent kinetics energy is dissipated as heat by molecular viscosity and expressed as [88]:

$$\eta = (\nu^3/\varepsilon)^{0.25}, \tag{2.15}$$

where, $\nu$, is the kinematic viscosity and $\varepsilon$, is the dissipation rate.

The Taylor scale is the intermediate length scale and expressed as [89]:

$$\lambda = 15^{0.25} {R_\lambda}^{0.5} \eta, \tag{2.16}$$

where $R_\lambda$ is the Taylor scale Reynolds number is given by:

$$R_\lambda = \frac{u'\lambda}{\nu}. \tag{2.17}$$

The turbulent Reynold number, based on the integral length scale is defined as:

$$R_L = \frac{u'L}{\nu} \quad . \tag{2.18}$$

Thus, the integral length scale is:

$$L = \frac{\lambda R_\lambda}{A}. \tag{2.19}$$

Here A is a constant and A = 16 [89]. The integral length scale represents the largest scale

within filed, characterized by the mean dimension of eddies that most substantially influence the kinetic energy within turbulent flows [87]. The integral length scale is defined as the integral of the autocorrelation function of the velocity fluctuations and given by:

$$l = \int_0^\infty R_{uu}(r)\, dr = \int_0^\infty \frac{\overline{u'(x)u'(x+r)}}{u'(x)^2}\, dr \tag{2.20}$$

Here $R_{uu}(r)$ is the autocorrelation function and this function measures the correlation between velocity fluctuations at two locations separated by distance $r$. The $u'(x)$ is the velocity fluctuation at position x, $u'(x+r)$ is the velocity fluctuation at a position a distance $r$ away from $x$, $r$ is the separation distance between two points in the flow field for which we are evaluating the correlation.

In turbulent premixed flames, the burning velocity is predominantly governed by the root-mean-square turbulence velocity. At any given point within the turbulent flow, velocity components in x, y and z directions exhibit temporal fluctuations. As illustrated in Fig. 2.6, the instantaneous velocity $U$ comprises two components: the mean velocity, $\bar{u}$, and a fluctuating component, $u$ [90]:

$$U(t) = \bar{u} + u(t). \tag{2.21}$$

Similarly, for the y and z direction the expressions are: $V(t) = \bar{v} + v(t)$ and $W(t) = \bar{w} + w(t)$.

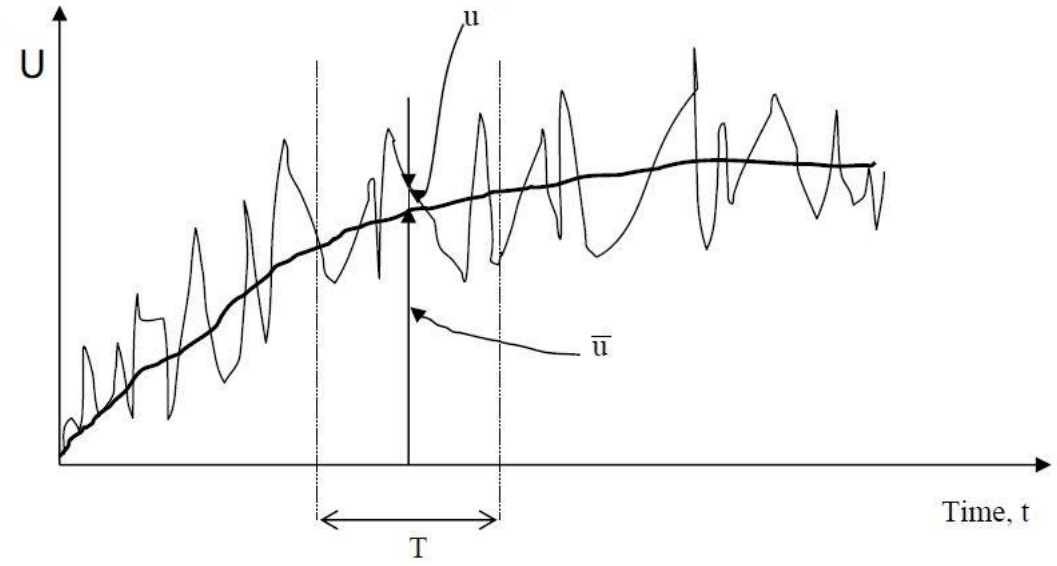


Figure 2.6. Schematic description of velocity variation alone x direction as function of

time [89].

The mean velocity, $\bar{u}$, is computed as the average of $N$ instantaneous velocities, $U(n)$, given by:

$$\bar{u} = \frac{1}{N}\sum_{n=1}^{N} U(n) \tag{2.22}$$

The rms turbulent velocity, $u'$, is defined as:

$$u' = \sqrt{\frac{\sum u(n)^2}{N}} \tag{2.23}$$

In the case of homogeneous and isotropic turbulence, where $u' = v' = w'$, the total RMS turbulence velocity, $U'$, can be simplified to:

$$U' = \sqrt{((u')^2 + (v')^2 + (w')^2)/3} = u' \tag{2.24}$$

Thus, for the isotropic turbulence the $u'$ is equal to $U'$.

### 2.2.2 Turbulent Combustion Regimes

Various diagrams and methodologies have been proposed to classify premixed turbulent flames into different regimes [91-95]. One of the most commonly used is the Peter-Borghi diagram [93,94]. This diagram employs laminar flamelet method, utilizing two ratios $\frac{u'}{u_l}$ and $\frac{L}{\delta_l}$ to identify premixed combustion region as shown in Fig. 2.7. The ratio, $\frac{u'}{u_l}$, quantifies the magnitude of the eddy turnover velocity relative to the laminar burning velocity. The ratio, $\frac{L}{\delta_l}$ measures the size of turbulent eddies in terms of integral length scale relative to the laminar flame thickness. Larger eddies tend to wrinkle the flame surface, whereas eddies smaller than the flame thickness primarily exist within the reaction zone, contributing to localized heat and mass diffusion processes.

The Peter-Borghi diagram classifies premixed turbulent flames into four distinct regimes based on three dimensionless parameters: the turbulent Reynolds number ($R_L$), turbulent Damköhler number ($D_a$), and turbulent Karlovitz number ($K$). The Damköhler number represents the ratio of eddy lifetime to chemical lifetime, given by [97]:

$$D_a = (L/u')/(\delta_l/u_l). \tag{2.25}$$

The Karlovitz number is based on the Kolmogorov turbulent scale and expressed as [97]:

$$K = (\delta_l/u_l)/(\eta/u_\eta). \quad (2.26)$$

where $u_\eta$ is the eddy turnover velocity on the Kolmogorov scale and given by [97]:

$$u_\eta = 15^{0.25} u'/{R_\lambda}^{0.5}. \quad (2.27)$$

In the Peter-Borghi diagram, flames with $R_L < 1$ are considered laminar and exist where both $\frac{u'}{u_l}$ and $\frac{L}{\delta_l}$ are small. The unity value of $R_L$ separate the laminar and turbulent flames. Two subtypes within the flamelet regime are the wrinkled and corrugated flamelets and both are characterized by the relation $R_L > 1$ (turbulence), and $K_a < 1$. In this region, the chemical lifetime is shorter than the eddy lifetime on the Kolmogorov scale, resulting in minor wrinkling but no significant changes to the flame's internal structure. The transition between wrinkled and corrugated flamelets is defined by the unity value of $\frac{u'}{u_l}$.

For the wrinkled flamelet, here $u' < u_l$, and the flame structure is slightly wrinkled as it interacts with the eddies. For the corrugate flamelet, conversely $u' > u_l$, indicating a more intense interaction between the flame front and the eddies, which corrugates the flame surface.

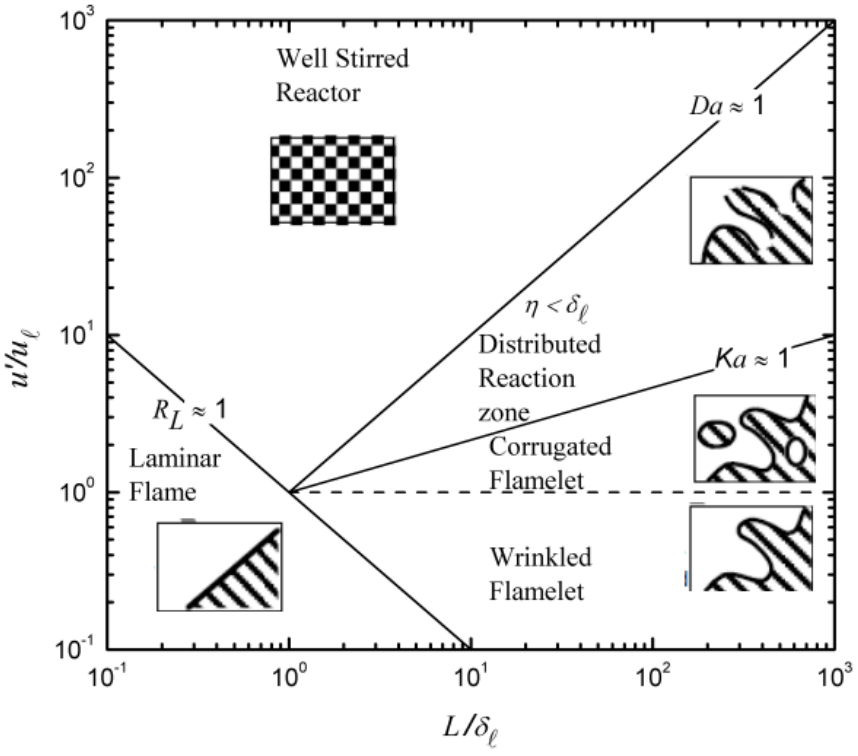


Figure 2.7. Peter-Borghi's diagram of turbulent combustion regimes [96].

In the distributed reaction zone, $K_a$ > 1 and $D_a$> 1, and thus, $\frac{L}{u'} > \frac{\delta_l}{u_l} > \frac{\eta}{u_\eta}$. In this regime, the time scale of chemical reactions is longer than the lifetime of the smallest, Kolmogorov-scale eddies. Consequently, these minuscule eddies can penetrate the flame thickness, enhancing both heat and mass transfer rates. The chemical reaction time is insufficient to fully consume the smallest eddies before they disintegrate, thereby fragmenting the reaction zone.

In the well-stirred reactor regime, $K_a$ > 1 and $D_a \leq 1$, and thus, $\frac{\delta_l}{u_l} > \frac{L}{u'} > \frac{\eta}{u_\eta}$. Here, the chemical lifetime is longer than the lifetime of the integral-scale eddies. This allows turbulent eddies of all sizes to penetrate the preheat zone, significantly increasing the heat and mass transfer rates. Such enhancement leads to a rapid decrease in flame temperature, ultimately resulting in flame extinction. In this study, the turbulent ethane-air flames are positioned within the turbulent combustion regimes diagram, as shown in Chapter 5, Figure 5.15, encompassing both the corrugated flamelet and distributed reaction zone regimes. Furthermore, simulations of large-scale, open-space ethane-air turbulent flame propagation in Chapter 6, including DDT, commence with a laminar flame front. Interaction with baffles introduces turbulence, catalyzing a progression through various stages: from wrinkled flamelets to corrugated flamelets, then to distributed reaction zones, and potentially concluding in a well-stirred reactor scenario.

### 2.2.3 Turbulent Reference Radius and Turbulent Burning Velocities

Compared to laminar premixed flames, turbulent premixed flames burn more rapidly, due to the presence of large turbulent eddies that wrinkle the flame surface. This wrinkling effect increases the effective surface area for combustion, as seen in the Schlieren images of ethane-air turbulent premixed flames shown on the right side of Fig. 2.8. The wrinkled flame surface complicates the definition of key parameters such as flame surface, flame radius, and burning velocity of turbulent flame. To address these complexities, several definitions of premixed turbulent flame and their associated surface have been proposed [98-101].

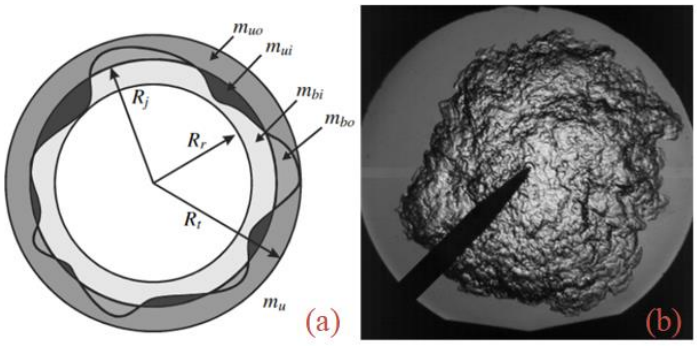


Figure 2.8. Reference radii, associated masses of burned and unburned gas (a) [69] and Schlieren image (b).

Bradley et al. [98] employed both Mie scattering and Schlieren imaging techniques to investigate the distribution and surface definition of premixed turbulent flames. The schematic of a typical premixed turbulent flame is illustrated in Fig. 2.8 (a), where three distinct radii are defined: $R_j$, $R_r$ and $R_t$. Here, $R_t$ and $R_r$ represents the outermost tip and the innermost root radius, respectively. The mixture inside $R_r$ are all burned and outside $R_t$ remains unburned. While $R_j$ serves as a reference radius for the analysis. The mass variables $m_{bi}$, $m_{bo}$, $m_{ui}$ and $m_{uo}$ represent the masses of burned and unburned gases inside and outside the reference radius $R_j$.

According to the study by Bradley et al. [98], the volumetric turbulent burning velocity denoted as $u_{tr}$ is obtained when the $R_j$ is set equal to the volumetric reference radius, $r_v$. If the total volume of burned gas outside the sphere with $r_v$ is equal to total volume of unburned gas inside it, $m_{ui}\rho_u = m_{bo}\rho_b$, then the $u_{tr}$ can be expressed as:

$$u_{tr} = \frac{\rho_b}{\rho_u}\frac{dr_v}{dt}. \tag{2.28}$$

Fortunately, the measurements [98] compared both $r_v$ and $r_{sch}$, and demonstrated that the $u_{tr}$ from Schlieren measurements can be expressed as:

$$u_{tr} = \left(\frac{1}{1.11}\frac{\rho_b}{\rho_u}\right)\frac{dr_{sch}}{dt}. \tag{2.29}$$

Equation 2.29 is employed in the present work for determining the volumetric turbulent burning velocity.

### 2.2.4 Effective Turbulent RMS Velocities

Abdel-Gayed et al. [102] and Bradley et al. [103] conducted experimental studies on

turbulent flame propagation in combustion vessels. They observed that the turbulent propagation speed continually increases as the flame radius grows. These studies also highlighted that the wrinkling of the turbulent flame surface is influenced by increasing wavelengths of turbulence. To better quantify this behavior, Bradley et al. [103] introduced a new parameter known as the effective rms turbulence velocity, $u_k'$. This parameter effectively quantifies the wrinkling of the flame and is found to be less than the $u'$. As $u_k'$ approaches $u'$ the flame grows large enough to engulf the entire turbulent spectrum. Consequently, the ratio of $u_k'/u'$ represents the fraction of entire turbulence spectrum contributes to the wrinkling and this ratio is related to the power spectral density as follows:

$$u_k' = u'[\frac{15^{0.5}}{R_\lambda}\int_{\bar{k}_{\eta 1}}^{\bar{k}_{\eta 2}} \bar{S}(\bar{k}_\eta) d\bar{k}_\eta]^{0.5}. \quad (2.30)$$

The dimensionless power spectral density, $\bar{S}(\bar{k}_\eta)$, is based on the Kolmogorov length scale and is a function of a dimensionless wave number $\bar{k}_\eta$. This dimensionless wave number is derived from the wave number multiplied by the Kolmogorov length scale, $\eta$. where the upper limit, $\bar{k}_{\eta 2}$, corresponds to the smallest possible wavelengths and the lower limit, $\bar{k}_{\eta 1}$, represents the largest wavelengths close to the diameter of the flame. The expression of $\bar{S}(\bar{k}_\eta)$ is expressed as [103]:

$$\bar{S}(\bar{k}_\eta) = \frac{0.01668{R_\lambda}^{2.5}+3.74{R_\lambda}^{0.9}-70{R_\lambda}^{-0.1}}{1+(0.127{R_\lambda}^{1.5}\bar{k}_\eta)^{5/3}+(1.15{R_\lambda}^{0.622}\bar{k}_\eta)^4+(1.27{R_\lambda}^{0.357}\bar{k}_\eta)^7}, \quad (2.31)$$

$\bar{k}_\eta$ is the dimensionless wavenumber, written as [89]:

$$(\bar{k}_\eta) = \frac{2\pi\eta}{\eta_k L} = (\frac{32\pi}{15^{0.25}\eta_k}){R_\lambda}^{-1.5}. \quad (2.32)$$

Here, $\eta_k$ represents the wavelength, calculated using the formula $\eta_k = 2r_{0.5}/L$, where $r_{0.5}$ is the mean turbulent flame radius. In this study $r_{0.5}$ is equivalent to $r_v$. Figure 2.9 below illustrates the relationship between $u_k'/u'$ and $\eta_k$ for different values of $R_\lambda$ in an ethane-air mixture. The ratio of $u_k'/u'$ exhibits an increasing trend as $\eta_k$ increases, indicating that $u_k'$ also increases with the enlargement of the turbulent wavelength. Given that $\eta_k$ is a function of $r_v$, and in the context of turbulent flame propagation, it follows that the turbulent wavelength increases alongside $r_v$.

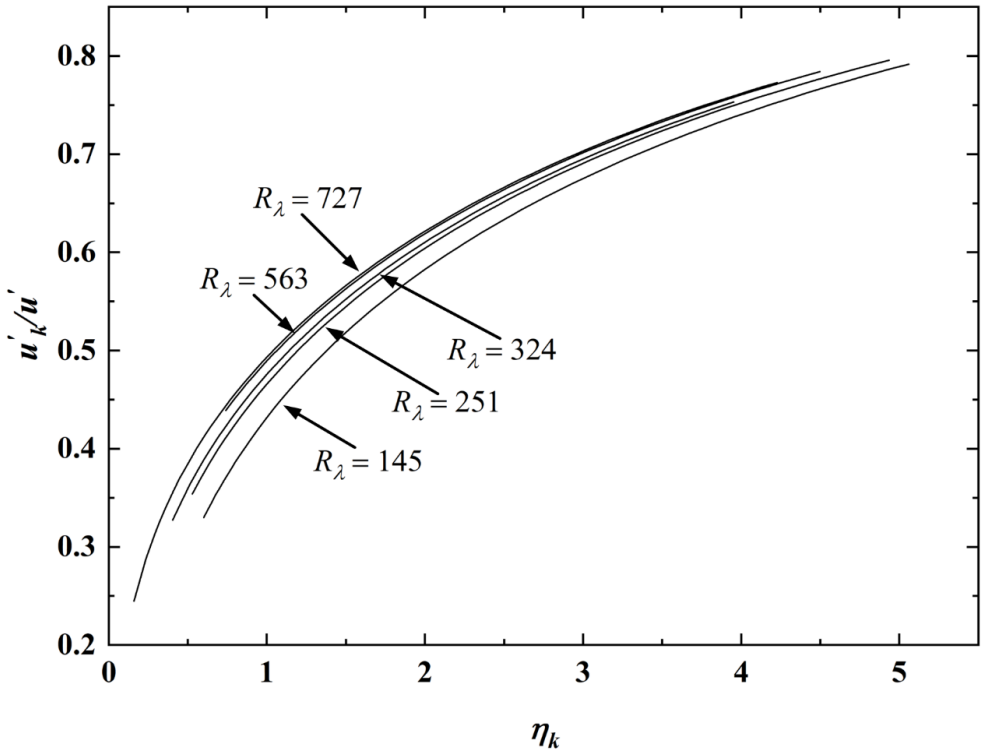


Figure 2.9. Variation of $u_k'/u'$ with increasing $\eta_k$ for different $R_\lambda$ for ethane-air mixture.

### 2.2.5 Turbulent Burning Velocities Correlations

In contrast to laminar flames, evaluating turbulent flames is more complex due to numerous variables that influence them. Over the years, various correlations and empirical models have been proposed to estimate turbulent burning velocity [104-107]. Damköhler [104] firstly reported that an increasing $u'$ leads to greater wrinkling of the flame front, thereby augmenting its surface area. He postulated a direct proportional relationship between the turbulent to laminar burning velocity ratio, $u_t/u_l$, and the flame surface area ratio, $A/a$. Building on this, Clavin and Williams [105] presented a straightforward equation to describe the relationship:

$$\frac{u_t}{u_l} = 1 + (\frac{u'}{u_l})^2. \tag{2.33}$$

Subsequently, Abdel-Gayed et al. [102] introduced a correlation involving the dimensionless Karlovitz number, $K$, backed by extensive turbulent burning velocity data. This correlation was further refined by Bray [106], who suggested that the dimensionless, $u_t/u_l$, should be correlated with $K$ multiplied by $u'/u_l$ and expressed as:

$$\frac{u_t}{u_l} = 0.875K^{-0.392}u'/u_l. \quad (2.34)$$

Most recently, Bradley et al. [107] conducted comprehensive experiments using seven different fuels under varying conditions, including equivalence ratios and pressures up to 3.5 MPa. A new correlation between $u_t/u_k{}'$ and $K$ to highlight the effectiveness of turbulence in increasing flame surface wrinkling and effects of strain rate on the turbulent flame, expressed as:

$$U = \frac{u_t}{u_k{}'} = \alpha K^{\beta}, \quad (2.35)$$

where $\alpha$ and $\beta$ are constants, these two constants are function of the strain rate Markstein number, $Ma_{sr}$. For positive $Ma_{sr}$:

$$\alpha = 0.023(30 - Ma_{sr}), \quad (2.36)$$

$$\beta = 0.0103(Ma_{sr} - 30). \quad (2.37)$$

For the negative $Ma_{sr}$:

$$\alpha = 0.085(7 - Ma_{sr}), \quad (2.38)$$

$$\beta = -0.0075(Ma_{sr} + 30). \quad (2.39)$$

The Karlovitz number, $K$, is the ratio of chemical reaction time, $\delta_l/u_l$, to the turbulent eddy time based on the Taylor length scale, $\lambda/u'$ and expressed as:

$$K = (\delta_l/u_l)/(\lambda/u') \ . \quad (2.40)$$

where $\lambda$ is the Taylor length scale, and for the isotropic turbulence the relationship to Taylor length scale into integral length scale, $L$, is:

$$\frac{\lambda^2}{L} = \frac{Av}{u'}. \quad (2.41)$$

The constant integral length scale, $L$, is given as 20 mm in the Leeds MK-II combustion vessel based on the PIV measurements in [108]. By combining Eq. 2.41 into Eq. 2.40, $K$ can be expressed as a function of the integral length scale:

$$K = 0.25(u'/u_l)^2(u'L/v)^{-0.5}. \quad (2.42)$$

As depicted in Fig. 2.10, the turbulent burning velocity calculated based on Eq. 2.35 and commonly referred to as the *U/K* diagram is categorized into three distinct regimes: A, B, and C.

- Regime A ($K < 0.1$): This regime characterizes unstable laminar flamelets, where

wrinkling primarily occurs due to instabilities in the flame structure.

- Regime B ($0.1 < K < 1$): within this range, the turbulence enhancement increases with increasing $K$ and $U$ also increases as $Ma_{sr}$ become increasingly negative.
- Regime C, $K > 1.0$, this remains less well-defined. However, it is noteworthy that beyond a certain threshold indicated by the dotted lines in Fig. 2.10, flame quenching begins to develop at high $K$ values.

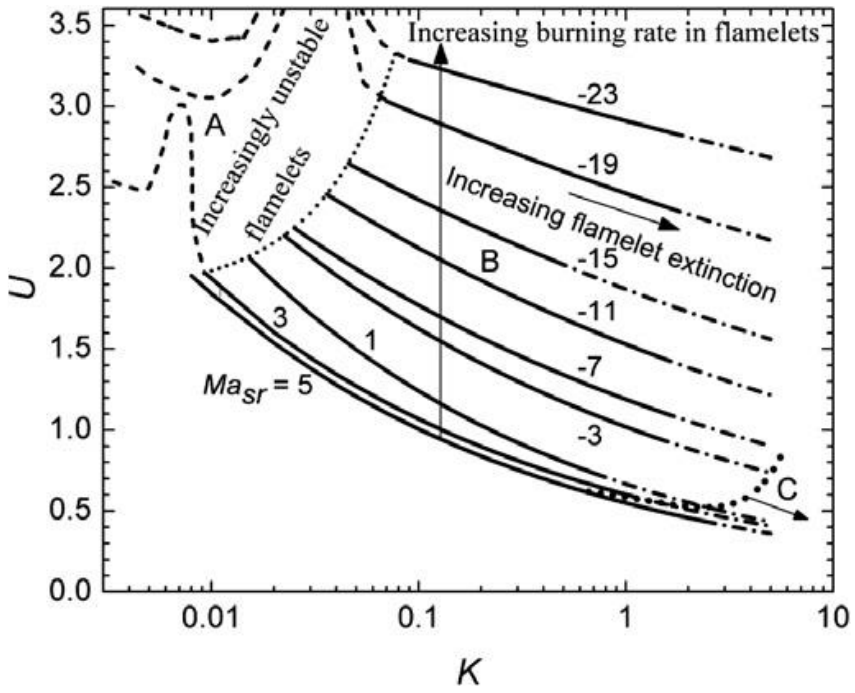


Figure 2.10. The turbulent combustion regime based on *U/K* correlation [107].

However, the *U/K* turbulent burning velocity correlation faces limitations in its practical application, as accurately measuring $Ma_{sr}$ has proven to be a significant challenge. Previous experimental efforts to quantify $Ma_{sr}$ have encountered considerable variability and wide error margins, leading to results with a relatively low coefficient of determination, $R^2$, which ranges between 0.66 and 0.88 [107]. Such inconsistency underscores the need for a simplified and improved correlation that more effectively captures the dynamics of ethane-air combustion and its role in turbulent flame propagation modeling. For a comprehensive explanation of the ethane-air *U/K* turbulent burning velocity correlation, readers are directed to Section 5.3.7.

## 2.3 Autoignition and DDT

Within the intricate landscape of combustion phenomena, autoignition and detonation emerge as particularly noteworthy, given their vital roles in scenarios ranging from combustion engine operation to the mechanics of explosive events. These processes significantly different from the behaviors of laminar and turbulent deflagration flames, typically taking place under conditions of elevated temperatures and pressures. This section provides a comprehensive overview of the autoignition process and its key parameters such as ignition delay time and chemical excitation time. And it also explores the structure of the detonation wave and outlines the mechanisms underlying the DDT. Concluding the section, a theoretical $\xi$ - $\varepsilon$ detonation peninsula diagram, employed to quantify various autoignition modes, is discussed in detail.

### 2.3.1 Autoignition and Engine Knock

Autoignition is the spontaneously self-ignition process of the fuel-air mixture when reaching a threshold temperature and pressure [109]. This phenomenon initiates a series of chemical chain-branching reactions sustained by thermal feedback. The exothermic nature of these reactions elevates the temperature, which in turn accelerates the overall reaction rate. Initially, chain-branching begins with slow thermal reactions that generate a pool of reactive radicals within the system. These radicals expedite the oxidation of additional fuel species and their corresponding oxidation products, perpetuating the creation of even more radical species via chain-branching reactions. As the concentration of radicals increases, so does the overall rate of the reaction, culminating in a rapid, explosive surge in temperature, radical concentrations, and oxidation rates. At this point, autoignition has occurred.

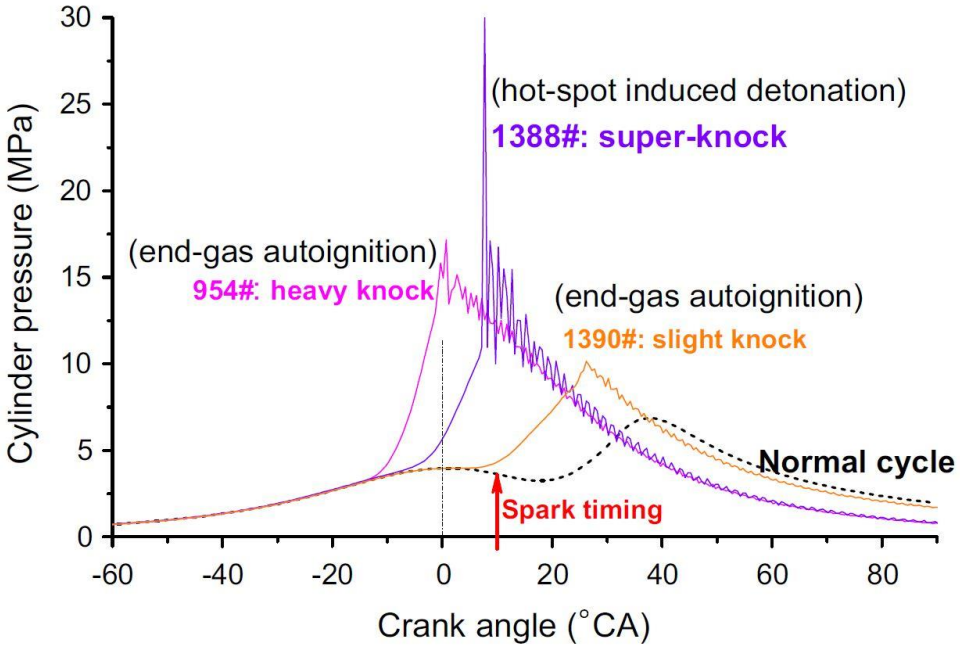


Figure 2.11. Typical knock-free, knock and super-knock pressure curve [113].

Engine knock refers to an abnormal autoignition process within the engine and is a significant combustion phenomenon that restricts the application of higher compression ratios in modern, thermally-efficient engines [110]. It is widely accepted that engine knock is caused by strong autoignition in the unburned fuel-air mixture, which occurs before this mixture can be ignited by the primary flame front originating from the initial ignition point [111-116]. Figure 2.11 from [113] illustrates the typical pressure curves for knock-free, knock, and super-knock conditions across various cycle numbers. A knock-free pressure cycle features a smooth curve, indicative of the absence of pressure oscillations. Conversely, knock, demonstrated by cycle No. 1390, shows pronounced pressure oscillations due to end-gas autoignition, while the heavy knock condition, represented by cycle No. 954, exhibits slightly less pronounced pressure oscillations. The super-knock scenario, identified with cycle No. 1388, is marked by a significantly large amplitude of pressure oscillations, attributed to detonation induced by hot spots. Engine knock can be explained as a situation where the expansion of the primary flame compresses the unburned fuel-air mixture to a point where both temperature and pressure exceed its autoignition threshold, resulting in end-gas autoignition. This phenomenon triggers oscillating pressure waves within the combustion chamber. Super knock is a more

severe form of engine knock, characterized by substantial pressure oscillations with significant amplitude changes. It is primarily associated with hot spot-induced detonation. Studies of super knock visualization [114-116] have reported that the super knock is initiated by a transition to detonation. Following this transition, a shock wave forms and reflects between the cylinder walls within the combustion chamber. These impact pressures, though short in duration, are high in magnitude.

### 2.3.2 Ignition Delay Time Measurements

The ignition delay time, $\tau_i$, serves as a key metric for characterizing autoignition behavior. Ignition delay time (IDT) is the time interval required for a fuel-oxidizer mixtures to react at specific temperature and pressure conditions. $\tau_i$ is a parameter that typically varies with temperature, pressure, equivalence ratio, and the type of fuel. Various methods can be used to measure $\tau_i$ such as flow/jet reactors [117-119], shock tubes [120-123], and RCMs [124-126]. Figure 2.12 illustrates the thermal operating conditions of these experimental devices. Jet reactors operate within a low-to-intermediate temperature range of 500 to 1200 K, but they are limited to lower pressures of up to 30 bar. RCMs cover a similar temperature range but extend to a wider pressure range, reaching up to 80 bar. In contrast, shock tubes can operate in an intermediate-to-high temperature regime, ranging from 800 K to 1500 K, and also accommodate pressures up to 80 bar. The transition to detonation in engine conditions is favored at temperatures above around 900 K and pressures exceeding 1 MPa [113]. However, these thermal conditions vary with different fuels and equivalence ratios, while the operational conditions of RCMs are within the scope that facilitates this transition to detonation. In theory, an ideal RCM serves as a homogeneous reactor, designed to achieve adiabatic compression of a specific fuel-air mixture through rapid piston movement, reaching predetermined temperature and pressure conditions. At the end of compression (EOC), the piston is held in place, stabilizing the combustion chamber pressure and temperature. This setup enables the direct observation of the fuel mixture's autoignition behavior through the measurement of the reaction chamber pressure. A detailed description of the Leeds optical RCM is provided in Section 3.2.

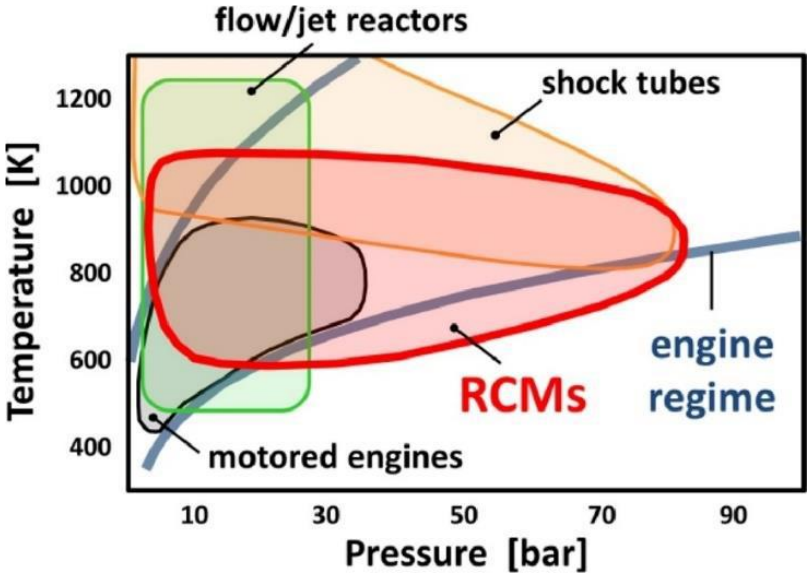


Figure 2.12. Typical temperature and pressure regimes covered by the operating conditions of various experimental devices [127].

Both OH radical emissions [123, 128] and pressure traces [129-134] are employed as reliable indicators for determining the ignition delay time. While OH radicals are commonly utilized in shock tube experiments due to their role as combustion products that signify the onset of autoignition, pressure traces are indicators used in both RCMs and shock tubes to pinpoint the commencement of ignition.

In the RCM experiments, Figure 2.13, derived from results in Chapter 4, depicts a typical pressure trace. In this instance, the piston rapidly compresses the mixture, achieving an EOC pressure of 2 MPa, which is then maintained at a constant level. The beginning of autoignition is clearly evidenced, marked by a pressure increase to approximately 2.6 MPa, signaling the start of ignition. This precise moment of transition highlights the critical phase of the experiment, providing valuable insights into the ignition process under controlled conditions. The ignition delay time, $\tau_i$ was defined as the time between the end of compression and the point at which the maximum gradient of the pressure rises (*dP/dt*) and this definition is widely adopted in [129-134].

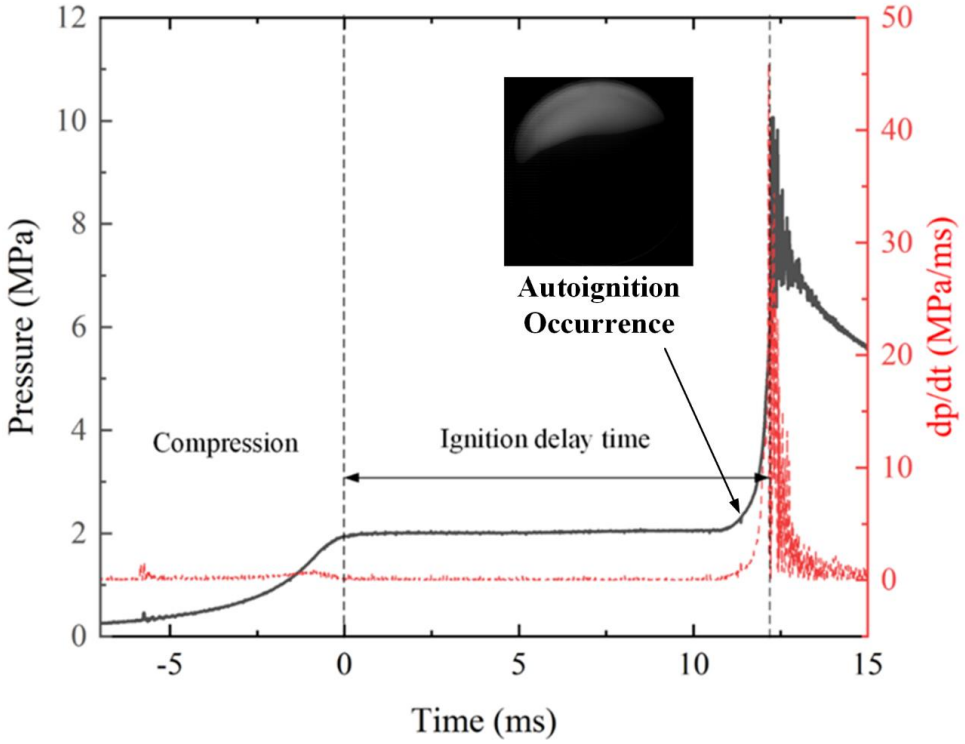


Figure 2.13. Typical pressure (black solid) and pressure derivative (red dashed) time history for *i*-octane-oxygen mixtures at 900 K, 2.0 MPa.

### 2.3.3 Negative Temperature Coefficient

The Negative Temperature Coefficient (NTC) regime represents a unique region in hydrocarbon oxidation where, counterintuitively, the overall reaction rate decreases as temperature rises. This behavior is opposite to the Arrhenius temperature dependence, which typically dictates a monotonic increase in the global reaction rate with increasing temperature [134]. Figure 2.14, derived from Chapter 4, displays the measured ignition delay times for stoichiometric *i*-octane-oxygen mixtures at varying end-of-compression temperatures, specifically focusing on the NTC regime (spanning 715 K to 830 K). In this NTC regime, the ignition delay time $\tau_i$ increases with the rising temperature. In contrast, in the normal temperature regime $\tau_i$ decreases as temperature increases.

Frédérique's study suggests that the emergence of the NTC zone is intricately tied to specific behaviors in alkane oxidation, notably the occurrence of 'cool flames' around a temperature of 650 K [135]. These cool flames manifest as single or multiple minor temperature fluctuations accompanied by faint blue light emissions, primarily from excited formaldehyde. At the level of chemical kinetics, NTC is primarily attributed to

the increased reversibility of the alkyl radical's reaction with oxygen, represented as $R\cdot + O_2 \leftrightarrows ROO\cdot$ [135]. Understanding the NTC phenomenon is essential for the validation of chemical kinetic models. Some researchers even postulate that the NTC effect could influence the transition to detonation or reduce the initiation length scale required for detonation [136]. Although the fundamentals of chemical kinetics related to NTC are not explored in the RCM experiments in Chapter 4, the unique characteristics of autoignitive propagation speed within the NTC regime are discussed.

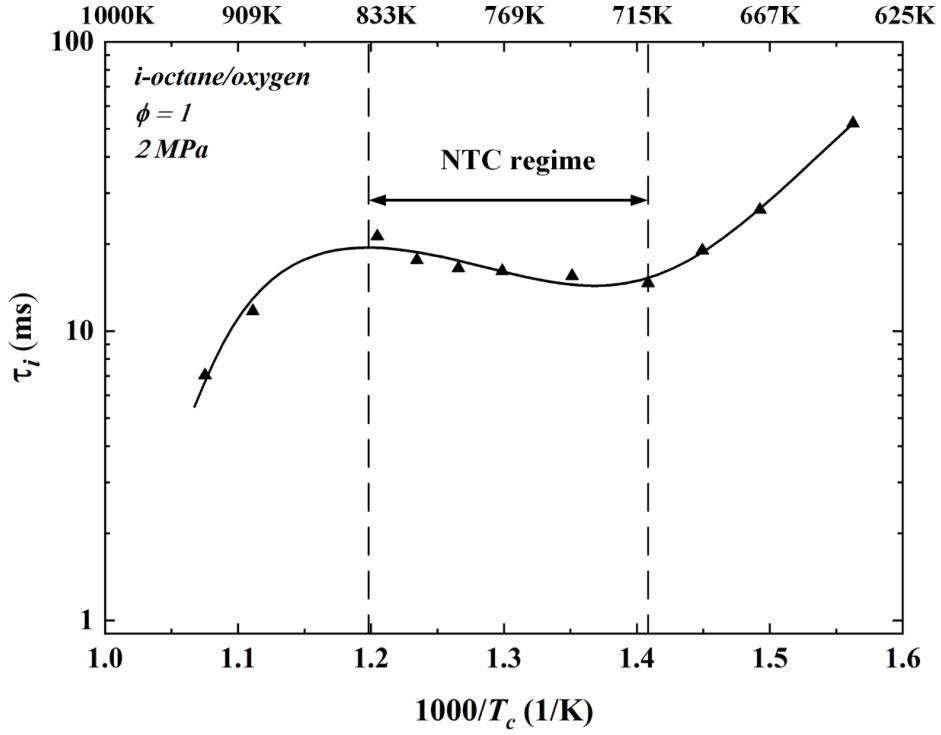


Figure 2.14. The measured logarithm ignition delay time of stoichiometric *i*-octane-oxygen mixtures at end of compression pressure with inverse temperature.

### 2.3.4 Deflagration to Detonation Transition

Deflagration describes a subsonic mode of combustion in which chemical reactions largely take place at a constant pressure. In contrast, the detonative mode of combustion is marked by supersonic front propagation speeds. In this latter case, the chemical reactions occur due to adiabatic shock heating, resulting in a tightly coupled relationship between the shock wave and the subsequent reaction zone [136]. Figure 2.15 presents a two-dimensional structure of detonation wave formed by the intersection of transverse shock waves with the leading shock front. The formation of cell boundaries is a

consequence of the intersection between transverse shocks and the main shock wave, creating triple-point Mach configurations. Originating at these cellular interfaces, layers of shear and new transverse shocks move into the following reactive area. These shocks travel sideways over the main shock wave, where they encounter and occasionally merge with reactive layers. This interaction is especially noticeable near the image's midpoint. Additionally, these interactions with the shock waves induce variability in the front of the leading shock, which results in its wavelike motion along the path of propagation. This motion manifests as a sequence of strong Mach reflections and weaker incident shocks.

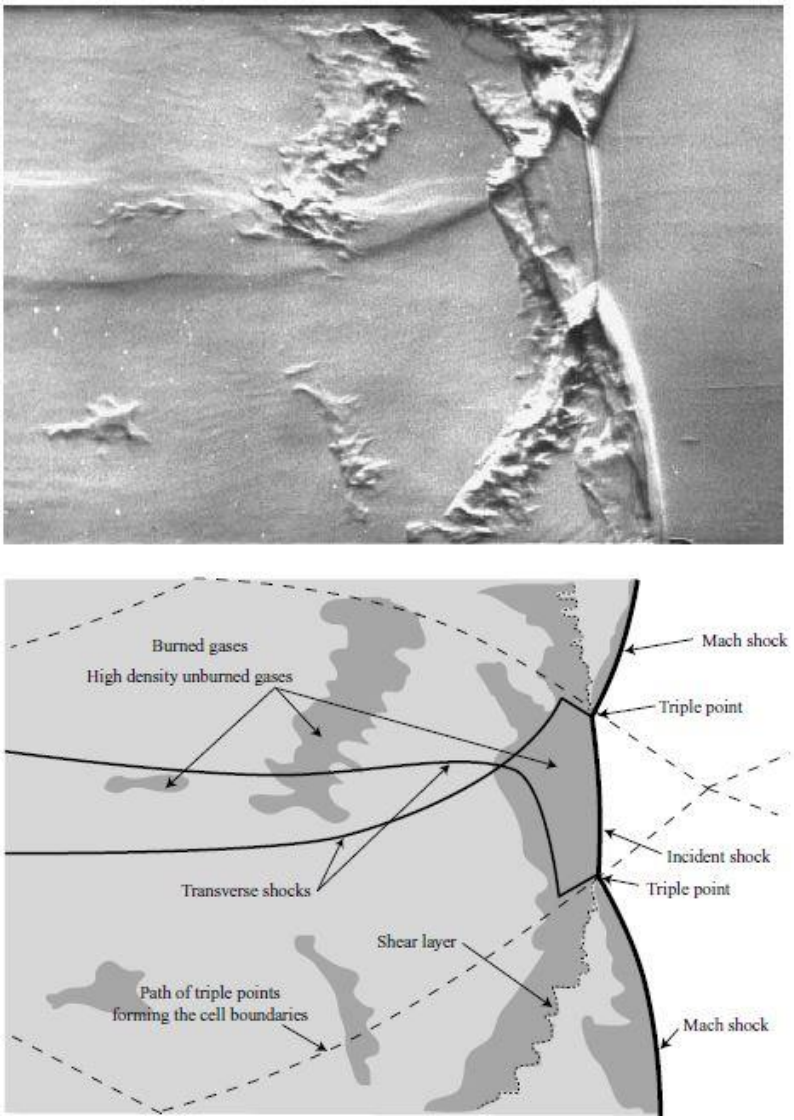


Figure 2.15. Schlieren photograph (top) and explanatory sketch (bottom) of detonation structure in a cross-section channel [126].

To unravel the mechanisms underlying the transition from deflagration to detonation

(DDT), early studies by Merzhanov [137] and Borisov [138] highlighted the role of hot spot could lead to detonation. Later on, a more general gradient concept was proposed by Zeldovich [139], showing that the autoignitive velocity coupling with acoustic velocity indicating the transition to detonation. Drawing inspiration from Zeldovich's theory, Gu and Bradley [140] proposed the detonation peninsula diagram with ξ and ε to quantify the detonation regime. Recently, the focus has shifted towards the role of turbulence in flame acceleration and DDT. The theoretical calculation of Bradley et al. [16] reported that the maximum turbulent burning velocity creates the shock wave formed ahead of flame, and if the shock wave is strong enough, it compresses the unburned mixture into autoignition induced detonation. The numerical simulation conducted by Oran and Gamezo [6] demonstrated that the DDT in the baffled tube is initiated by the auto-ignition of hot spots, while turbulence and shock waves create conditions conducive to the formation of these hot spots. As the expanding flame front interacts with obstacles, turbulence is generated, which in turn wrinkles the flame front. This wrinkling increases the effective surface area of the flame, thereby enhancing the turbulent burning velocity. When the turbulent burning velocity becomes sufficiently high, it generates a strong shock wave ahead of the flame. This shock wave compresses the unburned mixtures in front of it, leading to the initiation of detonation.

### 2.3.5 $\xi$ - $\varepsilon$ Detonation Peninsula Diagram

This section describes the theoretical method referring to the dimensionless $\xi$ - $\varepsilon$ detonation peninsula, which is employed to study autoignition modes. This approach is based on the Zeldovich hot spot theory [139], which calculates the reaction wave propagation speed based on the gradient of $\tau_i$ with temperature and temperature gradient alone a hot spot. Later on, Gu, Bradley and Bates [19,20,111] developed and categorized this approach into the different regimes using two dimensionless parameter $\xi$ and $\varepsilon$. Due to its effectiveness, this approach has gained significant popularity and stands as a primary method for investigating autoignition modes, engine knock studies, and DDT [141-145]. More recently, $\xi$ - $\varepsilon$ parameters have been employed by Liu et al. [116] in their spark ignited RCM studies of *i*-octane flame propagation. Similarly, Gorbatenko et al.

[133], in a combined chemical kinetic and RCM study of the anti-knock effects of *n*-butanol, were able to identify regimes of subsonic autoignition and deflagration. Robert et al. [142] utilized LES simulation alongside the $\xi$ - $\varepsilon$ diagram to predict the transition from deflagration to detonation in a downsized spark ignition engine.

Figure 2.16, adapted from [19], showcases the detonation peninsula diagram, which delineates four distinct regimes: deflagration, subsonic autoignition, developing detonation, and thermal explosion, based on the parameters $\xi$ and $\varepsilon$. The boundaries of the detonation peninsula are demarcated by the upper and lower limits, $\xi_u$ and $\xi_l$ respectively. These boundaries have been established through extensive simulations and engine experiment results, as indicated by the various symbols in Fig. 2.16.

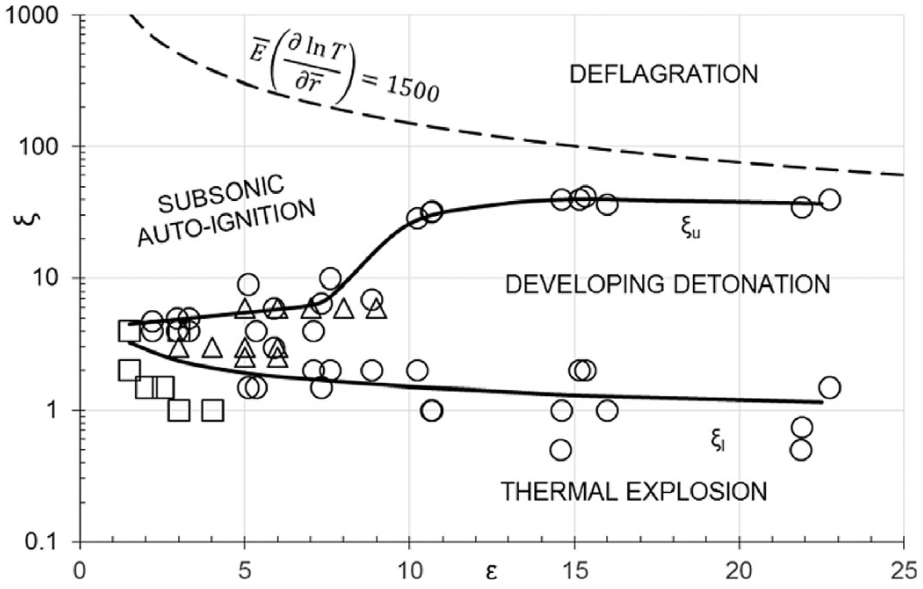


Figure 2.16. The $\xi$ - $\varepsilon$ detonation peninsula diagram [19].

The dimensionless parameter $\xi$ is relevant to the development of detonation, indicates the proximity of the autoignitive wave propagation transition to detonation. It is defined by the ratio of local acoustic velocity to the autoignitive velocity:

$$\xi = \frac{a}{u_a}, \tag{2.43}$$

where, $a$ is the acoustic velocity through the reactive mixture, $u_a$ is the autoignitive velocity. The latter can be further defined as:

$$u_a = \frac{\partial r}{\partial \tau_i} = \left(\frac{\partial r}{\partial T}\right)\left(\frac{\partial T}{\partial \tau_i}\right). \tag{2.44}$$

In this context, $\frac{\partial T}{\partial \tau_i}$, is the inversely proportional to the gradient of ignition delay time with temperature and, $\frac{\partial T}{\partial r}$ is the temperature gradient alone the autoignition hot spot with the radius. Therotically, a transition to detonation occurred when $\xi = 1$, indicating that the autoignitive velocity is coupling with the acoustic velocity. If $\xi > 1$, the acoustic velocity surpasses the autoignitive velocity, and no coupling takes place, leading to subsonic autoignition or deflagration. The thermal explosion occurred when $\xi < 1$, the autoignitive velocity is larger than the acoustic wave, causing the reaction wave of the hot spot to advance ahead of the acoustic wave. Essentially, the thermal explosion represents a homogenous reaction with a zero-temperature gradient, causing all reactions to occur instantaneously.

For detonation to be initiated, the rate of chemical energy release by auto-ignition must fast transfer into the emerging acoustic front as it moves through the hot spot during its transit time. Another dimensionless parameter, $\varepsilon$, reflects the rate of energy input from a reactive hot spot with radius $r_0$, into an auto-ignitive flow, written as:

$$\varepsilon = \frac{r_0}{a\tau_e}, \tag{2.45}$$

where $r_0$ is the hot spot radius and $\tau_e$ is the chemical excitation time. The ratio of $r_0$ over $a$ indicates the residence time of acoustic wave inside the hot spot. Lutz et al. [146] introduced the concept of chemical excitation time, $\tau_e$, which refers to the period during which exothermic chemical reactions accelerate and rapidly release thermal energy. It is the time interval from the point with 5% of the maximum total heat release rate to the attainment of that maximum value. A typical temporal profile of rapid total heat release rates in a constant volume chamber is shown in Fig. 4.8 in Chapter 4. This theoretical approached was implemented in Chapter 4 to investigate the autoignition modes of *i*-octane in Leeds RCM.

### 2.3.6 Review of Explosions and Mitigation Measures

Accidental fires and explosions have resulted in significant losses of life and property. Among these, vapor cloud explosions stand out as particularly hazardous, especially in large, congested areas. These explosions can lead to DDT, characterized by propagation

speeds exceeding 1800m/s and pressures surpassing 1.8 MPa [147]. DDT has been identified in several notable incidents, including the 1986 Chernobyl disaster, which was triggered by the overheating of a nuclear reactor leading to hydrogen explosions; the 2004 Skikda explosion; the 2005 Buncefield incident, caused by the release of winter-grade gasoline from an overfilled tank; and 2011 Fukushima Daiichi disasters, which involved hydrogen explosions that severely damaged nuclear reactors [147-149].

In order to understand the details and mechanism of DDT in large scale, extensive experimental research has been undertaken [21, 147, 150-152]. These experiments employed a range of obstacles designed to accelerate the flame and create the turbulent shock-flame complex to record the over-pressure and flame propagation speed. Recent advancements in computational capabilities have made it possible to simulate turbulent flame propagation and DDT. A wide range of numerical simulations [1, 6, 153-157] has provided detailed insights into temperature, pressure, density, flame speed, and flow field distribution arising from flame acceleration and DDT. However, the focus of these simulations has been on hydrogen, methane, and their mixtures. Overall, the DDT in these simulations is divided into three stages: the first one is the flame accelerating crossing the obstacles region the predominate mechanism for the growing of turbulence, the second is the transition to detonation, where the local area with post-shocked temperature and pressure triggered the DDT and last one is the steady robust detonation propagating.

The research findings from studies [1, 6, 16] have highlighted the critical role of turbulence generation in accelerating the flame and enhancing the Deflagration-to-Detonation Transition (DDT). Therefore, controlling the generation of turbulence emerges as an effective strategy to mitigate DDT risks. This implies that in gas or oil storage facilities, any forms of congestion, such as vehicles, pipes, poles, trees, and hedges, can significantly influence flame acceleration. As the gas flow, driven by flame propagation, moves through these obstacles, their interaction induces turbulence. This, in turn, increases the flame surface area, the burning rate, and the gas velocity ahead of the flame, thereby accelerating the combustion process. A second effective mitigation strategy involves avoiding stoichiometric fuel-air mixtures and instead diluting the

mixture to create lean conditions. The theoretical research conducted by Bradley [16] indicates that when the equivalence ratio of a hydrogen-air mixture is reduced below 0.5, the transition to detonation is effectively prevented. This is attributed to the fact that lean mixtures, as opposed to stoichiometric ones, are characterized by lower burning velocities and a tendency towards quenching, thereby reducing the likelihood of DDT.

# 3. Experimental Apparatus and Simulation Approach

In this chapter, the setup of the Leeds MK-II fan stirred combustion vessel, the optical RCM, and the in-house CFD code "MG" are described. The combustion vessel is implemented to measure laminar and turbulent flame characteristics of ethane-hydrogen-air mixtures, essential for understanding flame behaviors in DDT. The optical RCM plays a key role in measuring ignition delay time and investigating the mechanisms of transition to detonation, crucial factors in DDT. Lastly, the MG code, informed by these measurements, simulates the turbulent flame propagation and DDT process in ethane-air mixtures, demonstrating its significance in predicting and analyzing DDT.

## 3.1 Leeds MK-II Fan-Stirred Combustion Vessel

As shown in Fig. 3.1, a spherical stainless-steel fan-stirred constant-volume combustion vessel with 380-mm-diameter, with a total internal volume of 0.30372 $m^3$, the Leeds MK-II vessel, has been employed in the present study for experimental measurements. The Leeds MK-II combustion vessel is designed with two pairs of 150 mm diameter orthogonal quartz windows, which enable visualization of the flame propagation in the central region of the vessel. Two 2 kW internal coiled electric heaters mounted inside the vessel wall were equipped to heat the vessel and mixtures to 360 K.

The combustion vessel was equipped with four identical, eight-bladed fans arranged in a tetrahedron configuration The Leeds MK-II spherical combustion vessel has been successfully employed and validated over many years of experience for laminar and turbulent burning characteristics of different fuels, e.g. hydrogen, methane, iso-octane,

etc. [44,46,55,98,107,158-164].

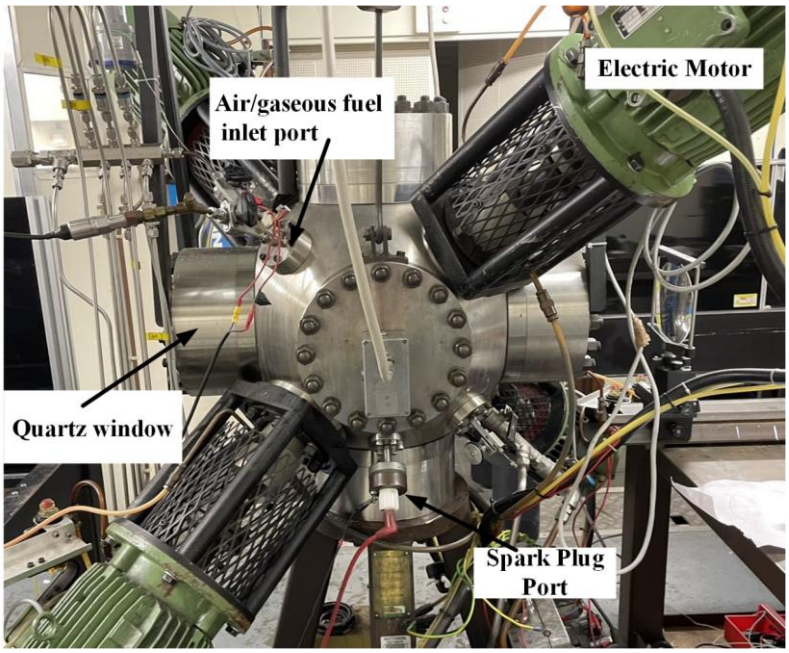


Figure 3.1. Leeds spherical combustion vessel.

### 3.1.1 Pressure Measurement

During mixture preparation, a static pressure transducer (Druck PDCR 911) with a range of 0 to 1.5 MPa was employed. This static pressure transducer, mounted flush with the inner wall of the vessel and connected to an LCD display, was used to measure the absolute pressure inside the vessel. The volume of gaseous fuel and air injected into the vessel was regulated using the partial pressure method. Before ignition, a Swagelok ball valve isolated the transducer to protect it from rapid pressure increases during explosions. For pressure measurements during combustion, a Kistler 701A dynamic pressure transducer with a range of 0 to 25 MPa was utilized, flush-mounted to the inner wall of the vessel. The output charge from this transducer was converted to a 0 to 10V analog signal by a Kistler 5007 charge amplifier, which was sampled at 50 kHz. With initial pressures of 0.1 MPa and 0.5 MPa, the amplifier's range was set at 0.5 v/MPa to optimize the signal-to-noise ratio. Finally, a Microlink 4000 analogue-to-digital converter digitized this signal for processing with LabVIEW software.

### 3.1.2 Heating System and Temperature Control

A pair of 2 kW coiled heating elements were used to heat the vessel and the mixture. As illustrated in Fig. 3.2, these elements were affixed to the inner side of the access cover.

The initial temperature of the vessel and the mixture was measured by a Type K thermocouple made from 25 μm Chromel-Alumel wire, housed in a 1.5 mm diameter stainless steel tube. This thermocouple was positioned 75 mm from the vessel's inner surface to ensure minimal interference from the radiation and conduction effects of the vessel wall [126]. A PID controller (CAL Controls, CAL3200), located on the control panel within the laboratory's protected area, was used to set and monitor the temperature, receiving signals from the thermocouple. For each experiment conducted at an initial temperature of 360 K, the target temperature was set to 450 K, with heating sustained for a duration of two hours. During the heating process, four fans, operating at a constant speed of 500 rpm, were used to generate turbulent flow, thereby enhancing convective heating and ensuring uniform heat distribution within the vessel. Once the target temperature was reached, the heating element was automatically turned off, allowing the vessel's temperature to decrease to 360 K. At this point, thermal conduction ensured an even temperature distribution across the vessel's surface [157].

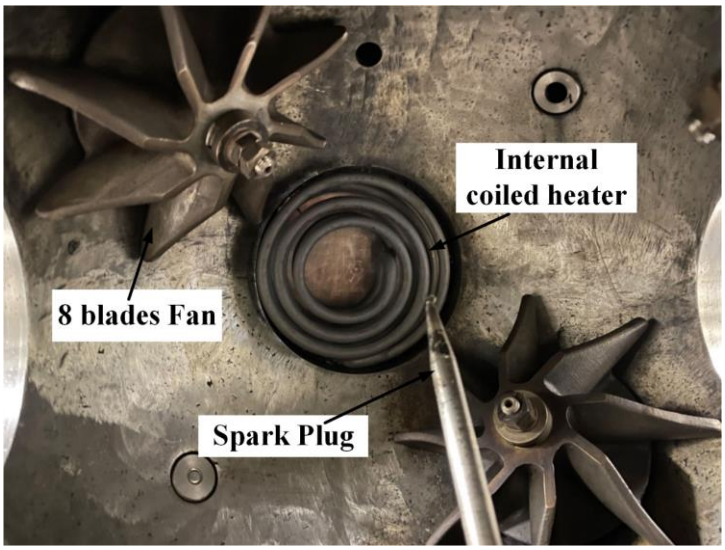


Figure 3.2. Internal coiled electric heaters, 8 blades fan and spark plug of Leeds combustion vessel-internal view.

### 3.1.3 Ignition System

As shown in Fig. 3.2, a centrally located spark plug was employed in this study as the ignition source for all mixtures. The detail of the spark plug is shown in Fig. 3.3; this spark plug consists of a 1.5 mm diameter carbon steel anode, encased in ceramic

insulation. Surrounding this anode is a 6.35 mm diameter stainless steel tube acting as a cathode. As depicted in Fig. 3.1 (labelled as "spark plug"), this tube is affixed through the vessel's bottom wall, and the external stainless-steel casing is grounded. The anode electrode connects to a Lucas 12 V transistorized automotive ignition coil system using a high tension (HT) cable. To ensure the mixture ignites with the minimum spark energy, a factor that affects the speed of flame propagation, adjusting the spark plug gap is essential to ensure the minimum energy needed for different pressures. Drawing on empirical data, the spark plug gap was set to 1 mm for experiments conducted at an atmospheric pressure of 0.1 MPa. For experiments at a higher pressure of 0.5 MPa, the gap was reduced to 0.5 mm. This adjustment is because higher pressure increases the density of the fuel-air mixture between the spark plug electrodes, leading to a higher electrical breakdown threshold. Reducing the gap under high pressure conditions lowers the required voltage to overcome this threshold.

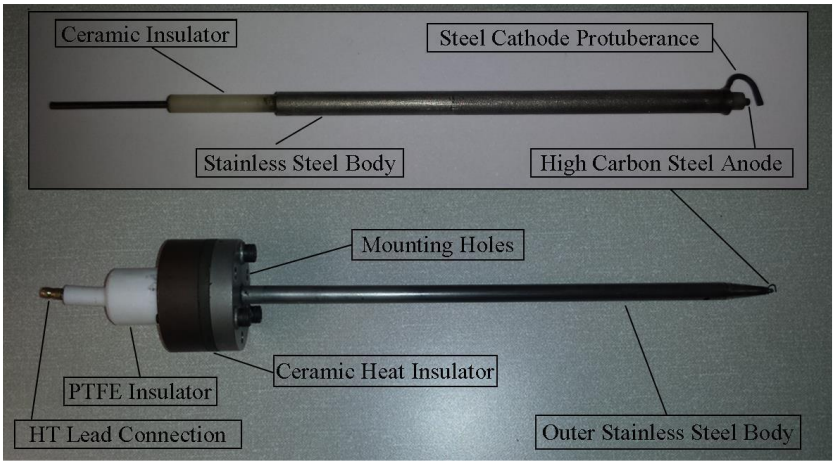


Figure 3.3. Spark tip and plug of Leeds spherical explosion bomb [22].

### 3.1.4 High Speed Digital Schlieren Photography

The Schlieren ciné-photography technique is a common method for capturing the flame front through density gradients between burned and unburned mixtures, leading to varying light refraction intensities. This technique is widely used for laminar and turbulent flame measurements [44, 46, 55, 98, 107, 158-163]. In Chapter 5, for the laminar flame, the captured images are processed to derive the flame radius/speed, Markstein length/number and laminar burning velocity. For the turbulent flame, the images are

processed to derive turbulent flame speed and turbulent burning velocity.

Figure 3.4 illustrates a schematic of the Leeds high-speed Schlieren ciné-photography setup. The apparatus employs a 150-watt adjustable tungsten lamp (MI-150 Dolan-Jenner) that acts as a near point light source, expanded by a plane-convex lens with a focal length of 1000 mm. This collimates a 150 mm beam passing through the vessel and its contents, directing it towards another plano-convex lens with a focal length of 1000 mm. Subsequently, this lens focuses the beam onto a pinhole with 0.5 mm diameter, directly onto a high-speed digital camera (SpeedSense 2640, DANTEC DYNAMICS Co., Ltd, UK). Camera recording rates were set at 5, 000 frames/s for laminar flames. For turbulent flames, the speeds were adjusted to 10, 000 frames/s at $u'$ = 1 m/s, 15, 000 frames/s at $u'$= 3 m/s, and 25000 frames/s at $u'$ = 5 m/s. A consistent resolution of 0.265 mm/pixel and dimensions of 512 x 512 pixels were maintained for all experimental runs. This specific pixel configuration ensures adequate precision and detail, meeting the accuracy requirements essential for the objectives of our current measurements. Pixel size calibration is conducted at the beginning of each experimental day to ensure accuracy. This involves capturing a mounted transparent Perspex sheet with a 10 mm$^2$ imprinted grid located within a section of the collimated beam, using the camera. The pixel size is determined based on the 10 mm grid and its corresponding pixel resolution.

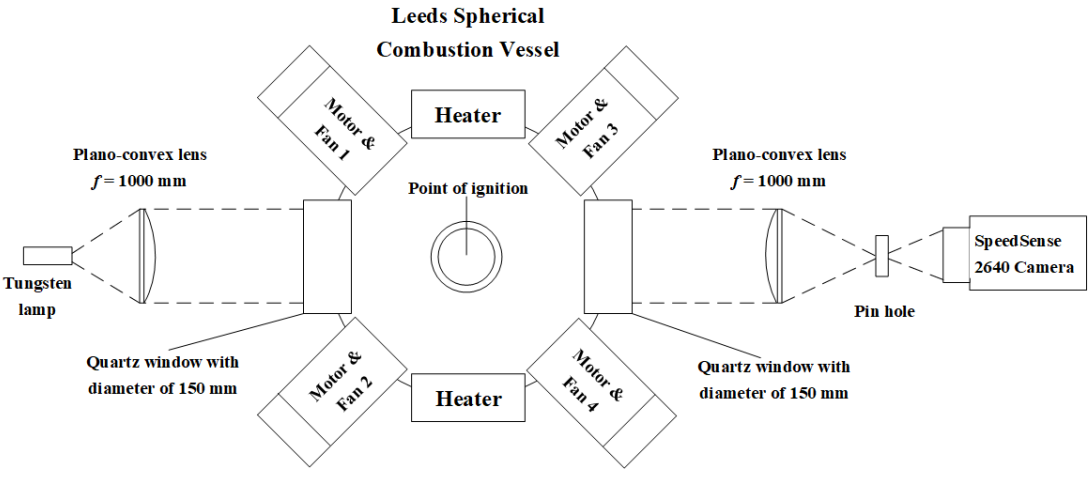


Figure 3.4. Schematic of the Leeds Spherical combustion vessel and schlieren set-up.

### 3.1.5 Fans Controlled System

The combustion vessel was equipped with four identical, eight-bladed fans which were

arranged in a tetrahedron configuration, as shown in Fig. 3.1, to optimize homogenous isotropic turbulence. As shown in Fig. 3.2, each individual fan is equipped with eight blades, each approximately 75 mm in length, and the distance between the edges of each blade is roughly 72 mm. Each fan is driven by an 8-kW electric motor, and a motor is controlled by a solid-state variable frequency converter with a speed control range of 200 - 10000 rpm. In the laminar explosion experiment, the fans operated at 500 rpm to ensure a homogeneous mixing of the mixture and were turned off prior to ignition. In contrast, for the turbulent explosion experiment, the fans remained operational throughout the entire process. The mean rms turbulence velocity, $u'$, and integral length scale inside the MK-II combustion vessel have been determined by using particle image velocimetry (PIV) technology in [108]. The previous measurements [108] suggest the turbulence is close to homogeneous and isotropic in the central area of the Leeds MK-II combustion vessel and the correlation between the rms turbulence velocity and fan speed expressed as:

$$u' = 0.00124f. \tag{3.1}$$

This correlation has been validated for all operating pressures, temperatures and mixture viscosities. The integral length scale, $L$, is 20 mm as given the PIV measurements in [108] and this value was found to be independent of all operating variables.

### 3.1.1 Schlieren Image Post-Processing

The current experiments in the combustion vessel involve both laminar and turbulent Schlieren images. A MATLAB code developed by Sharpe [167], which is based on the "binarizing-thresholding" technique [168], is utilized in this study to determine flame radius of both the laminar and turbulent flame. The MATLAB code utilizes the "imread" command to digitize and convert all the images into two-dimensional matrices of pixel values. The code initially utilizes a Schlieren image taken before ignition to identify the outer edges of the window and the spark plug. Subsequently, the spark plug is masked out, and the code processes only the area within the window boundaries. Following this, the pixel size obtained from the calibration work and the threshold value are inputted. Within the digitized image matrix, elements with intensity values higher than the threshold are identified as the burned area. Figure 3.5 presents a comparison between the

post-processed binarized images and the raw schlieren images of a stoichiometric laminar ethane-air flame at 300 K and 0.1 MPa. In the binarized image, the white areas indicate the burnt regions. This comparison suggests that the code accurately detects the laminar burned area.

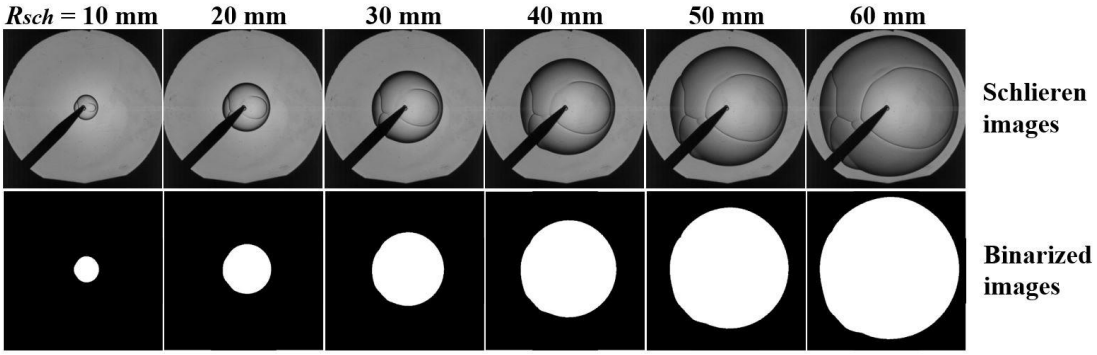


Figure 3.5. Post-processed binary images and schlieren images of laminar stoichiometric ethane-air flame at 300 K, 0.1 MPa.

Post-processing turbulent flames poses significant challenges, primarily because the wrinkled flame edge is highly sensitive to the threshold value. Figure 3.6 contrasts the binary images with the turbulent Schlieren images for a stoichiometric ethane-air flame at $u'$ = 3 m/s, 300 K, and 0.1 MPa. The observation reveals that the turbulent flame exhibits significant deformation, deviating from a spherical shape and displaying varied spatial distribution. However, a limitation arises from the schlieren imaging technique, which only captures a 2D cross-sectional view of the turbulent flame. This is the limitation by using schlieren technique to measure the turbulent flame. Despite these limitations, the schlieren technique remains a valuable tool for turbulent flame studies, as evidenced by its application in several laboratories [169-171] for similar research purposes. Notably, this code can accurately detect the wrinkled surface in the current measurements, demonstrating its effectiveness in post-processing turbulent flames. For both laminar and turbulent flames, the mean Schlieren flame radius, $R_{sch}$, is derived from the white pixels area:

$$R_{sch} = \sqrt{A/\pi}, \tag{3.2}$$

where A is the burned area and is computed by multiplying the total number of pixels that

represent the burned area in the image by the area of a single pixel. In the context of turbulent flame analysis, A represents the cross-sectional burned area of the turbulent flame, while $R_{sch}$ denotes the equivalence radius based on burned area for the turbulent flame. After the post-processing of the laminar schlieren images, a data set of radii as a function of time is generated. The stretched flame speed, stretch rate, laminar flame speed, Markstein length and number can be determined from Eq. 2.11 and 2.13 in Section 2.1.4. For the turbulent flame, once $R_{sch}$ is known, though the process explained in Section 2.2.3 Turbulent flame speed and burning velocity can be determined from Eq. 2.28.

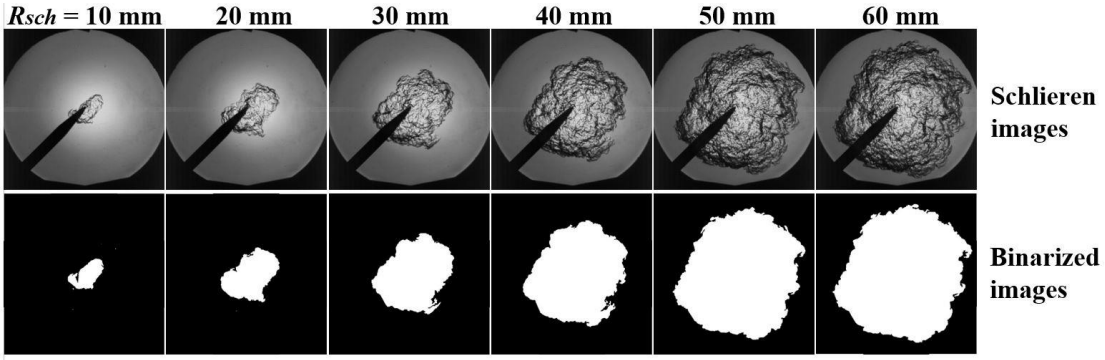


Figure 3.6. Post-processed binary images and schlieren images of turbulent stoichiometric ethane-air flame at $u'$ = 3 m/s, 300 K, 0.1 MPa.

### 3.2 Leeds Rapid Compression Machine

The RCM features a rapidly compressing piston designed to emulate the combustion process of compression engines, operating under conditions reflective of modern engine technology. It is extensively utilized in combustion research to acquire experimental insights, notably in the realms of autoignition, fuel chemistry, the intricate processes leading to detonation, and the complex phenomenon of super-knock [127]. The RCM was originally designed and built in 1968 by Affleck and Thomas [172] at the Shell Thornton Research Centre, and later acquired by the University of Leeds with modification of optical access. In Chapter 4, the ignition delay time, autoignition images of stoichiometric *i*-octane mixtures were conducted using the Leeds optical RCM. Over the years, this RCM at Leeds has been successfully employed and has proven its reliability for characterizing the ignition properties of transportation fuels [132,173-179]. Figure 3.7 displays the

current configuration of the Leeds optical RCM, equipped with a high-speed camera system. This setup comprises a combustion chamber, a hydraulic damped chamber, a pneumatic driving reservoir, a displacement laser system, a mixing chamber, and the high-speed camera system. The operating parameters for both the Leeds RCM and the high-speed camera system care given in Table. 3.1.

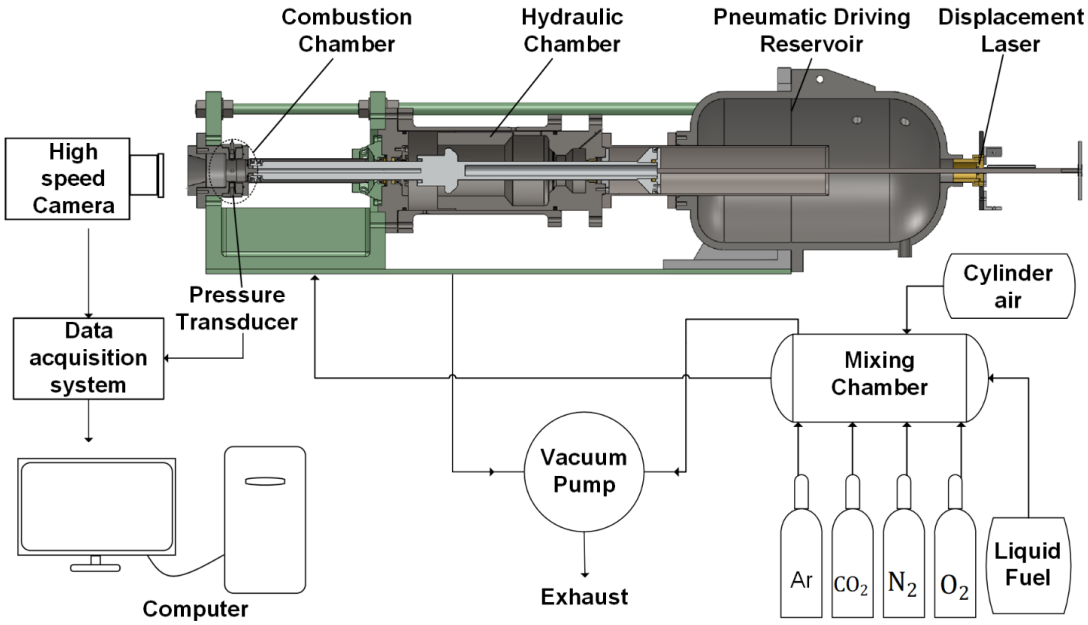


Figure 3.7. The overall layout of the Leeds optical RCM rig and high-speed imaging

Table 3.1. A summary of operating parameters for the Leeds RCM.

| Operating Parameter | Value |
|---|---|
| Pneumatic Driving Pressure | 1.35 MPa |
| Hydraulic Locking Pressure | 4.0 MPa |
| End of Compression Pressure | 1 - 3 MPa |
| End of Compression Temperature | 600 - 1000 K |
| Compression Ratio | 12-14 |
| Compression Time | 20 ms |
| Average Piston Speed | 13.4 m/s |
| Piston Bore | 44.5 mm |
| Combustion Cylinder Volume | 413 $mm^3$ |
| Maximum initial combustion chamber temperature | 473 K |

| | |
|---|---|
| Maximum initial combustion chamber pressure | 0.15 MPa |

For each experiment, the heater system warms the combustion chamber, mixing chamber, and connection pipe to the target initial temperature, $T_i$. This heating continues for three hours to ensure a homogeneous temperature distribution and reaching the target $T_i$. A vacuum pump evacuates both the mixing and combustion chambers. The *i*-octane, oxygen, and dilution gases (Ar, $N_2$, and $CO_2$) are then mixed using the partial pressure method and are heated in a 1.77 L stainless steel mixing chamber for two hours to achieve homogeneity. The utilization of the dilution gases is to adjust the ratio of specific heat capacities, $\gamma$, and thus the end of compression temperature, $T_c$ (see Eq. 3.3). For each experiment, the combustion chamber is evacuated to a maximum absolute pressure of 10 mbar. Due to the pressure difference, the mixtures from the mixing chamber are then transferred to the combustion chamber. The volume of the inlet mixtures is calculated based on the partial pressure method.

Hydraulic oil is pumped into the damping chamber until it reaches a pressure of 4.0 MPa. This pressure holds the piston while the pneumatic driving reservoir is filled with high-pressure driving air up to a pressure of 1.35 MPa. The firing of RCM is controlled by a trigger that releases the hydraulic oil pressure. Following this, the high-pressure driving air forces the piston forward completing the compression in 20 ms and compressing the reactive mixtures to the end of compression temperature, $T_c$, and pressure, $P_c$, inside the combustion chamber.

The ideal compression process of RCM adheres to the adiabatic core hypothesis proposed by Mittal et al. [180]. This hypothesis posits a perfect core gas region where there is no heat exchange with chamber walls or heat loss during the compression stroke. Desgroux et al. [181] and Griffiths et al. [182] reported that compression in the RCM is not entirely adiabatic owing to heat loss across the gas core. The temperature at $T_c$ can be deduced by the actual pressure at $P_c$, which is measured by a pressure transducer in RCM and $T_{eoc}$ can be expressed as:

$$\int_{T_i}^{T_c} \frac{1}{\gamma-1}\left(\frac{dT}{T}\right) = \ln\left(\frac{P_c}{P_i}\right), \tag{3.3}$$

where, $T_i$ is the initial temperature of the mixture, $P_i$ is the initial pressure in the combustion chamber, $\gamma$ is the ratio of specific heat capacities and it is varying with the temperature.

### 3.2.1 Optical Combustion Chamber and Pressure Measurements

Figure 3.8 provides a side cross view of the optical combustion chamber. The stainless-steel combustion chamber is specifically designed to endure the high temperature and pressure associated with autoignition and even detonation of fuel mixtures. The cylinder has an internal diameter of 46 mm and a length of 228 mm. The combustion chamber has an internal diameter of 44.5 mm and a length of 21.5 mm ahead of it covering a high strength quartz window with 69 mm visibility diameter and a 40 mm thickness to achieve full vision access. Certainly, compared to the metal head with heater configuration, the quartz window introduces more heat loss during compression. However, a comparison of the pressure traces from both setups indicates that these amounts of heat loss do not significantly influence the results. The combustion chamber incorporates four ports situated around its circumference. One port houses a dynamic pressure transducer (Kistler 6045A) that's mounted flush with the cylinder wall, capturing in-cylinder pressure signals at a 100 kHz sampling rate and is further amplified by a charge amplifier (Kistler 5015A). Another port remains sealed off. There's also an inlet port that facilitates the entry of mixtures from the mixing chamber and an exhaust/vacuum port for venting post-combustion products. To pre-warm the piston cylinder, multiple band-heaters are wrapped around the cylinder's length. Temperature monitoring and control are achieved with a single thermocouple, ensuring that both the piston and cylinder reach the target initial temperature $T_i$.

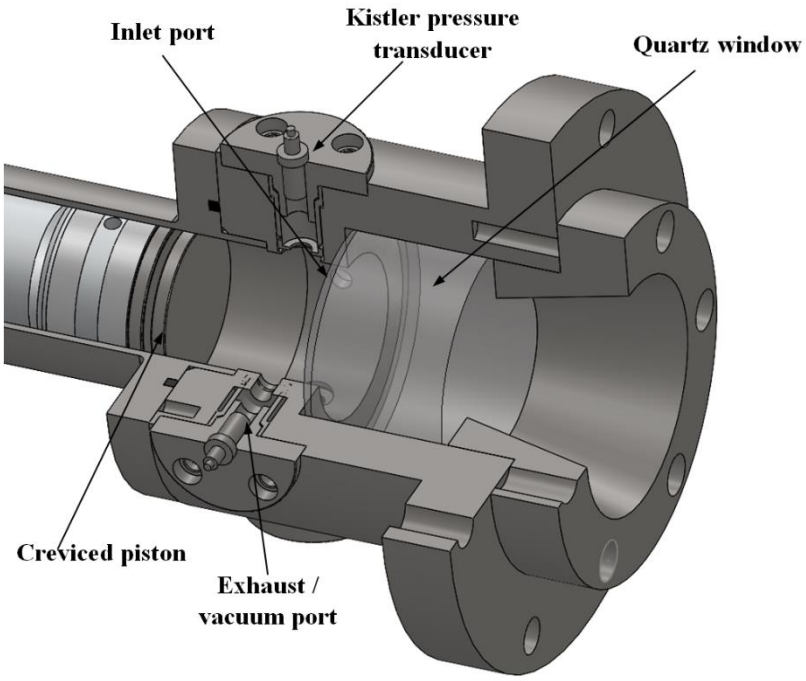


Figure 3.8. The view of the combustion chamber of Leeds RCM.

### 3.2.2 Piston Rod Assembly

In Fig. 3.9, the piston rod assembly, a crucial component of the Leeds RCM, is illustrated in detail. This assembly spans several key components of the Leeds RCM from the laser displacement device to the combustion chamber. Moving from left to right, the assembly comprises a circular reflection plate, a connection rod, a driving end, a damping ring and a creviced double-lips piston. The circular reflection plate functions as the reflecting surface for the laser, facilitating precise piston displacement measurements, as detailed in Section 3.2.5. The pneumatic driving reservoir exerts high-pressure air on the driving end, propelling the entire piston rod assembly forward. As the piston approaches its end compression position, the damping ring engages with a groove, acting as a damper to halt the piston rod's movement.

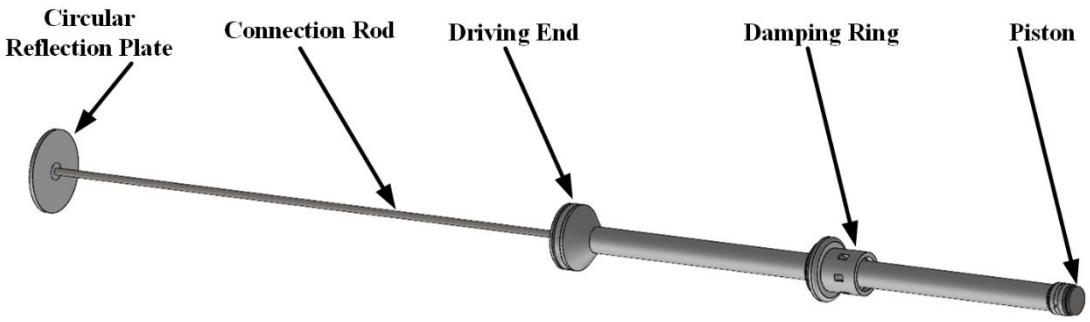


Figure 3.9. Piston rod assembly of Leeds RCM.

To mitigate the formation of roll-up vortices during piston compression, the study by Sung and Curran [130] demonstrates that using a creviced piston can diminish the vortex. The Leeds RCM incorporates this design, employing a creviced piston specifically to minimize aerodynamic mixing effects throughout the compression phase. Additionally, it's designed to operate over a broad spectrum of pressures (1.0-3.0 MPa) and temperatures (600-1000 K) at the End of Compression (EOC). The dimensions of the double-lipped creviced piston used in the Leeds RCM are illustrated in Fig. 3.10. The piston is constructed from stainless steel. The top lip has a diameter of 42 mm, while the bottom lip measures 44 mm in diameter. The crevice features gaps of approximately 2.6 mm, and the total volume of the creviced gap is about 3 $cm^3$

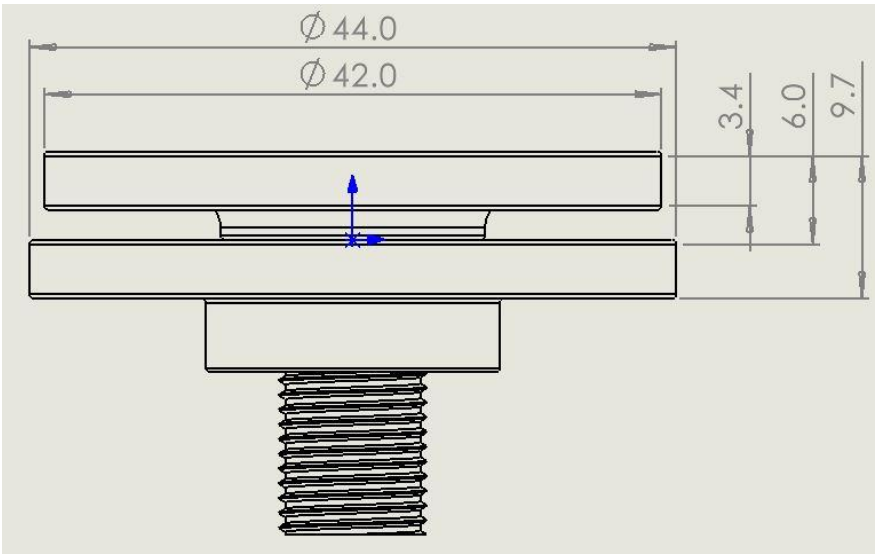


Figure 3.10. Drawing of double-lipped creviced piston.

### 3.2.3 Hydraulic Damping and Locking

In the Leeds RCM, the hydraulic chamber performs both locking and damping functions,

with the design details of this hydraulic system illustrated in Fig. 3.11. With the piston at its bottom dead center, hydraulic oil is pumped into the chamber at a pressure of 4.0 MPa via the oil inlet port. This hydraulic pressure enables the high-pressure cylinder to be filled with air at 1.35 MPa in the driving reservoir, yet the piston rod assembly remains locked until the RCM is fired. Upon firing, the hydraulic pressure is released, allowing the piston to traverse the combustion cylinder's length. As the piston approaches the EOC, the damping ring enters the damping groove. This groove offers clearance to the damping ring, resulting in oil being squeezed through the tight space between the ring and groove. The subsequent frictional forces produce the desired damping effect.

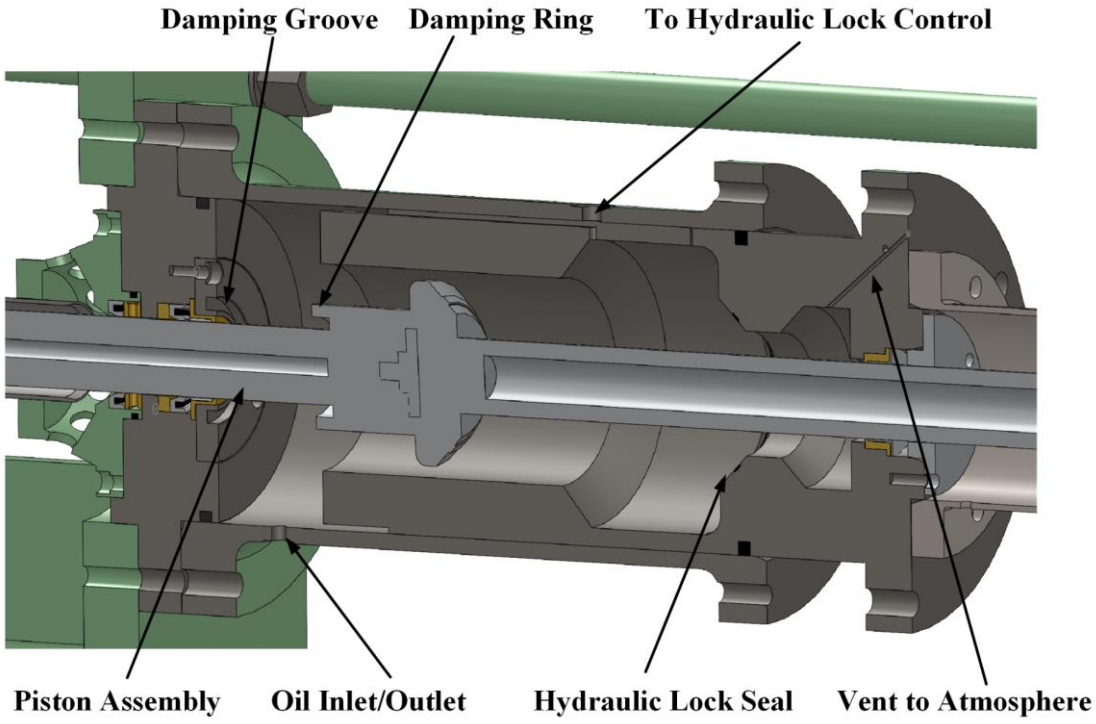


Figure 3.11. Hydraulic damping and locking system of Leeds RCM.

### 3.2.4 Mixing Chamber

The Leeds RCM employs a separate mixing chamber for preparing the liquid fuel/oxygen mixtures. Shown in Fig. 3.12, this chamber is constructed from a stainless-steel cylindrical tube, which is sealed by two stainless steel circular caps. One of the caps is designed with four ports: an inlet for oxygen and dilution gases ($CO_2$, $N_2$, and Ar); a static pressure transducer; an inlet for the liquid fuel; an outlet for the mixture which connects via a pipe to the combustion chamber; and a pressure vacuum port that connects to a

vacuum pump. To achieve the desired initial temperature, $T_i$, an external 2 kW Mica band heater is wrapped around the inner cylinder. The temperature is closely monitored and adjusted by a K-type thermocouple. A vacuum pump is linked to the mixing chamber, capable of producing vacuum conditions down to 10 mbar. The introduction of fuel, oxygen, and dilution gases is guided by the partial pressure method to achieve the specified experimental conditions. The combined vacuum and heated environment ensure the full evaporation of the liquid fuel. The mixing chamber is designed to withstand a maximum internal pressure of 0.5 MPa and has an internal volume of 1.77 L. A single preparation of the fuel/oxygen mixture can support up to 25 firings in the RCM.

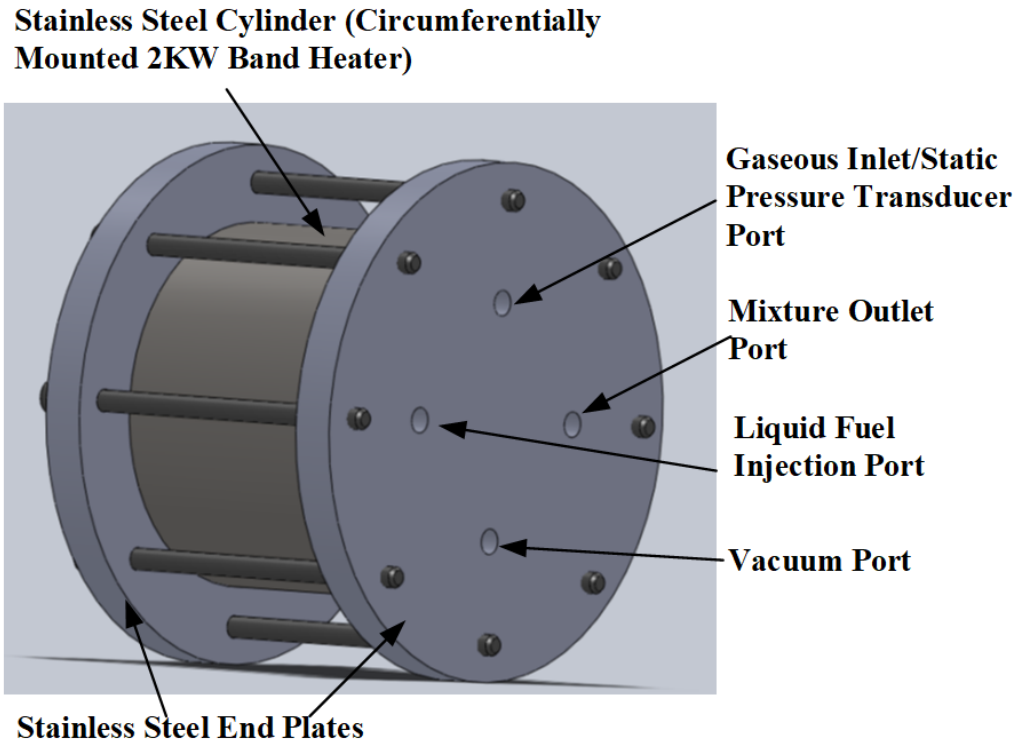


Figure 3.12. Schematic of Leeds RCM mixing chamber. Adapted from [169].

### 3.2.5 Pneumatic Driving Reservoir and Laser Displacement System

A cross-section view of pneumatic driving reservoir and Laser displacement system of Leeds RCM are shown in Fig. 3.13. The driving reservoir in the Leeds RCM is designed to store high-pressure compressed air, which propels the piston assembly forward. This reservoir is linked to two air sources: a laboratory air compressor (up to 6.5 bar) and a compressed air cylinder (up to 20 bar). For each compression cycle, the driving reservoir is initially filled with lab air up to 6.5 bar to conserve the compressed cylinder air. It is

then further pressurized with the compressed cylinder air up to 13.5 bar. This reservoir is engineered to tolerate pressures up to 30 bar. For safety considerations, a pressure relief valve is integrated, set to activate if pressures reach 20 bar. Upon the release of the hydraulic pressure, the compressed air within the driving reservoir propels the piston rod assembly forward by acting on the piston's driving end.

Figure 3.13 also illustrates the Leeds RCM equipped with a Keyence LK-G32 linear displacement laser and sensor pack, enabling precise piston displacement measurements. This system facilitates the monitoring of piston bounce and accurately determines the time when the piston reaches the EOC. The laser diode emits a beam directed at the reflection plate, and the sensor captures the reflected laser from this plate. As the piston rod moves, the angle of the reflected laser alters, and the displacement is determined based on this changing reflection angle. This laser system works at a sampling rate of 20 kHz and provides a measurable range of 30 mm. Although this range is considerably less than the stroke length of 230 mm, it is sufficient for the monitoring of piston bounce and indicating when the piston reaches EOC.

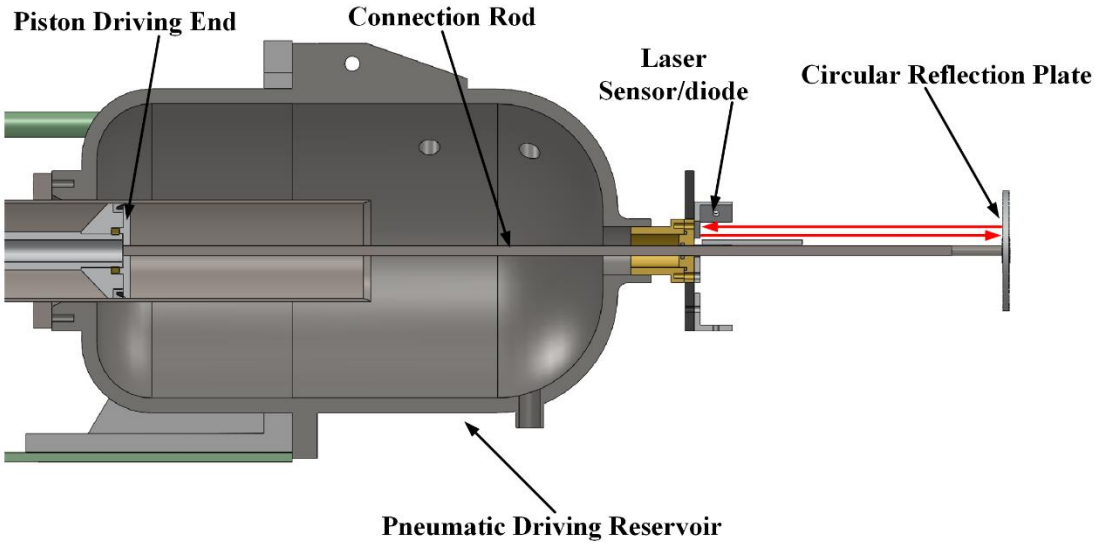


Figure 3.13. Pneumatic driving reservoir and piston displacement measurement of Leeds RCM.

### 3.2.6 High Speed Digital Camera and Synchronization System

As shown in Fig. 3.14, A monochrome high-speed CMOS camera (Photron Fastcam

SA1.1) coupled with a Tokina AT-X PRO lens with f/2.8 aperture. This setup was strategically positioned right in front of the quartz window of the combustion chamber to capture radiations from the reactions. As shown in table 4.2, two resolution setups were employed 256 x 256 and 512 x 512 pixels. For the 256 x 256 resolution, the camera operated at a framing rate of 67,500 frames per second (fps) and a pixel size of 0.176 mm/pixel. On the other hand, the 512 x 512-pixel resolution ran at 20,000 fps with a pixel size of 0.0879 mm/pixel. Throughout the experiments, the shutter speed was consistently maintained at 14.81 μs. The camera's focal plane targeted the front of the piston front which located at the EOC position. Before the experiments, the calibration work was performed by matching the pixel size and focal plan. To eliminate undesired reflections, the piston front was painted black. This high-speed camera is equipped with three ports: power, data, and trigger. The power port connects to a charger, ensuring continuous operation. Images are transferred from the camera to a computer via an Ethernet cable connected to the data port.

Table 3.2 A summary of operating parameters for the high-speed camera system.

| | |
|---|---|
| Camera Frame Rate | 20000 and 67500 fps |
| Image Resolution | 512x512, 256x256 |
| Shutter Speed | 14.81 μs |
| Aperture | 2.8 |
| Pressure Transducer Sampling Rate | 100 kHz |

For control and data acquisition, a National Instruments BNC-2110 terminal block was used. This terminal block interfaces with the laser displacement system, pressure amplification system, and the camera's trigger port. Upon the firing of the RCM, both the pressure transducer and laser displacement system were synchronized to trigger simultaneously. The camera itself was activated by the laser displacement signal, with timing set to initiate when the piston was 12 mm away from the EOC.

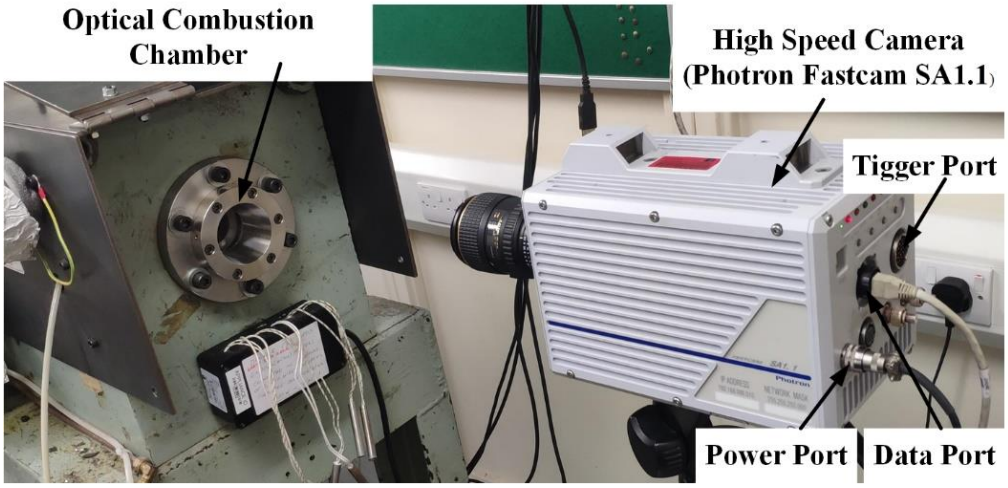


Figure 3.14. High-speed camera system of Leeds RCM.

### 3.2.7 Image Post-Processing Techniques

Similar to the methodology of the Schlieren images post-processing from the Leeds combustion vessel, a code utilizing binarizing-thresholding technique [168] based on the MATLAB environment [183] was developed to post-process the monochrome images from Leeds RCM. This method has been widely used in [115,116,184,185] to post-process the images from RCM. The MATLAB code processes monochrome images from each experiment, generating a matrix based on pixel numbers for every image, which is then binarized using a threshold. Pixels that exceed this intensity threshold are categorized as the burned mixture, whereas those beneath it are considered unburned. The Burned Mass Fraction (BMF) is calculated as the ratio of the number of burned area pixels to the total of both burned and unburned pixels.

As shown in Fig. 3.15, the second row presents sample images of combustion-related luminosity in an *i*-octane-oxygen mixture from the Leeds optical RCM. The top row displays binarized images resulting from the binarizing-thresholding approach, with the distinct white regions marking the burned areas. The bottom time scale indicates moments following the initial observation of a reaction spot. Once the burned area has been determined, the mean radius of the burned area, $R_b$, is given by:

$$R_b = \sqrt{A/\pi}, \tag{3.4}$$

where A is the burned area and it is calculated by multiplying the BMF by the cross-

sectional area of combustion chamber (1558.5mm$^2$). The measured propagation speeds of the reaction wave, $S_m$, are defined by:

$$S_m = \frac{dR_b}{dt}, \tag{3.5}$$

where $dt$ equals $5 \times 10^5$ seconds for the camera setup with 20000 fps and $1.48 \times 10^5$ seconds for the 67500 fps.

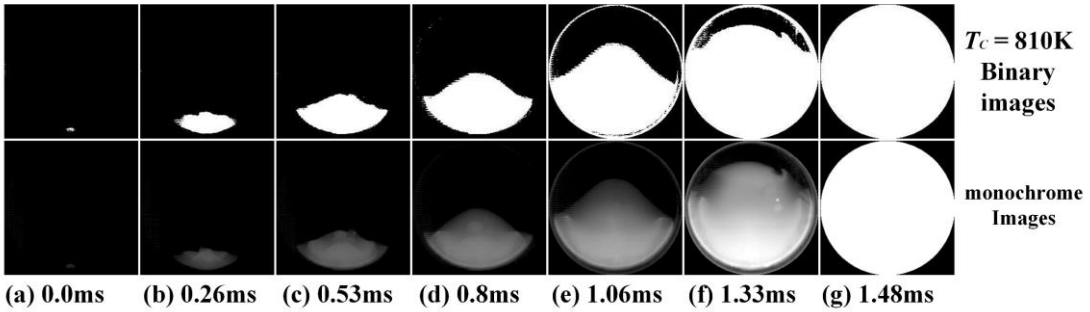


Figure 3.15. Sample images showing combustion-related monochrome images and binary from the stoichiometric *i*-octane-oxygen mixtures within Leeds optical RCM ($T_c$ = 810 K, $P_c$ = 2.0 MPa).

### 3.3 Finite Volume "MG" Code

In this section, the "MG" finite volume code, developed by Mantis Numerics Ltd. [186], is introduced. This code employs a second-order Godunov Riemann solver, enhanced by the adaptive mesh refinement (AMR) technique. The computational approach is based on ensemble-averaged, density-weighted conservation equations for mass, momentum, total energy, and a reaction progress variable. Integration of these equations is informed by the compressible $k$ - $\varepsilon$ turbulence model [187]. Subsequent sections provide detailed formulations of these equations. The MG code, as applied in this study, simulates the large-scale explosion of ethane-air mixtures, delving into the DDT of ethane-air, which is further elaborated in Chapter 6.

#### 3.3.1 Governing Equations

In the framework of the MG code, a detailed understanding of the governing equations is necessary. The compressible form of the reactive Navier-Stokes equations serves as a cornerstone for this code. These equations encapsulate the core conservation principles, which are vital for accurately simulating the intricacies of fluid dynamics, particularly in

reactive flows. This section presents a comprehensive outline of conservation equations for mass, momentum, and total energy and this equation can be found in [186]. Starting with the conservation of mass equation:

$$\frac{\partial \rho}{\partial t} + \frac{\partial (\rho u)}{\partial x} + \frac{\partial (\rho v)}{\partial y} + \frac{\partial (\rho w)}{\partial z} = 0. \tag{3.6}$$

Here $\rho$ presents the density of the fluid, while $x$, $y$ and $z$ represent the spatial coordinates. The velocity in the $x$, $y$ and $z$ directions are symbolized by $u$, $v$ and $w$, respectively. This equation emphasizes that any change in density within a control volume is countered by the flux of mass across its boundaries.

The conservation of momentum or the Navier-Stokes equations depict the balance between the forces acting on a fluid element and its momentum change. These equations are detailed for the $x$, $y$ and $z$ directions as follows:

X-momentum:

$$\frac{\partial (\rho u)}{\partial t} + \frac{\partial (\rho u^2)}{\partial x} + \frac{\partial (\rho uv)}{\partial y} + \frac{\partial (\rho uw)}{\partial z} = -\frac{\partial P}{\partial x} + \frac{\partial \tau_{xx}}{\partial x} + \frac{\partial \tau_{xy}}{\partial y} + \frac{\partial \tau_{xz}}{\partial z}. \tag{3.7}$$

Y-momentum:

$$\frac{\partial (\rho v)}{\partial t} + \frac{\partial (\rho uv)}{\partial x} + \frac{\partial (\rho v^2)}{\partial y} + \frac{\partial (\rho vw)}{\partial z} = -\frac{\partial P}{\partial y} + \frac{\partial \tau_{xy}}{\partial x} + \frac{\partial \tau_{yy}}{\partial y} + \frac{\partial \tau_{yz}}{\partial z}. \tag{3.8}$$

Z-momentum:

$$\frac{\partial (\rho w)}{\partial t} + \frac{\partial (\rho uw)}{\partial x} + \frac{\partial (\rho vw)}{\partial y} + \frac{\partial (\rho w^2)}{\partial z} = -\frac{\partial P}{\partial z} + \frac{\partial \tau_{xz}}{\partial x} + \frac{\partial \tau_{yz}}{\partial y} + \frac{\partial \tau_{zz}}{\partial z}. \tag{3.9}$$

The term, $\tau$, is the total stress tensor and expressed as:

$$\tau_{xx} = 2(\mu + \mu_T)\left(\frac{\partial u}{\partial x}\right) - \frac{2}{3}\mu_T\left(\frac{\partial u}{\partial x} + \frac{\partial v}{\partial y} + \frac{\partial w}{\partial z}\right) - \frac{2}{3}\rho k), \tag{3.10}$$

$$\tau_{yy} = 2(\mu + \mu_T)\left(\frac{\partial v}{\partial y}\right) - \frac{2}{3}\mu_T\left(\frac{\partial u}{\partial x} + \frac{\partial v}{\partial y} + \frac{\partial w}{\partial z}\right) - \frac{2}{3}\rho k), \tag{3.11}$$

$$\tau_{zz} = 2(\mu + \mu_T)\left(\frac{\partial w}{\partial z}\right) - \frac{2}{3}\mu_T\left(\frac{\partial u}{\partial x} + \frac{\partial v}{\partial y} + \frac{\partial w}{\partial z}\right) - \frac{2}{3}\rho k), \tag{3.12}$$

$$\tau_{xy} = \tau_{yx} = (\mu + \mu_T)\left(\frac{\partial u}{\partial y} + \frac{\partial v}{\partial x}\right), \tag{3.13}$$

$$\tau_{xz} = \tau_{zx} = (\mu + \mu_T)\left(\frac{\partial u}{\partial z} + \frac{\partial w}{\partial x}\right), \tag{3.14}$$

$$\tau_{yz} = \tau_{yx} = (\mu + \mu_T)\left(\frac{\partial v}{\partial z} + \frac{\partial w}{\partial y}\right), \tag{3.15}$$

here $\mu$ is molecular viscosity and $\mu_T$ is the turbulent viscosity and is equal to $0.09\frac{\rho k^2}{\varepsilon}$

for $k-\varepsilon$ and $\frac{\rho k}{\omega}$ for $k-\omega$. The term $k$, $\varepsilon$ and $\omega$ represent the turbulent kinetic energy, the turbulent dissipation rate and the specific turbulence dissipation rate, respectively, with their detailed formulation in Section 3.3.2. The conservation of energy represents the conservation of total energy for $k-\varepsilon$ the in the fluid domain and expressed as:

$$\frac{\partial(\rho e_T)}{\partial t}+\frac{\partial(\rho u e_T+Pu)}{\partial x}+\frac{\partial(\rho v e_T+Pv)}{\partial y}+\frac{\partial(\rho w e_T+Pw)}{\partial z}=\frac{\partial}{\partial x}\Big[u\tau_{xx}+v\tau_{yx}+w\tau_{zx}+\left(\frac{\mu+\mu_T}{P_r}\right)\frac{\gamma}{\gamma-1}\frac{\partial T}{\partial x}\Big]+\frac{\partial}{\partial y}\Big[u\tau_{xy}+v\tau_{yy}+w\tau_{zy}+\left(\frac{\mu+\mu_T}{P_r}\right)\frac{\gamma}{\gamma-1}\frac{\partial T}{\partial y}\Big]+\frac{\partial}{\partial z}\Big[u\tau_{xz}+v\tau_{yz}+w\tau_{zz}+\left(\frac{\mu+\mu_T}{P_r}\right)\frac{\gamma}{\gamma-1}\frac{\partial T}{\partial z}\Big]+\rho S_E, \quad (3.16)$$

Here, $P$ represents the pressure, $T$ denotes the temperature of the mixture, $P_r$ is the Prandtl number, and $\gamma$ is the ratio of specific heats. The toral energy density $e_T$ is $0.5(u^2+v^2+w^2)+\frac{p}{(\gamma-1)\rho}$. The source term for the energy, $S_E$ is defined as $S_C(\frac{P}{\rho_u})(\frac{\rho_u}{\rho_b}-1)\frac{\gamma}{\gamma-1}$. $S_C$ is the source term for the progress variable detailed in Section 3.3.3.

For the $k-\omega$ model, the energy equation is slightly difference:

$$\frac{\partial(\rho e_T)}{\partial t}+\frac{\partial(\rho u e_T+Pu)}{\partial x}+\frac{\partial(\rho v e_T+Pv)}{\partial y}+\frac{\partial(\rho w e_T+Pw)}{\partial z}=\frac{\partial}{\partial x}\Big[u\tau_{xx}+v\tau_{yx}+w\tau_{zx}+\left(\frac{\mu+\mu_T}{P_r}\right)\frac{\gamma}{\gamma-1}\frac{\partial T}{\partial x}+(\mu+\sigma^*\mu_T)\frac{\partial k}{\partial x}\Big]+\frac{\partial}{\partial y}\Big[u\tau_{xy}+v\tau_{yy}+w\tau_{zy}+\left(\frac{\mu+\mu_T}{P_r}\right)\frac{\gamma}{\gamma-1}\frac{\partial T}{\partial y}+(\mu+\sigma^*\mu_T)\frac{\partial k}{\partial y}\Big]+\frac{\partial}{\partial z}\Big[u\tau_{xz}+v\tau_{yz}+w\tau_{zz}+\left(\frac{\mu+\mu_T}{P_r}\right)\frac{\gamma}{\gamma-1}\frac{\partial T}{\partial z}+(\mu+\sigma^*\mu_T)\frac{\partial k}{\partial z}\Big]+\rho S_E, \quad (3.17)$$

The closure terms $\sigma^*$ is 0.8.

### 3.3.2 Turbulence Model: $k-\varepsilon$ and $k-\omega$ Model

The closure of the momentum and total energy equation was achieved via compressibility-corrected forms of the both $k-\varepsilon$ and $k-\omega$ model. For the $k-\varepsilon$ model, the equation for the transport and balance of turbulent kinetic energy $k$ is expressed as:

$$\frac{\partial(\rho k)}{\partial t}+\frac{\partial(\rho u k)}{\partial x}+\frac{\partial(\rho v k)}{\partial y}+\frac{\partial(\rho w k)}{\partial z}=\tau_{xx}\frac{\partial u}{\partial x}+\tau_{yx}\frac{\partial u}{\partial y}+\tau_{zx}\frac{\partial u}{\partial z}+\tau_{xy}\frac{\partial v}{\partial x}+\tau_{yy}\frac{\partial v}{\partial y}+\tau_{zy}\frac{\partial v}{\partial z}+\tau_{xz}\frac{\partial w}{\partial x}+\tau_{yz}\frac{\partial w}{\partial y}+\tau_{zz}\frac{\partial w}{\partial z}-\rho\varepsilon+\frac{\partial}{\partial x}[(\mu+\mu_T)\frac{\partial k}{\partial x}]+\frac{\partial}{\partial y}[(\mu+\mu_T)\frac{\partial k}{\partial y}]+$$

$$\frac{\partial}{\partial z}[(\mu+\mu_T)\frac{\partial k}{\partial z}]. \quad (3.18)$$

The temporal term, $\frac{\partial(\rho k)}{\partial t}$, Represents the rate of change of turbulent kinetic energy with time inside a fluid particle. The convection term, $\frac{\partial(\rho u k)}{\partial x}$, represents transport or advection of turbulent kinetic energy due to the motion of the fluid in the x direction. The production term, for example, is $\tau_{xx}\frac{\partial u}{\partial x}$ and accounts for the production of turbulent kinetic energy due to the interaction of the mean flow velocity gradients and the Reynolds stresses. The dissipation term, $\rho\varepsilon$, represents the dissipation rate of turbulent kinetic energy to molecular internal energy. The diffusion term, $\frac{\partial}{\partial x}[(\mu+\mu_T)\frac{\partial k}{\partial x}]$, account for the diffusion of turbulent kinetic energy due to both molecular and turbulent viscosity in x direction. The turbulent dissipation rate equation is expressed as:

$$\frac{\partial(\rho\varepsilon)}{\partial t}+\frac{\partial(\rho u\varepsilon)}{\partial x}+\frac{\partial(\rho v\varepsilon)}{\partial y}+\frac{\partial(\rho w\varepsilon)}{\partial z}=\frac{\varepsilon}{k}[C_1(\tau_{xx}\frac{\partial u}{\partial x}+\tau_{xy}\frac{\partial u}{\partial y}+\tau_{xz}\frac{\partial u}{\partial z}+\tau_{yx}\frac{\partial v}{\partial x}+\tau_{yy}\frac{\partial v}{\partial y}+$$
$$\tau_{yz}\frac{\partial v}{\partial z}+\tau_{zx}\frac{\partial w}{\partial x}+\tau_{zy}\frac{\partial w}{\partial y}+\tau_{zz}\frac{\partial w}{\partial z})-C_2\rho\varepsilon]+\frac{\partial}{\partial x}[(\mu+\sigma\mu_T)\frac{\partial\varepsilon}{\partial x}]+\frac{\partial}{\partial y}[(\mu+\sigma\mu_T)\frac{\partial\varepsilon}{\partial y}]+$$
$$\frac{\partial}{\partial z}[(\mu+\sigma\mu_T)\frac{\partial\varepsilon}{\partial z}]. \quad (3.19)$$

Similar as the Eq. 3.18, it includes the temporal, convection, production, diffusion terms. Where, the closure terms, $\sigma$, is equal to 1/1.3. The constant, $C_1$ and $C_2$ denote the production and dissipation of turbulence with value of 1.55 and 2.0 respectively. The boundary condition for $k$ sets the value in the first cell adjacent to a solid to zero.

For the $k-\omega$ model, the equation for the transport and balance of turbulent kinetic energy $k$ is expressed as:

$$\frac{\partial(\rho k)}{\partial t}+\frac{\partial(\rho u k)}{\partial x}+\frac{\partial(\rho v k)}{\partial y}+\frac{\partial(\rho w k)}{\partial z}=\tau_{xx}\frac{\partial u}{\partial x}+\tau_{yx}\frac{\partial u}{\partial y}+\tau_{zx}\frac{\partial u}{\partial z}+\tau_{xy}\frac{\partial v}{\partial x}+\tau_{yy}\frac{\partial v}{\partial y}+$$
$$\tau_{zy}\frac{\partial v}{\partial z}+\tau_{xz}\frac{\partial w}{\partial x}+\tau_{yz}\frac{\partial w}{\partial y}+\tau_{zz}\frac{\partial w}{\partial z}-\beta^*\rho\omega+\frac{\partial}{\partial x}[(\mu+\sigma^*\mu_T)\frac{\partial k}{\partial x}]+\frac{\partial}{\partial y}[(\mu+\sigma^*\mu_T)\frac{\partial k}{\partial y}]+$$
$$\frac{\partial}{\partial z}[(\mu+\sigma^*\mu_T)\frac{\partial k}{\partial z}]. \quad (3.20)$$

In here, the turbulent diffusion term is defined as $\mu_T=\frac{\rho k}{\omega}$. The closure terms $\sigma^*$ is 0.8 and $\beta^*$ is 0.09. The turbulent dissipation rate equation is expressed as:

$$\frac{\partial(\rho\omega)}{\partial t}+\frac{\partial(\rho u\omega)}{\partial x}+\frac{\partial(\rho v\omega)}{\partial y}+\frac{\partial(\rho w\omega)}{\partial z}=\alpha\frac{\omega}{k}\left[\left(\tau_{xx}\frac{\partial u}{\partial x}+\tau_{xy}\frac{\partial u}{\partial y}+\tau_{xz}\frac{\partial u}{\partial z}+\tau_{yx}\frac{\partial v}{\partial x}+\tau_{yy}\frac{\partial v}{\partial y}+\tau_{yz}\frac{\partial v}{\partial z}+\tau_{zx}\frac{\partial w}{\partial x}+\tau_{zy}\frac{\partial w}{\partial y}+\tau_{zz}\frac{\partial w}{\partial z}\right)\right]-\beta\rho\omega^2+\sigma_d\frac{\rho}{\omega}\left[\frac{\partial k}{\partial x}\frac{\partial\omega}{\partial x}+\frac{\partial k}{\partial y}\frac{\partial\omega}{\partial y}+\frac{\partial k}{\partial z}\frac{\partial\omega}{\partial z}\right]+\frac{\partial}{\partial x}\left[(\mu+\sigma\mu_T)\frac{\partial\omega}{\partial x}\right]+\frac{\partial}{\partial y}\left[(\mu+\sigma\mu_T)\frac{\partial\omega}{\partial y}\right]+\frac{\partial}{\partial z}\left[(\mu+\sigma\mu_T)\frac{\partial\omega}{\partial z}\right]. \quad (3.21)$$

The closure terms are given by $\alpha$ is 0.52 and $\beta$ is 0.0708. For $\frac{\partial k}{\partial x}\frac{\partial\omega}{\partial x}$ is greater than zero, $\sigma_d$ is set as 0.125, otherwise, $\sigma_d$ is zero.

### 3.3.3 Premixed Combustion Model

The interaction between the turbulence and premixed combustion was evaluated by Catlin et al. [188]. This method incorporates the experimental measured turbulent burning velocity correlation with effects of kinetics and turbulence influences upon the turbulent burning velocity of flame, while remaining a realistic flame thickness throughout the computation. The conservation equations representing a reaction progress variable of the mixture are defined as Eq. 3.22 [188]:

$$\frac{\partial}{\partial t}(\rho\tilde{c})+\frac{\partial}{\partial x}(\rho u\bar{c})+\frac{\partial}{\partial y}(\rho v\bar{c})+\frac{\partial}{\partial z}(\rho w\bar{c})=\frac{\partial}{\partial x}\left(\Gamma_c\frac{\partial\tilde{c}}{\partial x}\right)+\frac{\partial}{\partial y}\left(\Gamma_c\frac{\partial\tilde{c}}{\partial y}\right)+\frac{\partial}{\partial z}\left(\Gamma_c\frac{\partial\tilde{c}}{\partial z}\right)+\overline{\rho S(c)} \quad . \quad (3.22)$$

With diffusivity coefficient, $\Gamma_c=(\mu_l+\mu_f)/\sigma_c$ .In addition, the reaction progress variable in the modeling is defined as:

$$\tilde{c}=1-(\tilde{Y}_f/\tilde{Y}_{f,o}). \quad (3.23)$$

The progress variable is used to describe the flame front and so that $\tilde{c}=0$ is the unburned mixture and $\tilde{c}=1$ is the burned mixture. $\tilde{E}$ is the density-weighted average total energy of mixture and it defined as:

$$\tilde{E}=\tilde{e}+\frac{(\tilde{u}^2+\tilde{v}^2+\tilde{w}^2)}{2}+k, \quad (3.24)$$

where $\tilde{e}$ is the internal energy of the system and it defined as:

$$\tilde{e}=\int_{T_0}^{T}c_v\,dT\,, \quad (3.25)$$

Here, $c_v$, is the specific heat at constant volume. The source term of the progress variable in Eq. 3.22 is written as:

$$\overline{\rho S(c)}=\overline{\rho R_c}\,, \quad (3.26)$$

where,

$$\overline{\rho R_c} = \bar{\rho} R \tilde{c}^4 (1 - \tilde{c}) (\frac{\rho_u}{\rho_b})^2. \quad (3.27)$$

The reaction rate constant is a function of the turbulent burning velocity and flame thickness.

$$R = 0.8 * u_t \Lambda_2 / (\delta_t \Lambda_1) \quad (3.28)$$

Where, flowing the work of Catlin et al. [188] the eigenvalue $\Lambda_1$ and $\Lambda_2$ are suggested as 0.346 and 3.575 respectively.

### 3.3.4 Dimensionless Scales

In the MG code, parameters are initially inputted in the CGS (centimeter-gram-second) system. However, these parameters are normalized by the various scales to become dimensionless. Transitioning to dimensionless units offers a more streamlined computational approach. The dimensionless process benefit lies in reducing the risk of errors due to unit mismatches, particularly evident when consolidating various physical phenomena, each having unique inherent units. Adopting dimensionless units facilitates standardizing the computational problem, rendering the calculations both consistent and less susceptible to errors. To implement this normalization in the MG code, specific scales for density, pressure, velocity, and time have been established, with the source detailed in [189]. The density scale, $\rho_{scale}$, with unit in g/cm$^3$ is described as:

$$\rho_{scale} = \frac{P \bar{M} m_a}{K_B T}, \quad (3.29)$$

where, $\bar{M}$ is the mean molar mass, $m_a$ represents the atomic mass, $K_B$ is the Boltzmann constant. Given the density scale, the pressure scale is a function of $\rho_{scale}$ with unit in barye (Ba) and expressed as:

$$P_{scale} = \frac{\rho_{scale} K_B}{\bar{M} m_a} = \frac{P}{T}. \quad (3.30)$$

Next, the velocity scale, $v_{scale}$, with unit in cm/s is the square root of pressure to density scale ratio:

$$v_{scale} = \sqrt{\frac{P_{scale}}{\rho_{scale}}}. \quad (3.31)$$

Lastly, the time scale, $t_{scale}$, with unit in second is derived by considering a specific

length or characteristic dimension of the problem and relating it to the velocity scale:

$$t_{scale} = \frac{L_{scale}}{v_{scale}}. \tag{3.32}$$

The $L_{scale}$ corresponds to a single unit of the domain, and its specific value is determined based on the requirements of the study. By integrating these scales, every physical parameter in the MG code is dimensionless.

### 3.3.5 Leeds ARC4 High Performance Computing (HPC) Cluster

During this research, the computational tasks associated with the MG code were carried out on the Leeds Advanced Research Computing 4 (ARC4) HPC cluster, running on a Linux-based platform. Further details on the ARC4 setup are elaborated in [190]. ARC4 employs the power of Intel Xeon Gold 6138 CPUs, functioning at a base clock rate of 2.0 GHz. The system, boasting a memory bandwidth of 800 MHz for each core, has been fine-tuned to engage its turbo-boost capabilities, particularly when there's reduced core activity, thus ensuring peak performance. The ARC4 infrastructure encompasses diverse node configurations, including a significant count of 149 standard nodes. Each standard node is armed with 40 cores and a memory of 192GB. They also feature an integrated SSD, providing an additional storage capacity of 170GB. In aggregate, these nodes contribute to a sum of 5,960 cores geared towards standard computational operations. In our research endeavors, these standard nodes were predominantly employed, with all 40 cores being utilized during each simulation. Notably, the MG code was optimized using 40 cores with Message Passing Interface (MPI) to expedite computing times.

For streamlined remote interfacing with ARC4, the MobaXterm personal edition v21.4 [191] is selected to connect with ARC4 cluster. Renowned for its robust terminal capabilities and an array of utilities optimized for distant computing, MobaXterm facilitated a flawless SSH connection to ARC4. This integration simplified the process of job submissions, offered real-time task monitoring, and enabled quick data transfers between our local systems and the ARC4 cluster.

# 4. Reaction Propagation Prior to Developing Detonation in a RCM

## 4.1 Introduction

An ideal RCM instantaneously compresses a reactive mixture instantaneously a reactive mix and then holds it steady without losing any heat, until it spontaneously ignites in a thermal explosion. This process enables the calculation of the autoignition delay time based on observed characteristics, such as those shown in Fig. 4.1.

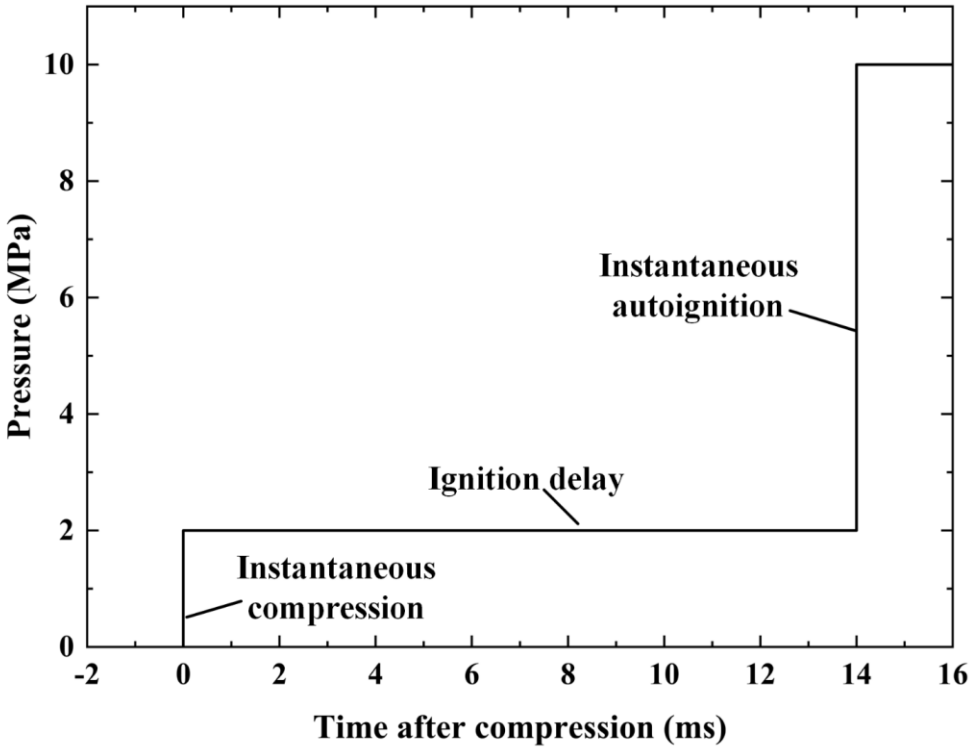


Figure 4.1. Idealised Rapid Compression Machine Pressure-time characteristic.

In real RCM, the compression process is sufficient quick enough, and the movement of piston produces turbulence roll-up vortices. Heat loss and chemical reactions occur both during and following the compression. Sung and Curran [130] have thoroughly examined these and other significant characteristics of RCM. Another Study [192] explored the varying impacts of chemical reactions during the compression phase in diverse RCMs. This current research focuses on the distinct modes of reaction propagation that take place in the cylinder after compression, prior to the rapid rise in pressure that marks the end of the autoignition delay. The various propagation modes such as laminar flame propagation

and autoignitive propagation, including a NTC regime, are presented. These modes may subsequently result in the creation of acoustic waves, which can cause either mild or strong detonative propagation.

A theoretical framework to comprehend these modes and the eventual detonation is offered by the concept of the detonation peninsula. Within this peninsula, conditions are such that detonation might take place [19]. The coordinates of the peninsula are defined by two dimensionless parameters $\xi$ and $\varepsilon$. The detailed explanation of the detonation peninsula and these two dimensionless parameter $\xi$ and $\varepsilon$, can be found in Section 2.3.5. These parameters can indicate the different reaction propagation modes. They have been used to assess the nature of knock in engines and identify the super knock regime [193], the closest approach to near-instantaneous autoignition.

The present RCM study is of the diverse reaction modes that can be pre-cursors to detonative autoignition. The changing modes in a cylindrical reaction chamber, were viewed through a high strength optical window, and a high-speed camera system that recorded the initiation, propagation, and transformation of reactions. Pressures were measured with a pressure transducer. To study the effects of an NTC regime and the transition to detonation in engine conditions, following Liu et al. [116], a stoichiometric mixture of *i*-octane and $O_2$ with variable proportions of different inert gases, $N_2$, Ar, and $CO_2$ was employed to vary the specific heat ratio, thereby achieving different temperatures at the end of compression. The pressure, was always 2 MPa at the end of compression, but the end of compression temperatures, $T_c$, varied between 640 K and 930 K, dependent upon the concentrations of the inert gases. However, Liu et al. [116] did not observe the unique behavior of NTC, as the implementation of spark ignition for flame generation rather than compression autoignition.

## 4.2 Different Properties of the Mixtures

### 4.2.1 Specifications of *i*-octane Mixtures

All experiments discussed in the present work (Chapter 4) were conducted using the Leeds optical RCM that has been successfully employed and validated over many years

of experience for characterizing the ignition properties of transportation fuels. The detailed description of Leeds RCM can be found in Section 3.2. Eleven stoichiometric mixtures of *i*-octane and oxygen exhibited varied $T_c$ values due to differences in inert diluent concentrations. Pressures were consistently measured, and the temperatures during the autoignition were calculated from them using the isentropic relationship shown in Eq. 4.1.

$$T = T_c(\frac{P}{P_c})^{\frac{\gamma-1}{\gamma}}, \quad (4.1)$$

Where $\gamma$ is the ratios of specific heats were sourced from the GASEQ code [48] and $P_c$ is always 2 MPa. All mixtures were stoichiometric, with constant mole fractions of *i*-octane and $O_2$, of high purity (>99.99%). Compositions of all eleven mixtures and their temperatures after compression, $T_c$, are given in Table 4.1. Pressures at the end of compression were always 2.0 MPa. Examinations of the flame images and pressure records showed different modes of reactive propagation, indicated in the second column. These include: Laminar burning, *L*, autoignitive propagation, *A*, generation of pressure pulses, *P*, of increasing strength and, ultimately, initiation of detonation and full detonation, *D*. There were five instances in which an explosion terminated with a detonation. Each experimental condition listed in Table 4.1 was repeated five times to ensure the repeatability and reliability of the experiment. Details such as pressure, corresponding temperature, and monochrome images for each $T_c$ are available in Figures 4.12 through 4.22.

Table 4.1 Mixture compositions, compression temperature, $T_c$, and ignition modes.

| | | | Mixture Composition Mole Fractions (%) | | | | |
|---|---|---|---|---|---|---|---|
| $T_c$ | Mode | $\tau_i$ (ms) | *i*-octane | $O_2$ | $N_2$ | Ar | $CO_2$ |
| 640 | *L* | 52.3 | 1.65 | 20.66 | 18.62 | 0 | 59.2 |
| 670 | *A* | 26.3 | 1.65 | 20.66 | 38.23 | 0 | 39.4 |
| 690 | *A* | 19 | 1.65 | 20.66 | 47.1 | 0 | 30.6 |
| 710 | *P, A* | 14.7 | 1.65 | 20.66 | 58.9 | 0 | 18.8 |
| 740 | *P, A* | 15.5 | 1.65 | 20.66 | 67.8 | 0 | 9.9 |

| | | | | | | | |
|---|---|---|---|---|---|---|---|
| 770 | *P, A* | 16.1 | 1.65 | 20.66 | 77.7 | 0 | 0 |
| 790 | *P, D* | 16.5 | 1.65 | 20.66 | 65.9 | 11.8 | 0 |
| 810 | *P, D* | 17.6 | 1.65 | 20.66 | 56.1 | 21.6 | 0 |
| 830 | *P, D* | 21.3 | 1.65 | 20.66 | 48.2 | 29.5 | 0 |
| 900 | *P, D* | 11.7 | 1.65 | 20.66 | 21.6 | 56.1 | 0 |
| 930 | *P, D* | 7 | 1.65 | 20.66 | 11.8 | 65.9 | 0 |

### 4.2.2 Laminar Burning Velocity

The possibility of obtaining near-stoichiometric laminar burning velocities under RCM conditions was always checked prior to the experimental measurement. These were calculated using a 1D freely propagation planar laminar flame model in CHEMKIN software [194], incorporating the *i*-octane oxidation kinetics found in the detailed Lawrence Livermore National Laboratory (LLNL) gasoline surrogate chemical kinetics [195]. The values of $u_l$ obtained from the LLNL gasoline surrogate chemical kinetics are shown in Fig. 4.2 at different temperatures, with pressures of 0.1 and 2 MPa. An empirical expression in [44] for the dependency on temperature and pressure of the laminar burning velocity is in the form:

$$u_l = 1.363 \left(\frac{T}{640}\right)^{2.2} \left(\frac{P}{0.1}\right)^{-0.27}, \quad (4.2)$$

With $T$ in K and $P$ in MPa. The dashed lines in Fig. 4.2 demonstrate this expression provides good fits to the computed data. The lamniar flame speed, derived from Eq. 4.2 multiplied by the density ratio, is used in Sections 4.3.1 and 4.3.2 for comparison with measured and calculated autoigntive speeds. However, it is important to recognize that dilution with $CO_2$ notably decreases the laminar burning velocity when compared to air. At temperatures of 640, 670, 690 and 710 K the laminar burning velocities have been repredicted by the same chemical kinetics mechanism to account for the dilution effects of $CO_2$.

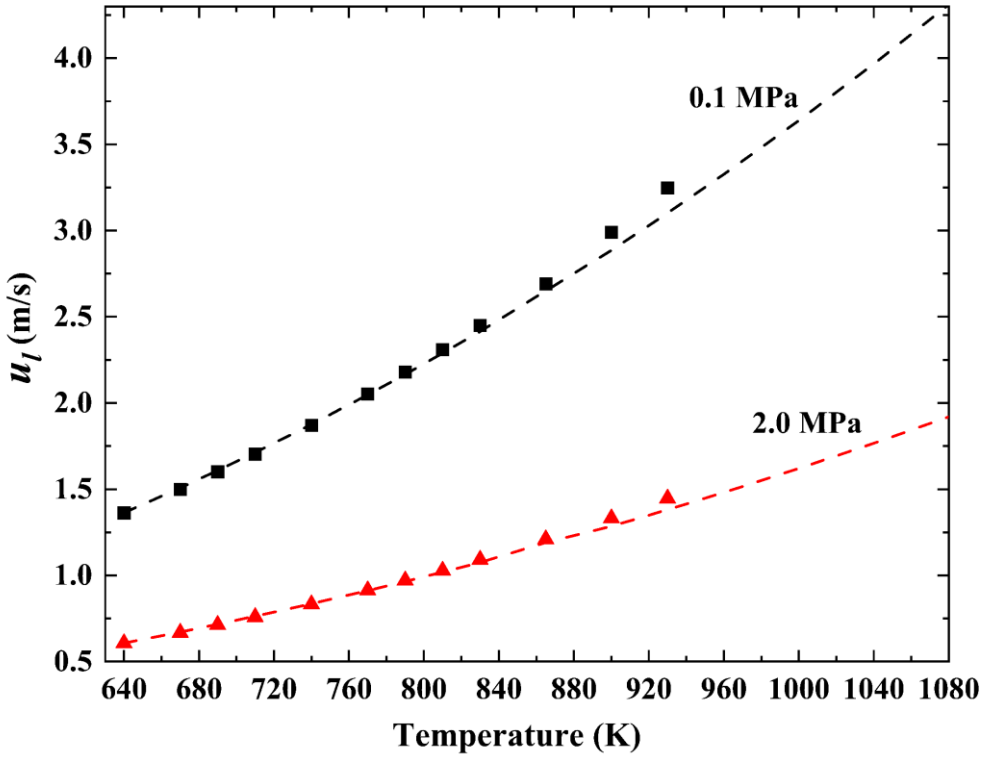


Figure 4.2. Laminar burning velocity calculated from LLNL gasoline chemical kinetics [187] of *i*-octane-air at 0.1 MPa and 2 MPa. More empirically the data were extended to higher temperatures and pressure using Eq. 4.2.

### 4.2.3 Autoignition Delay Time

Autoignitive propagation speeds are dependent upon autoignition delay times, $\tau_i$. These were meausred in the RCM at the different compression temperatures, $T_c$, and are shown in Fig. 4.3. The error bars in Fig. 4.3 represent the standard deviation of $\tau_i$ across five experiments, with the small size of the error bars indicating high repeatability of the experiments. The extent of the NTC regime is indicated from 727 to 830 K. Within it, the value of $\tau_i$ increases with temperature. Figure 4.3 also includes the measured $\tau_i$ values from different RCMs of stoichiometric *i*-octane at 2.0 MPa [127]. The current measurements are in satisfactory aggreements with the additional data of others [127].

To thoroughly investigate the propagtion and ignition modes during the reaction wave propagation in RCM, it is necessary to examine the effects of temperature and pressure on $\tau_i$ extending up to 1200 K and 10 MPa, respectively. This approach allows gaining an insight on the variation of $\tau_i$ during the reaction wave propagation in which the in-cylinder pressure and temperature present dynamic change. The filled triangle symbols

in Fig. 4.4 are the values of $\tau_i$ derived from the current measurements, corresponding to 2 MPa and kinetically, modelled values from CHEMKIN software [194] with detailed LLNL gasoline surrogate chemical kinetics [195] at 2, 4, and 10 MPa, and at temperatures between 640 K and 1200 K. Chemical kinetically, there was a close similarity between the current experimental mixtures and the stoichiometric *i*-octane-air mixtures.

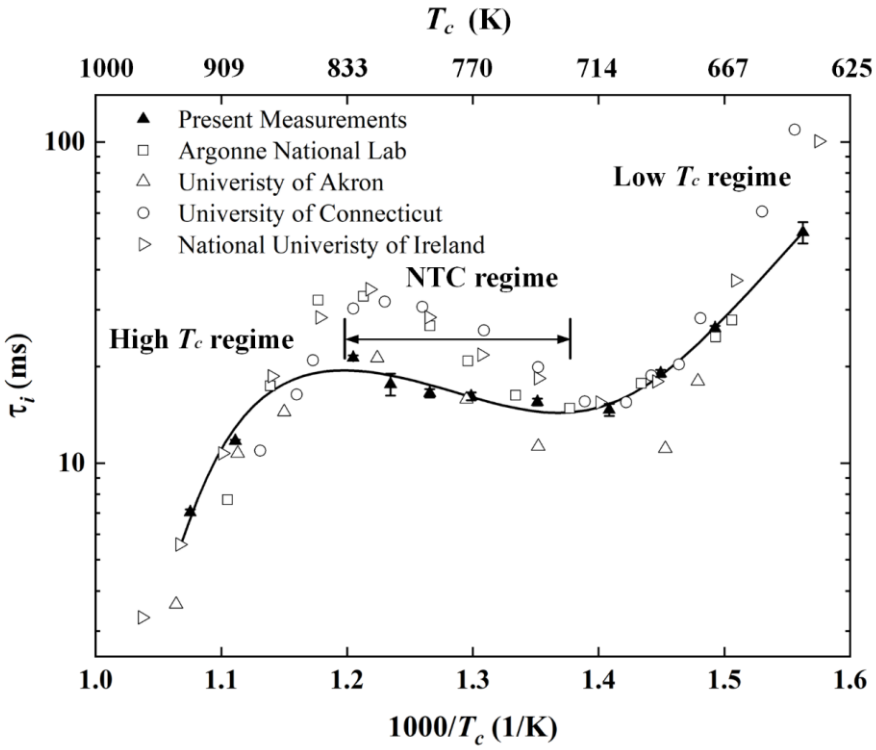


Figure 4.3. Currentliy RCM measured values of $\tau_i$ for stoichiometric *i*-octane-oxygen mixturesv (with error bar), compressed to 2 MPa with $T_c$ values between 640 and 930 K, as listed in Table 1. Additional data is from the 2nd International RCM Workshop [127].

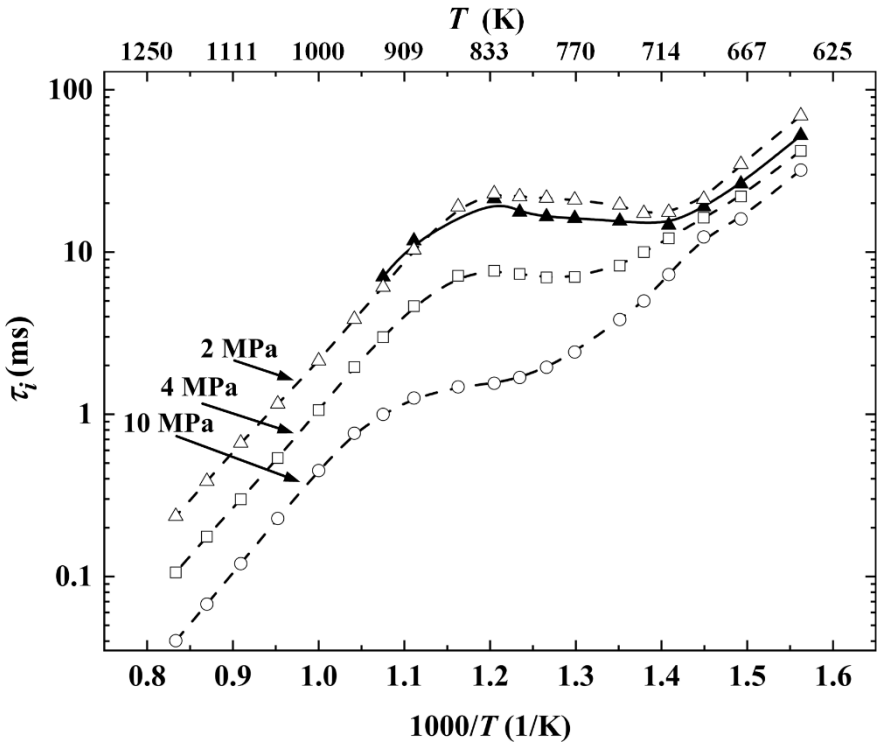


Figure 4.4. Values of $\tau_i$ for stoichiometric *i*-octane-oxygen mixtures for current experiments at 2 MPa and *i*-octane-air chemical kinetic values at 2, 4, and 10 MPa.

### 4.2.4 Autoignitive Velocity and Chemical Excitation Time

For autoignitive propagation, the therotical autoignitive velocity, $u_a$ is determiend as:

$$u_a = \frac{\partial r}{\partial \tau_i} = (\frac{\partial r}{\partial T})(\frac{\partial T}{\partial \tau_i}). \tag{4.3}$$

The aututoignitive propagation speed, $S_a$, is $u_a$ multiplied by the same density ratio as for the flame speed. In a hot spot, the temperature decreases with distance from the center, leading to a negative temperatrue gradient of $(\frac{\partial r}{\partial T})$. Simultaneously, $\tau_i$ reduces with an increase in temperature, resulting in a negative derivative $\left(\frac{\partial T}{\partial \tau_i}\right)$, which contributes to a positive $u_a$. Conversely, under NTC conditions, $\tau_i$ extends as temperature ascends, producing a positive derivative $\left(\frac{\partial T}{\partial \tau_i}\right)$. In this regime, it is expected that cool spots will ignite in areas of lower temperature, characterized by a positive temperature gradient $(\frac{\partial r}{\partial T})$. Thus, with NTC, the derivative $\left(\frac{\partial T}{\partial \tau_i}\right)$ remains positive, and at a cold spot, both the temperature gradient $(\frac{\partial r}{\partial T})$ and $u_a$ are positive. However, accurately measuring the temperature gradient around hot or cool spots is challenging, with precision often being

elusive. Kalghatgi and Bradley [141] chose a constant temperature gradient of $\frac{\partial T}{\partial r}$ = -2 K/mm for a hot spot based on its strong alignment with experimental engine data. This assumption has been broadly adopted in various studies [19, 133, 193]. Momentarily, from Eq. 4.3, a NTC can generate values of $\left(\frac{\partial \tau_i}{\partial T}\right)$ that are close to, or even equal to, zero, with implied infinite, or very large, values of $u_a$. Numerically, following the methodology in [193], $\tau_i$ and $\tau_e$ were empirically approximated using multiple regression method, with temperature and pressure as the independent variables is adopted here:

$$\tau_i, \tau_e = A \times e^{(\boldsymbol{B/T})} \times (\frac{P}{2})^C. \quad (4.4)$$

For the NTC regime (725 - 830 K)

$$\tau_i = A \times e^{(\boldsymbol{B \times T})} \times (\frac{P}{2})^C. \quad (4.5)$$

With $\tau_i$ in ms, $\tau_e$ in μs, $P$ in MPa and $T$ in K.

The partial derivative of Eqs. 4.4 and 4.5 with respect to temperature yields Eqs. 4.6 and 4.7:

$$\partial \tau_i / \partial T = B \times \tau_i / T^2 , \quad (4.6)$$

For the NTC regime (727 - 830 K)

$$\partial \tau_i / \partial T = B \times \tau_i, \quad (4.7)$$

Table 4.1. Constants A, B and C for $\tau_i$ and $\tau_e$ in *i*-octane-air mixture.

| | $\tau_i$ | | | $\tau_e$ |
|---|---|---|---|---|
| Temperature | 640 - 727 K | 727 - 830 K | 830 - 1200 K | 640 - 1200 K |
| A | $1.31\times 10^{-4}$ | 1.81 | $5.59 \times 10^{-6}$ | 0.61 |
| B | 8231 | 0.0029 | 13003 | 1790 |
| C | -0.3 | -1.2 | -1.15 | -0.25 |

Equation 4.3 shows the crucial importance of $\frac{\partial \tau_i}{\partial T}$ and Figure 4.4 shows a plot of $\frac{\partial \tau_i}{\partial T}$ for stoichiometric *i*-octane-air against temperature at pressures of 2, 4 and 10 MPa. The value increases with the temperature, approaching zero in the NTC regime, then becomes slightly positive. Figure 4.5 illustrates a comparison between the ignition delay times derived from these empirical equations and those predicted by the LLNL mechanism.

This comparison reveals that our empirical correlations closely align with the mechanism's predictions. This is evidenced by the data points lying near the equivalence line and a strong correlation coefficient ($R^2$ value) of 0.98, underscoring the accuracy of our empirical correlations.

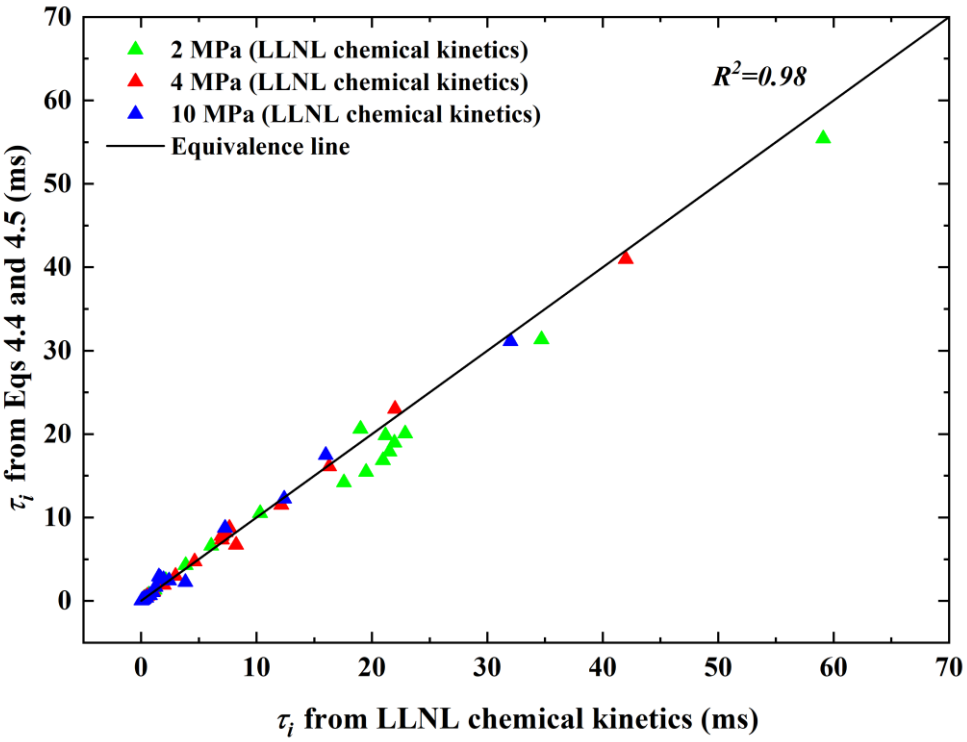


Figure 4.5. Ignition delay time from Eqs. 4.4 and 4.5 compared with from LLNL chemical kinetics mechanism.

The values of $\frac{\partial \tau_i}{\partial T}$ in Eqs. 4.6 and 4.7 are employed in Eq. 4.3 to derive $u_a$. These values are shown in Fig. 4.6. The expression for $u_a$, and the possible closeness of the value of $\frac{\partial \tau_i}{\partial T}$ to zero, creates an abnormally amplified sensitivity of the value of $u_a$, with a near zero $\frac{\partial \tau_i}{\partial T}$ leading to a very high $u_a$. The problem is compounded with the uncertainty about the assumed constant value of $\frac{\partial r}{\partial T}$. Figure. 4.7 shows that, initially, $u_a$ is very small but increases with temperature on entering into the NTC regime, only to fall in value on leaving it for the high temperature regime. There, with increasing temperature, there is a sharp increase in $u_a$, particularly at high pressure. Values of $u_a$ derived by this method, are applied in Section 4.3.1 and 4.3.2 to enable the autoignitive speeds associated

with the pressure trace to be found. This is also utilised to ascertain the dimensionless parameter, $\xi$ for the detonation peninsula in Section 4.3.3 and 4.3.4.

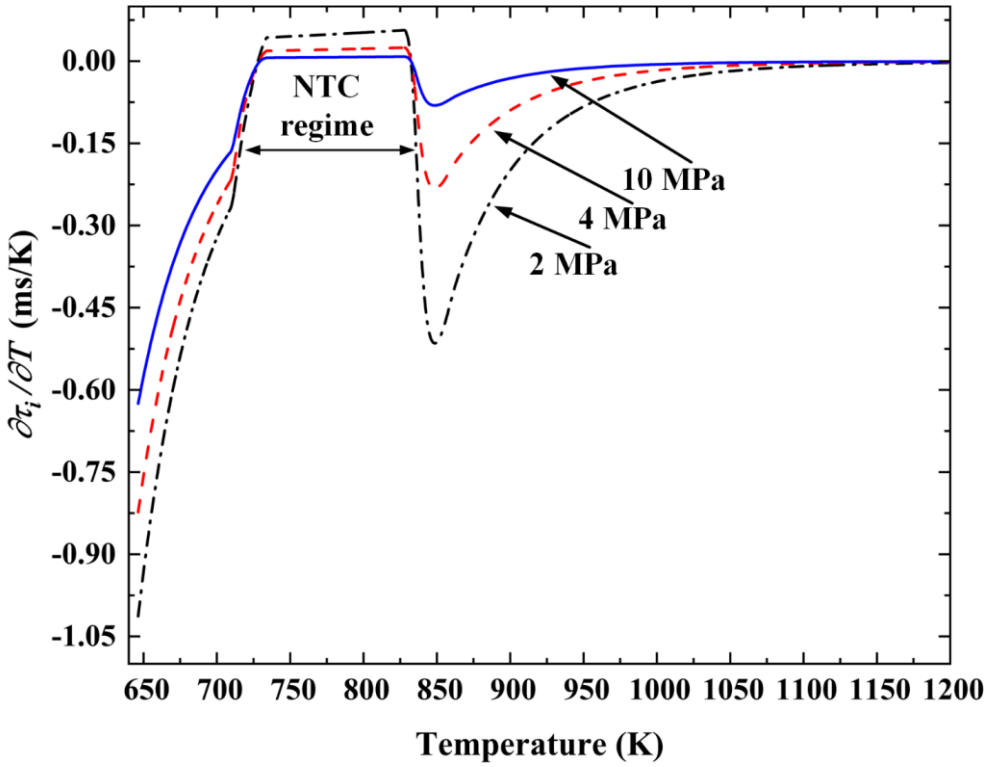


Figure 4.6. Values of $\partial\tau_i/\partial T$ for stoichiometric *i*-octane-air, derived from chemical kinetic values at 2, 4 and 10 MPa.

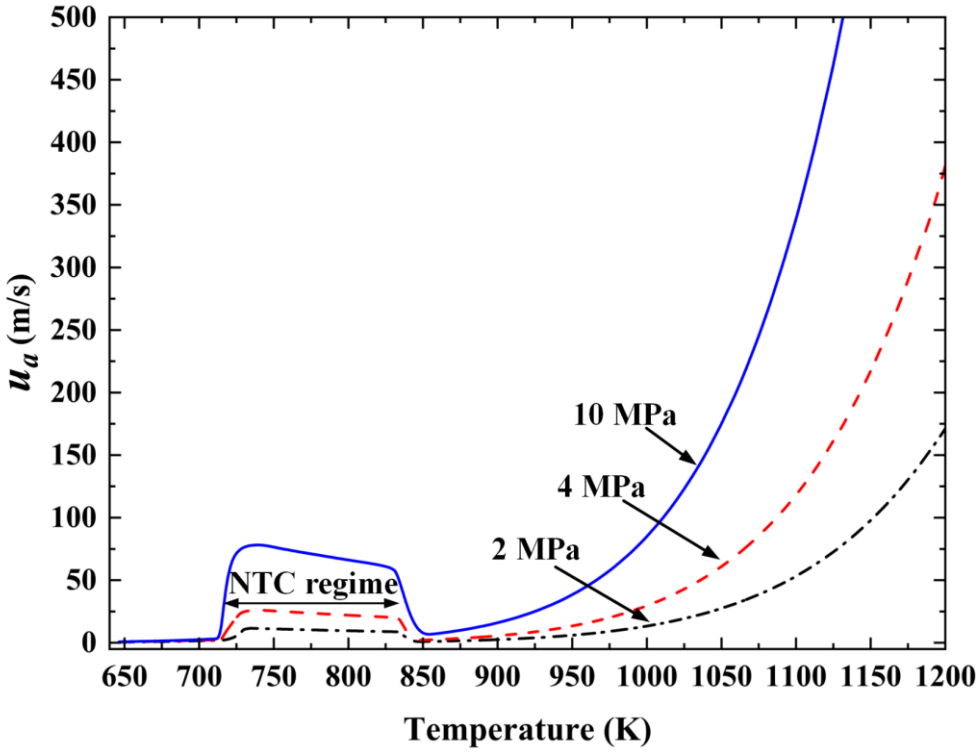


Figure 4.7. $u_a$ for stoichiometric *i*-octane-air derived from chemical kinetic values at

2, 4 and 10 MPa.

The chemical excitation time $\tau_e$ is the key parameter in the evalutation of $\varepsilon$. It was evaluated using the CHEMKIN's closed homogeneous batch reactor [194], with detailed gasoline surrogate chemical kinetics [195], for the *i*-octane-air mixtures. A typical temporal profile of total heat release rates in a constant volume chamber is shown in Fig. 4.8. Lutz et al. [146] introduced the concept of chemical excitation time, $\tau_e$, which refers to the period during which exothermic chemical reactions accelerate and rapidly release thermal energy. It is the time interval from the point with 5% of the maximum total heat release rate to the attainment of that maximum value. Very many reactions are involved and at the highest temperatures the chain branching H + $O_2$ reaction is particularly significant.

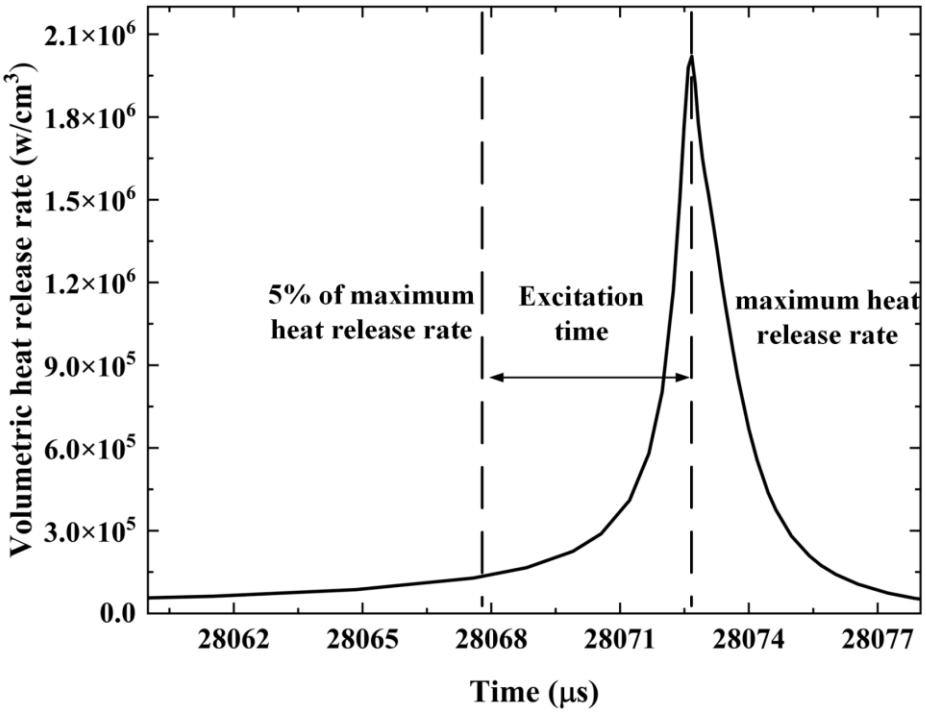


Figure 4.8. Total heat release rate for the stoichiometric *i*-octane-air mixtures, at 2 MPa and $T_c$ = 830 K.

Values of, $\tau_e$, found in this way at different value of temperatures and pressure are shown in Fig. 4.9. The dashed lines are good fits to the temperature and pressure dependencies.

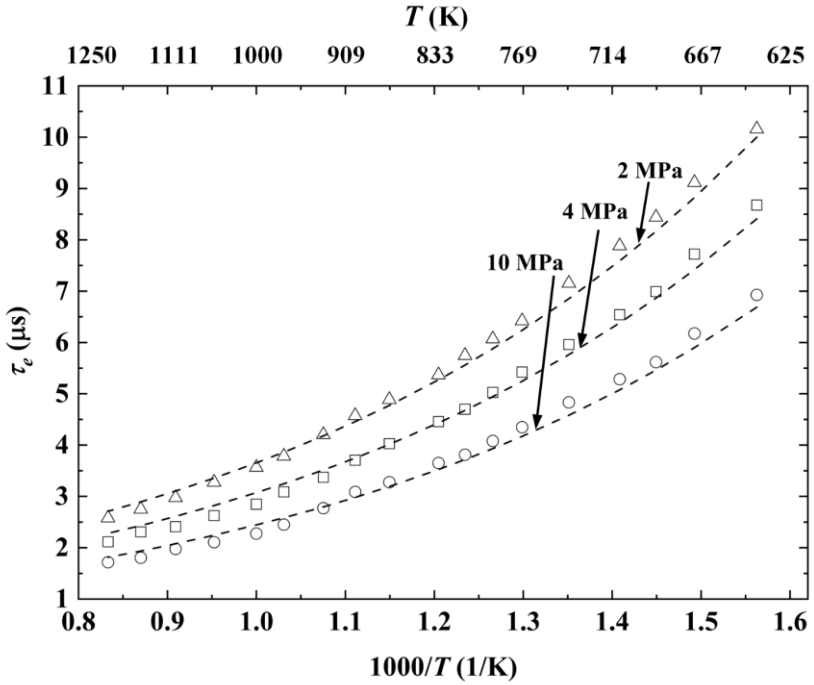


Figure 4.9. Computed chemical excitation times, $\tau_e$, for stoichiometric *i*-octane-air mixtures plotted against 1000/$T$ , at 2, 4 and 10 MPa.

### 4.2.5 Autoignition Parameters, $\xi$ and $\varepsilon$.

The proximity of the autoignitive velocity $u_a$, to the acoustic velocity, *a,* is significant in the context of detonation development. The autoignitive parameter, $\xi$, is defined as the ratio of $a/u_a$. The related excitation factor, $\varepsilon$, expresses how rapidly an acoustic wave can be accelerrated by chemical energy gained at the hot or cold spot of the chemical energy. The residence time of the acoustic wave at a hot or cold spot of radius $r_o$, is, $r_o/a$ and the excitation time for the greatest heat release rate is $\tau_e$. If the chemical heat release time is short enough to flow into the wave, it will reinforce it, and the relevant parameter is the excitation factor, $\varepsilon = \frac{r_0}{a\tau_e}$. Following [19, 133, 184, 193] a hot spot radius of $r_0 = 5$ mm is assumued. The value of acoustic velocity, $a$, is obtained from the GASEQ code [48]. It later will be shown how a low value of $\xi$ and a high value of $\varepsilon$ are condicive to a detonation. Figure. 4.10 shows values of $\xi$ for stoichiometric *i*-octane-air at different temperatures and pressures of 2, 4, and 10 MPa. In the low temperature regime, both increasing temperature and pressure decrease $\xi$. In the NTC regime, the value of $\xi$ rapidly decreases due to the gradient, $\frac{\partial \tau_i}{\partial T}$, approaching zero. When leaving the NTC regime, it increases. In

the high temperature regime, it sharply decreases with increasing temperature. It reaches unity as the temperature reaches 1150 K, and a pressure of 10 MPa. Figure. 4.11 shows the relationship of $\varepsilon$ under the same conditions as $\xi$, demonstrating a clear trend of its value escalating in tandem with increases in both temperature and pressure.

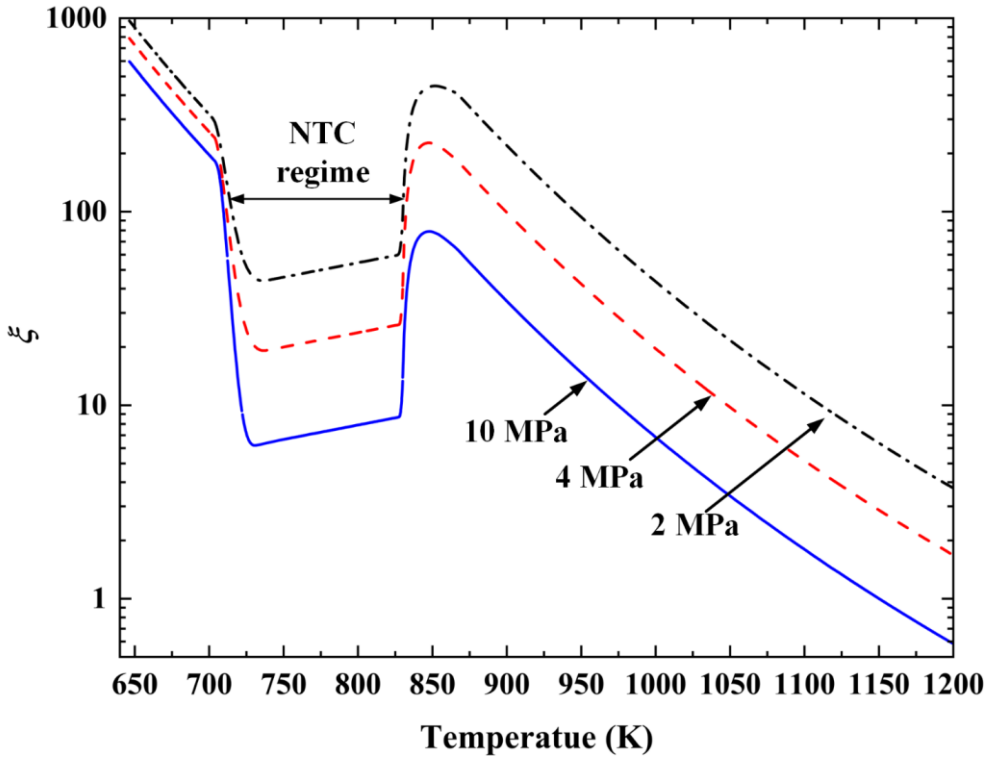


Figure 4.10. Values of $\xi$ for stoichiometric *i*-octane-air from chemical kinetic values at 2, 4 and 10 MPa.

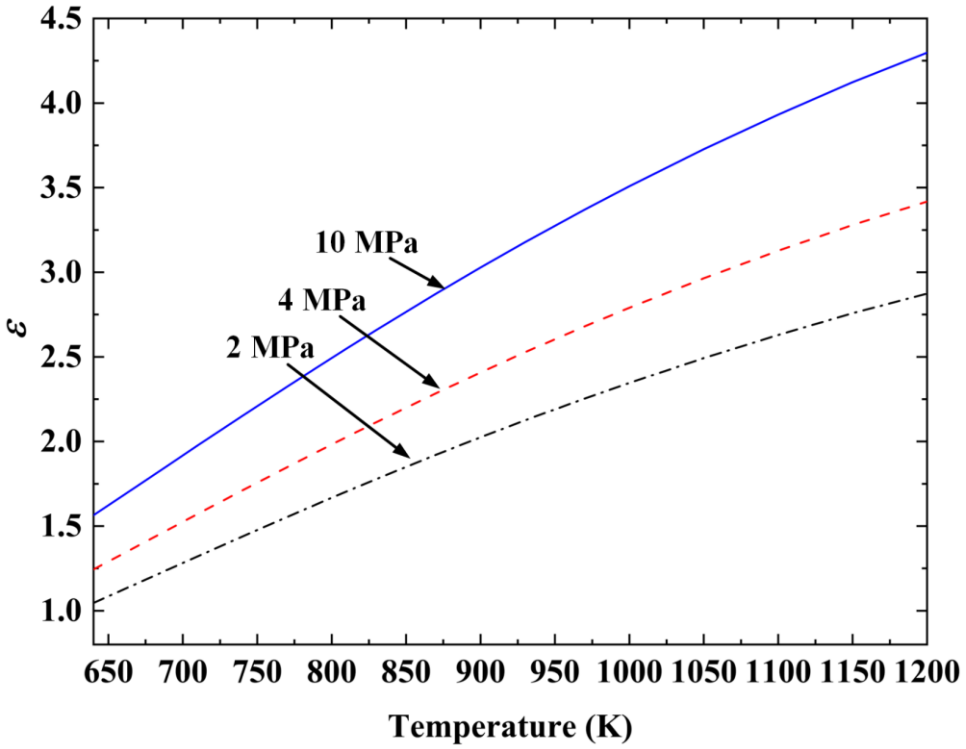


Figure 4.11. Values of $\varepsilon$ for stoichiometric *i*-octane-air derived from chemical kinetic values at 2, 4 and 10 MPa.

## 4.3 Reaction After Compression

### 4.3.1 Processing of Experimental Images and Measurements

This section describes the processing of fhe experimental images and measurements of reaction fronts throughout the explosions. Values of $\frac{\partial \tau_i}{\partial T}$ are required to compute the autoignitive speed for each explosion and its increasing values of $T$. Each set of images and measured data, including pressure and temperature, are associated with one of the 11 values of $T_c$, such as can be seen in Fig. 4.12. In all the flame imaging, sequences of binary and monochrome images were obtained, but only the former are shown in this sequence. This first sequence starts with the lowest value of $T_c$ = 640 K. The propagating reaction waves, usually are initiated close to of the cylinder wall with a changing velocity. Measured and calculated propagation speeds, are shown on the left, under the images. Measured pressures, and derived unburned gas temperatues are on the right. The associated $T$ and $P$ values during the autoignition, enable laminar flame and autoignitive

speeds to be calculated. These are shown by the chain-dotted and dashed curves, respectively, on the left. Burned Mass Fractions, BMF, are shown above each binary image. It is assumed no combustion in the black area behind the reaction front and the reaction front is the boundary between the burned and unburned regions.

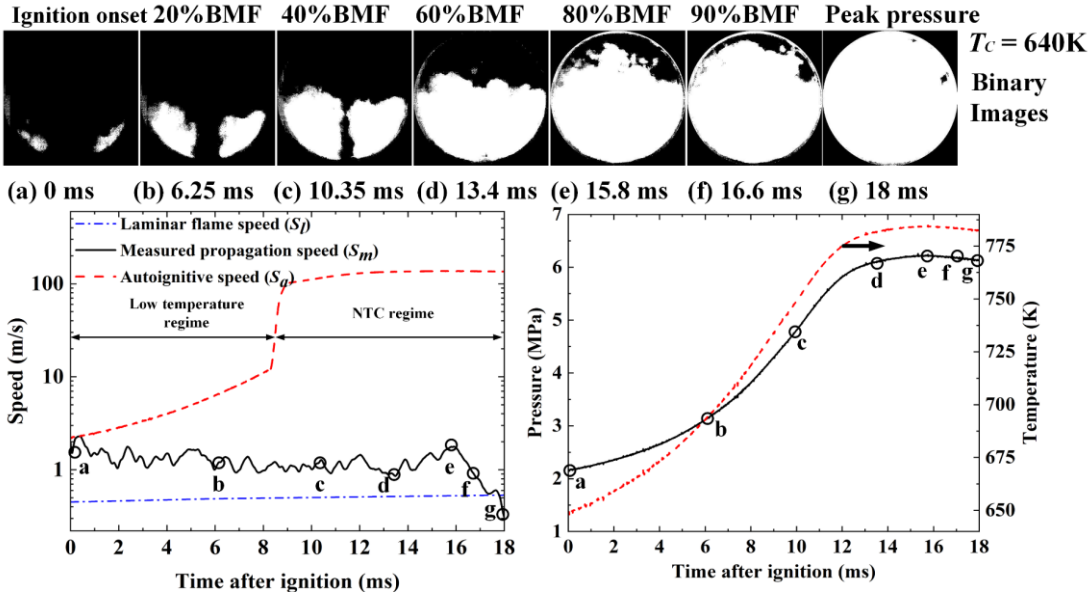


Figure 4.12. Speeds of reactive fronts (left) and profiles of pressure and unburned gas temperature (right) at $T_c$ = 640 K.

In Fig 4.12, binary images from the monochrome high-speed camera initially show two small ignition areas or hot spots, to emerge instantaneously from both left and right at the bottom of cylinder wall and start to propagate towards the centre of chamber. The measured propagation speed, $S_m$, is in this instance, close to the computed laminar flame speed, $S_l$, whilst the computed autoignitive speed, $S_a$, is significantly higher, suggesting the initial dominance of laminar flame propagation. The observed wrinkling of the propagation front may be attributed to either turbulence generated during the compression process or the hydrodynamic instability. This turbulence-induced wrinkling, leading to an increased flame propagation speed, could account for the measured propagation speed exceeding the laminar flame speed.

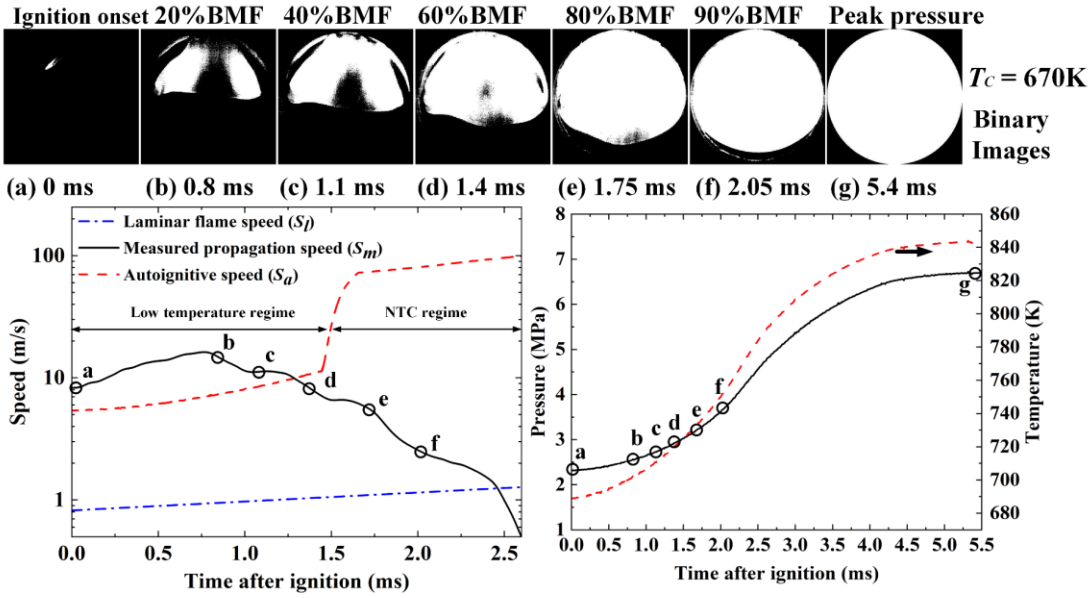


Figure 4.13. Speeds of reactive fronts (left) and profiles of pressure and unburned gas temperature (right) at $T_c$ = 670 K.

As depicted in Figure 4.13 (a), with a $T_c$ of 670K, the initial binary image reveals a small initiating kernel on the left, which is subsequently joined by another from the right. Initially, the $S_m$ are closer to the $S_a$, as calculated in Section 4.2.4. The fact that $S_m$ is considerably greater than the laminar flame speed indicates the presence of an autoignitive propagation mode.

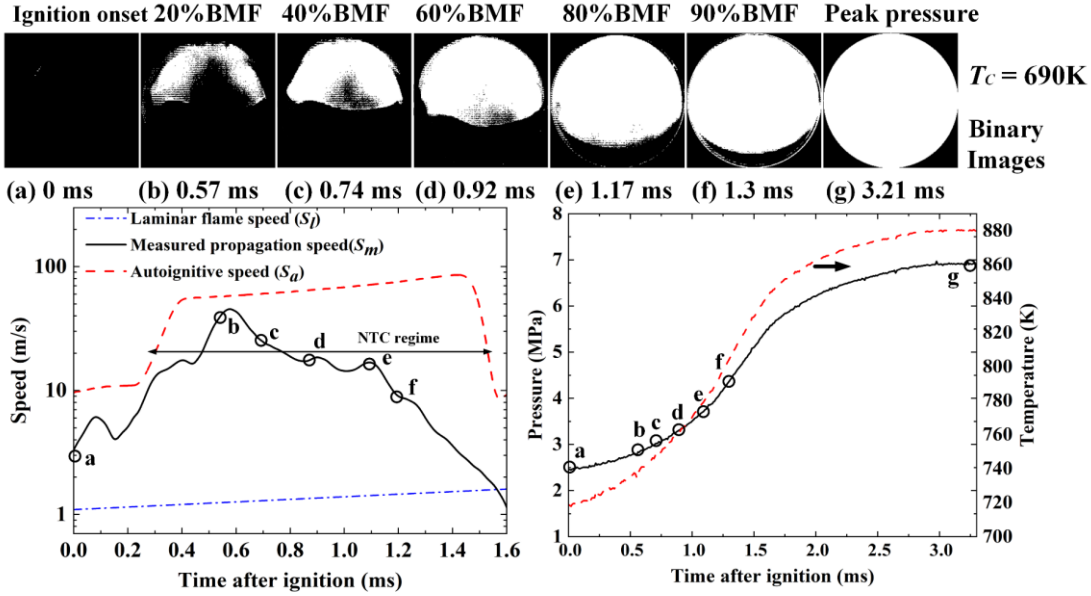


Figure 4.14. Speeds of reactive fronts (left) and profiles of pressure and unburned gas temperature (right) at $T_c$ = 690 K.

The binary images in Figure 4.14 (a) and (b) illustrate that initially, there are two separate

reaction centers which later become closely interconnected. In the early stages, the measured propagation speed is similar to the calculated laminar flame speed. However, as the temperature enters the NTC regime, the measured propagation speed shows a notable interaction and tends to align more closely with the autoignitive speed. Subsequently, it shifts back towards the calculated laminar value. This event marks the final explosion that occurs without substantial pressure oscillation.

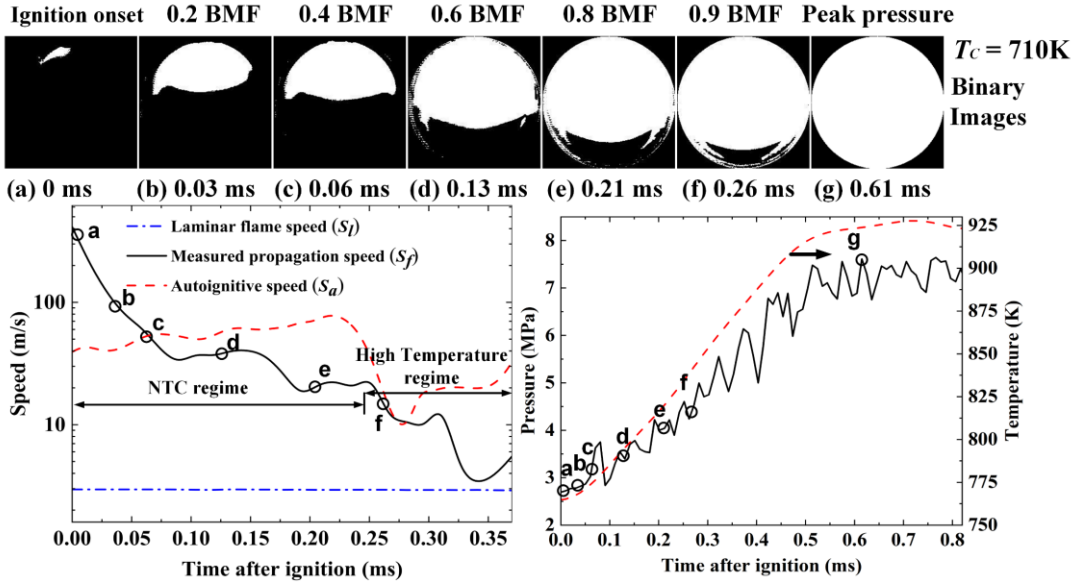


Figure 4.15. Speeds of reactive fronts (left) and profiles of pressure and unburned gas temperature (right) at $T_c$ = 710 K.

At $T_c$ = 710 K, as shown in Fig. 4.15, the autoignition occurs near the NTC regime. This proximity to the NTC regime appears to cause an increase in autoignitive speed, as indicated in Fig. 4.7. This increase is further confirmed by the measured propagation speed. Notably, for the first time, significant pressure oscillations begin early and increase in amplitude. At the onset of ignition, a high measured propagation speed of 330 m/s is observed.

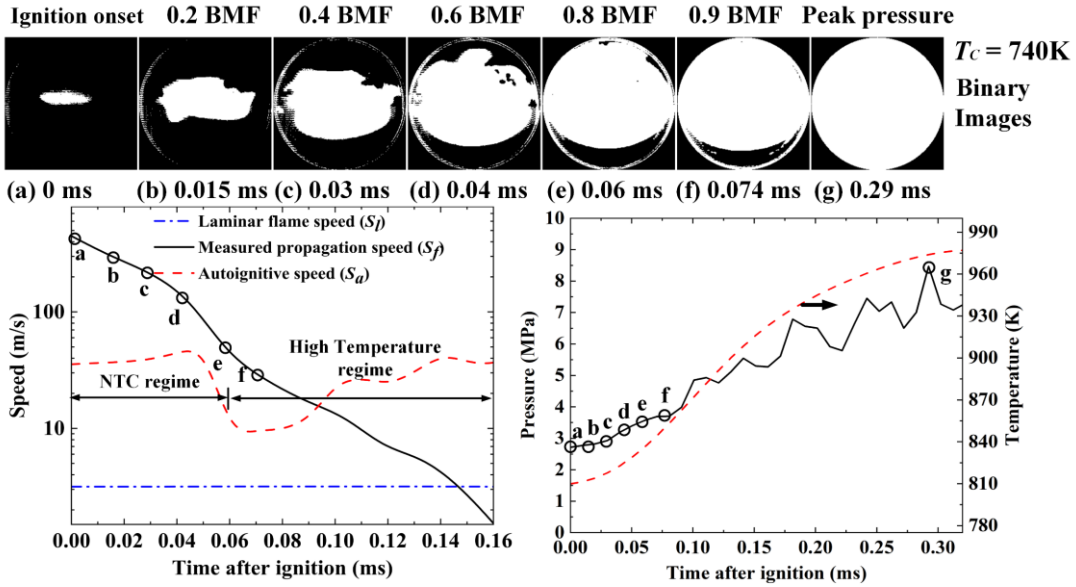


Figure 4.16. Speeds of reactive fronts (left) and profiles of pressure and unburned gas temperature (right) at $T_c$ = 740 K.

At a $T_c$ of 740 K, the system enters the NTC regime. Figure 4.16 illustrates that the initially high, but subsequently diminishing, measured propagation speed receives only partial support from autoignitive computations. At the onset of ignition, particularly in a cool spot, a maximum measured propagation speed of 390 m/s is recorded. Additionally, there is an observed increase in the amplitude of pressure fluctuations.

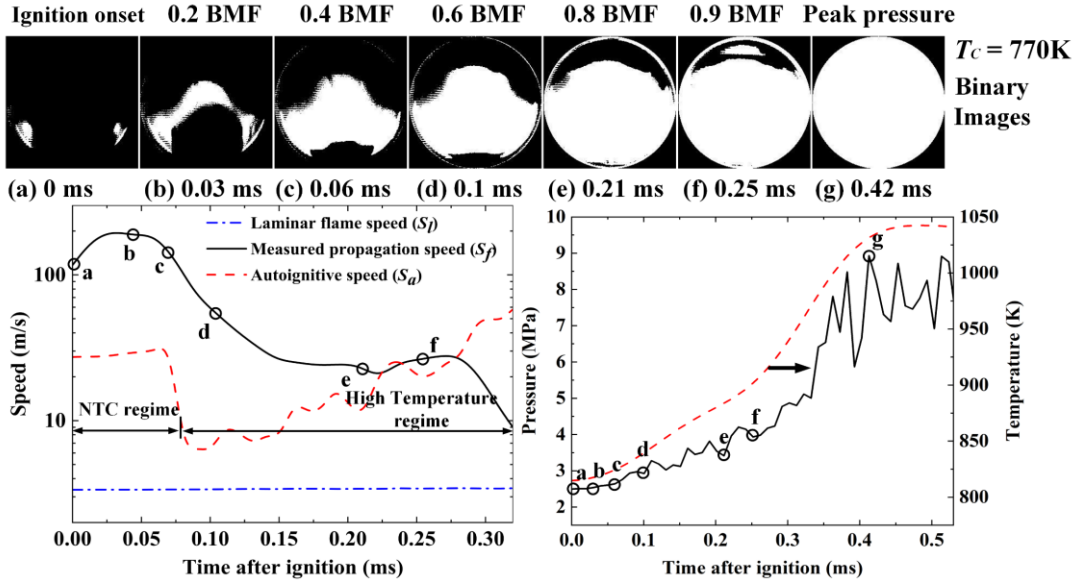


Figure 4.17. Speeds of reactive fronts (left) and profiles of pressure and unburned gas temperature (right) at $T_c$ = 770 K.

Figure 4.17 showcases that within the NTC regime, there is an increase in the amplitudes

of pressure fluctuations and high initial measured propagation speeds. These speeds initially receive some support from autoignitive speed computations.

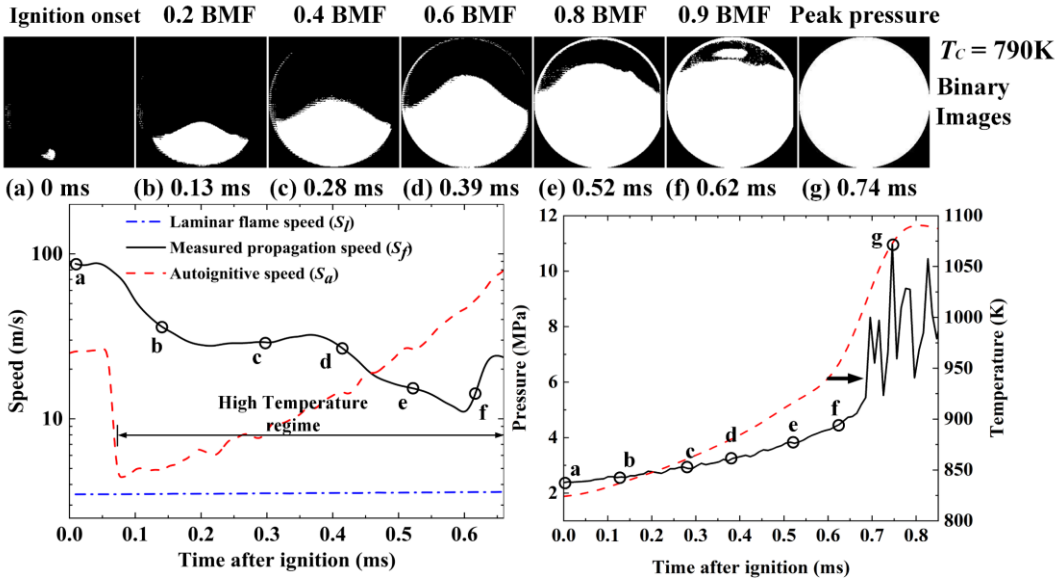


Figure 4.18. Speeds of reactive fronts (left) and profiles of pressure and unburned gas temperature (right) at $T_c$ = 790 K.

In Fig. 4.18, at $T_c$ = 790 K, the binary images depict an initial hot spot propagating from the bottom left of the cylinder. By the time of image (f), there is a noticeable new autoignition area forming above the propagation front. Initially, between points (a) and (b), the calculated autoignitive speed aligns with the measured speed. This alignment reemerges after point (f), accompanied by an increase in the measured propagation speed and a pressure rise to 10 MPa, resulting in oscillations with an amplitude of 2.5 MPa. Still within the NTC regime, the scenario is characterized by high measured propagation speeds and intensifying pressure oscillations, indicating an approach towards detonation. The transition to an ultimate detonation is underway and is discussed in detail in Section 4.3.3.

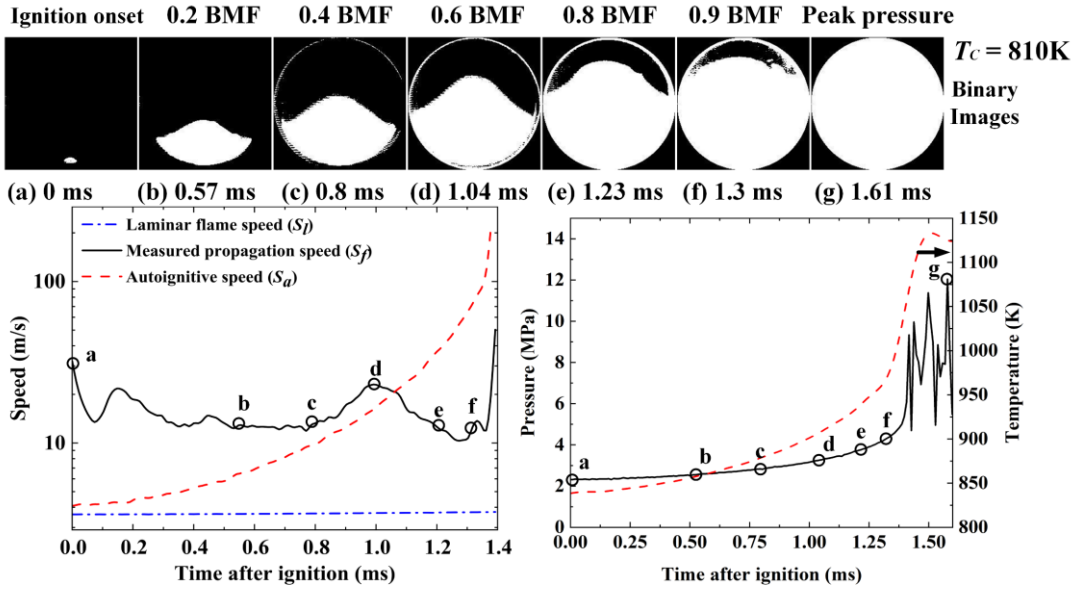


Figure 4.19. Speeds of reactive fronts (left) and profiles of pressure and unburned gas temperature (right) at $T_c$ = 810 K.

The binary images in Fig 4.19 (a) present a single initiating hot spot at a $T_c$ of 810 K, with an upward propagation observed. Initially, the computed autoignition speed nearly matches the measured speed, but this similarity is not maintained throughout. However, there is a notable final surge in both the measured and computed speeds, accompanied by the development of strong pressure oscillations. This scenario occurs near the high-temperature boundary of the NTC regime, which is around 830 K.

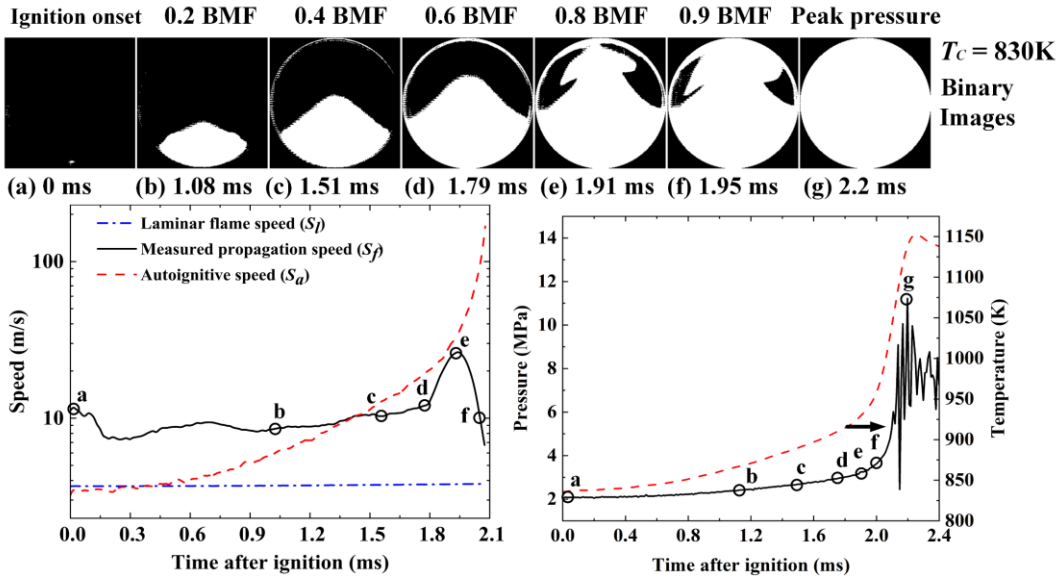


Figure 4.20. Speeds of reactive fronts (left) and profiles of pressure and unburned gas temperature (right) at $T_c$ = 830 K.

Figure 4.20, set at a $T_c = 830$ K, shows that the measured propagation speed surpasses the theoretical autoignitive values until approximately 880 K. This phase is marked by strong pressure oscillations, ultimately leading to detonation. Between points (c) and (d), the measured propagation speed and the theoretical autoignitive speeds converge, followed by a significant decrease in the measured values as the temperature continues to rise. This suggests that the reaction becomes more concentrated in the final stages.

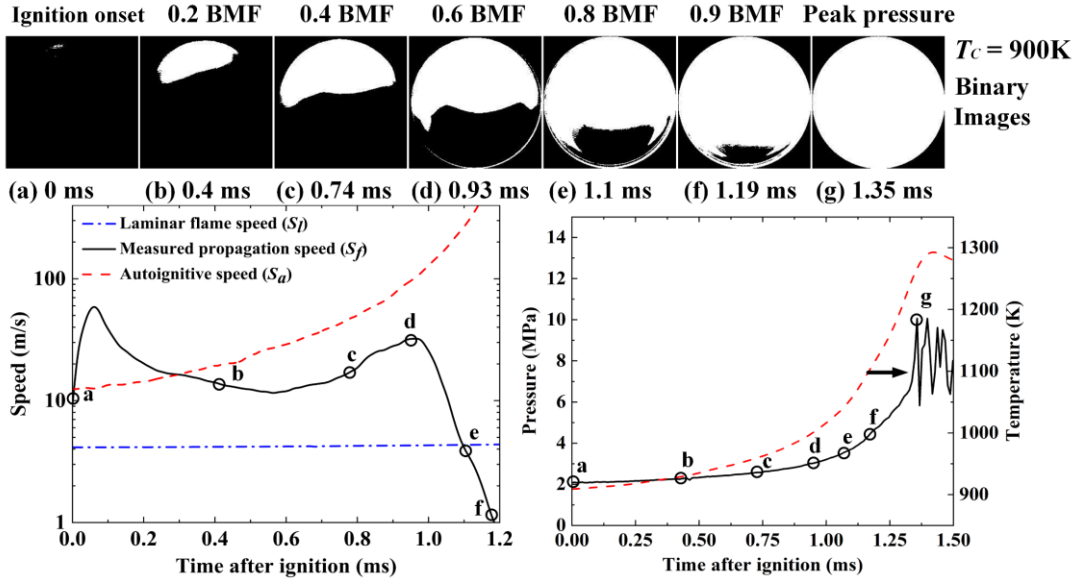


Figure 4.21. Speeds of reactive fronts (left) and profiles of pressure and unburned gas temperature (right) at $T_c = 900$ K.

In Figure 4.21, binary image (a) depicts the ignition hot spot starting at the top left of the cylinder. From the initial ignition at point (a) to point (d), the computed autoignitive speed aligns reasonably well with the measured propagation speed. However, in later stages, it starts to decrease as pressure oscillations intensify and detonation begins to form, remaining moderately close to the autoignitive speed. Following this, there is a marked decline in the measured propagation speed. This final drop in speed is likely linked to the reaction wave nearing the cylinder wall, coupled with the emergence of pressure oscillations reaching an amplitude of 2.0 MPa. Despite the absence of a distinctly coherent reaction front, a high reaction rate is observed, likely indicating the onset of detonation.

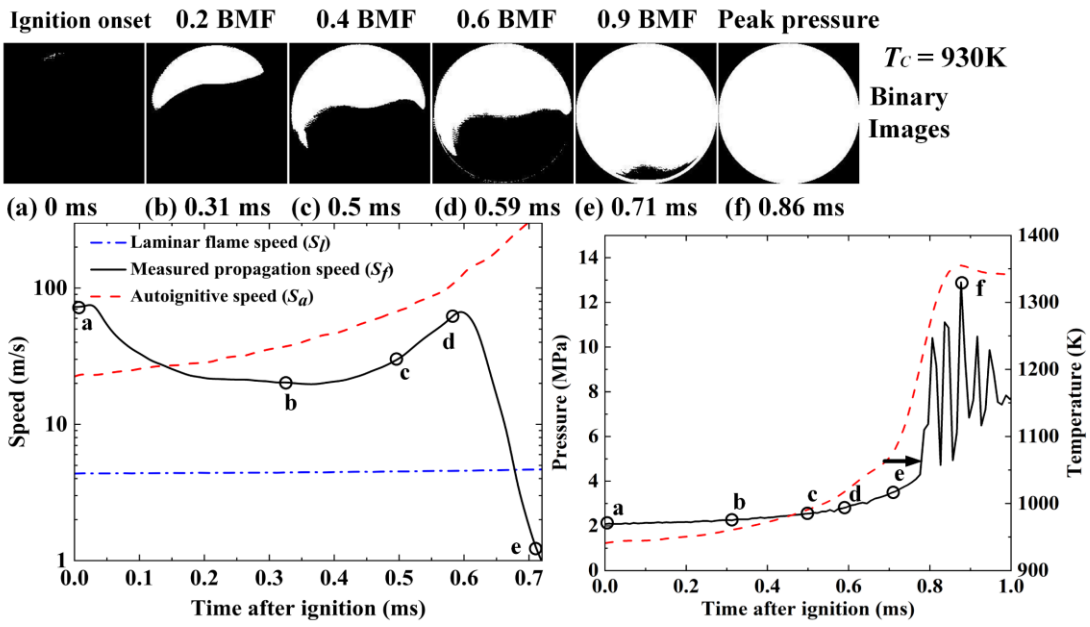


Figure 4.22. Speeds of reactive fronts (left) and profiles of pressure and unburned gas temperature (right) at $T_c$ = 930 K.

In Figure 4.22, at the highest $T_c$ = 930K, the patterns of ignition and propagation direction are noted to be similar to those observed at $T_c$ = 900 K. There is a notable alignment between the measured propagation speeds and the calculated autoignitive speeds, which is maintained until the final stages where the reaction wave interacts with the wall and detonation starts to develop. After point (e), pressure oscillations are observed, reaching an amplitude of 4.0 MPa.

### 4.3.2 Summary of Propagation Speeds and Ignition Modes

The data presented in Fig. 4.23 provides a comprehensive summary of all reaction propagation speeds discussed. These speeds cover the NTC regime but exclude the transition to detonation. This figure reveals that out of all the recorded ignitions, five started at the top and six at the bottom of the cylinder. The figure displays the measured propagation speeds ($S_m$), the calculated autoignitive speeds ($S_a$), and the laminar flame speeds ($S_l$), all recorded just after compression at $T_c$. The $S_m$ values are determined as the mean propagation speed from the onset of autoignition to the point where a 5% burned mass fraction is reached. Both $S_a$ and $S_l$ represent speeds at their respective $T_c$ and an end of compression pressure of 2.0 MPa.

At the outset, with $T_c$ = 640 K, the measured propagation speed closely matched the

laminar flame speed and was lower than the theoretical autoignitive speed. However, as $T_c$ increased to 670 K and 690 K, the measured propagation speeds rose to 9.3 m/s and 18.8 m/s, respectively. These values are about ten times higher than the laminar flame speed and slightly exceed the calculated autoignitive speed, indicating a shift towards autoignitive propagation.

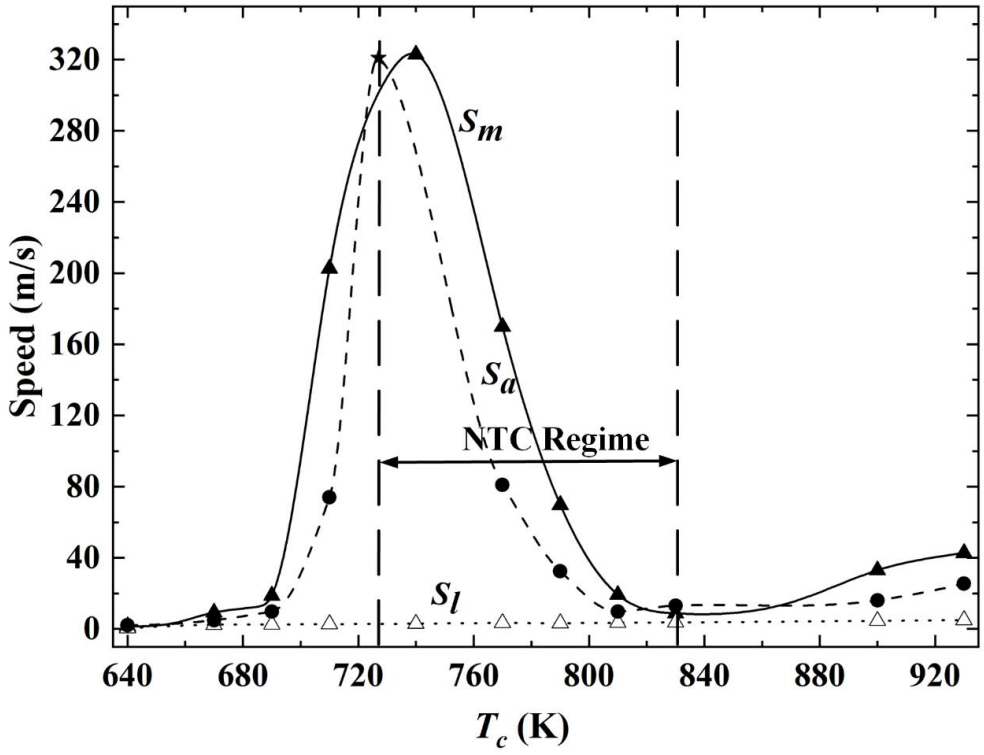


Figure 4.23. Measured propagation speed, $S_m$, calculated autoignitive speed, $S_a$, and laminar flame speed, $S_l$, plotted against $T_c$, for explosions, from 640 K to 930 K.

Close to the onset of the NTC regime, there is a significant increase in the $S_m$, reaching up to 210 m/s, whereas the computed $S_a$ only rises to 72 m/s. Deeper into the NTC regime, specifically at a $T_c$ of 740 K, $S_m$ peaks at a maximum of 323 m/s. As noted in Section 4.24, calculating autoignitive velocity, $u_a$, in the NTC regime is particularly challenging, a fact also evident from the values of $\frac{\partial \tau_i}{\partial T}$ illustrated in Fig. 4.6.

In the analysis presented in Fig 4.24, a finer temperature interval of 0.1 K was used to assess its effects on $\frac{\partial \tau_i}{\partial T}$, and $u_a$ at a constant pressure of 2 MPa. The entrance into the NTC regime is marked at 727.4 K, where $\frac{\partial \tau_i}{\partial T}$ drops below -0.0001 ms/K. This shift corresponds with an $u_a$ reaching as high as 7000 m/s. Theoretically, further refining the

temperature interval suggests that $\frac{\partial \tau_i}{\partial T}$ approaches zero, implying an infinitely high $u_a$. Based on these observations, a gradient of 0.0037 ms/K at 727.2 K was selected from the derived values of $\frac{\partial \tau_i}{\partial T}$ in Fig 4.24. This low gradient resulted in a $S_a$ of 315 m/s, which is indicated on Fig. 4.23 with an asterisk.

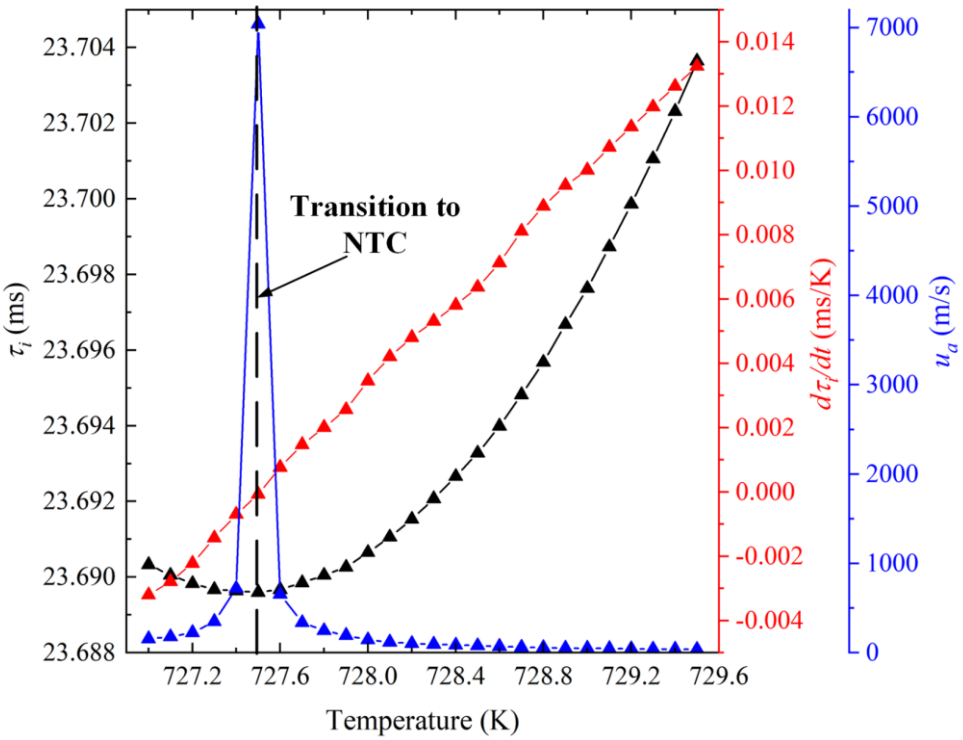


Figure 4.24. Variation of $\tau_i$, its derivative $\frac{d\tau_i}{dT}$ and autoignitive velocity $u_a$, across the NTC regime.

Uncertainties regarding the temperature gradient along the hot spot, denoted as $\frac{\partial T}{\partial r}$, particularly within the NTC regime, lead to considerable variability in the calculated values of the autoignitive speed. However, at the upper limit of the NTC regime, which is around 830 K, just after exiting this regime $S_m$ and $S_a$, converge at approximately 8 m/s. Beyond this point, in the high temperature regime, both the observed and calculated autoignitive speeds increase markedly, aiding in the transition to detonation.

### 4.3.3 Processing the Onset of Detonation

The final stages in the data processing involve the early development of detonations and the associated increases in pressure and temperature. The transition to detonation involves

a significant contribution from the $\xi$ and $\varepsilon$ parameters, both within and outside the detonation peninsula. Figures 4.25 and 4.26 illustrate how, with increasing rapidity, values of $\xi$ decrease while those of $\varepsilon$ rise, signaling the imminent arrival of detonation. The methodology for calculating $\xi$ and $\varepsilon$ is detailed in Section 4.2.5. In this context, these parameters are determined for the measured variables and are presented in conjunction with them. Concurrently, there is an increase in the amplitudes of pressure oscillations as the reaction front nears the chamber wall.

Despite the monochrome images in these two figures having limited optical contrast, they still provide a clearer visual representation of the expanding detonation front. Notably, after initiation at points (d) and (e), a pronounced increase in pressure oscillations (super-knock) is observed. This observation indicated that the super-knock in the engine conditions is caused by the transition to detonation.

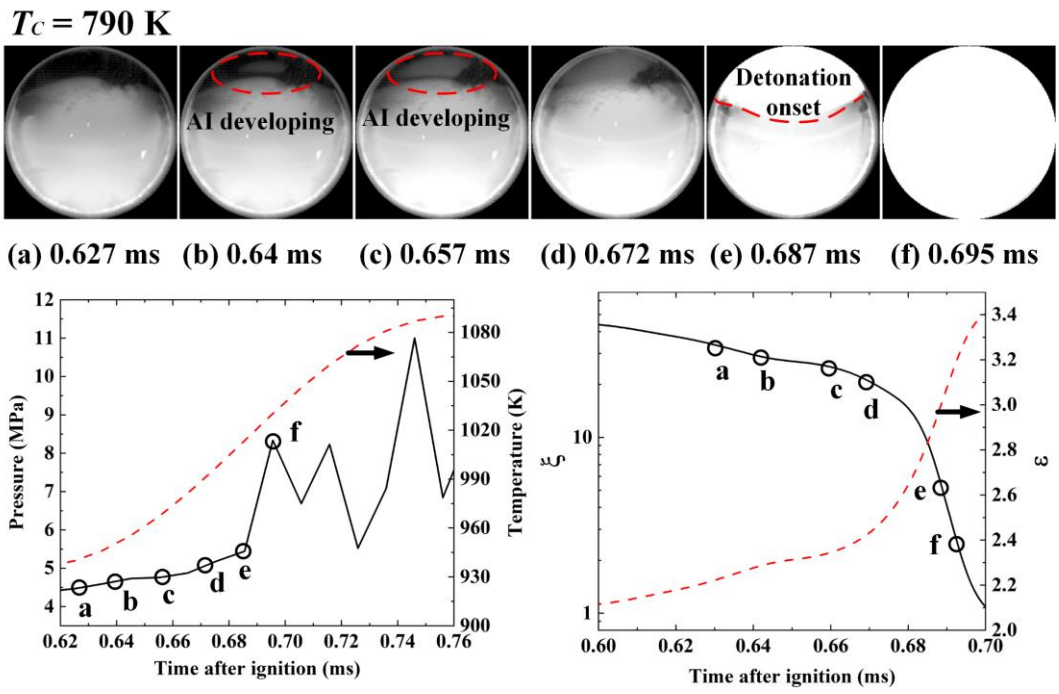


(a) Pressure and mixture temperature profiles (b) $\xi$ and $\varepsilon$ profiles

Figure 4.25. High Speed Detonation Images, derivations of $\xi$ and $\varepsilon$ at $T_c$ = 810 K.

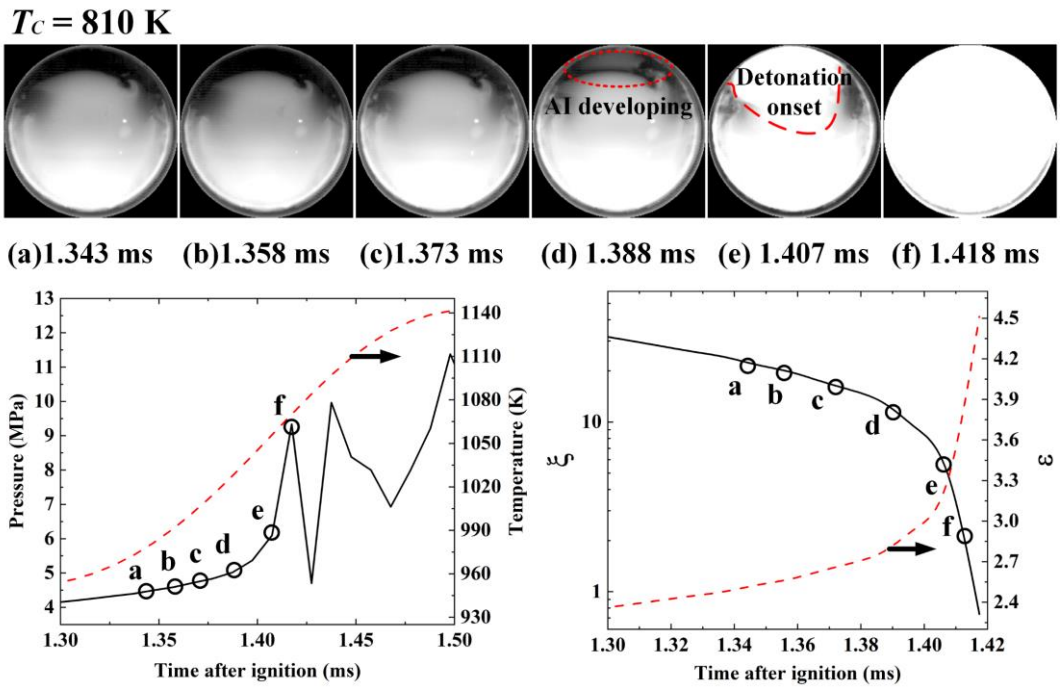


(a) Pressure and mixture temperature profiles (b) $\xi$ and $\varepsilon$ profiles

Figure 4.26. High Speed Detonation Images, derivations of $\xi$ and $\varepsilon$ at $T_c$ = 810 K.

### 4.3.4 Detonation Peninsulas

The values of $\xi$ and $\varepsilon$, which mark the Detonation Peninsula, within which detonations occur, along with its ancillary boundaries, were taken from [140]. A comprehensive discussion on the boundaries of the detonation peninsula, along with an in-depth analysis of the parameters $\xi$ and $\varepsilon$ is provided in Section 2.3.5. Outside this Peninsula, any propagation events are likely to be either subsonic autoignition or deflagration. Deflagration refers to the subsonic propagation of a flame, which is distinct from subsonic autoignition. The latter involves spontaneous ignition occurring under conditions of higher initial temperature and pressure.

The relative severities of different autoignitions can be assessed. The various mixtures are categorized in Table 4.1 based on their $T_c$ values. On all peninsulas, triangle symbols denote the absence of significant pressure oscillations. The size of a circular symbol corresponds to the amplitude of the pressure oscillations, and the numeral to the right signifies the average oscillating pressure in MPa. Regarding the explosion characteristics, three pairs of explosions are analyzed under varying $T_c$ values. The explosions at $T_c$ = 790

K and 810 K resulted in moderate detonations, representing the ultimate outcomes for the experiments detailed in Figures 4.25 and 4.26. Before these detonations developed, there were periods of subsonic autoignitions. A detonation at $T_c$ = 790 K, characterized by $\varepsilon$ = 3.5 and $\xi$ = 2.4, presents the lowest detonation parameter, $\varepsilon/\xi$, at 1.46.

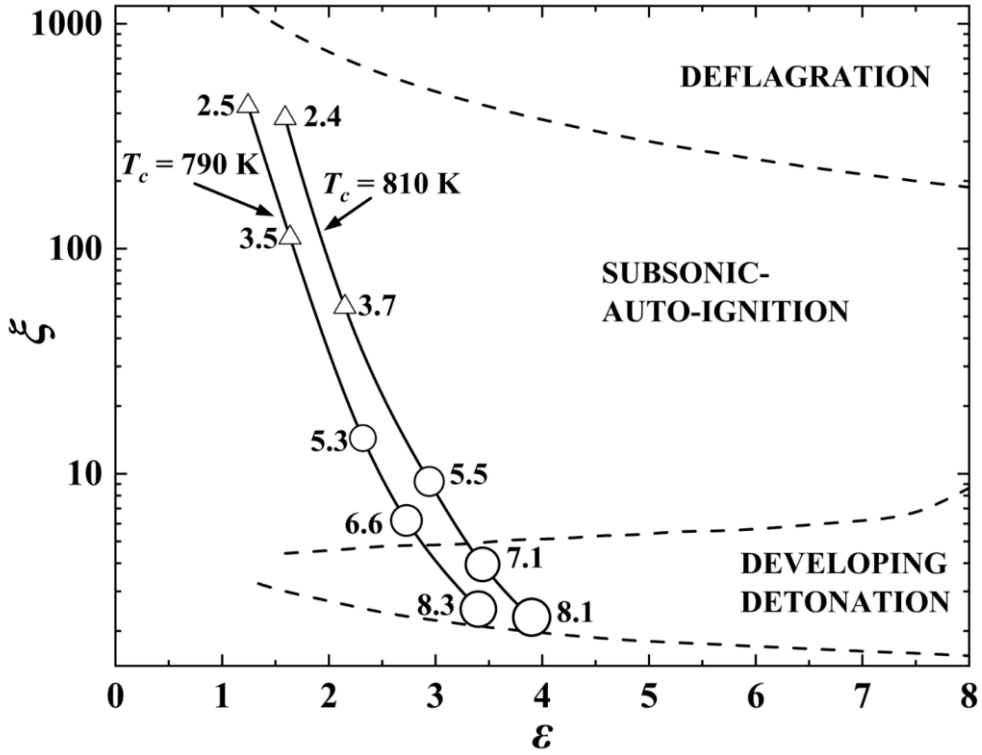


Figure 4.27. Peninsulas $\xi$ - $\varepsilon$ diagram for $T_c$ = 790 K and 810 K.

The notable aspect of the results in Fig. 4.28, at $T_c$ of 710 K and 770 K is the absence of detonations and the infrequency of strong autoignitions, indicating low reactivity outcomes. This experimental data is presented in Figures 4.15 and 4.17. At no point do the derived values for these temperatures enter the Detonation Peninsula, confirming that there are no detonations, only subsonic autoignitions.

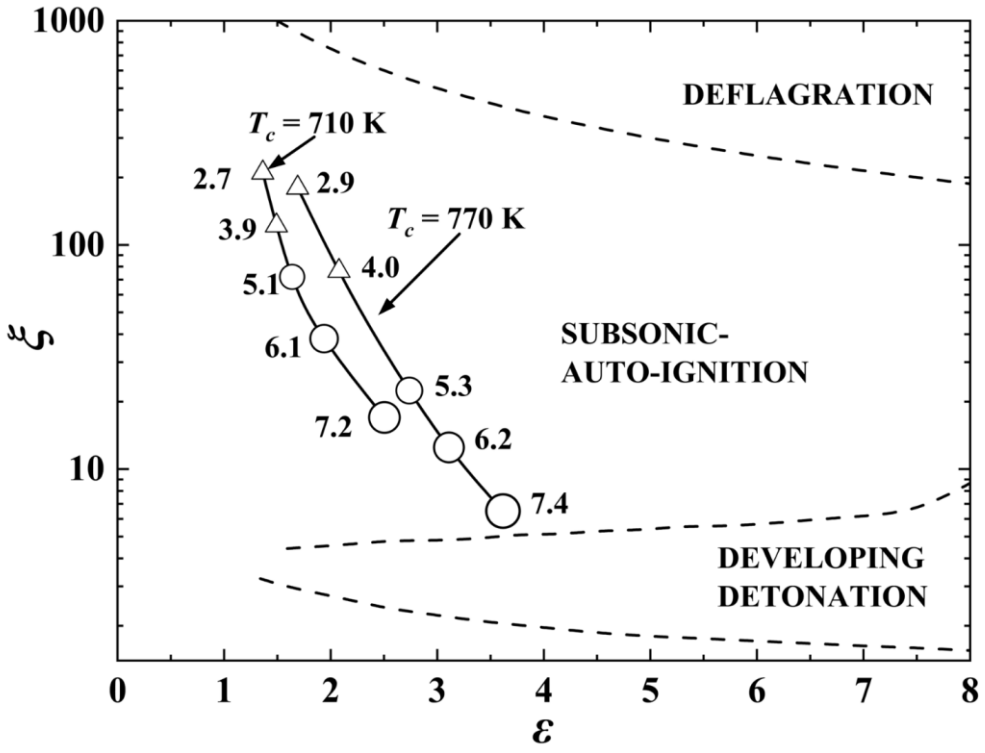


Figure 4.28. Peninsulas $\xi$ - $\varepsilon$ diagram for $T_c$ = 710 K and 770 K.

At $T_c$ = 830 K and 930 K, the experiments both quickly led to detonations, and are similarly reactive. Figure 4.29 highlights a rapid increase in $\varepsilon$ to 5.1 at a relatively low $\xi$ value of around 1.8, indicating that a significant amount of energy is being rapidly inputted into a developing acoustic wave. If this rate is sufficiently high, it may be classified as super knock. According to [193], super knock is associated with more severe detonations, characterized by $\varepsilon$ values as high as 11 and $\xi$ values as low as 2.7. However, a high $\varepsilon$ value can be offset by a high $\xi$ value.

In contrast, it is interesting to compare these findings with the results at the lowest $T_c$ of 640 K. For this temperature, all $\varepsilon$ values were below than unity, and all $\xi$ values exceeded 30. This condition was marked by the absence of pressure oscillations and detonations, and it was possible to support laminar flame propagation.

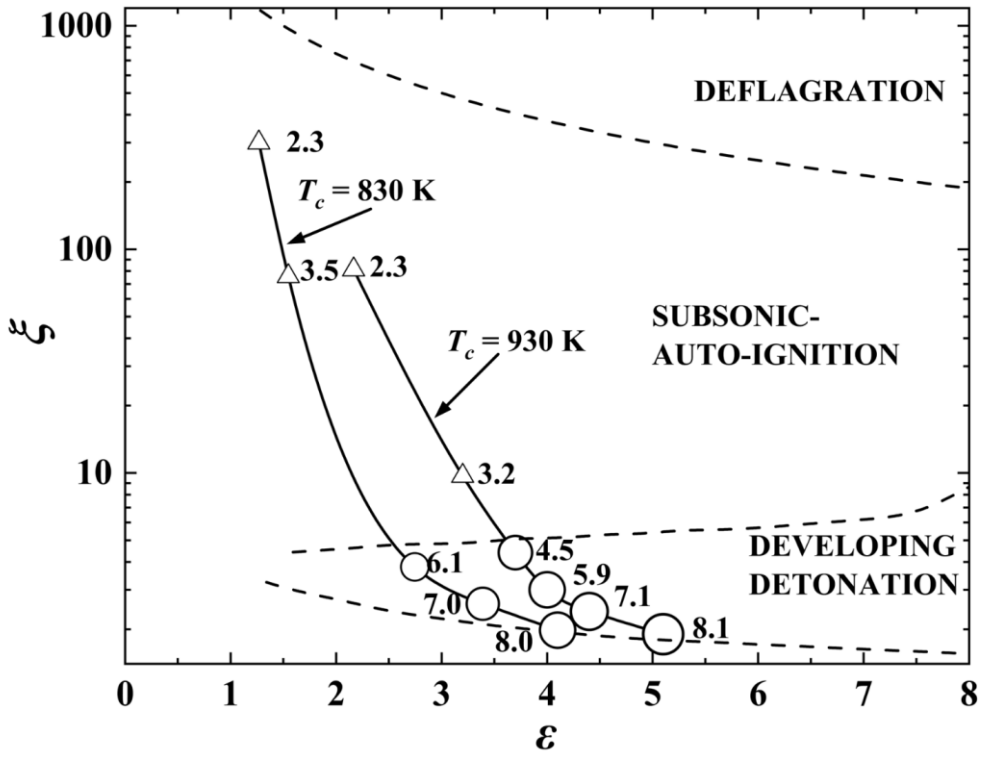


Figure 4.29. Peninsulas $\xi$ - $\varepsilon$ diagram for $T_c$ = 830 K and 930 K.

### 4.4 Pressure Perturbations

The trend towards detonation is marked by increasing oscillations in the pressure record, making it useful to plot the normalized amplitudes of the pressure oscillations ($\Delta P/P$) against a Detonation Parameter ($\varepsilon/\xi$). This is comprehensively demonstrated across a wide range of conditions in Fig 4.30. In the initial low-temperature regime characterized by brief laminar flames, no pressure amplitudes were detected, and here the ($\varepsilon/\xi$) ratio was estimated to be less than 0.002. As $T_c$ increased, so did the autoignitive velocities and the amplitudes of the pressure fluctuations. This type of plot is particularly insightful for distinguishing between different operational regimes.

With $T_c$ at 710 K, a temperature slightly below the threshold for entering the NTC regime, the increasingly rapid autoignitive speeds significantly heightened the amplitudes of the pressure oscillations. The exceptionally high autoignitive velocity within the NTC regime, as shown in Fig. 4.23 at $T_c$ = 740 K, and further increasing $T_c$ = 790 K, led to higher pressures developing close to the chamber walls, ultimately culminating in detonation. This is most comprehensively displayed in Fig. 4.29, and as knock and super-knock in

Fig. 4.30. Super-knock is observed with an ($\varepsilon/\xi$) ratio of 6.8 and a $\Delta P/P$ of 0.42.

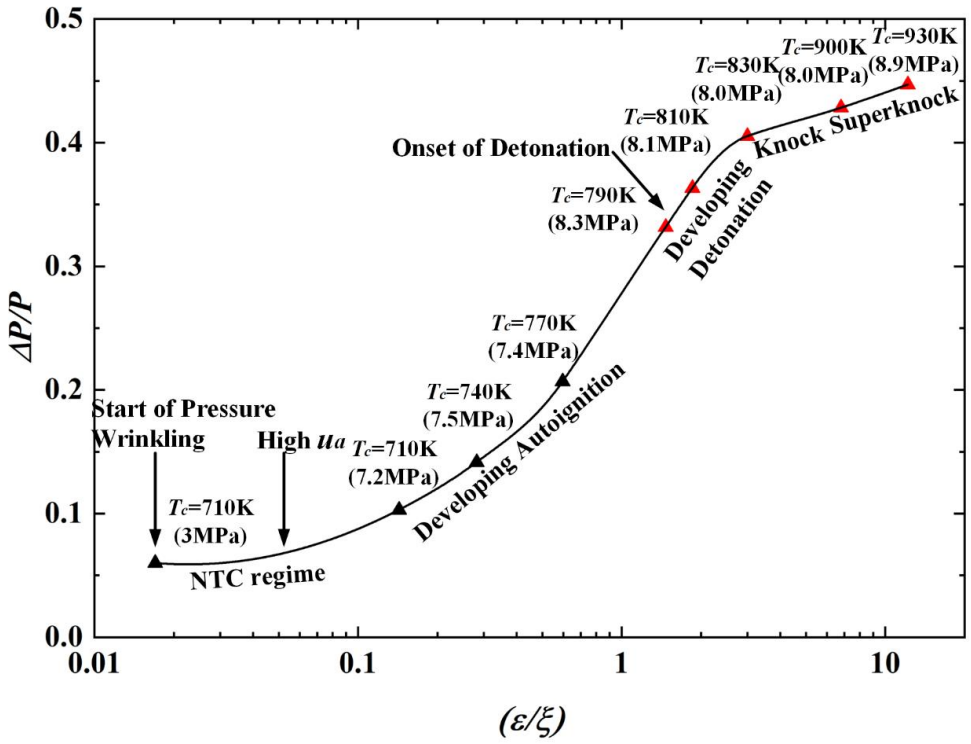


Figure 4.30. $\Delta P/P$ as a function of Detonation Parameter ($\varepsilon/\xi$).

## 4.5 Conclusions

Pressures, temperatures, reaction propagation speeds, and transitions to detonation have been measured and analyzed after rapid compression to 2.0 MPa of a stoichiometric mixture *i*-octane-oxygen mixture, with variable proportions of inerts. Starting with the lowest compression temperature, $T_c$ = 640 K a reaction propagation speed was that of a slightly wrinkled laminar flame. At the higher values of $T_c$, autoignitive propagation developed, with diminishing evidence in the later stages of minor laminar burning. Up to $T_c$ = 710 K, there was a reasonably good alignment between the measured propagation speed and the calculated autoignitive speed. At this temperature, entering the NTC regime, pressure oscillations with increasing amplitude began to manifest, although they were not yet detonative. Inside the NTC regime, at about $T_c$ = 740 K, the measured propagation speed attained a high peak value of 323 m/s. This might be explained by the vagaries of this speed being inversely proportional to $\frac{\partial \tau_i}{\partial T}$. With a possible low value of 0.0037 ms/K the computed speed became 315 m/s, resulting in a high autoignitive propagation velocity.

In this study, the detonation peninsula serves as a tool to quantify the transition to detonation within the RCM. The onset of this transition was marked when $T_c$ reached 790 K, resulting in a mild detonation characterized by values of $\xi$ = 2.4 and $\varepsilon$ =3.5 and ($\varepsilon/\xi$) = 1.46. Among the eleven explosions catalogued in Table 1, five exhibited a transition to detonation (from $T_c$ = 790 K until $T_c$ = 930 K). Typically, this transition into the Detonation Peninsula was associated with lower values of $\xi$, and higher value of $\varepsilon$ between 3.0 and 5.1. The monochrome images combined with the pressure traces highlight an increase in pressure oscillation amplitude, indicative of the transition to detonation. Within the RCM, this transition is instigated by the formation of a new autoignition spot, a result of the compression effect of the reaction wave on the unburned gas situated at the cylinder wall corner.

The use of a detonation parameter, ($\varepsilon/\xi$), is proposed, as an indicator of progress towards detonation. A maximum value of 12.2, for $T_c$ = 930 K, is associated with a super-knock value of 11 in [193]. The lowest value observed in the study was 0.016 for $T_c$ = 710 K.

This study shows the chemical transformations occurring in an RCM to be chemically complex and different from the ideal cycle. Nevertheless, overall measured ignition delay times are practically valuable in the avoidance of both knock in internal combustion engines and the occurrence of hazardous explosions [127].

# 5. Laminar and Turbulent Burning Characteristics of Ethane-Hydrogen-air Mixtures

## 5.1 Introduction

Over 70% of primary energy within UK is supplied by burning primary liquid and gaseous fuels, while more than 40% of power generation relies on the combustion of natural gas that is composed mostly of methane including varying amounts of other higher alkanes, e.g. ethane, propane. Ethane is an important petrochemical production from petroleum refining and after methane, it is the second most abundant component of

natural gas and its compositions varies from 0.5% to 13.3% by volume [8]. In industry scale, the ethane is mainly used as feedstock for ethylene production and used for power generation [8]. Hydrogen's addition to hydrocarbons, like ethane, can be beneficial in multiple ways. It can mitigate pollutant emissions, bolster performance, and broaden the operability range in combustion systems, such as gas turbines [196, 197] and combustion engines [198, 199].

However, despite the extensive studies, knowledge gaps remain, especially concerning the Markstein length/number, flame instability, and the influences of hydrogen addition on ethane-air combustion characteristics. For practical applications like gas turbines, combustion engines, and hazard analysis, understanding turbulent flame characteristics is paramount. However, to the best of current knowledge, there is no relative literature that reports the turbulent characteristic of ethane-air flames. In addition to applications in combustion power generation, the review study by Skjold et al. [148] points out that high-quality experimental data on fundamental combustion properties, such as laminar and turbulent burning velocity, Markstein number, flame instability, as well as the effects of temperature, pressure, and turbulence, are essential for accurately predicting explosions and DDT. Furthermore, given the safety concerns related to storage and potential fire hazards, there is a highlighted need for studying both laminar and turbulent combustion properties of ethane-air mixtures.

In this study, the Leeds MK-II fan-stirred combustion vessel, equipped with schlieren photography, was used to investigate the propagation of laminar premixed ethane-hydrogen-air and turbulent premixed ethane-air mixtures. The detailed description of MK-II combustion vessel and schlieren photography system can be found in Section 3.1. This Chapter presents the measured data on both laminar and turbulent flame characteristics. This research offers the first comprehensive investigation into the both laminar/turbulent burning velocity of premixed ethane-hydrogen-air mixtures. It offers invaluable insights for future research in this domain and will particularly serve as a foundational reference for simulating turbulent flame propagation and DDT of ethane-air, as detailed in Chapter 6.

## 5.2 Experimental Results of Laminar Burning Velocity of Ethane-Hydrogen-Air Mixtures

Section 5.2 reports the laminar burning velocities, burned gas Markstein length/number, and instability parameters such as the critical radius and Peclet number for ethane-hydrogen-air across various equivalence ratios, temperatures, pressures, and hydrogen addition. Furthermore, correlations describing the effects of initial temperature, pressure, and hydrogen additions on the laminar burning velocity of ethane-hydrogen-air were developed. A generalized correlation that delineates the stable propagation regime for the ethane-hydrogen-air flame, based on the dependences of Peclet number and Markstein number, is also purposed.

### 5.2.1 Experimental Conditions

The combustible ethane-hydrogen ($X_{H_2}$ = 0%, 25%, 50%, 75% and 100% hydrogen by volume) mixtures were prepared quantitively in the Leeds MK-II combustion vessel with concentrations based on the partial pressure method. The purities of ethane and hydrogen were 99.9% and 99.95% respectively. The percentage of hydrogen $X_{H_2}$ based on the volume of ethane-hydrogen-air mixtures was calculated as: $X_{H_2} = V_{H_2}/(V_{H_2} + V_{C_2H_6})$, where $V_{H_2}$ and $V_{C_2H_6}$ are the hydrogen and ethane volume fractions in the fuel blends, respectively. The total equivalence ratio $\phi$ is calculated as:

$$\phi = \frac{F/A}{(F/A)_{st}} \tag{5.1}$$

Where (*F/A*) is the total fuel to air ratio and $(F/A)_{st}$ is the stoichiometric value of fuel to air ratio. The chemical combustion formular for ethane-hydrogen-air mixtures can be expressed as:

$$\left(1 - X_{H_2}\right)C_2H_6 + X_{H_2}H_2 + \left(\frac{3.5}{\phi}\left(1 - X_{H_2}\right) + \frac{X_{H_2}}{2\phi}\right)(O_2 + 3.76N_2) \tag{5.2}$$

The measurements of the laminar propagation flame cover a wide range of equivalence ratio, hydrogen addition, temperature and pressure as detailed in Table 5.1.

Table 5.1. Laminar propagation flame experimental conditions for ethane-hydrogen-air mixtures.

| Mix Type ($X_{H_2}$) | Equivalence ratio | Temperature (K) | Pressure (MPa) |
|---|---|---|---|
| 0% | | 300, 360 | 0.1 and 0.5 |
| 25% | 0.7, 0.8, 0.9, 1.0, | 300 | 0.1 |
| 50% | 1.1, 1.2, 1.3 | 300, 360 | 0.1 and 0.5 |
| 75% | | 300 | 0.1 |
| 100% | | 300 | 0.1 |

For each experimental condition, three explosions were performed. Average values from sets of three experiments were used, to increase the certainty of our measurements. The standard deviation error bar was defined to be the square root of the variance (a sum of squared deviation divided by the number of data points, 3, for each test condition). The error bars were plotted around the mean values in all experimental results.

### 5.2.2 Effect of Stretch Rate on the Laminar Flame Speed

The laminar burning velocity of ethane-hydrogen-air are determined in this study. Fig 5.1 shows the effects both temperature and pressure on the propagation of ethane-air flame with $\phi$ = 1.1. At 0.1 MPa, the smooth spherical flame was observed with no cracking and cellular structure on flame surface even the radius reaching 60 mm. While, at 0.5 MPa and 300 K, the cracks is first observed at 15 mm, as the flame expanding the cellular structure or cellular instability occurred at 45 mm.

Compared with temperature, clearly the pressure dominates the flame cellular instability of ethane-air mixtures, this tendency consistent with others hydrocarbons for example, methane-air [49], ethanol-air [161], and even with the hydrogen-air flame [55]. This enhancement of cellular instability with increasing pressure was explained as the decreasing of flame thickness due to the rising pressure enhance hydrodynamic disturbances and increases the effects of unstable thermal diffusion on flame [55]. To better understand the effect of stretch rate on flame speed and instability, the variations of flame speed against the stretch rate for different initial pressures and temperatures were presented in Fig. 5.2.

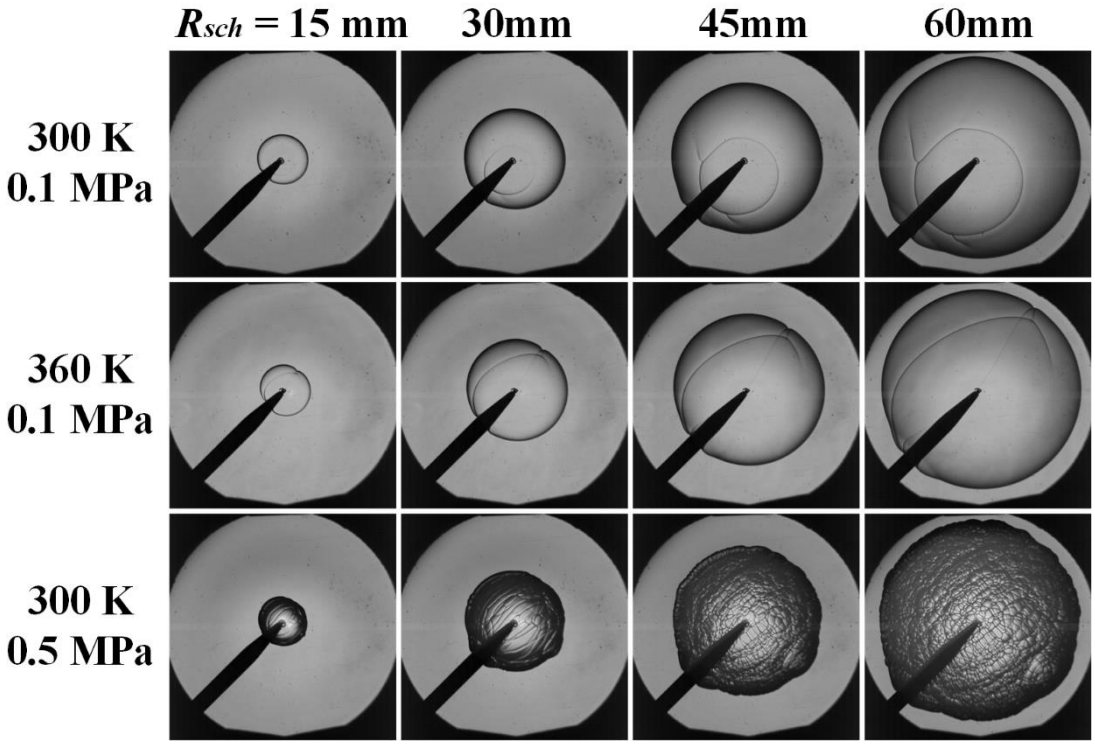


Figure 5.1. Schlieren images showing the effects of initial temperature and pressure on the developments of laminar ethane-air flame at $\phi$ = 1.1.

Initially, the flame speed was unstable due to the effects of spark energy and as the effect of spark energy negligible, the combustion was fully established. The spark affected region must be excluded when analyzing the stable flame propagation [200]. Thereafter, a fully developed laminar flame is obtained, as shown in Fig. 5.2 almost the linear regime of flame speed against stretch rate. At large radii and small stretch, flames become unstable and cellular which can cause the flame to accelerate due to the increase in surface area by the cellular structure. As show in Fig. 5.2, the # symbol shows the start of self-sustained propagation with free of spark energy and the critical radius $r_{cl}$ marks the onset of cellular instability for the condition 0.5 MPa, 300 K. The stable regime for the determination of Markstein lengths, $L_b$ lies between these points

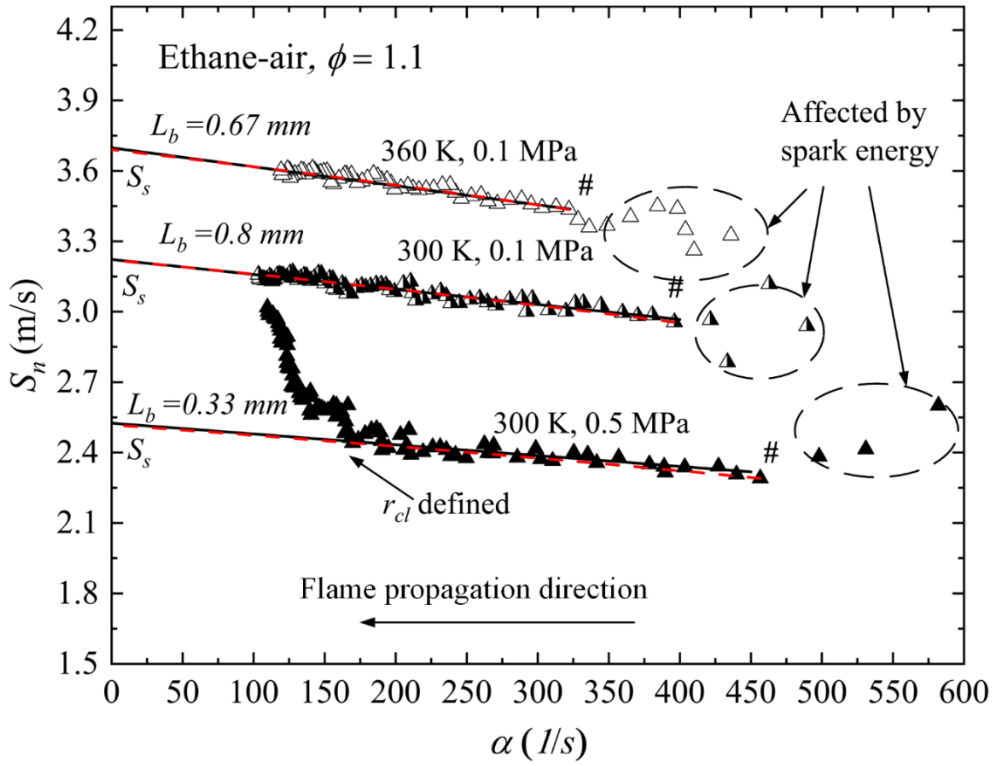


Figure 5.2. Variations of measured flame speeds, $S_n$, with stretch rate,$\alpha$, for the conditions of Fig. 5.1. (Solid black line representing the linear extrapolation, red dashed line representing the nonlinear extrapolation)

Both linear and nonlinear extrapolation method (discussed in Section 2.1.4) were implemented to derive the unstretched flame speeds. The comparison of both methods was shown in Fig. 5.2&5.4 with various mixtures and conditions as the black solid line representing the linear extrapolation, the red dashed line representing the nonlinear extrapolation. This comparison suggests both methods almost give the identical unstretched flame speed with negligible differences. Therefore, following the works of [44, 46, 49, 55, 201], in this study the classic linear extrapolation method was adopted to determine the unstretched laminar burning velocity. The unstretched flame speeds, $S_s$, have been derived by linear extrapolation at zero stretch rate and the gradient of solid line represents the -$L_b$. Shown in Fig. 5.2, an increase in initial temperature leads to the increase of $S_s$, and the increase of initial pressure suppresses the laminar burning velocity. The effects of hydrogen additions ($X_{H_2}$ = 25%, 50%, 75% and 100%) on the flame propagation of ethane-air mixtures with $\phi$ = 1.0, 0.1 MPa and 300 K are illustrated in Fig. 5.3. The smooth spherical flame was observed with no cracking and cellular even the

radius reaching 60 mm for mixtures with hydrogen addition ≤ 50%. As the hydrogen addition rising to $X_{H_2}$ = 75%, the large crack is first observed at 30 mm, and no cellular structure until the flame reaching 60 mm. While, the pure hydrogen flame shows the strongest instability, the large crack starts at 30 mm radius and cellular structure occurs at 60 mm radius with small cells on the flame surface.

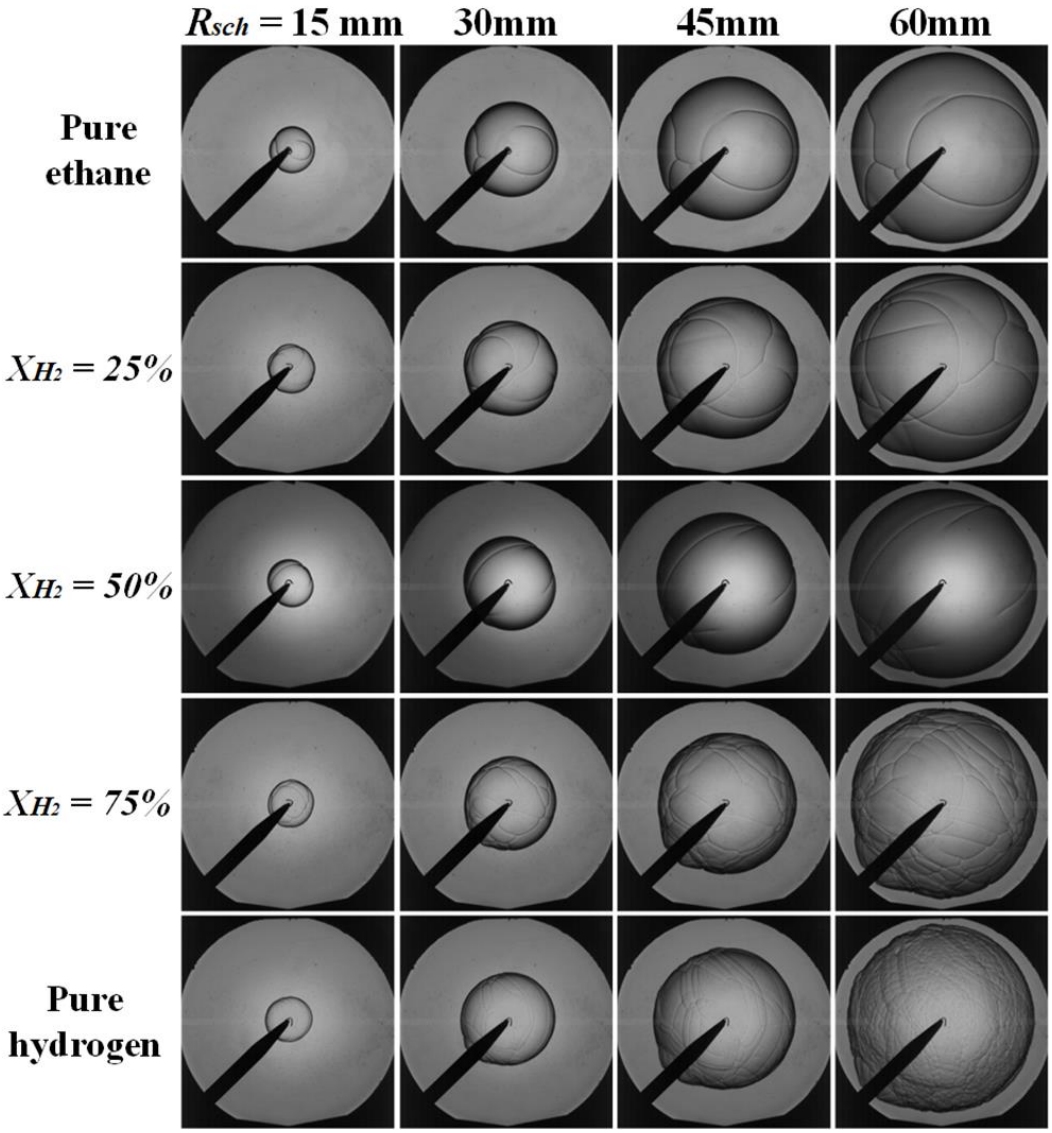


Figure 5.3. Schlieren images showing the effects of hydrogen additions on the developments of stoichiometric laminar ethane-hydrogen-air flame at 300 K and 0.1 MPa.

Figure 5.4 shows the effects of hydrogen additions on the flame speed against with stretch rate. The unstretched flame speed is increasing with the hydrogen addition, while Markstein lengths, $L_b$, decreases with the increasing hydrogen additions which indicates

the increases of flame instability.

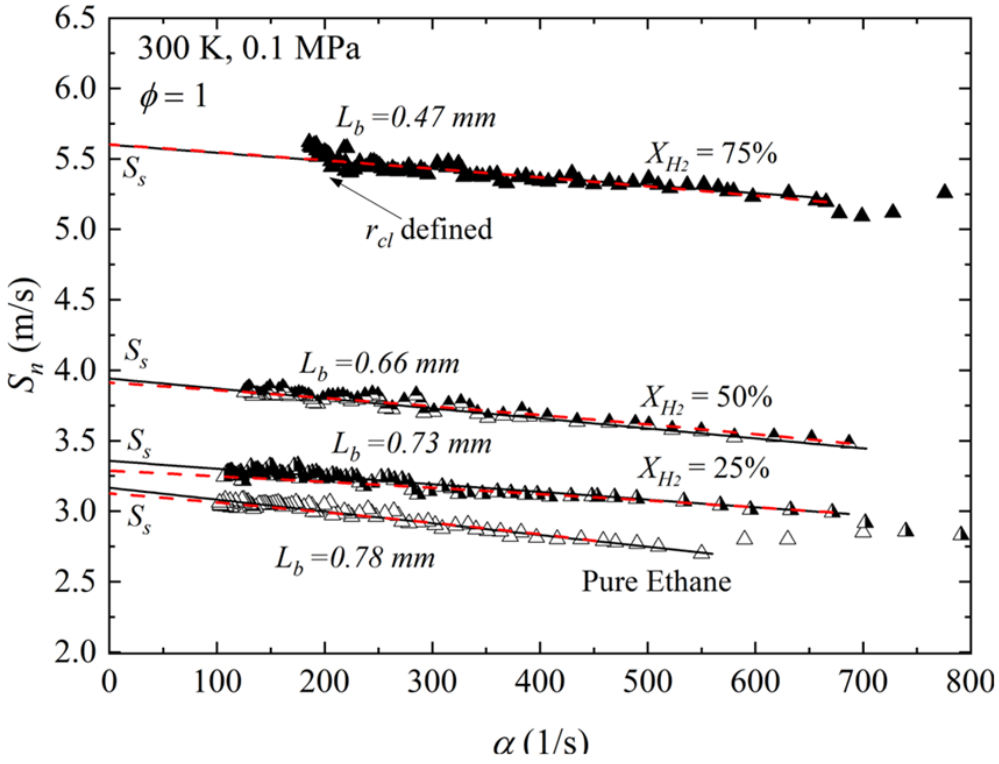


Figure 5.4. Variations of measured flame speeds, $S_n$, with stretch rate,$\alpha$, for the conditions of Fig. 5.3.

### 5.2.3 Unstretched Laminar Burning Velocity

The unstretched laminar burning velocities of pure ethane-air mixtures are presented in Fig. 5.5. Here the laminar burning velocity is calculated from Eq. 2.10, which is the unstretched laminar flame speed multiple the density ratio of burned to unburned gases. The equivalence ratio varies from lean side 0.7 to the rich side 1.3, initial temperature from 300 K to 360 K and pressure from 0.1 MPa to 0.5 MPa. The maximum laminar burning velocity located at equivalence ratio 1.1. The increases of initial temperature leading to the increase of laminar burning velocity while the pressure shows the opposite effect. The measured laminar burning velocities of ethane-air mixtures by Lowry et al. [58] and Goswami et al. [61] are plotted along with the present work. They showed a good agreement with each other.

The chemical kinetics of small hydrocarbon combustion, specifically $CH_4$ and $C_2H_6$, have been developed by several research groups. Notable among these are AramcoMech 1.3 [202], GRI 3.0 mechanism [203], San Diego mechanism [204], and the USC mech

Version II [205]. Comparative analyses of the measured laminar burning velocities of methane-hydrogen-air, ethane-air, and methane-ethane-air mixtures [60-62] with these kinetic mechanisms reveal that both USC Mech II and AramcoMech 1.3 aligns most closely with the measurements. This close alignment, coupled with substantial validation databases, underscores the reliability of both USC Mech II and AramcoMech 1.3 for studying the ethane-hydrogen-air mixture. Consequently, this study adopts both mechanisms for comparisons with measurements. Therefore, the predicted laminar burning velocities was calculated by using one dimensional steady freely propagating planar flame code, CHEMKIN PRO software [194] incorporating the ethane oxidation kinetics embedded in the detailed USC Mech II [205] and AramcoMECH 1.3 mechanisms [202].

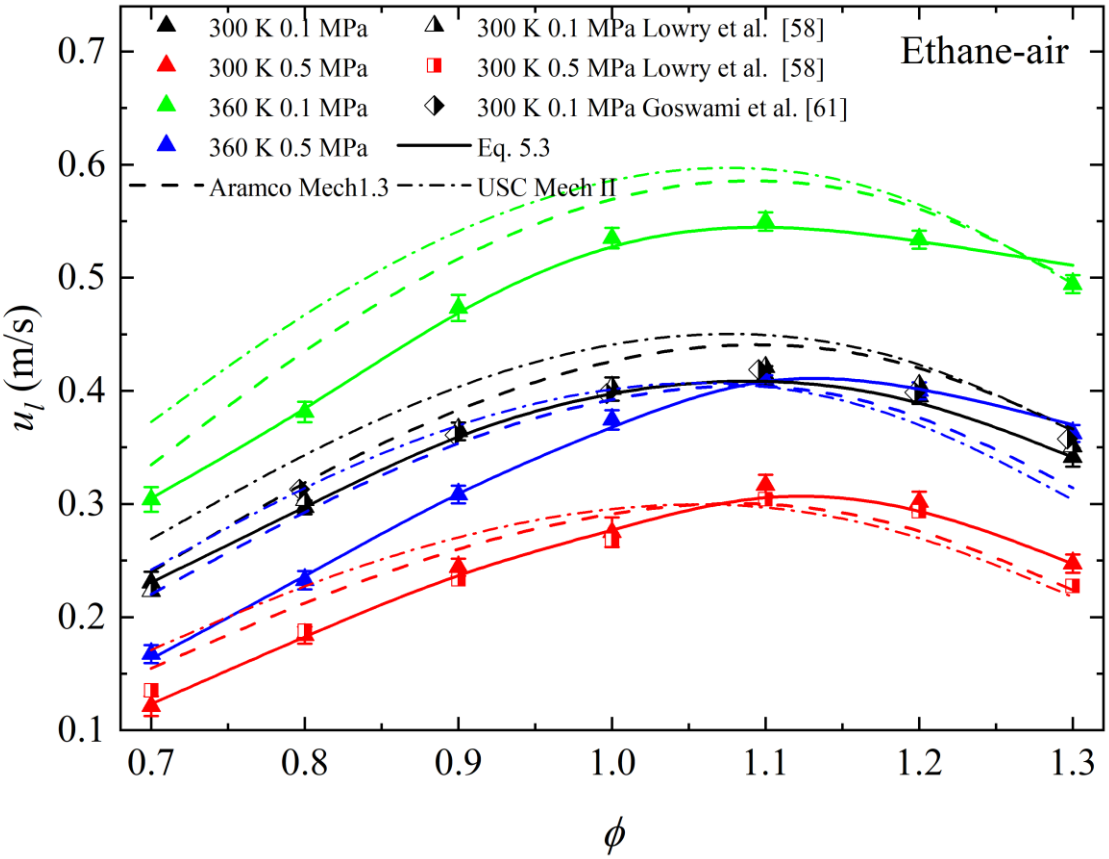


Figure 5.5. Laminar burning velocity of ethane-air at $\phi$ = 0.7-1.3, $T_i$ = 300, 360 K, $P_i$ = 0.1, 0.5 MPa.

The kinetics modelling shows a better performance at low temperature (300 K) conditions. At the high temperature (360 K), both kinetics are over predicted about 10% compared

with present measured data. It is possible because the USC Mech II [205] and AramcoMECH 1.3 mechanism [202] has only been validated for the pressure-dependent reaction rates at 300 K, without consideration the temperature impact. For precise predictions of the laminar flame propagation in ethane-air mixtures, it is advisable to enhance and validate both mechanisms against experimental data obtained at high temperatures. Moreover, the solid line in Fig. 5.5 represents the laminar burning velocity from the correlation (Eq. 5.3) which consider the effects of pressure and temperature and compared with the kinetics this correlation can perfectly fit with the measured data.

The laminar burning velocity of ethane-hydrogen-air ($X_{H_2}$ = 50%) flames at initial temperature of 300, 360 K and pressure of 0.1, 0.5 MPa are illustrated in Fig. 5.6. Since no experimental data for ethane-hydrogen-air has been reported in the literature, the present experimental data (symbols and solid lines) has been only compared to those of kinetics modelling (dashed and dashed dot lines) and correlations (solid). While both laminar burning velocities predicted from kinetics and correlations have good agreements with the measured data.

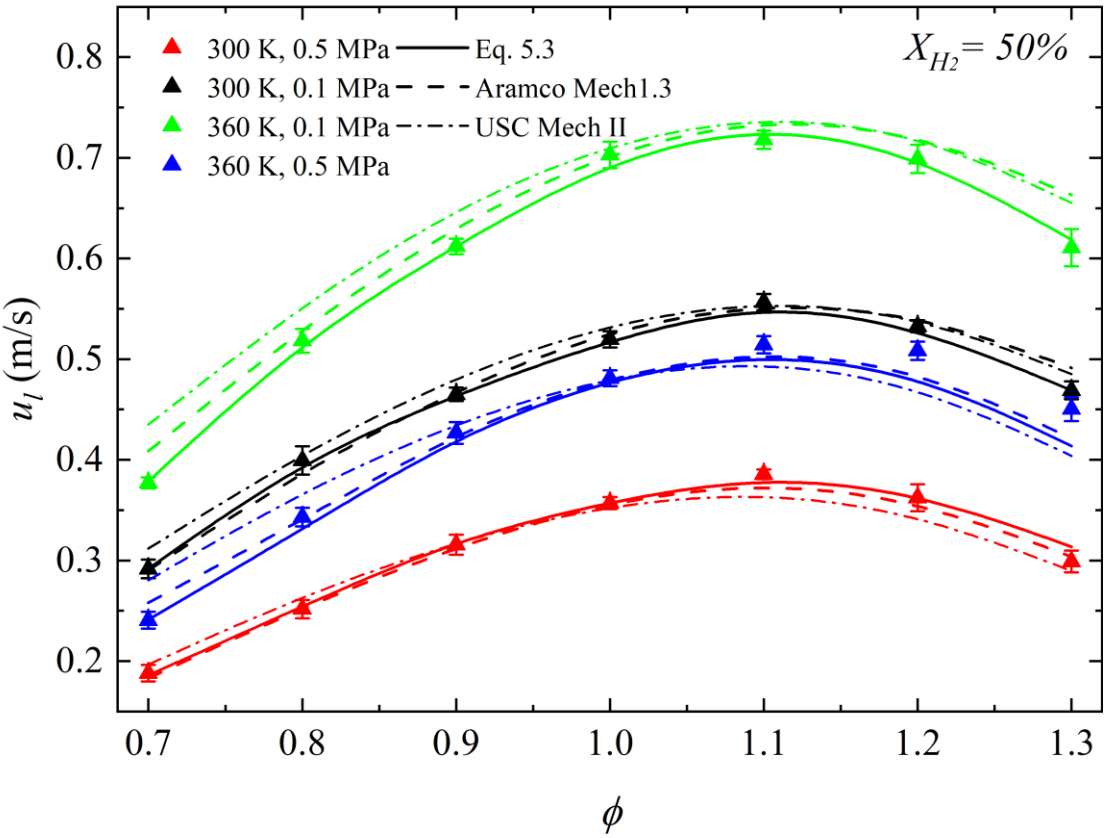


Figure 5.6. Laminar burning velocity of ethane-hydrogen-air ($X_{H_2}$ = 50%) at $\phi$ = 0.7-1.3, $T_i$ = 300, 360 K, $P_i$ = 0.1, 0.5 MPa.

The effects of hydrogen additions ($X_{H_2}$ = 25%, 50% and 75% by volume) on the laminar burning velocity of ethane at 300 K, 0.1 MPa are presented in Fig. 5.7. For a given equivalence ratio, the higher the hydrogen additions, the faster the mixture burns. For all hydrogen additions, the maximum laminar burning velocity appears at $\phi$ = 1.1. It is apparent the kinetic modelling shows a better performance as the hydrogen addition increases. This is because the ethane kinetics becomes predominant at the low hydrogen addition ($X_{H_2}$ ≤ 25%). Since the ethane kinetics has not been thoroughly validated, this error caused the noticeable discrepancy between modelling and measurement. Therefore, the blending law, which is based on the mass fraction from Eq. 5.4 and depicted as a solid line, is compared with current measurements, demonstrating a good fit with the measured data.

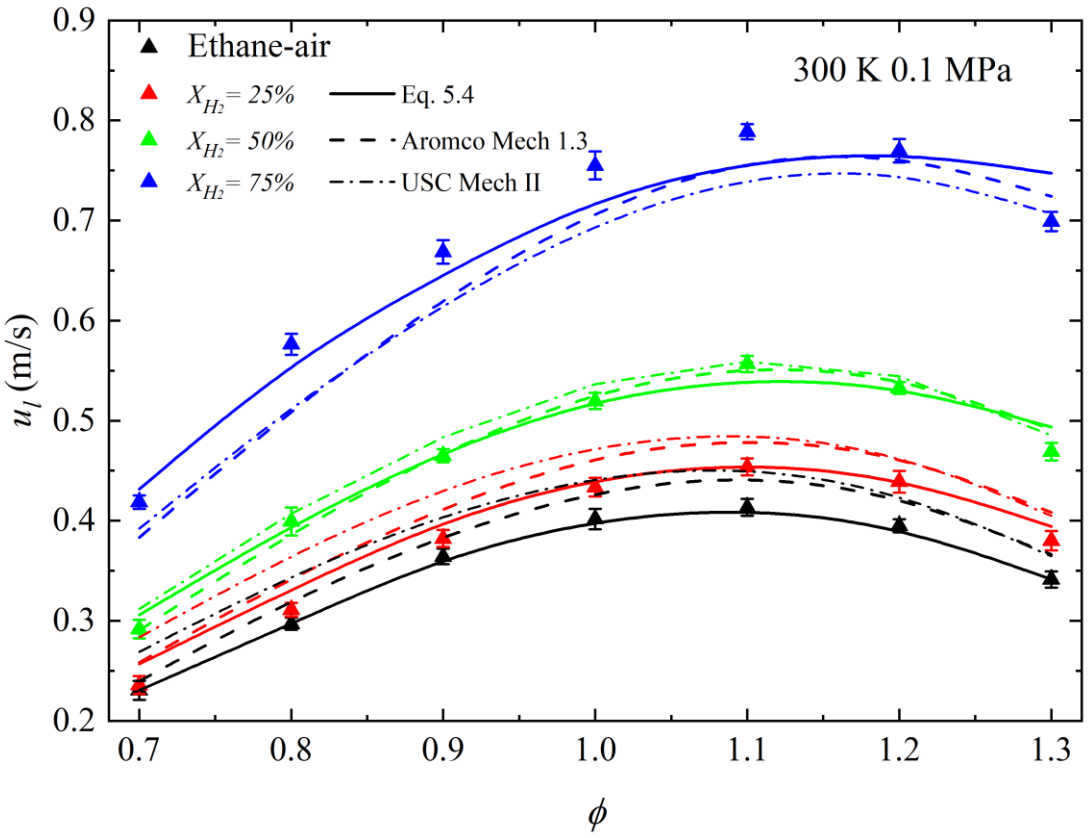


Figure 5.7. Laminar burning velocity of ethane-hydrogen-air flame with volume of hydrogen, $X_{H_2}$ = 0; 0.25; 0.5; 0.75, at $\phi$ = 0.7-1.3, $T_i$ = 300 K, $P_i$ = 0.1 MPa.

Moreover, the laminar burning velocity of hydrogen-air was measured and shown in Fig. 5.8 below. Contrary to typical hydrocarbons, which exhibit their maximum laminar burning velocity at $\phi$ = 1.1, hydrogen reaches its peak laminar burning velocity at a higher $\phi$ = 1.5 as reported in [55]. This phenomenon is attributed to the maximum chemical kinetics effects occurring at $\phi$ = 1.5 for hydrogen-air mixtures, due to the maximum concentration of H and OH radicals at this specific equivalence ratio. The measured data with solid triangle symbols in present study were compared with the measured data from Xie et al. [55] and Dayma et al. [206] and the current measurement is perfectly fitting the data from Xie et al. [55] but about 10% higher than the measurements of Dayma et al. [206].

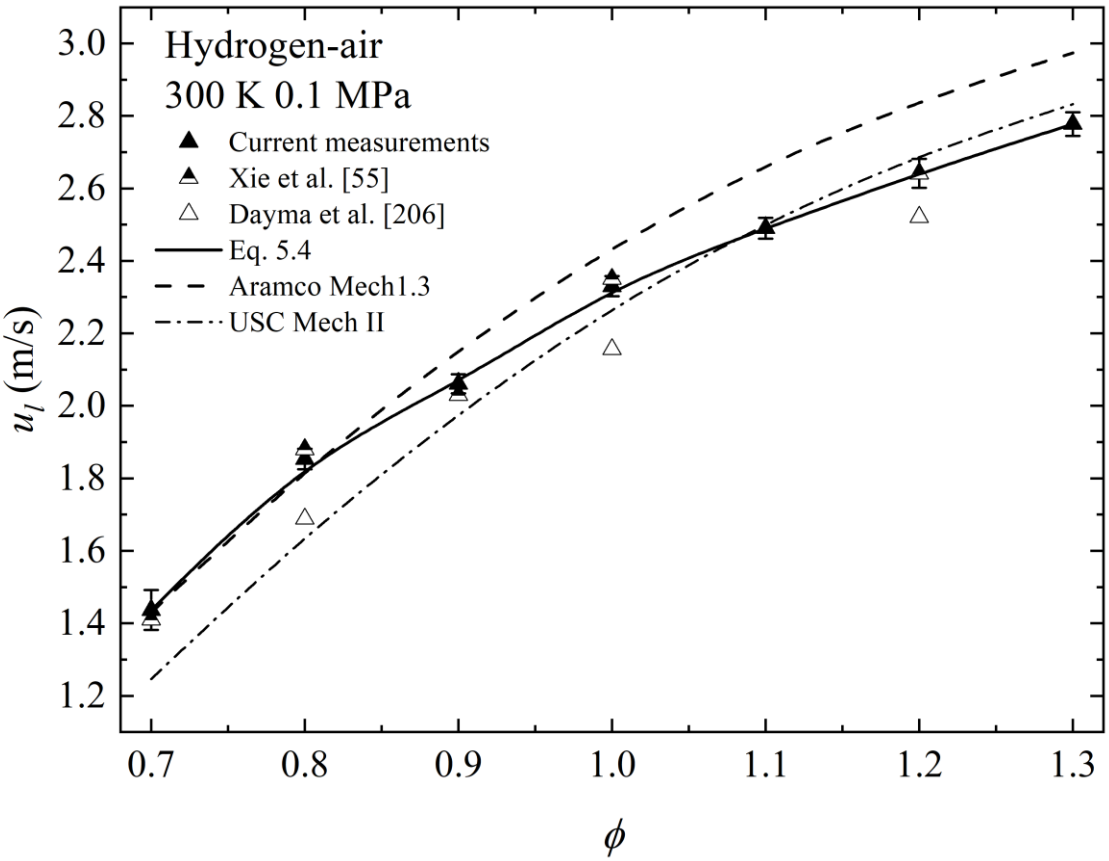


Figure 5.8. Laminar burning velocity of hydrogen-air flame at $\phi$ = 0.7-1.3, $T_i$ = 300 K, $P_i$ = 0.1 MPa.

### 5.2.4 Correlation of Laminar Burning Velocity

An empirical correlation of laminar burning velocity for ethane-hydrogen-air mixtures considering the effects of temperature and pressure becomes a matter of urgency. Such a correlation is crucial in detonation modeling, as it accurately reflects how shock waves compress unburned gases, elevating their temperature and pressure, and thereby augmenting the burning velocity. Metghalchi and Keck [207] proposed a laminar burning velocity correlation which consider the effects of temperature and pressure on laminar burning velocity under datum conditions shown in Eq. 5.3, and this correlation is used to show the effects of temperature and pressure on laminar burning velocity of methane-air [49] and *i*-octane-*n*-heptane- air mixtures [44].

$$u_l = u_{l,0} \frac{T_u}{T_0}^{\alpha_T} \frac{P_u}{P_0}^{\beta_P} \tag{5.3}$$

where, $u_{l,0}$ is the unstretched laminar burning velocity at a datum temperature $T_0$ = 300 K and $P_0$ = 0.1 MPa in the current measurements. The constants $\alpha_T$ and $\beta_P$, which

depends on the equivalence ratio representing the effects temperature and pressure on the laminar burning velocity of ethane-air.

Table 5.2 . The value of $u_{l,0}$, $\alpha_T$ and $\beta_P$ for pure ethane-air mixtures with $\phi$ from 0.7 to 1.3.

| $\phi$ | $u_{l,0}$ | $\alpha_T$ | $\beta_P$ |
|---|---|---|---|
| 0.7 | 0.231 | 1.53 | -0.39 |
| 0.8 | 0.297 | 1.38 | -0.30 |
| 0.9 | 0.364 | 1.44 | -0.26 |
| 1 | 0.402 | 1.55 | -0.23 |
| 1.1 | 0.413 | 1.57 | -0.17 |
| 1.2 | 0.395 | 1.64 | -0.17 |
| 1.3 | 0.341 | 2 | -0.2 |

Table 5.2 shows the values of $u_{l,0}$, $\alpha_T$ and $\beta_P$ for pure ethane-air, the value of $\alpha_T$ and $\beta_P$ are derived from experimental measurements of ethane-air cover the range of temperature from 300-360 K and pressure from 0.1-0.5 MPa. The solid lines in Fig. 5.5 representing the laminar burning velocity from this correlation and it is shown that the value from correlation is good fitting with the measured burning velocity. The correlation for the ethane-hydrogen-air ($X_{H_2}$ = 50%) mixtures is also purposed in this study. The values of $u_{l,0}$, $\alpha_T$ and $\beta_P$ for this mixture cover the range of temperature from 300-360 K, pressure from 0.1-0.5 MPa and equivalence ratio from 0.7 to 1.3 are shown in Table 5.3 below.

Table 5.3. The value of $u_{l,0}$, $\alpha_T$ and $\beta_P$ for ethane-hydrogen-air ($X_{H2}$ = 50%) mixtures with $\phi$ from 0.7 to 1.3.

| $\phi$ | $u_{l,0}$ | $\alpha_T$ | $\beta_P$ |
|---|---|---|---|
| 0.7 | 0.292 | 1.43 | -0.28 |
| 0.8 | 0.399 | 1.44 | -0.28 |
| 0.9 | 0.465 | 1.52 | -0.23 |
| 1 | 0.52 | 1.62 | -0.23 |

| | | | |
|---|---|---|---|
| 1.1 | 0.557 | 1.52 | -0.23 |
| 1.2 | 0.533 | 1.53 | -0.23 |
| 1.3 | 0.469 | 1.52 | -0.25 |

In Fig. 5.6, the solid line representing the burning velocity from correlation compared with the measured burning velocity, the good fitting indicating that this correlation can predict the laminar burning velocity accurately. For the effect of additional hydrogen on the burning velocity of ethane, the blending law based on the mass fraction of mixture reported in [208] is used in this study and expressed as:

$$u_l = x_i u_{li} + x_j u_{lj} \tag{5.4}$$

where $x_i$ is the mass fraction of the *i*-th ingredient mixture within the overall mass and $u_{li}$ is the laminar burning velocity of *i*-th ingredient mixture. For the ethane-hydrogen-air mixture, in terms of volume fraction, Eq. 5.4 can be reformulated as:

$$u_l = \frac{2X_{H_2}}{2X_{H_2}+30(1-X_{H_2})} u_{lH_2} + \frac{30(1-X_{H_2})}{2X_{H_2}+30(1-X_{H_2})} u_{lC_2H_6} \tag{5.5}$$

Where $u_{lH_2}$ and $u_{lC_2H_6}$ are the laminar burning velocity of hydrogen and ethane respectively. The solid line in Fig. 5.7 represents the predicted laminar burning velocity as per the blending law of mass fraction, demonstrating a good match with the measured data.

### 5.2.5 Thermal and Chemical Kinetics Effects

The introduction of hydrogen into ethane-air mixtures leads to an increase in laminar burning velocity, a phenomenon primarily due to hydrogen's enhancement of thermal and chemical kinetics effects [209]. The thermal effects are signified by the adiabatic flame temperature $T_{ad}$ while key radicals serve as indicators of the chemical kinetics effects [209]. Radicals like H and OH play a major role in promoting the laminar burning velocity, whereas the $C_2H_4$ radical is indicative of ethane decomposition. To illustrate this, $T_{ad}$, $u_l$, and the maximum mole fractions of H, OH, and $C_2H_4$ radicals are plotted against the $X_{H_2}$ at 300 K, 0.1 MPa, and an equivalence ratio of 1 in Fig. 5.9. This graph aims to showcase the influence of hydrogen addition on both thermal and chemical kinetics effects. The data for $T_{ad}$ and the radicals' maximum mole fractions are computed using

a one-dimensional, freely propagating laminar flame model from CHEMKIN-PRO software [194], in combination with Aramco Mech 1.3 [202]. The $u_l$ values, on the other hand, are derived from current measurements.

Generally, the $T_{ad}$, $u_l$ and maximum mole fraction of H, OH radicals exhibit an increasing trend with the increasing $X_{H_2}$. Conversely, the $C_2H_4$ radicals demonstrate a decreasing pattern. Specifically, $T_{ad}$ increases with $X_{H_2}$, ranging from 2260 K in ethane-air to 2390 K in hydrogen-air reflecting enhanced thermal effects with higher $X_{H_2}$, along with an increase $u_l$. The maximum mole fractions of H and OH radicals notably increase with $X_{H_2}$, especially the H radicals which show exponential growth when $X_{H_2}$> 90%, highlighting intensified chemical kinetics effects. In contrast, the maximum mole fractions of $C_2H_4$ radicals moderately increase with $X_{H_2}$ up to 50%, then decline due to the reduced ethane content in the fuel. Therefore, a higher $X_{H_2}$ enhances both thermal and chemical effects, leading to an increase in the laminar burning velocity for ethane-hydrogen-air mixtures.

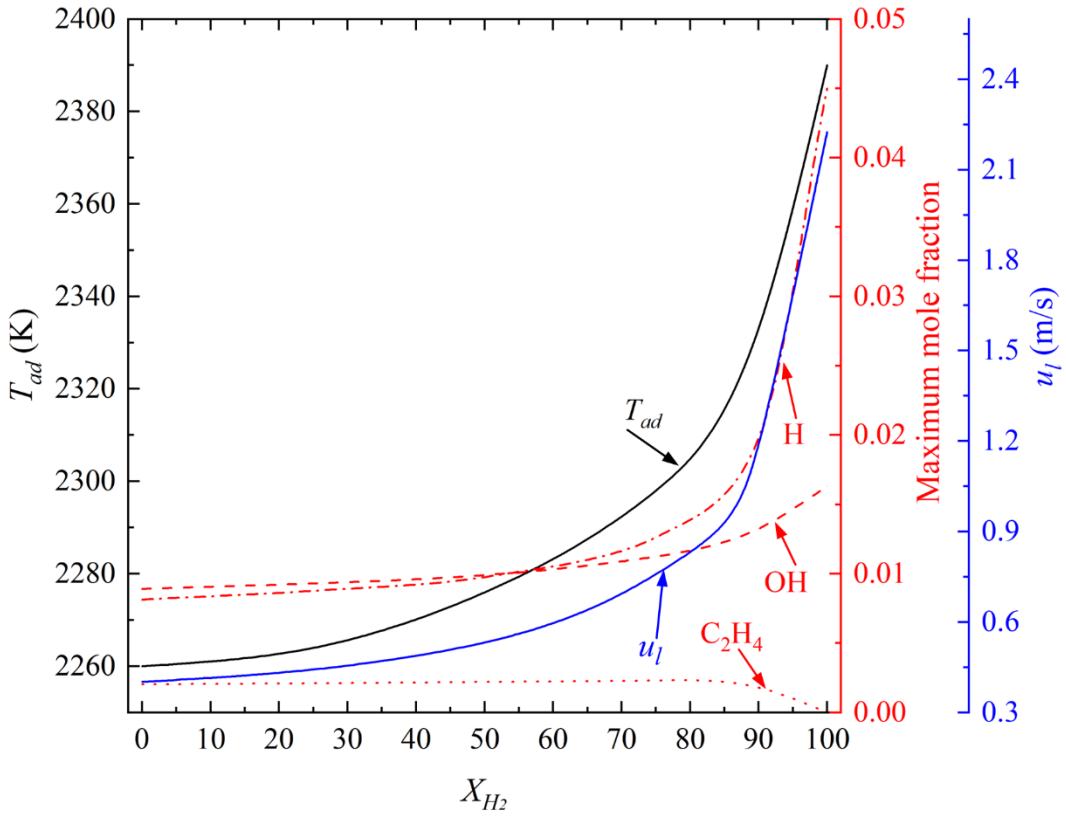


Figure 5.9. The modelling adiabatic flame temperature and maximum mole fraction of

H, OH, $C_2H_4$ radicals as a function of $X_{H_2}$ at 300 K, 0.1 MPa and $\phi$ = 1.

### 5.2.6 Flame Thickness, Thermal Expansion Coefficient and Effective Lewis Number

In the earlier discussion about flame instability in Section 2.1.5, it was established that the flame thickness, $\delta_l$ and the thermal expansion coefficient, $\sigma$ are crucial in driving hydrodynamic instability, while the Lewis number, $Le$ plays a key role in both hydrodynamic and thermal-diffusive instability. Referring to sources [210, 211], for binary fuels like ethane-hydrogen-air, the concept of an effective Lewis number is employed to characterize thermal-diffusive instability. This calculation is performed using the volume-weighted method and expressed as follows:

$$Le_{eff} = X_{H_2} Le_{H_2} + X_{C_2H_6} Le_{C_2H_6} \quad (5.6)$$

Where, $Le_{H_2}$ and $Le_{C_2H_6}$ represent the Lewis number of hydrogen and ethane, respectively. The mass and thermal diffusivity coefficients utilized in Eq. 2.14 to determine Lewis number are determined through modeling with the CHEMKIN-PRO software [194], in conjunction with the AramcoMech 1.3 mechanism [202]. These factors, specifically in the context of ethane-hydrogen-air mixtures, are depicted in Fig. 5.10. Referring to parts (a) and (b) of Fig. 5.10, which focus on flame thickness derived from Eq. 2.2, there is a noticeable trend where the flame thickness typically diminishes with an equivalence ratio ranging from 0.7 to 1.1, but then increases from 1.1 to 1.3 for all conditions and mixtures. A rise in temperature tends to marginally increase the flame thickness, whereas a higher pressure notably diminishes it, often by several times. Additionally, the inclusion of more hydrogen in the mixture leads to a reduction in flame thickness. Consequently, both an increase in pressure and the addition of hydrogen enhances the effects of hydrodynamic instability.

Figure 5.10 (c) clearly shows that the thermal expansion coefficient (unburned to burned density ratio) which derived from the GASEQ code [48] is highly responsive to changes in temperature. As the temperature rises, there is a corresponding decrease in the thermal expansion coefficient. At the same time, an increase in pressure leads to a slight elevation in this coefficient. Additionally, Figure 5.10 (d) reveals that augmenting the hydrogen

content in the mixture tends to reduce the coefficient as well. According to Figure 5.10 (e), factors like pressure, temperature, and equivalence ratio have negligible impact on the $Le_{eff}$, whereas an increase in hydrogen content results in its reduction. The $Le_{eff}$ values larger than unity are evident at pure ethane and $X_{H_2}$= 25%, transitioning to less than unity as $X_{H_2}$ increases to 50%, 75% and 100%. This suggests a strengthening in the effects of thermal-diffusivity instability with the increasing $X_{H_2}$. Notably, in scenarios where $X_{H_2}$= 50%, $Le_{eff}$ is nearly unity, indicating a near absence of thermal-diffusivity instability effects.

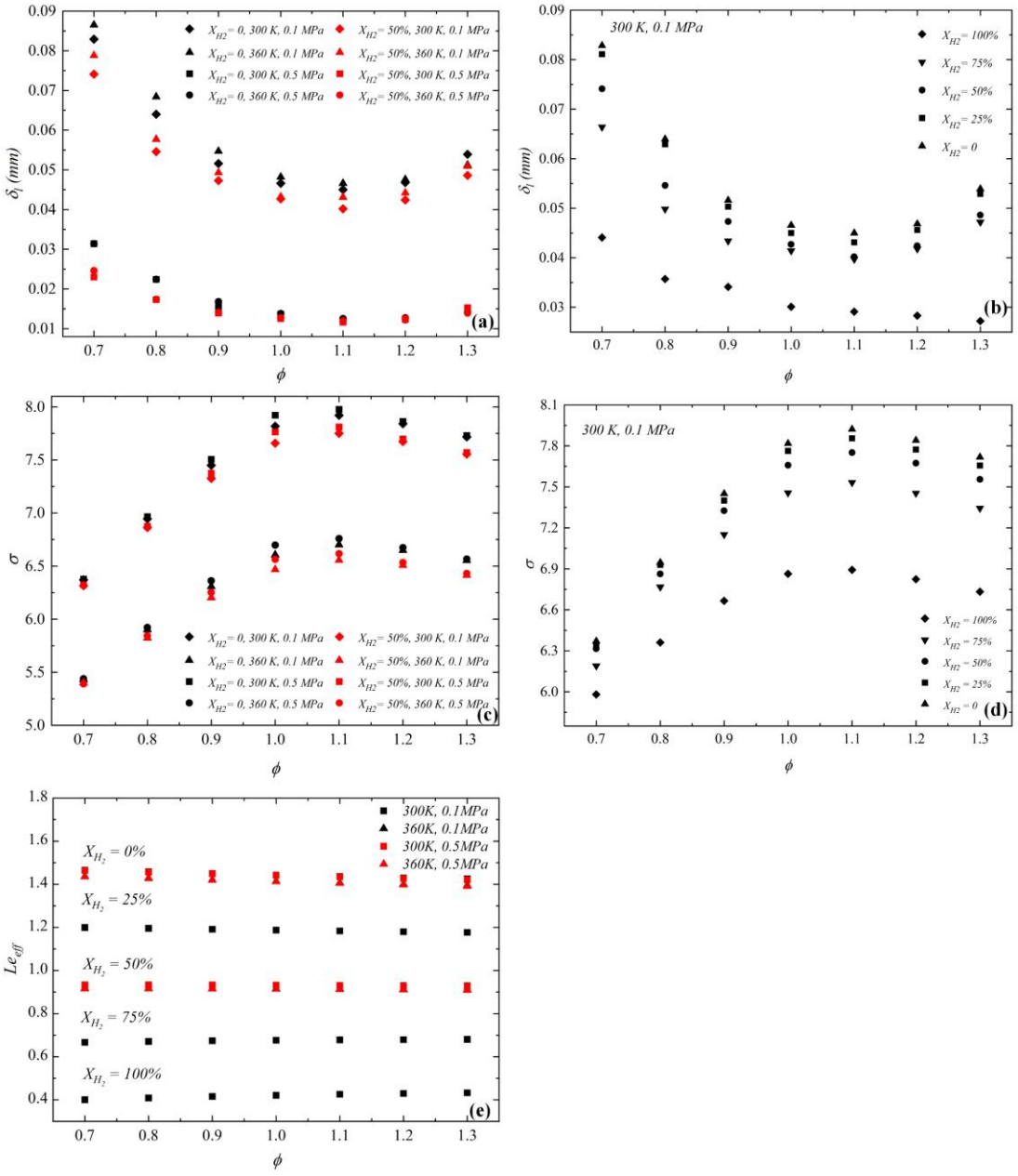


Figure 5.10. The variation of the flame thickness, $\delta_l$, thermal expansion coefficient, $\sigma$,

and the effective Lewis number, $Le_{eff}$ of ethane-hydrogen-air mixture at 300 K and 360 K under pressures of 0.1 and 0.5 MPa, as functions of the equivalence ratio.

### 5.2.7 Markstein Length and Markstein Number

The detailed method to derive the burned gas Markstein length/number can be found in Section 2.1.4. The burned gas Markstein length, $L_b$, of ethane-hydrogen-air mixtures were measured and presented in Fig. 5.11 at the initial temperature 300-360 K, pressure 0.1-0.5 MPa, with hydrogen addition $X_{H_2}$ = 0%, 25%, 50%, 75% and 100%. The burned gas Markstein length, $L_b$ represents the effect of stretch rate on the flame speeds, the positive value of $L_b$ indicating the decreasing of stretch rate accelerate the flame speed and negative value of $L_b$ has reverse effect. As shown in Fig. 5.11 from (a) to (d), for both $X_{H_2}$ = 0% and 50%, the $L_b$ decreases as pressure increase indicating the influence of stretch rate on the flame speed declining at high pressure. This general declining effect is consisting with the experimental work of Zuo et al. [63] for ethane-air and other hydrocarbons including methane-air [49, 63], propane-air [63] and *i*-octane-*n*-heptane [44] mixtures. While, increasing temperature from 300 K to 360 K, the $L_b$ only reduces slightly, meanwhile, $L_b$ keeps decreasing as mixture becomes richer for pure ethane indicating the decaying effects of stretch rate on burning velocity. Shown in Figs. 5.11 (e), compared with pure ethane-air mixture, hydrogen tends to reverse the trend of $L_b$ with equivalence ratio and negative $L_b$ observed at $\phi$ = 0.7 showing that the stretch rate has negative effects on the flame speed. Moreover, the additions of hydrogen lead to the decreases of $L_b$ with the same equivalence ratio indicating the decaying effects of stretch rate on flame speed of the ethane-hydrogen-air mixtures.

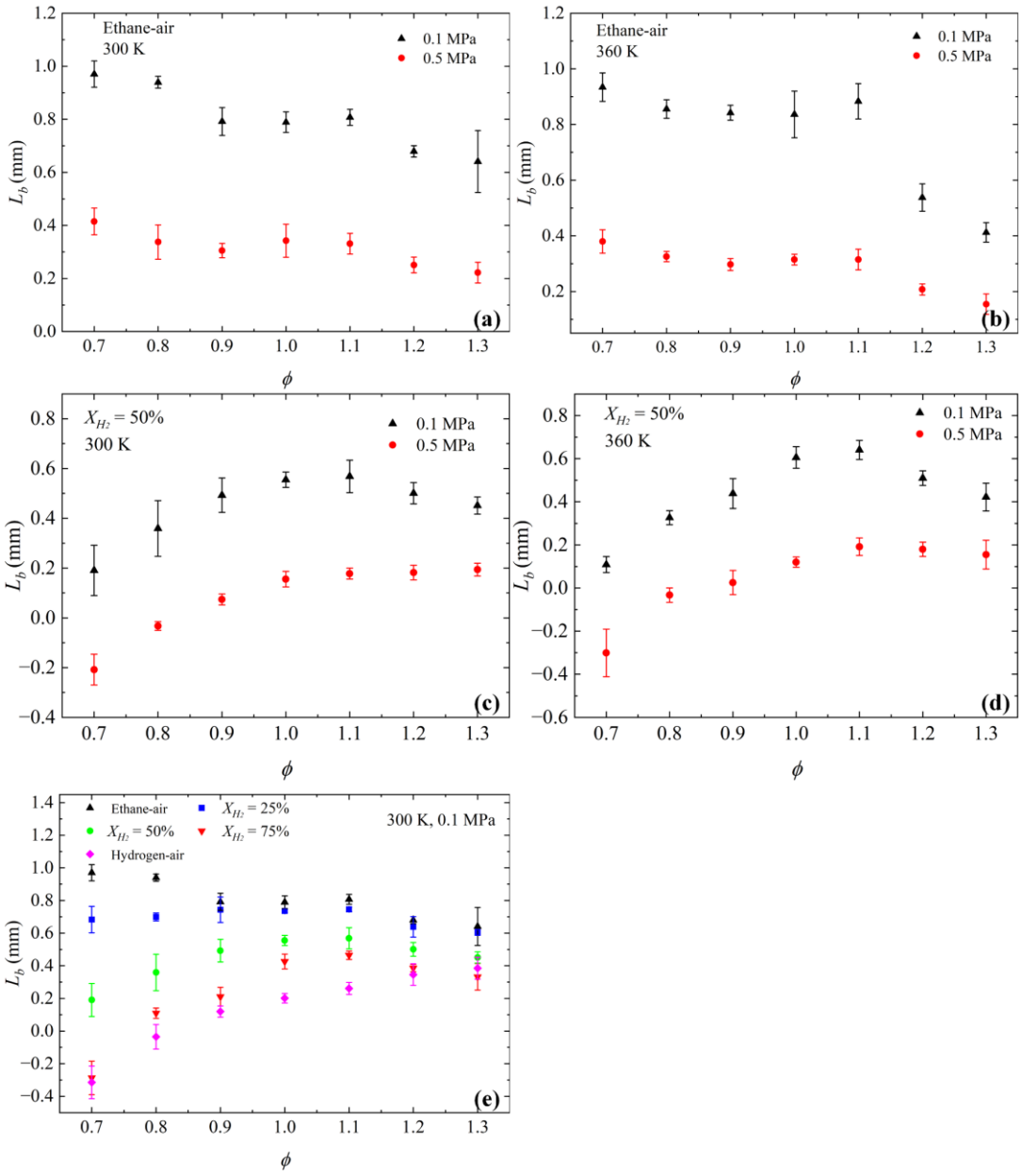


Figure 5.11. The variations of measured burned gas Markstein length, $L_b$, of ethane-hydrogen-air mixtures with $\phi$ at conditions initial temperature, $T_i$ = 300, 360 K, and initial pressure $P_i$ = 0.1, 0.5 MPa.

Figure 5.12 shows the measured burned gas Markstein number, $Ma_b$, at the same conditions as Fig 5.12. The $Ma_b$ is the dimensionless parameter which is the $L_b$ divided the flame thickness, $\delta_l$. Overall, $Ma_b$ increases first from lean to stoichiometric conditions and then decreases at rich side for $X_{H_2}$ = 0% - 75%. While for the pure hydrogen cases ($X_{H_2}$ =100%), the $Ma_b$ keeps increasing with the equivalence ratio from lean mixture with negative value to the rich mixture with positive value. Moreover,

compared with hydrogen-air, the ethane-air has bigger $Ma_b$ indicating the flame speed is more sensitive to the stretch rate.

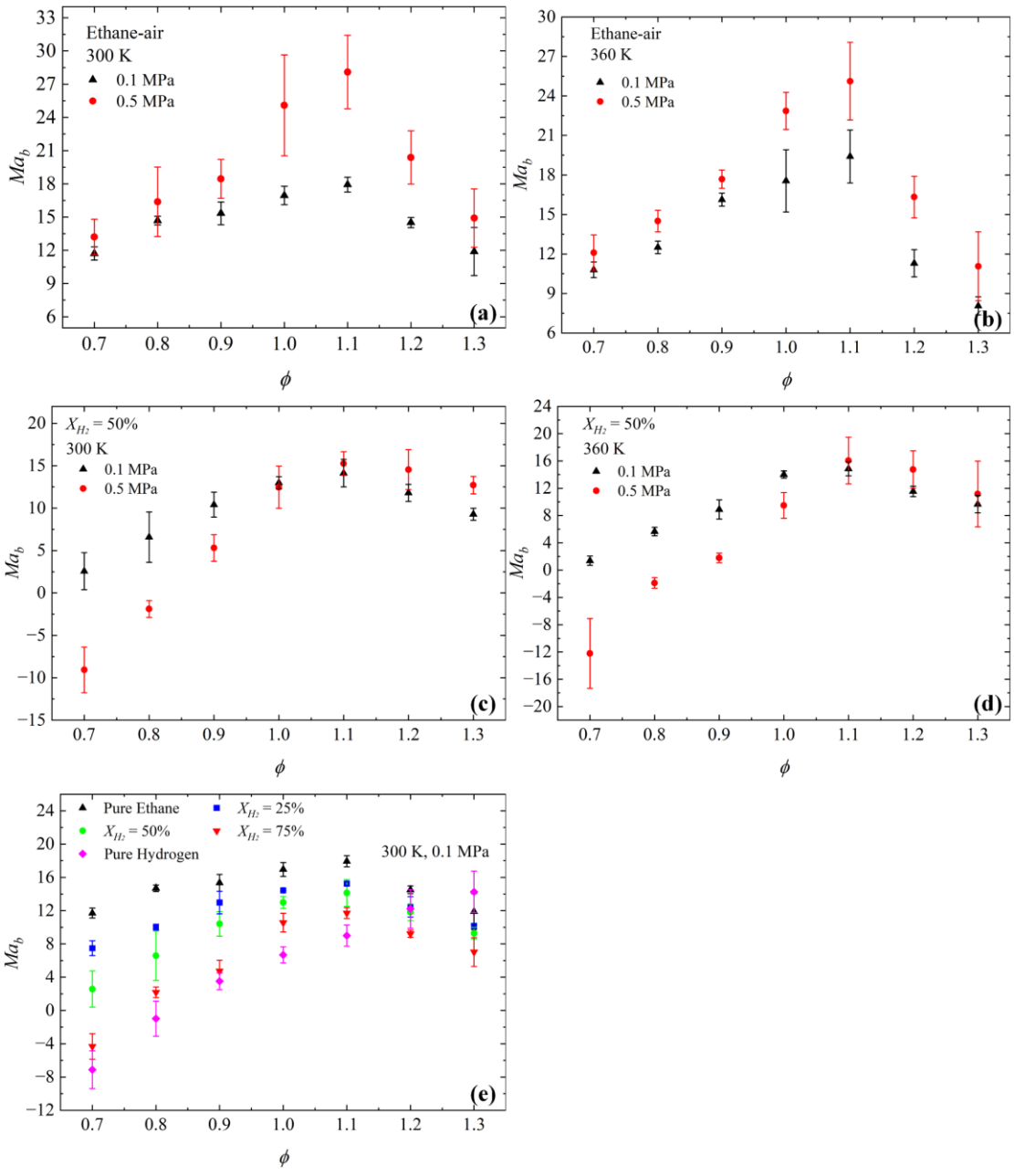


Figure 5.12. The variations of measured burned gas Markstein number, $Ma_b$, of ethane-hydrogen-Air mixtures with $\phi$ at conditions initial temperature, $T_i$ = 300, 360 K, and initial pressure $P_i$ = 0.1, 0.5 MPa.

### 5.2.8 Instability Parameters, $r_{cl}$ and $Pe_{cl}$

The critical radius, $r_{cl}$, is an important parameter to study the cellular instability of expanding premixed laminar flame. As shown in Fig. 5.2, this critical radius is defined as the onset of cellular instability where the flame speed is increasing significantly with the

stretch rate. The cellular structure of the flame surface is a result of the combined effects of hydrodynamic and thermal-diffusivity instabilities. Such instability is primarily caused by an expansion of the stretched flame front area, which boosts the rate of combustion volume, while the chemical kinetics effects remain consistent. In the scope of the current measurements ($r_{sch}$< 60 mm), and at a pressure of 0.1 MPa, no cellular instability was observed in ethane-air mixtures. This is attributed to $Le_{eff}$>1, where thermal diffusivity stabilizes the flame, and the impact of hydrodynamic instability is diminished due to the relatively thick flame thickness. As shown in Fig. 5.10 (b) and (e), an increase in $X_{H_2}$ leads to a decrease in flame thickness and $Le_{eff}$, consequently enhancing the influence of both hydrodynamic and thermal-diffusivity instability.

Figs. 5.13 (a)&(b) show the critical radius at temperature of 300 and 360 K, pressure 0.5 MPa with pure ethane, $X_{H_2}$ = 50% and pure hydrogen from [55]. The critical radius remains relatively unaffected by temperature variations when it increases from 300 K to 360 K, across all three mixture types. In the case of ethane-air mixtures at 0.5 MPa, cellular instability is primarily influenced by hydrodynamic instability. The critical radius begins at 46 mm for a mixture with an $\phi$=0.9 and gradually declines as $\phi$ increases, suggesting that richer mixtures are more susceptible to early cellular instability. Conversely, for hydrogen-air mixtures at 0.5 MPa, both hydrodynamic and thermal-diffusivity instability ($Le_{eff} \ll 1$) govern cellular instability. Here, the critical radius of hydrogen-air mixtures increases with $\phi$, indicating that lean hydrogen-air flames are more likely to experience combustion instabilities. For $X_{H_2}$= 50%, the impact of thermal-diffusivity instability is negligible due to the $Le_{eff}$ close to unity, leading to a predominant influence of hydrodynamic instability. From lean to stoichiometric conditions, $r_{cl}$ decreases with $\phi$, highlighting a strengthening of hydrodynamic instability, likely caused by reduced flame thickness and increased thermal expansion coefficient, as evidenced in Fig. 5.10 (a) and (c). However, transitioning from stoichiometric to rich conditions, $r_{cl}$ increases with $\phi$, indicating a reduction in hydrodynamic instability due to an increase in flame thickness and a decrease in the thermal expansion coefficient.

The critical Peclet number, $Pe_{cl}$, is calculated by normalizing the critical radius $r_{cl}$ with $\delta_l$, thereby characterizing the onset of flame cellularity. This dimensionless parameter is plotted against the $\phi$ in Fig. 5.13 (c) & (d), exhibiting a trend that closely mirrors that of $r_{cl}$. Many researchers have suggested that cellular instability is influenced by the stretch rate and have linked the $Pe_{cl}$ with the $Ma_b$ to delineate the stable and unstable regimes of expanding flames [55, 68, 163, 201, 213]. Xie et al. [55], Kim et al. [68], and Morsy and Yang [201] correlated $Pe_{cl}$ with $Ma_b$ to define the stable regime for hydrogen-air mixtures across a wide range of equivalence ratios, pressures, and temperatures. For hydrocarbon fuels, Law et al. [212] measured $Pe_{cl}$ and correlated with equivalence ratio to define the stable regime of for propane-hydrogen-air mixtures over a wide range of pressure. Oppong et al. [213] developed a correlation for ethyl acetate-air over a wide temperature range from 358 K to 418 K. Marwaan et al. [163] measured both $Pe_{cl}$ and $Ma_b$ for methane-hydrogen-air mixtures at pressures up to 1 MPa. Despite these efforts, there remains a gap in knowledge regarding the boundary of the stable regime for ethane-hydrogen-air mixtures. Thus, it is beneficial to integrate data from existing studies with recent measurements to establish a general correlation that applies to a variety of fuels.

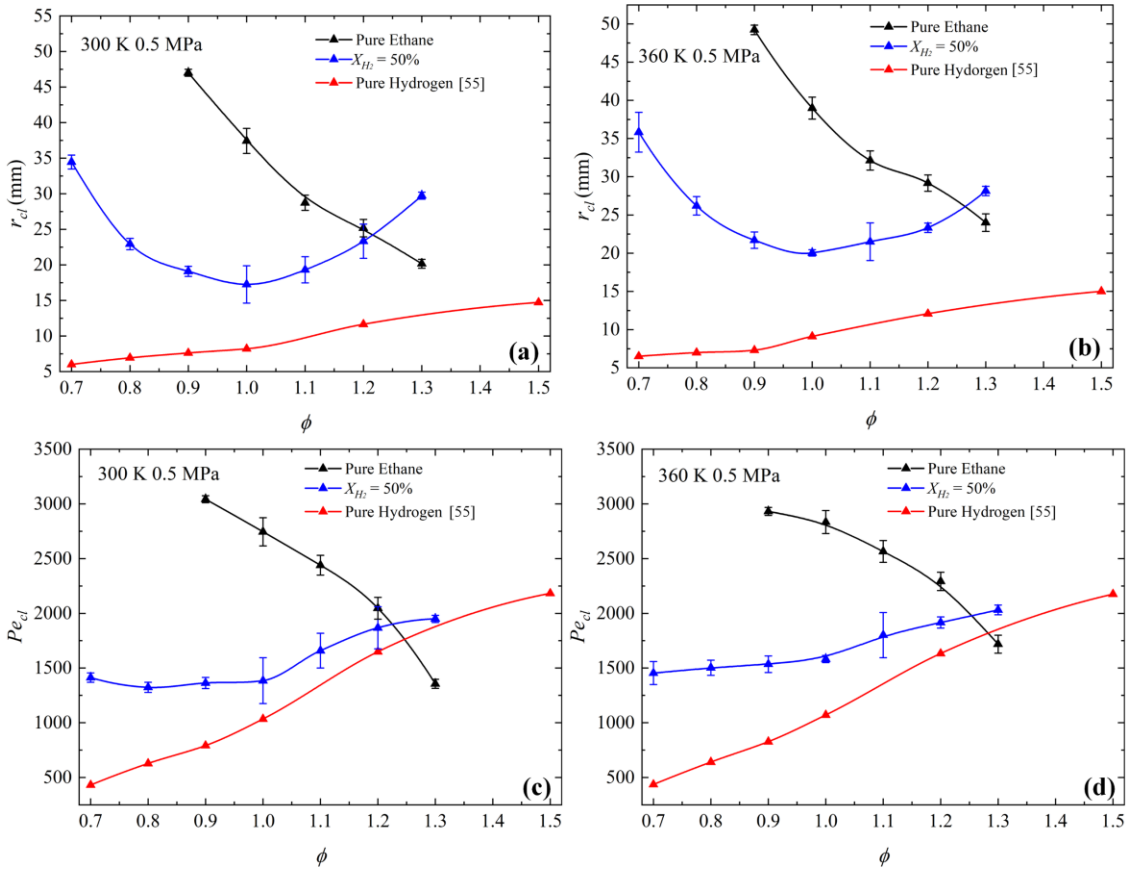


Figure 5.13. The variations of measured Peclect number, $Pe_{cl}$, and critical radius, $r_{cl}$, of ethane-hydrogen-air mixtures with equivalence ratio, $\phi$, at conditions initial temperature, $T_i$ = 300, 360 K, and initial pressure $P_i$ = 0.5 MPa.

The $Pe_{cl}$ with $Ma_b$ values for ethane-air and ethane-hydrogen-air mixtures ($X_{H_2}$= 50%) from the current study, along with data from Xie et al. [55] on hydrogen-air and Marwaan et al [163] on methane-hydrogen-air ($X_{H_2}$= 30%, 50% and 70%), are collectively presented in Fig. 5.14. These data encompass a broad range of equivalence ratios, temperatures, and pressures at 0.5 MPa. In alignment with the correlation formats adopted in [49, 55, 214], a non-linear correlation is proposed to optimally fit the measurements, aiding in the identification of the stable and unstable flame regimes:

$$Pe_{cl} = 877exp\ (0.04803Ma_b), \quad Ma_b \in (-30\ 30) \tag{5.7}$$

The solid curve in Fig. 5.14 represents this non-linear correlation, exhibiting an $R^2$ value of 0.82, demonstrating a good fit with the measured data. The stable regime is located below the curve, while the unstable regime is situated above it. Overall, the results illustrate that $Pe_{cl}$ increases with $Ma_b$ implying that the flames become more stable

with increasing $Ma_b$. The hydrogen-air, methane-hydrogen-air ($X_{H_2}$= 30%, 70% and 50%) and lean ethane-hydrogen-air ($X_{H_2}$= 50%) are mixtures are characterized by negative $Ma_b$ and minimal $Pe_{cl}$. This suggests that cellular instability occurs early with small flame radius and a limited stable flame propagation regime. Noted, in comparison to hydrogen/air mixtures, ethane-hydrogen-air ($X_{H_2}$= 50%) exhibit positive $Ma_b$ and large $Pe_{cl}$ demonstrating that adding ethane to hydrogen reduces the inherent cellular instability, expanding the stable regime relative to pure hydrogen. In ethane-air mixtures, strong positive $Ma_b$, values are prominent, leading to a more stable flame and cellular instability only occurring at large $Pe_{cl}$ and radius. When compared to methane-hydrogen-air mixtures at the same hydrogen level of $X_{H_2}$= 50% ethane-hydrogen-air mixtures exhibit superior resistance to cellular instability, displaying relatively larger $Ma_b$ and $Pe_{cl}$ values.

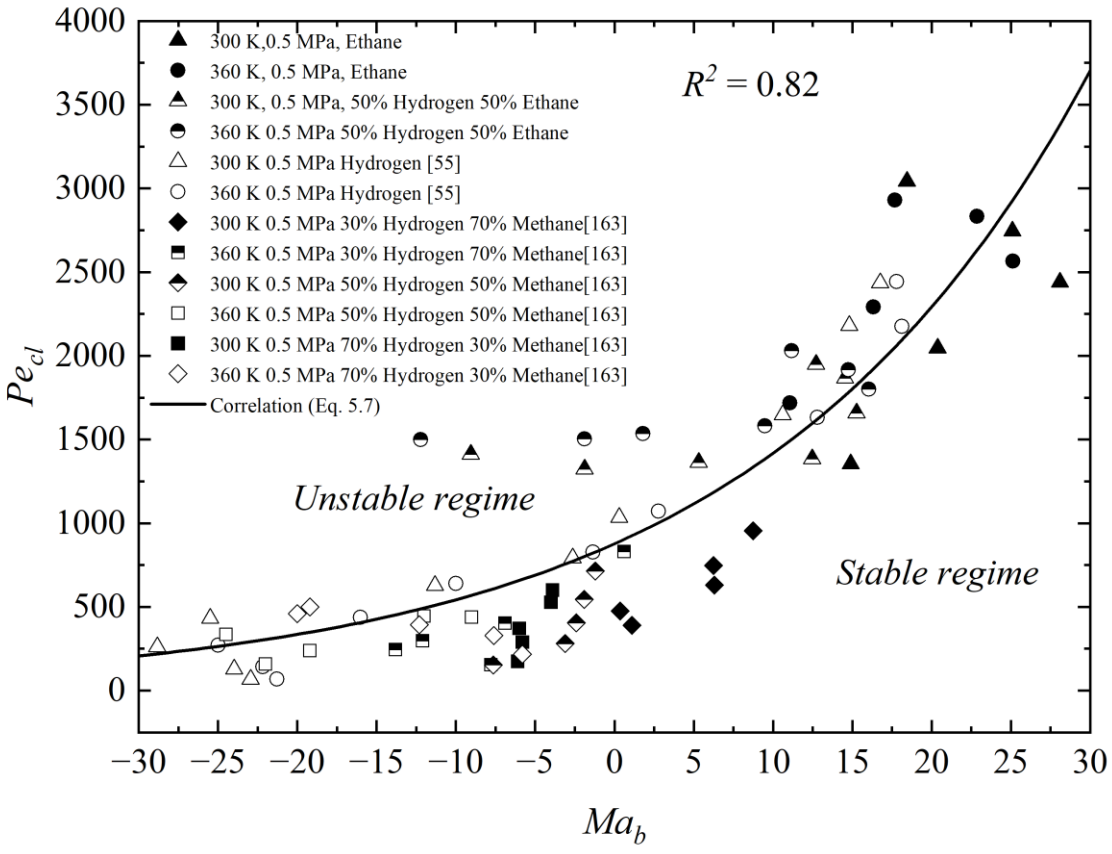


Figure 5.14. Variations of $Pe_{cl}$ with $Ma_b$ for ethane-air, ethane-hydrogen-air ($X_{H_2}$= 50%), methane-hydrogen-air ($X_{H_2}$= 30%, 50% and 70%) from [163] and hydrogen-air from [55] at 0.5 MPa. The solid curve represents the correlation (Eq. 5.7).

## 5.3 Experimental Results of Turbulent Burning Velocity of Ethane-Air Mixture

In Section 5.3, the research initially aims to bridge the existing knowledge gaps, focusing on the influence of turbulence on the propagation of expanding ethane-air flames over a wide range of conditions, including equivalence ratio, initial temperature, and pressure. Following this, a turbulent burning velocity correlation, grounded on the dimensionless parameters *U* and *K*, is proposed. This correlation aligns closely with the measured data, showcasing a robust fit with an $R^2$ value of 0.97.

### 5.3.1 Experimental Conditions

The experimental conditions and laminar flame parameter including laminar burning velocity, $u_l$, laminar flame thickness, $\delta_l$, burned gas markstein length, $L_b$, and burned gas markstein number, $Ma_b$, were shown in table. 5.4 below. Where $\rho_b$ and $\rho_u$ are the burned and unburned gas densities, respectively, which is predicted by using a chemical equilibrium program named GasEq [48]. The $\delta_l$ is given as $\delta_l = \frac{v}{u_l Pr}$ [22], $v$ is the kinematic viscosity, $P_r$ is the Prandtl number $P_r = \frac{v}{\alpha}$ where here $\alpha$ is the thermal diffusivity. Both $v$ and $\alpha$ were derived from the GasEq [48]. The current measurements of ethane-air mixtures covering equivalence ratio from 0.8 to 1.2, initial pressure 0.1 MPa and 0.5 MPa, initial temperature of 300 K and 360 K and $u'$ varied from 0 to 5 m/s.

Table 5.4. The experimental conditions and laminar flames parameters in the present study.

| Fuel | $\phi$ | $u'$ (m/s) | Pressure (MPa) | Temperature (K) | $\rho_u/\rho_b$ | $u_l$ (m/s) | $\delta_l$ (mm) | $L_b$ (mm) | $Ma_b$ |
|---|---|---|---|---|---|---|---|---|---|
| Ethane /air | 0.8 | 1, 3, 5 | 0.1 | 300 | 6.95 | 0.297 | 0.0640 | 0.941 | 14.7 |
| | 0.9 | 1, 3, 5 | 0.1 | 300 | 7.45 | 0.364 | 0.0516 | 0.792 | 15.3 |
| | 1.0 | 1, 3, 5 | 0.1 | 300 | 7.82 | 0.402 | 0.0466 | 0.802 | 16.9 |
| | 1.1 | 1, 3, 5 | 0.1 | 300 | 7.92 | 0.413 | 0.0450 | 0.807 | 17.9 |
| | 1.2 | 1, 3, 5 | 0.1 | 300 | 7.84 | 0.395 | 0.0468 | 0.679 | 14.5 |

| | | | | | | | | |
|---|---|---|---|---|---|---|---|---|
| 0.8 | 1, 3, 5 | 0.5 | 300 | 6.97 | 0.184 | 0.0224 | 0.337 | 16.4 |
| 0.9 | 1, 3, 5 | 0.5 | 300 | 7.51 | 0.244 | 0.0155 | 0.285 | 18.5 |
| 1.0 | 1, 3, 5 | 0.5 | 300 | 7.92 | 0.275 | 0.0136 | 0.342 | 25.1 |
| 1.1 | 1, 3, 5 | 0.5 | 300 | 7.98 | 0.317 | 0.0118 | 0.331 | 28.1 |
| 1.2 | 1, 3, 5 | 0.5 | 300 | 7.86 | 0.302 | 0.0123 | 0.251 | 20.4 |
| 0.8 | 1, 3, 5 | 0.1 | 360 | 5.90 | 0.381 | 0.0684 | 0.856 | 12.5 |
| 0.9 | 1, 3, 5 | 0.1 | 360 | 6.31 | 0.473 | 0.0547 | 0.882 | 16.1 |
| 1.0 | 1, 3, 5 | 0.1 | 360 | 6.61 | 0.535 | 0.0482 | 0.846 | 17.6 |
| 1.1 | 1, 3, 5 | 0.1 | 360 | 6.70 | 0.550 | 0.0466 | 0.904 | 19.4 |
| 1.2 | 1, 3, 5 | 0.1 | 360 | 6.65 | 0.534 | 0.0476 | 0.538 | 11.3 |
| 0.8 | 1, 3, 5 | 0.5 | 360 | 5.92 | 0.233 | 0.0224 | 0.325 | 14.5 |
| 0.9 | 1, 3, 5 | 0.5 | 360 | 6.36 | 0.308 | 0.0168 | 0.297 | 17.7 |
| 1.0 | 1, 3, 5 | 0.5 | 360 | 6.70 | 0.374 | 0.0138 | 0.315 | 22.9 |
| 1.1 | 1, 3, 5 | 0.5 | 360 | 6.76 | 0.409 | 0.0125 | 0.315 | 25.1 |
| 1.2 | 1, 3, 5 | 0.5 | 360 | 6.67 | 0.401 | 0.0127 | 0.208 | 16.3 |

Similar to the laminar flame experiments, each turbulent flame measurements was repeated three times. The same definitions for average value and standard deviation error bars were used. These error bars were plotted around the mean values for all turbulent experimental results

### 5.3.2 Turbulent Combustion Regime

The premixed turbulent flames occurred in the Leeds MK-II vessel can be classified using the Peter-Borghi's diagram [93, 94] shown in Fig. 5.15 below. The detailed explanation and discussion of Peter-Borghi diagram can be found in Section 2.2.2. All the turbulent flame cases with $u'$=1 m/s were in the corrugated flames regime. As the value of $K_a$ larger than unity, entering the distributed reaction regime, where the flame stretch is strong and even the smallest eddies can penetrate the flame structure broadening the flame structure [94]. While the transition from corrugated to distributed flame occurred at $u'$ = 3 m/s, and all the $u'$= 5 m/s turbulent flame cases are in distributed reaction zone.

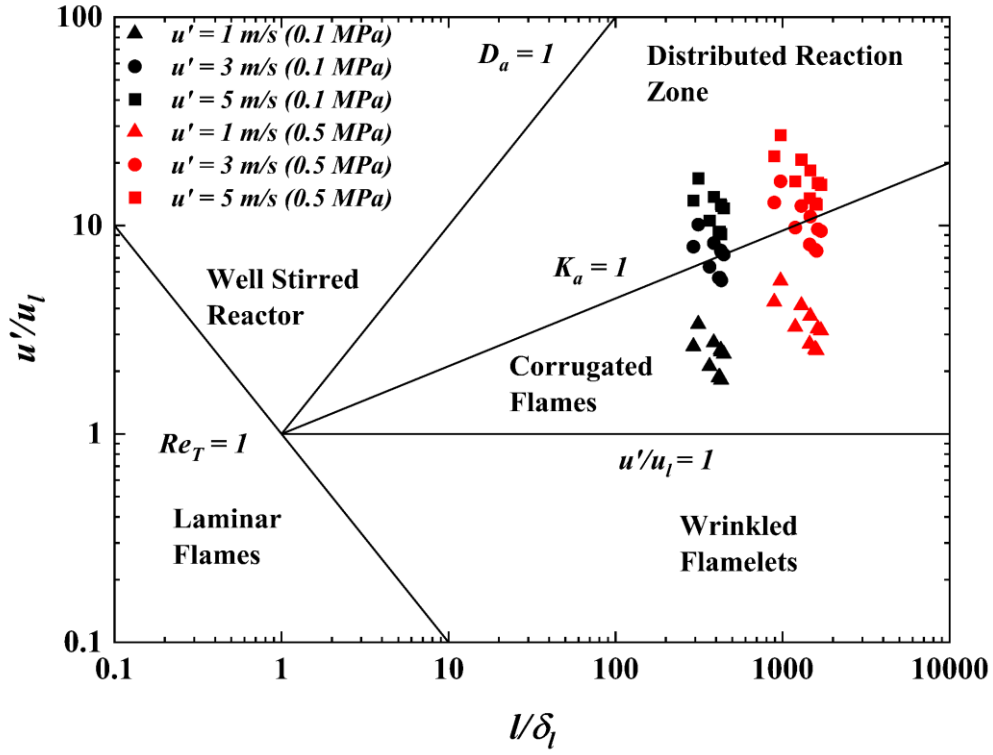


Figure 5.15. Peter-Borghi's regimes [64,65] of present experimental conditions on the turbulent combustion diagram.

The laminar and turbulent propagation of ethane-air flames under $P_0$ = 0.1 and 0.5 MPa are presented in Figs. 5.16&5.17, respectively. For laminar conditions at 0.1 MPa, the flame retains a spherical geometry within the current measurement range of a 60 mm flame radius. However, at 0.5 MPa, instability is observed with a cellular flame surface at an $r_{sch}$ = 30 mm. For all the turbulent flame, the increasement of turbulence intensity significantly modifies the flame structure. Particularly, under the highest turbulence intensity $u'$= 5 m/s, the flame surface was heavily wrinkled and irregular, a huge change in flame morphology was observed. Because, in the distributed reaction the smallest Kolmogorov scale eddies can penetrate the flame thickness, enhancing both heat and mass transfer rates. The chemical reaction time is insufficient to fully consume the smallest eddies before they disintegrate, thereby fragmenting the reaction zone. The similar turbulent flame morphology was reported by Wu et al. [215] with n-octane-air and the occurrence of local extinction may lead to the irregular flame front under high turbulence intensity.

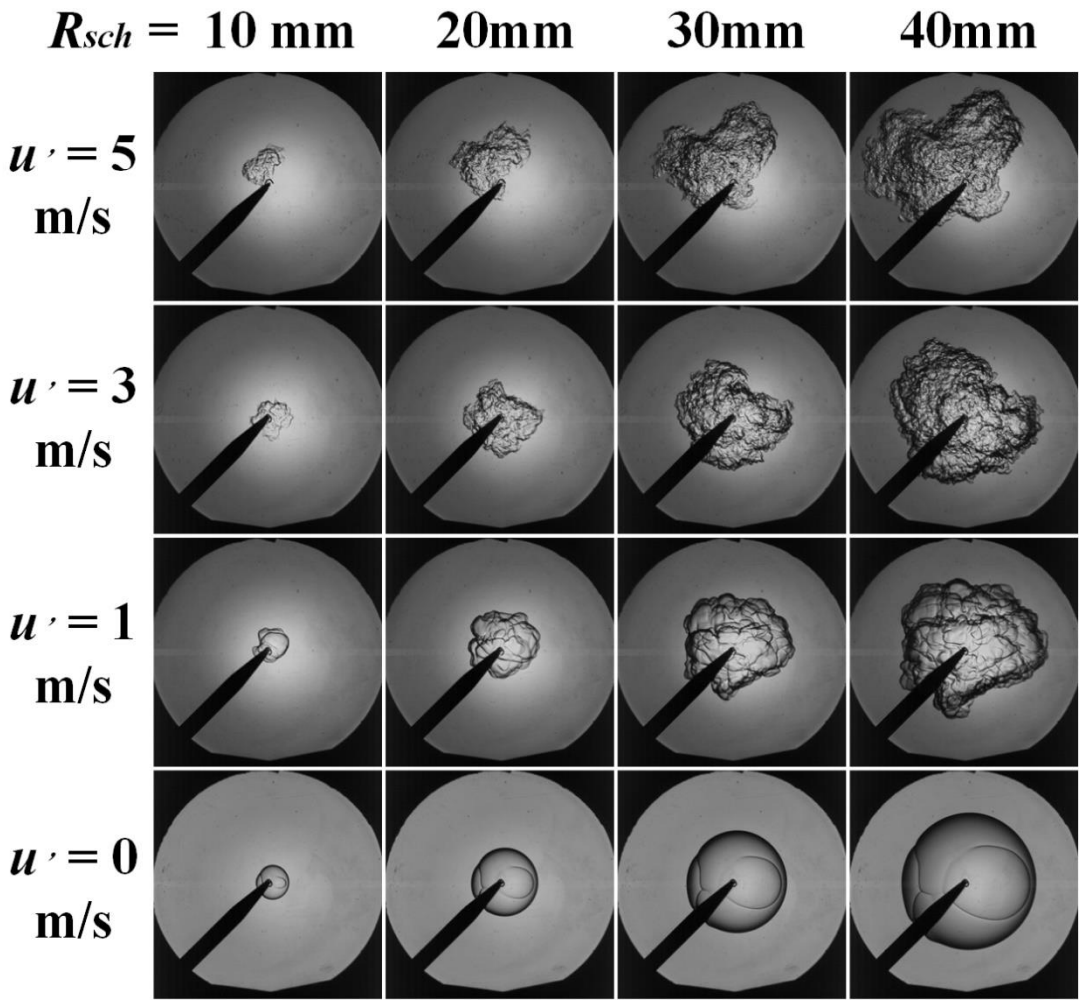


Figure 5.16. Laminar and turbulent flame images of stoichiometric ethane-air mixtures at condition of 300 K, 0.1 MPa.

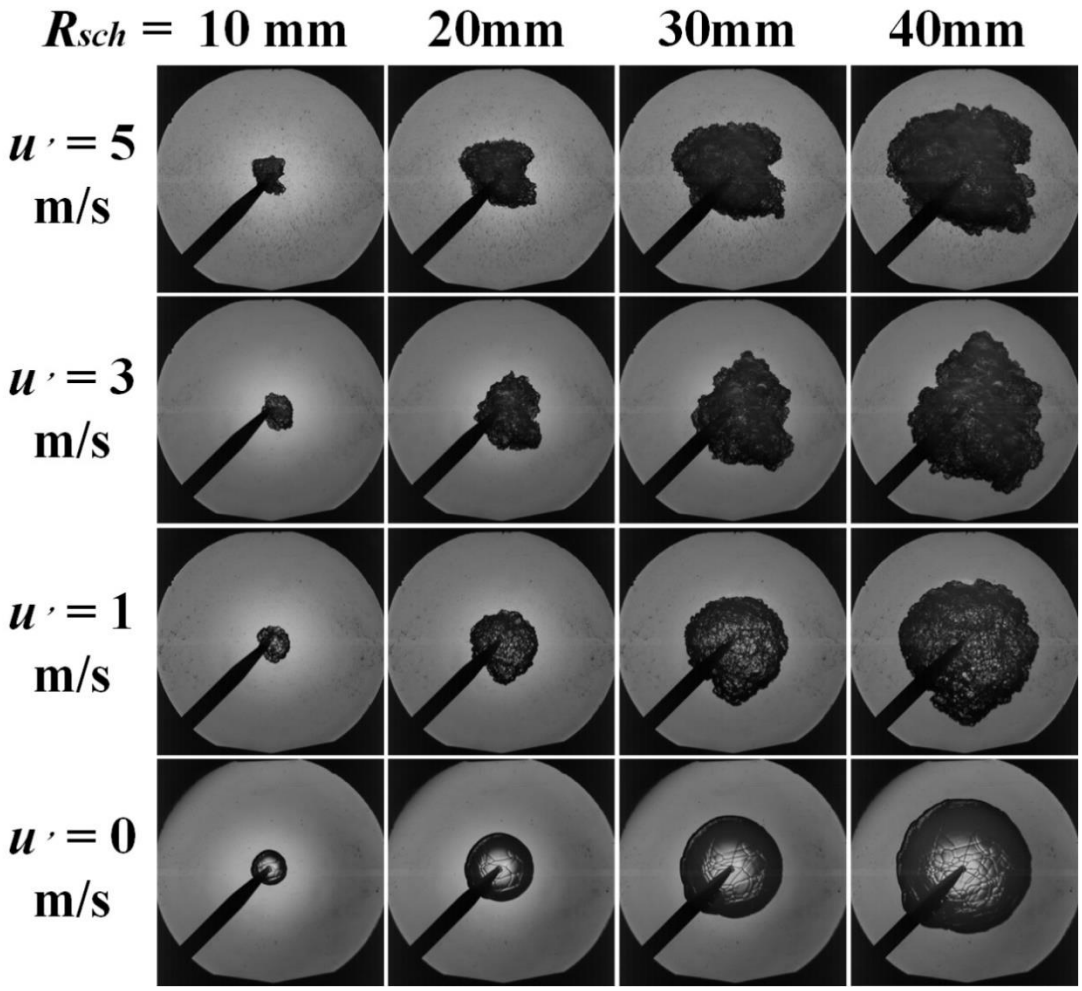


Figure 5.17. Laminar and turbulent flame images of stoichiometric ethane-air mixtures at conditions of 300 K, 0.5 MPa.

### 5.3.3 Turbulence Effect on Pressure Evolution

The pressure evolution inside the spherical combustion chamber was recorded and presented in Figs. 5.18&5.19 with two set of initial pressure 0.1 (Fig. 5.16) and 0.5 MPa (Fig. 5.17) and different level of turbulence intensity ($u'$ from 0 to 5 m/s). The evolution of the pressure inside the spherical vessel is strongly affected by the initial turbulence intensity. All the explosions roughly have the same maximum pressure, 0.8 MPa and 4.2 MPa for initial pressure of 0.1 MPa and 0.5 MPa, respectively. As the $u'$ increased increases, the time interval between ignition starts and peak pressure shortens, indicating a faster burning mixture. This trend aligns with the burning velocity in Figs. 5.23&5.24, where the burning velocity similarly rises with increasing $u'$. This observation is consistent with the lean hydrogen premixed turbulent flames of Goulier et. al [75]. Where

the turbulent flame speed of lean hydrogen flame increases drastically when the turbulence is increased.

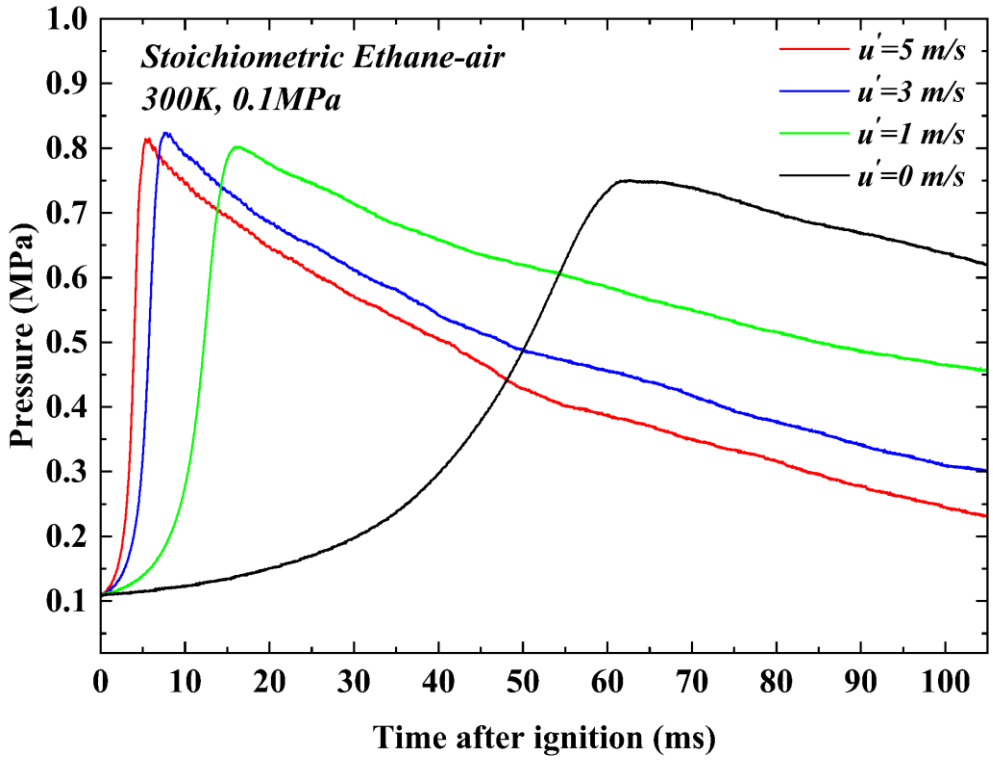


Figure 5.18. Impact of $u'$ on the pressure evolution of stoichiometric ethane-air mixtures at condition of 300 K, 0.1 MPa.

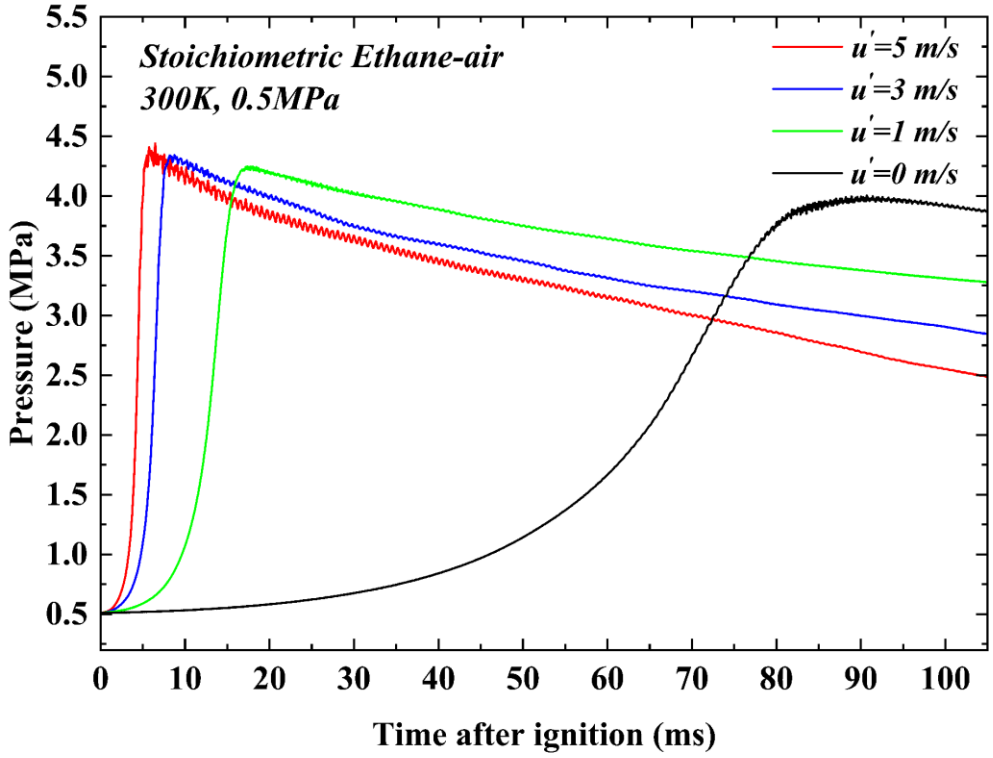


Figure 5.19. Impact of the $u'$ on the pressure traces of stoichiometric ethane-air

mixtures at condition of 300 K, 0.5 MPa.

### 5.3.4 The Effects of Turbulence Intensity on Turbulence Flame Speed

Shown in Figs. 5.20 and 5.21 are the stoichiometric ethane-air mean flame radii, $r_{sch}$, plotted against with time from the start of ignition at initial temperature of $T_0$ = 300 K and pressure of 0.1 and 0.5 MPa, respectively. During the early stage of flame propagation, the flame radii increase gradually, as the size of the flame radii smaller than the integral length scale of the bomb of 20 mm. Thereafter, the flame radii growth rate increases, this pattern is particularly prominent at $u'$= 5 m/s. This is attributed to the turbulent flame radius being influenced by the turbulent wavelength, as elaborated in Section 2.2.4. In Fig. 2.9, it is evident that an increase in the wavelength leads to a rise in the effective rms turbulent velocity, $u_k'$, resulting in a higher turbulent flame propagation speed. The gradient of these curves was then used to determine the flame propagation speeds.

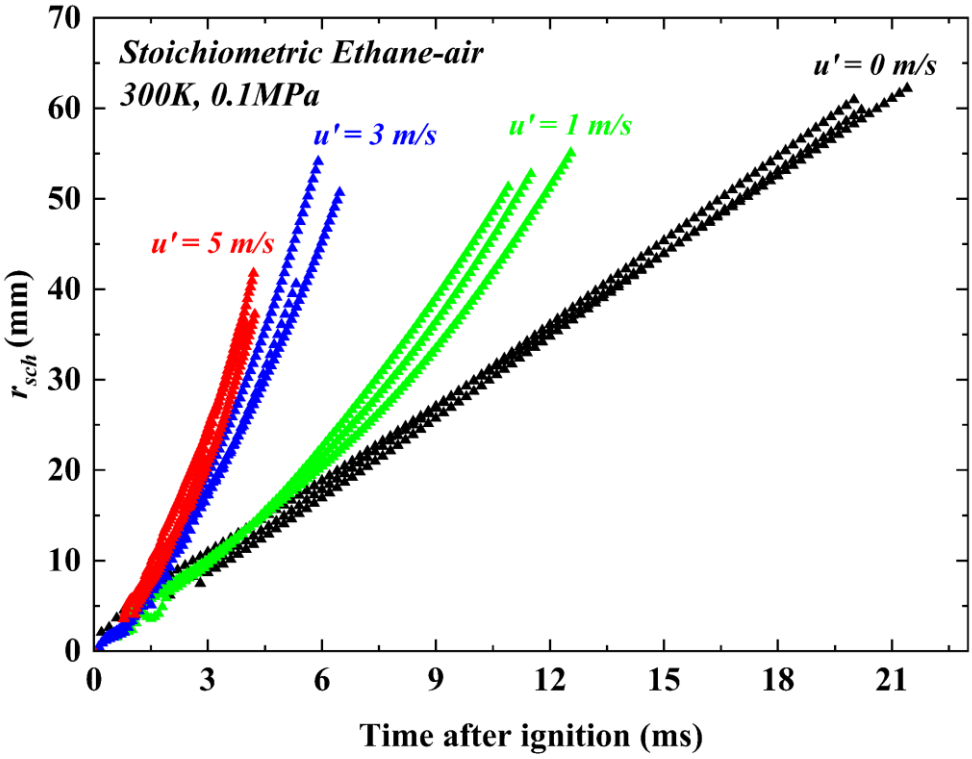


Figure 5.20. Impact of the *u'* on the mean flame Schlieren radii of stoichiometric ethane-air mixtures at condition of 300 K, 0.1 MPa.

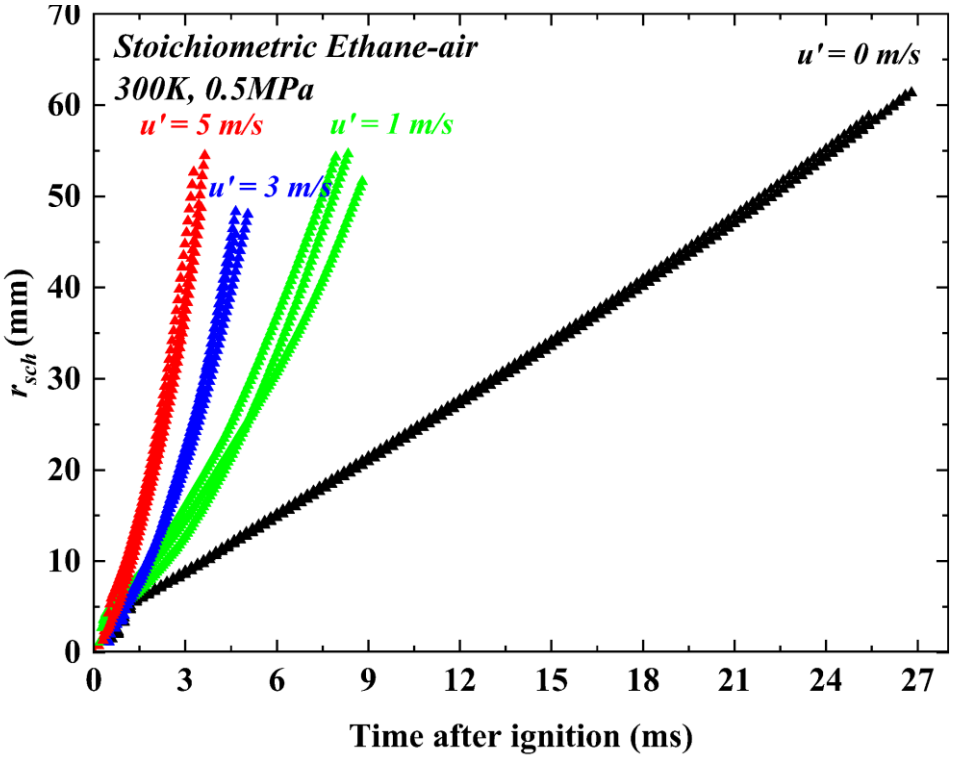


Figure 5.21. Impact of the *u'* on the mean flame schlieren radii of stoichiometric ethane-air mixtures at condition of 300 K, 0.5 MPa.

Shown in Fig. 5.22 are the ethane-air flame propagation speeds plotted against with the flame radii for ethane-air with $\phi$ = 0.8, 1 and 1.2 at $T_0$ = 300 K and $P_0$ = 0.1 and 0.5 MPa. The propagation flame speeds, $S_{sch}$, here are defined as $dr_{sch}/dt$. The inevitable stochastic nature of variation in turbulent flame propagation speed is clearly seen and each curve represents the average of three explosions. The error bar reported the standard deviation of three explosion and its magnitude increases with the $u'$. In general, the size of error bar is increasing with the $u'$. At a given value of $u'$ the turbulent flame propagation speed increased with the flame radii. Bradley et al. [103] reported that after the central ignition, the small flame kernel is initially wrinkled by the eddies smaller than the flame kernel and the effective rms turbulent velocity, $u_k'$, that effective in wrinkling the flame is lower than the actual rms turbulent velocity, $u'$, in the bomb. Thereafter, as the flame grows, it becomes increasingly wrinkled by larger eddies and both $u_k'$ and turbulent propagation speed increase. Finally, the turbulent flame is fully exposed by the entire turbulence spectrum and $u_k'$ equals to $u'$. A detail discussion and explanation of $u_k'$ effects on the turbulent flames, as well as their expressions. can be found in Section

2.2.4.

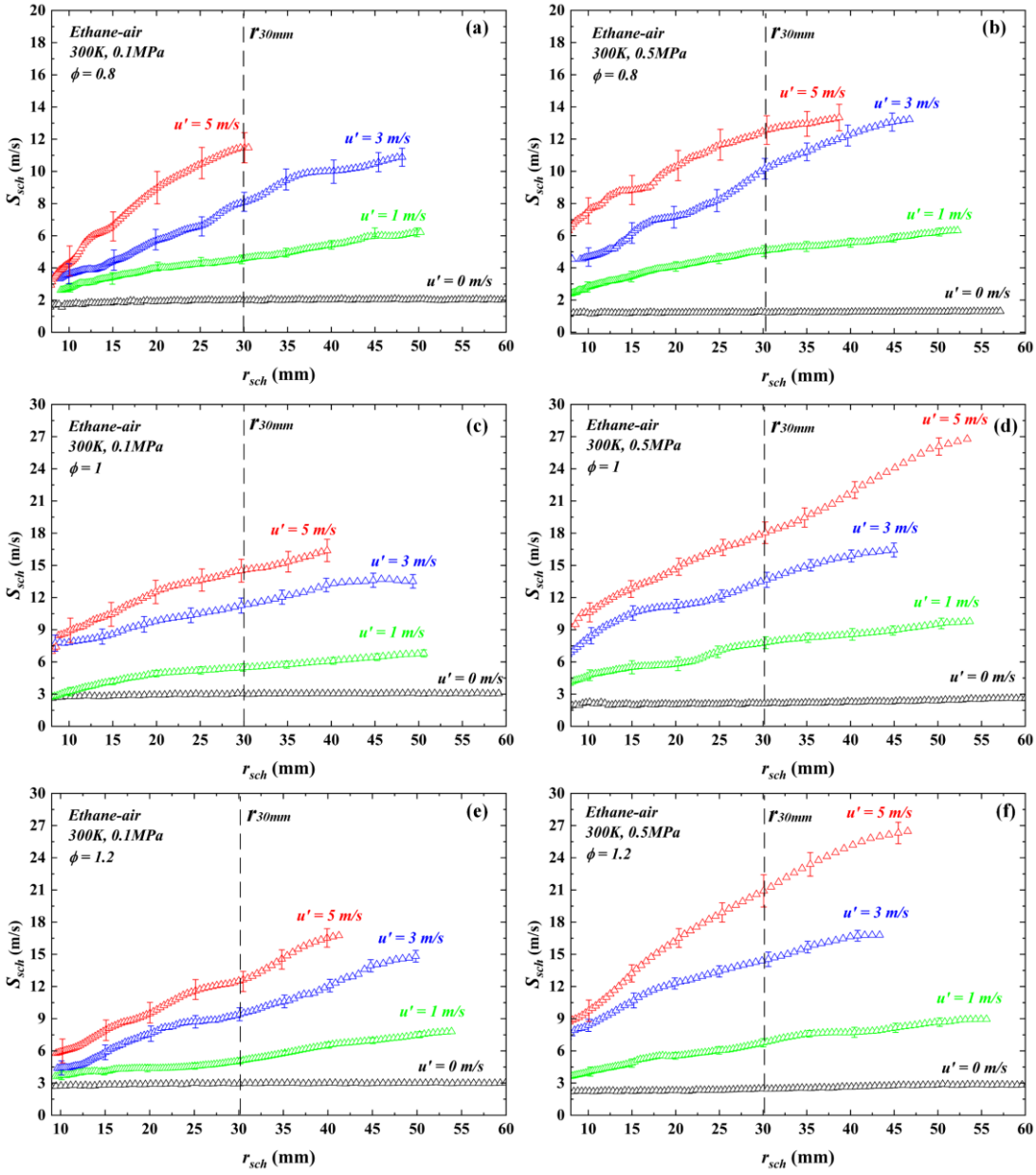


Figure 5.22. Variation of flame speed with increasing flame radius for different $u'$ (0 to 5 m/s) for $\phi$ = 0.8 at temperature of 300 K, pressure of 0.1 MPa (a) and 0.5 MPa (b), $\phi$ = 1 at temperature of 300 K, pressure of 0.1 MPa (c) and 0.5 MPa (d), and $\phi$ = 1.2 at temperature of 300 K, pressure of 0.1 MPa (e) and 0.5 MPa (f).

Clearly, for each subplot in Fig. 5.22, the $S_{sch}$ is enhanced by an increase in $u'$. Referring back to the turbulent combustion regime depicted in Fig. 5.15 an increase in $u'$ transitions the flame from a corrugated state to the distributed flame zone. This signifies that the lifetime of the smallest, Kolmogorov-scale eddies life scale is shorter than the

chemical reaction timescales. Consequently, these minuscule eddies can penetrate the flame thickness, enhancing both heat and mass transfer rates. The chemical reaction time is insufficient to fully consume the smallest eddies before they disintegrate. This causes the reaction zone to fragment, making the flame front appear more wrinkled and burning faster, as observed in the turbulent flame images in Figs. 5.16 and 5.17.

Comparing subplots (a), (c) and (e) in Fig. 5.22 shows the effects of equivalence ratio from 0.8 to 1.2 on the $S_{sch}$ at 0.1 MPa. Generally, $S_{sch}$ increased from lean mixtures of $\phi$ = 0.8 to stoichiometric mixture of $\phi$ = 1.0 and dropped slightly on rich side at $\phi$ = 1.2. Similar behaviour was also observed in premixed turbulent explosion experiments with hydrocarbons such as methane-air [80], *i*-octane-air [82] and ethanol-air [83]. Similar behaviour was also observed at 0.5 MPa with subplots (b), (d) and (f). Subplots (a) and (b), (c) and (d), (e) and (f) in Fig 5.22 show that, in general, increasing the initial pressure from 0.1 to 0.5 MPa increases the $S_{sch}$ of turbulent flame ($u'$ = 1, 3, 5 m/s), while the laminar flame ($u'$= 0 m/s) presented an opposite trend.

### 5.3.5 Turbulent Burning Velocities

In order to quantify the effects of $\phi$, pressure, temperature and $u'$ on the $u_{tr}$, the reference turbulent burning velocity, $u_{tr}$, at the point with $r_{sch}$ = 30 mm were selected to plot against with equivalence ratio, see Fig. 5.23 to 5.26. For a deeper understanding of the turbulent reference radii and the methodology behind calculating turbulent burning velocities, refer to Section 2.2.3. At high $u'$ values, such as 5 m/s, the turbulent flame is convicted away from the center of the optical window. This results in measurements of only moderate flame radii, typically around 30 mm, before parts of the flame kernel move beyond the observation range of the window [79].

Figs. 5.23 to 5.26 shows the burning velocity, with $u'$ = 0, 1, 3 and 5 m/s, covering a temperature range of 300 to 360 K, a pressure range of 0.1 to 0.5 MPa, and an equivalence ratio range of 0.8 to 1.2. Once again, $u'$ is the dominate parameter affecting the accuracy of burning velocity measurements, regardless of the pressure, temperature, or equivalence ratio, and the size of the error bar increases with $u'$. Overall, an increasing in $u'$ also leads to an increase in burning velocity.

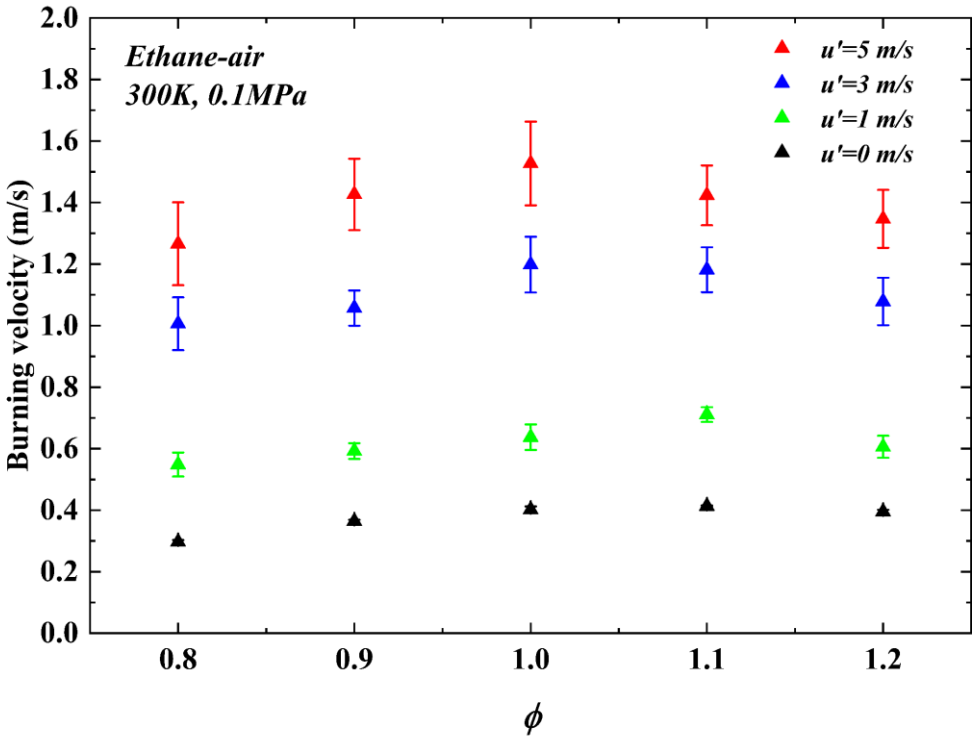


Figure 5.23. Impact of the $u'$ (from 0 to 5 m/s) on burning velocity ($u_{tr}$ at $r_{sch}$ = 30 mm) in ethane-air mixtures at 300 K and 0.1 MPa, plotted against the equivalence ratio.

For the turbulent burning velocity, $u_{tr}$, with $u'$ = 1 m/s its maximum occurred at $\phi$ = 1.1, while for stoichiometric with $u'$ = 3 and 5 m/s. Shown in Fig. 5.24 are the burning velocity at elevated initial pressure of 0.5 MPa, with 300 K temperature were presented against with $\phi$. The maximum burning velocity were observed at $\phi$ = 1.1 for all explosions.

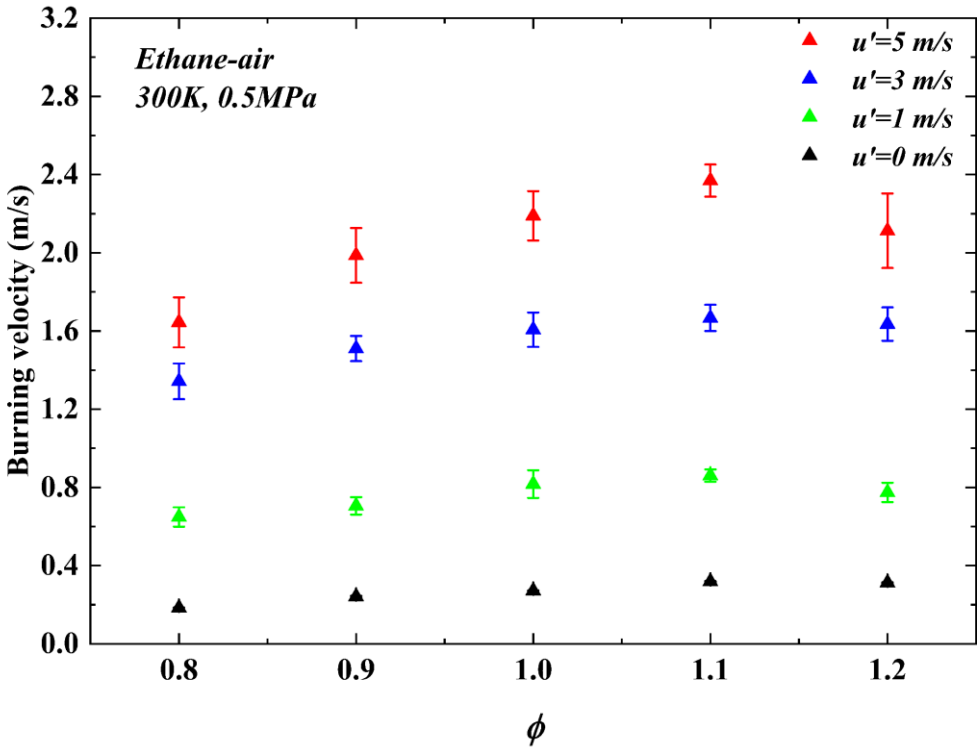


Figure 5.24. Impact of the $u'$ (from 0 to 5 m/s) on burning velocity ($u_{tr}$ at $r_{sch}$ = 30 mm) in an ethane-air mixture at 300 K and 0.5 MPa, plotted against the equivalence ratio.

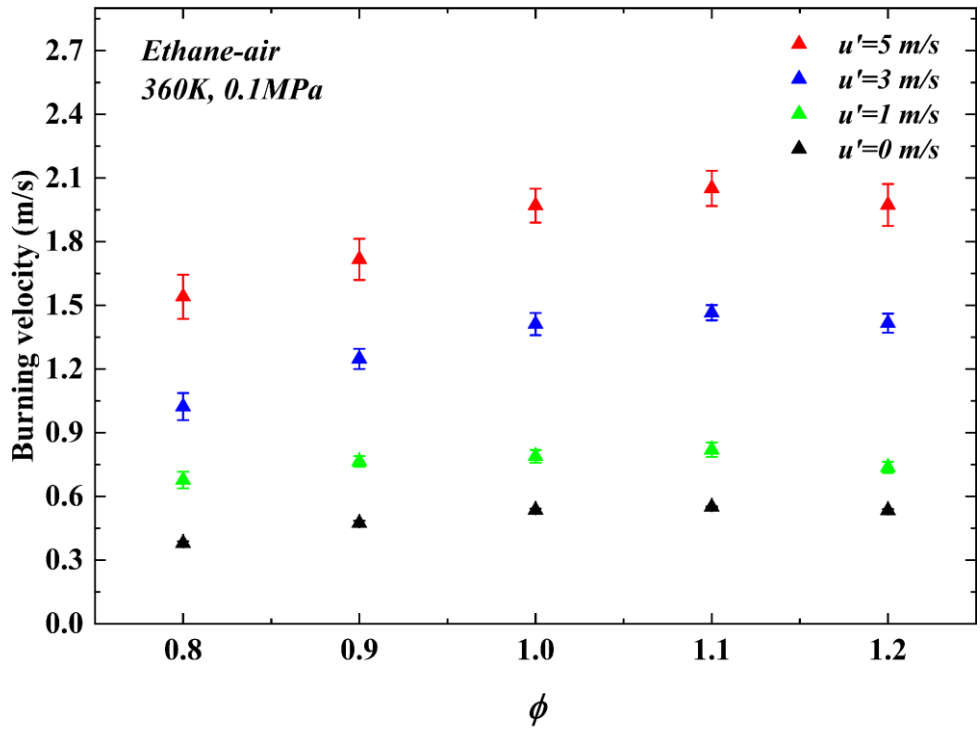


Figure 5.25. Impact of the $u'$ (from 0 to 5 m/s) on burning velocity ($u_{tr}$ at $r_{sch}$ = 30 mm) in an ethane-air mixture at 360 K and 0.1 MPa, plotted against the equivalence

ratio.

Fig. 5.25 moves to the higher temperature conditions with 360 K and 0,1 MPa pressure. An increase in temperature from 300 K to 360 K, enhance both $u_l$ and $u_{tr}$.

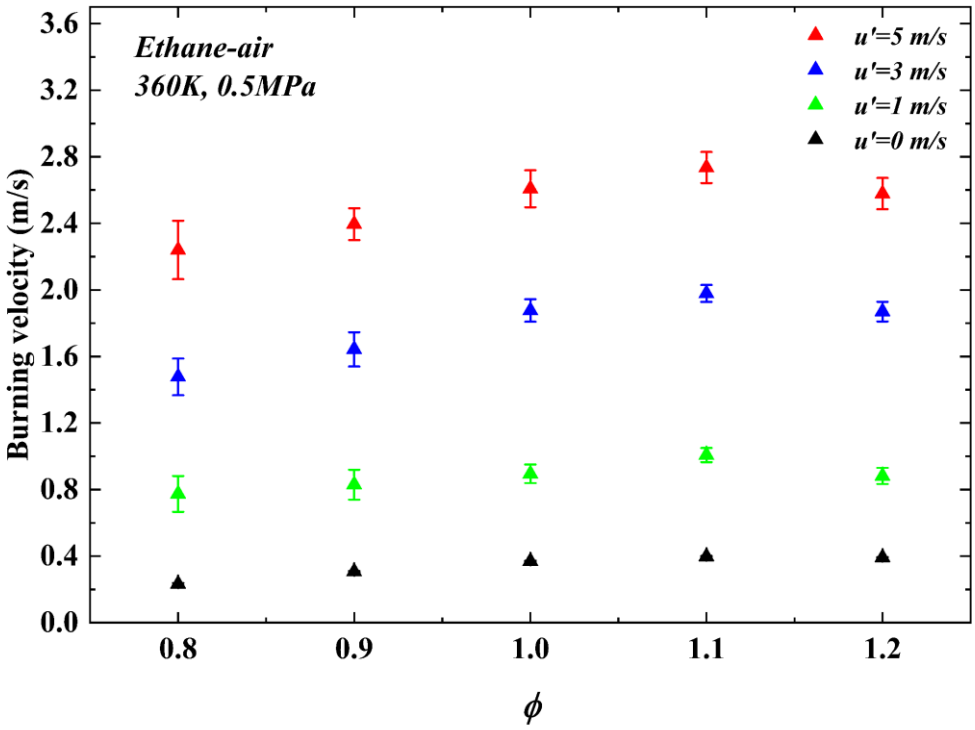


Figure 5.26. Impact of the $u'$ (from 0 to 5 m/s) on burning velocity ($u_{tr}$ at $r_{sch}$ = 30 mm) in an ethane-air mixture at 360 K and 0.5 MPa, plotted against the equivalence ratio.

The maximum $u_{tr}$ of 2.8 m/s in current measurements was observed with $u'$=5 m/s, 360 K, 0.5 MPa and $\phi$ =1.1.

### 5.3.6 The Effects of $u_k'/u'$ on $u_{tr}$

The ratio of $u_k'/u'$ signifies the fraction of entire turbulence spectrum that contributes to flame wrinkling. A more detailed explanation and expression of $u_k'$ can be found in Section 2.2.4. The evolution of $r_{sch}$ with $u_k'/u'$ for stoichiometric ethane-air at 300 K 0.1 MPa and 0.5 MPa with $u'$= 1, 3 and 5 m/s are illustrated in Fig. 5.27 (a) and (b). $u_k'/u'$ increases as the flame propagation represents the increasing effects of the turbulence spectrum on the flame surface. Refer to the reference $u_{tr}$ at $r_{sch}$ = 30 mm, as the ratio of $u_k'/u'$ varied around 0.7 for all $u'$ at 0.1 and 0.5 MPa, while this observation

is consistent with *i*-octane [82] and methane [160]. Consequently, a ratio of $\frac{u_k'}{u'} = 0.7$ at $r_{sch}$ = 30 mm has been employed in this turbulent flame study, further informing the turbulent burning velocity correlation discussed in Section 5.3.7. Even the $r_{sch}$ reaching 55 mm, which is the maximum visualization radius of the optical window, the ratio of $u_k'/u'$ reaches around 0.83, indicating that it is still not influenced by the entire turbulence spectrum. Consequently, the existing combustion vessel is unable to visualize a turbulent flame that is fully affected by the entire turbulence spectrum.

Figs. 5.27 (c) and (d) show the variations of $u_{tr}$ with $u_k'/u'$ for the same conditions and the $u_{tr}$ increases with the ratio $u_k'/u'$ for all $u'$ and pressure conditions. These two plotting shows that the growth of the flame radius leads to eddies with larger length scales wrinkling the flame surface, which increases the flame surface area and boosts the turbulent burning velocity, $u_{tr}$.

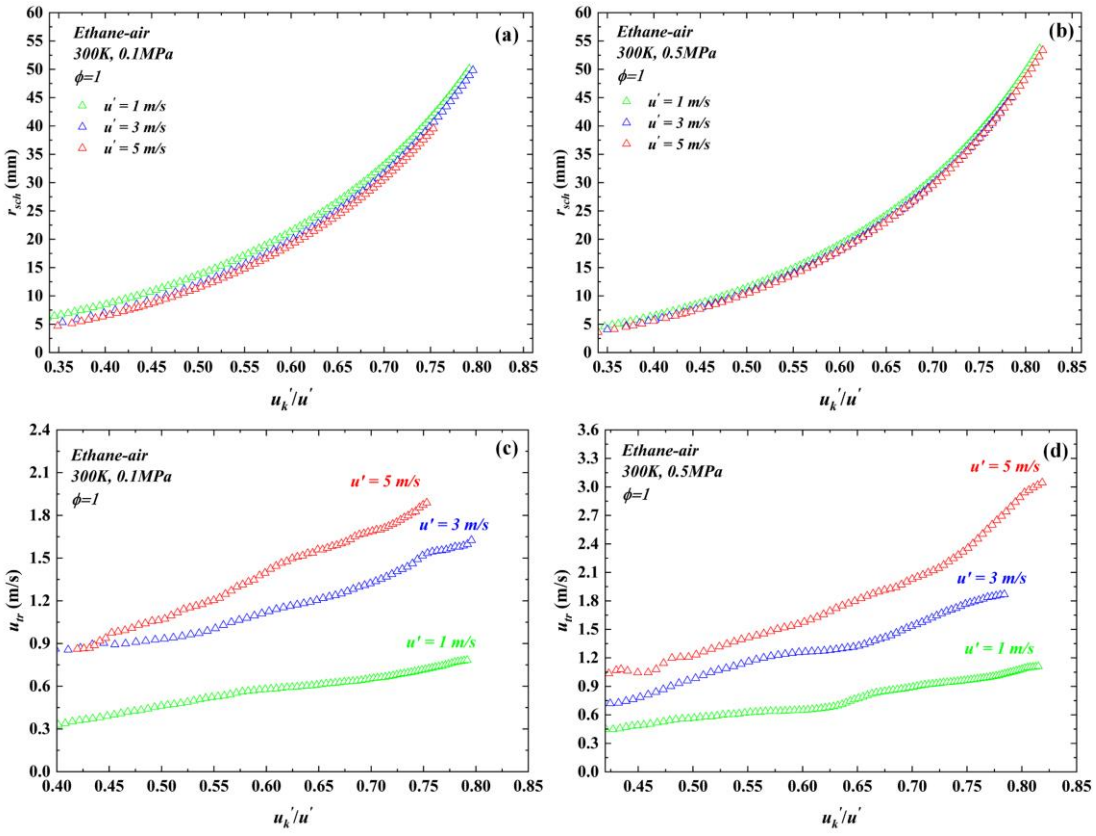


Figure 5.27. Variations of $r_{sch}$ with $u_k'/u'$ for stoichiometric ethane-air mixture of $u'$= 1, 3 and 5 m/s, with a temperature of 300 K, a pressure of 0.1 MPa in (a), 0.5 MPa in (b) and corresponding $u_{tr}$ with $u_k'/u'$ with a pressure of 0.1 MPa in (c) and 0.5

MPa in (d).

### 5.3.7 Correlation of Turbulent Burning Velocity, The *U/K* diagram

Correlating the measured turbulent burning velocity data with the dimensionless parameter is paramount. Such a correlation provides a foundation for deeper insights and facilitates subsequent research endeavors, particularly in the domains of turbulent flame modeling and simulation. Consequently, this study employs Bradley's *U/K* turbulent burning velocity correlation [107]. A comprehensive review of others turbulent burning velocities correlation, along with detailed explanations and expressions of the *U* and *K*, can be found in Section 2.2.5

Figure 5.26 shows the variation of $U$ with respect to $K$ for the current measurements listed in Table. 5.4. As discussed previously, the $U$ is the ratio of $\frac{u_t}{u_k{}'}$, where the $u_t$ is the average turbulent burning velocity (as shown in Figs. 5.23 - 5.26) at a reference flame radius of 30 mm, and the corresponding ratio $\frac{u_k{}'}{u'}$ is 0.7 (as shown in Fig 5.27 (a) and (b)). The value of $K$ is expressed in Eq. 2.41. The different symbols in Fig. 5.28 represent the measured data points, with triangle denoting $u'$= 1 m/s, circle denoting $u'$= 3 m/s circle, squares denoting $u'$= 5 m/s, and black and red in 0.1 MPa and 0.5 MPa, respectively. The full line curves in Fig. 5.28 represent the correlation curves to the current measurement data points, with black in 0.1 MPa and red in 0.5 MPa. Referring in Section 2.2.5 (Eq. 2.34), the original *U/K* turbulent burning velocity correlation comprises two constants, which are functions of the strain rate Markstein number, $Ma_{sr}$. Past measurements of $Ma_{sr}$ for different fuels including hydrogen [46], *i*-octane and *n*-heptane [44], methane [22] and ethanol [107], have demonstrated significant variability, accompanied by large error bars, introducing uncertainty in correlating the turbulent burning velocity. Moreover, calculating the $Ma_{sr}$ is a quite complicated. While the original correlation provides a general framework and is not pinpoint accurate. Given these considerations, using pressure as the correlating variable with *U* and *K* is both more straightforward and accurate.

For pressure with 0.1 MPa, with $R^2$ = 0.97 the correlation is expressed as:

$$U = \frac{u_t}{u_k} = 0.36K^{-0.29}. \quad (5.8)$$

For pressure with 0.5 MPa, with $R^2 = 0.932$, the correlation is expressed as:

$$U = \frac{u_t}{u_k} = 0.47K^{-0.29}. \quad (5.9)$$

Both correlations show good fit with the measured data, as evidenced by the high coefficient of determination, $R^2$, of 0.97 for 0.1 MPa and 0.93 for 0.5 MPa. Overall, for a given pressure, the increases in $u'$ leads to an increase in $K$ but a decrease in $U$, indicating that the rise in $u'$ dominates the flame wrinkling and the increased burning rate in flamelets. The increasing in pressure from 0.1 MPa to 0.5 MPa leads to an upward shift in the correlation line and this explained in [107] as increased burning rate in laminar flamelets.

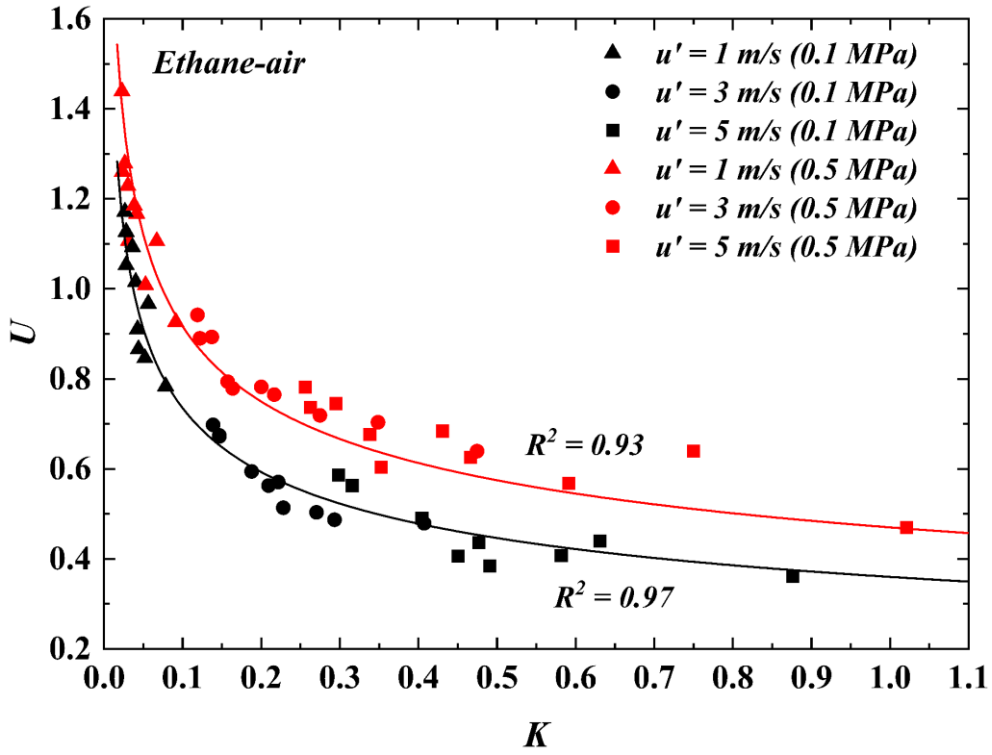


Figure 5.28. Correlation of $U$ with $K$ for different pressures under present experimental conditions listed in Table 5.4.

Figure 5.28 illustrates a comparison between the newly proposed ethane turbulent burning velocity and the original *U/K* turbulent burning velocity correlation, which is based on the $Ma_{sr}$. However, a discrepancy is observed between the measured correlation for ethane and the original correlation. This discrepancy arises because the original *U/K*

turbulent correlation was validated with fuels such as hydrogen, ethanol, methane, *i*-octane, and *n*-heptane, where the $Ma_{sr}$ range from mostly negative to positive values, up to 5, but it was not validated with an ethane-air mixture. It is suggested that the ethane-air mixture's response to the strain rate is not as pronounced, resulting in its correlation positioning below the original correlation.

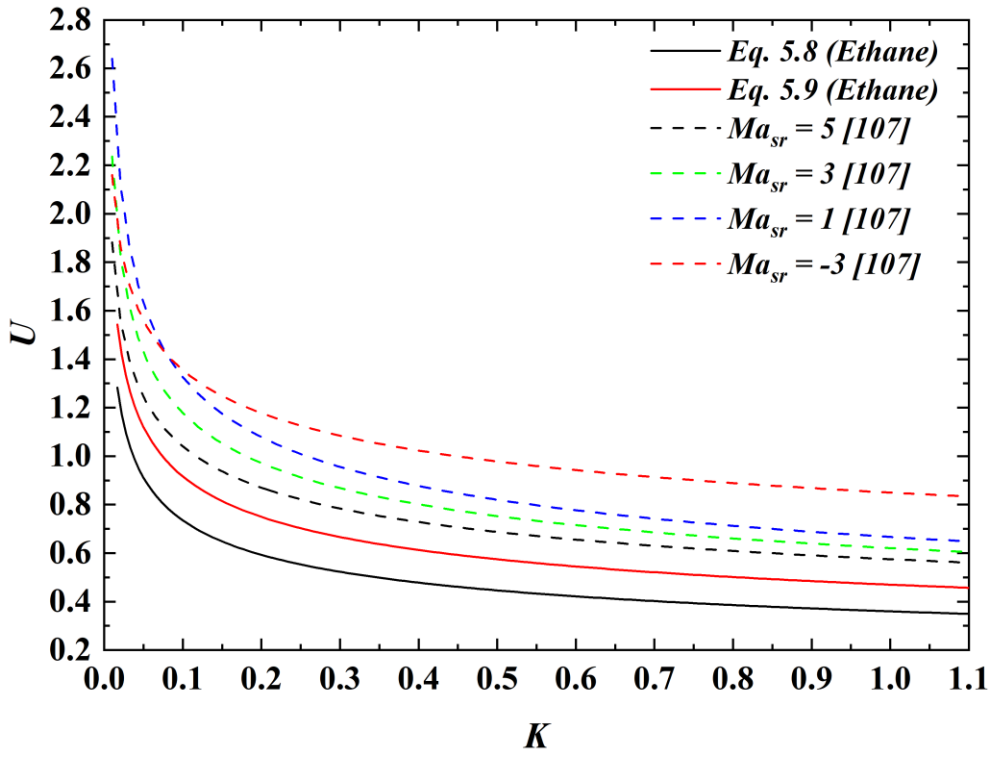


Figure 5.29. Comparative analysis of current turbulent burning velocity correlation for ethane against original *U/K* turbulent burning velocity correlation [107].

## 5.4 Conclusions

The premixed laminar flames measurements of ethane-hydrogen-air mixtures, with hydrogen additions were conducted in a combustion vessel. Their laminar burning velocities were then compared with existing literature and predictions from the AramcoMech 1.3 and USC Mech II chemical kinetic model. A good agreement has been achieved for room temperature conditions (300 K), but a notable discrepancy between prediction and measurement occurs at higher temperature of 360 K. The laminar burning velocities of ethane-air and ethane-hydrogen-air were analyzed using empirical

correlations, and a perfect agreement was observed. The Markstien length, $L_b$, and burned gas Markstein number, $Ma_b$, are measured and correlated with the cellular instability parameters critical radius, $r_{cl}$ and dimensionless Peclet number, $Pe_{cl}$. It is noticed at 0.1 MPa, no cellular instability weas observed with Ethane and even with $X_{H_2}$ = 75 %. A general correlation based on the $Pe_{cl}$ with the $Ma_b$ with pure hydrogen, ethane-hydrogen-air, methane-hydrogen-air at 0.5 MPa was reported to define the stable regime. Overall, the recent measurements bridge the knowledge gap concerning the Markstein length/number, flame instability, and the effects of hydrogen addition on ethane-air combustion characteristics. By introducing ethane into hydrogen, the impact of flame instability is mitigated, promoting stable flame propagation.

It was observed that the turbulent flame propagation speeds increased as the flame radius grew, contributing to an increase in the effective rms turbulent velocity, $u_k'$. The reference turbulent burning velocity, $u_{tr}$, at the point where $r_{sch}$ = 30 mm, were selected to quantify the effects of equivalence ratio, temperature, pressure and $u'$ on turbulent burning velocities. The current measurements of ethane-air mixture demonstrate that $u'$ is the main factor influencing the turbulent flame speed and, consequently, turbulent burning velocity. Increases in temperature and pressure lead to a rise in both turbulent flame speed and burning velocity. The turbulent burning velocity correlation, $U/K$ diagram has been updated with the present work with $R^2$ value up to 0.97. Such correlations are invaluable, laying a foundation for computational models and simulations related to ethane explosions.

# 6. Turbulent Flame Acceleration and Deflagration to Detonation Transition in Ethane-Air Mixture Modelling

## 6.1 Introduction

The DDT transition is a major unsolved problem in combustion research. Despite extensive research on DDT, to best of our knowledge, there is no literature has yet

reported on large-scale simulations of turbulent flame acceleration and DDT for ethane-air mixtures. The storage safety concerns and fire hazards associated with ethane have underscored the importance of simulating its DDT behavior on a large scale.

In this Chapter, a large-scale simulation of ethane-air flame propagation and DDT in congested rig is presented and compared with Shell large scale experimental work [21]. This simulation employs the finite volume code named "MG" which utilized a second-order Godunov Riemann solver complemented by adaptive mesh refinement (AMR), a system developed by Mantis Numerics Ltd [186]. The solution approach is predicated on the ensemble-averaged, density-weighted transport equations for mass, momentum, total energy, and a reaction progress variable as discussed in Section 3.3. Closure of this equation set was achieved via the standard $k-\varepsilon$ equations. Furthermore, a turbulent burning velocity correlation, which consider the effects of rms turbulent velocity, temperature and pressure on burning velocity for stoichiometric ethane-air has been integrated. The detailed expressions and explanations of the governing equations, turbulence model, progress variable and correlation can be found in Section 3.3. The simulation results exhibit a dependence on the different levels of mesh refinement. Notably, the results from the Level 3 mesh refinement align closely with the experimental findings presented in [21].

## 6.2 Experimental and Numerical Setup

### 6.2.1 Experimental Setup

In order to validate the simulation approach, it is critical to review the large-scale experimental study of ethane-air mixture is conducted by Andrzej et al. [21] in a congested rig in present study. This large-scale experimental study aimed to investigate whether the ethane-air can lead to the transition to detonation and also aimed to a safer plant design for the storage safety of ethane. The experiment was carried out within a steel structure, approximately 21 m in length, 6 m in width, and 3 m in height, stationed on a concrete pad as shown in Fig 6.1. The congested area containing steel pipes in an arrangement of 16 by 16 by 8 pipes, each of which had a diameter of approximately 76

mm and were set at a pitch of 342 mm. Shown in Fig. 6.1, the congested area was a regular cuboid array of vertical and horizontal steel pipes with a uniform dimension of about 5.2 m in length, 5.2 m in width, and 2.6 m in height. A single polythene sheet, covering the steel frame, was utilized to contain the ethane-air mixture before igniting. In this experiment, the ignition was achieved by an electrical spark which was located at the edge along the central line of congestion pipe line.

During the test rig's filling process, high purity ethane was used, with an infra-red analyzer employed to monitor and ensure the uniformity of the ethane-air mixture. Following a consultation with author Andrzej, it was confirmed that the equivalence ratio for this mixture is near stoichiometric, around 1.05. Two high speed video cameras were also used to monitor the flame progression and measured the reaction wave propagation speed ran at typically 3000 fps. The development of overpressure within the test rig was measured using 11 pressure transducers, which were distributed over a length of 21 meters and installed flush with ground level.

Figure 6.1. The congested rig of Shell large scale test in the frame of 20×6×3 m [21].

### 6.2.2 Turbulent Burning Velocity Correlation of Stoichiometric Ethane-Air

The measured experimental turbulent burning velocity, $u_t$ of different fuels and condition are not always available in the literature. However, the $u_t$ is an important

parameter in the combustion research such as flame propagation and the open space explosion simulation requires the knowledge of $u_t$ at different conditions. Thus, in this study, the turbulent burning velocity vary with effect turbulent velocity, temperature and pressure of ethane-air was measured from Leeds MK-II fan-stirred combustion vessel.

In the current study, the laminar and turbulent burning velocities were not measured at an equivalence ratio of 1.05. Instead, data for both laminar and turbulent velocities at stoichiometric conditions are provided. However, the marginal increase in the equivalence ratio by 0.05 does not significantly affect its laminar/turbulent burning velocity. Based on the extrapolation of data presented in Figures 5.5 and 5.23, the anticipated variation in burning velocities due to this adjustment in equivalence ratio should be less than 3%. Therefore, the correlation for turbulent burning velocity at stoichiometric conditions for ethane-air mixtures, presented below, is utilized in this analysis.

Based on the turbulent flame data of ethane-air presented in Section 5.3, the general correlation expressed in Eqs. 5.8&5.9 were refined for the specific case of stoichiometric ethane-air mixtures. This led to a significant improvement in model accuracy, yielding a fitting coefficient of determination, $R^2$ = 0.99. The correlation of turbulent burning velocity of stoichiometric ethane-air is shown in Fig. 6.2, the symbol representing the measured turbulent burning velocity and the solid line representing the prediction from the correlation in Eq. 6.1 below.

$$\frac{u_t}{u_k{}'} = 0.36K^{-0.29}\left(\frac{P}{P_0}\right)^{0.2}\left(\frac{T}{T_0}\right)^{0.5} \tag{6.1}$$

Where $u_k{}'$, is the effective rms turbulent velocity, $P_0$ and $T_0$ are the benchmark pressure and temperature at 0.1 MPa and 300 K respectively. The standard $k-\varepsilon$ model is implemented in this study and following the study of Catlin et al. [188], the $u'$ is expressed related to the turbulence kinetic energy, $k$:

$$u' = (2k/3)^{0.5}. \tag{6.2}$$

Given that the turbulent burning velocities are observed at $r_{sch}$ = 30 mm, therefore $u_k{}' = 0.7u'$. Consequently, Eq. 6.2 can be reformulated as:

$$u_k' = 0.7(2k/3)^{0.5}. \quad (6.3)$$

Following [26], the turbulent integral length scale expressed as:

$$L = C_\mu^{3/4} k^{3/2}/\varepsilon, \quad (6.4)$$

where, $C_\mu$ is the constant with the value of 0.09, $\varepsilon$ is dissipation rate of turbulent kinetic energy. In the simulation, the initial turbulent length scale is set at 2 cm consistent with the MK-II combustion vessel and the maximum length scale for this set up is capped at 10 cm.

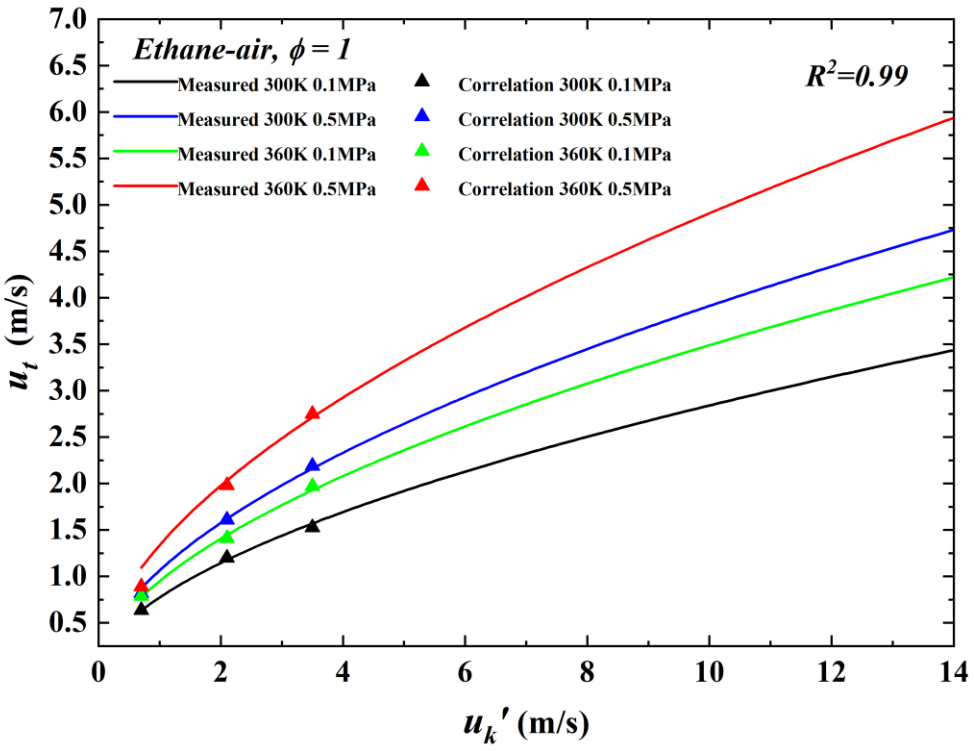


Figure 6.2. Measured and correlation of stoichiometric ethane-air turbulent burning velocity with temperature, pressure, and effective rms turbulent velocity.

The effects of temperature and pressure on the laminar burning velocity expressed as:

$$u_{l2} = u_{l1}(T_2/300)^{1.55}(P_2/0.1)^{-0.24} \quad (6.5)$$

Where, $u_{l1}$ is the laminar burning velocity at 300 K and 0.1 MPa, with value 0.402 m/s. The measured laminar burning velocity is from Table 6.1.

The kinematic viscosities of ethane-air are derived from the calculation of GASEQ [48] and its correction as function of temperature and pressure expressed as:

$$v_2 = v_1(T_2/300)^{1.74}(P_2/0.1)^{-1} \quad (6.6)$$

Overall, as shown in Fig. 6.2, the effective rms turbulent velocity $u_k'$ predominates the magnitude of $u_t$, which exhibits a proportional increase with $u_k'$. This proportional trend was previously explained in Chapter 6 discussion of turbulent theory. Concurrently, an increase in both initial temperature and pressure has been observed to induce a rise in $u_t$. This rise can be attributed to the enhancement in heat release rate, which in turn, amplifies the reactivity of the mixtures.

### 6.2.3 Boundary Conditions and Simulation Setup

In the simulation, the equivalence ratio for ethane-air mixtures is set to 1.05, aligning with the Shell setup in [21], and is uniformly distributed throughout the channel. Additionally, both temperature and pressure are meticulously aligned with the experimental setup, being maintained at 300 K and 0.1 MPa, respectively. The physical parameters and initial conditions are shown in Table 6.1 below. The unburned/burned density, kinematic viscosity, thermal diffusivity and Prandtl number of stoichiometric Ethane-air mixture is derived from the calculation of GASEQ code [48] while the measured laminar burning velocity is from Fig. 5.5 in Section 5.2.3.

Table 6.1. Physical parameters of ethane-air with $\phi = 1.05$ used in simulation.

| Fuel | Ethane-air |
|---|---|
| Equivalence ratio | 1.05 |
| Temperature | 300 K |
| Pressure | 0.1 MPa |
| Laminar burning velocity | 0.402 m/s |
| Prandtl number | 0.812 |
| Kinematic viscosity | $0.151e^{-5}$ $m^2/s$ |
| Unburned density | 1.175 kg/m3 |
| Burned density | 0.149 kg/m3 |
| Thermal diffusivity | $1.87e^{-5}$ $m^2/s$ |

The simulation is in 2 dimensions channel with x and y axes, the length of x-axis is in 2100 cm and y-axis is in 300 cm, which is consistent with experimental setup in Fig. 6.1.

The configuration of solid wall, cylindrical obstacles and ignition point are schematically shown in Fig. 6.3 below. In the simulation, both the solid walls and cylindrical obstacles are treated as non-slip reflecting solid. The solid wall is specifically configured to cover only the bottom of the channel, thereby simulating the ground as per the experimental setup. The Shell experimental rigs, enclosed by thin plastic sheets to contain the ethane-air mixture, experience rupture of these sheets upon ignition due to the combined effects of burning gases and overpressure. This simulation does not account for the impact of the plastic sheets on flame propagation, given their destruction as the flame approaches. The ethane-air mixture is set to be stationary and contained within the domain, while the boundaries at the top, left, and right sides are modeled as free. As shown in Fig. 6.4 the cylindrical obstacles are in uniformly 8x16 setup and each obstacle with radius of 7 cm. As shown in Fig. 6.4, the distance for each row is 35 cm and for reach column is 37 cm, the first row of obstacles is set with 25 cm from the top wall and the first column of obstacles is set with 100 cm from the left wall.

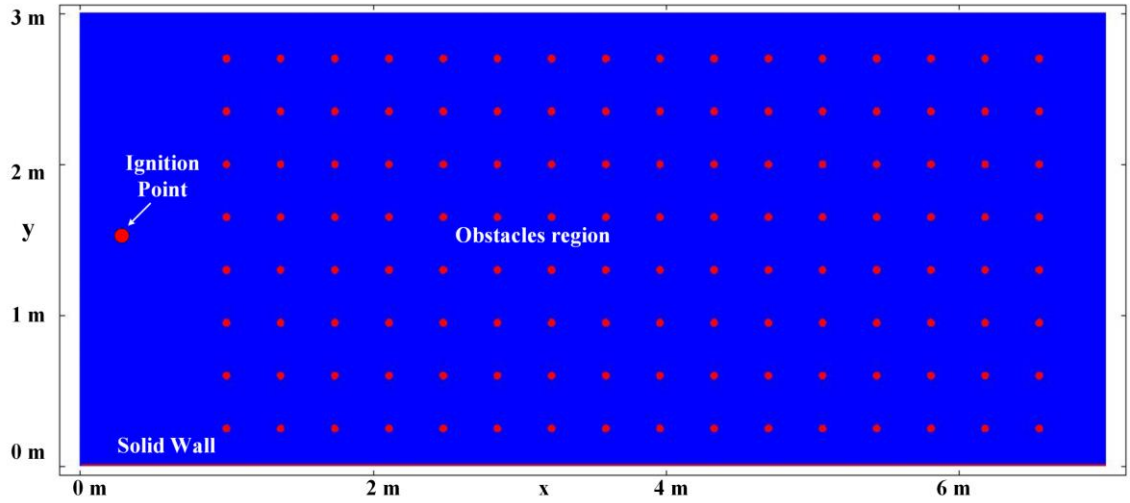


Figure 6.3. Schematic configuration of simulation setup: Solid wall, obstacles region and ignition point.

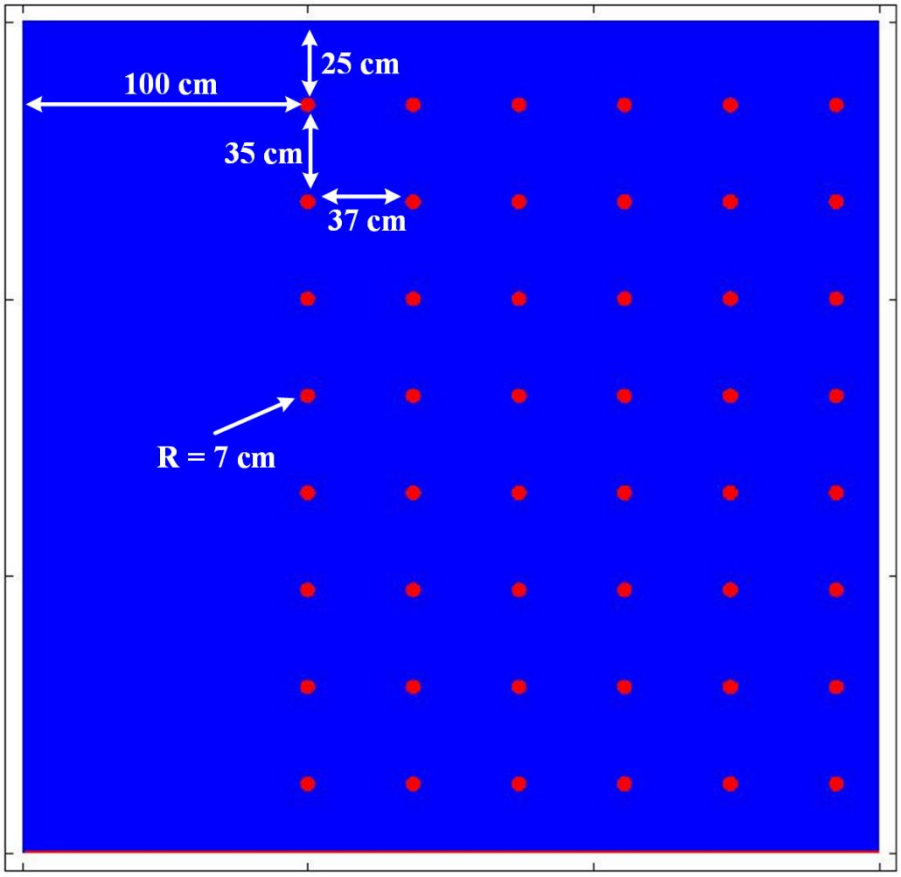


Figure 6.4. Location of obstacles in simulation setup.

This simulation employs AMR up to level 3 to enhance the resolution in the flame front area while preserving computational efficiency. The configurations for mesh levels 1, 2, and 3 in the burned region are contrasted in Fig. 6.5. In the level 1 mesh configuration, a cell size equivalent to 1 cm corresponds to the turbulent length scale being resolved by two cells. This equates to a total cell count of approximately 630,000 for the entire channel. The level 2 mesh resolution doubles the cell density, with a cell size of 0.5 cm. This results in at least four cells spanning the turbulent flame thickness and a total cell count of approximately 3,720,000. For the level 3 mesh, the highest resolution used in this study, the cell size decreases to 0.25 cm, corresponding to at least eight cells to solve the flame thickness to ensure the accurate of the simulation. Running the full simulation on a 40-cores Leeds ARC 4 cluster necessitated approximately 16000 CPU hours, demonstrating the computational intensity of the detailed simulation.

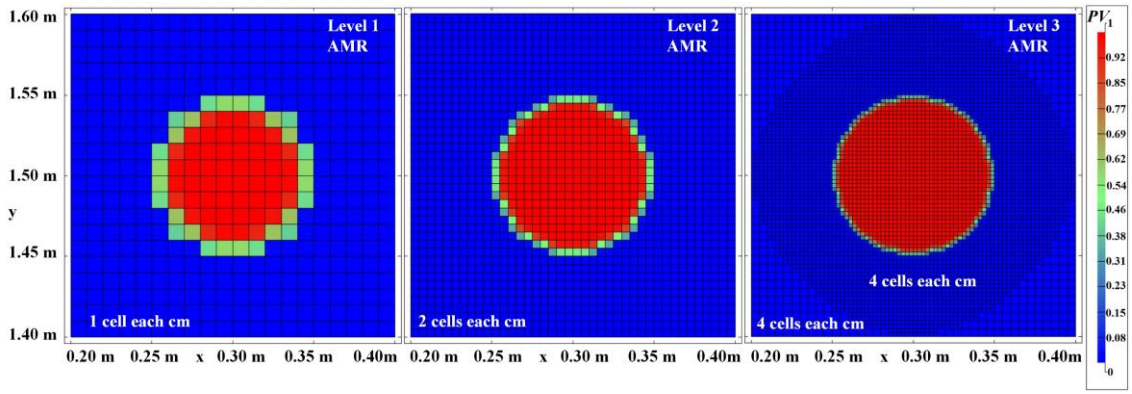


Figure 6.5. Comparison of level 1, 2 and 3 AMR computational domain showing the adaptive mesh refined for flame front.

## 6.3 Results and Discussions

### 6.3.1 Turbulent Flame Propagation

In the present study, the level 3 AMR is applied and the configuration of channel shown in Fig. 6.2 is used to simulate the flame propagation in the channel with obstacles. It is noticed that the length of the channel in this simulation is 21 m and the domain with length from 0 to 6 m is selected with the time sequences of reaction progress variable field crossing the obstacles region are shown in Fig. 6.6 where time representing the time after the ignition triggered. The red area represents the burned gases while the blue area represents the unburned gases. At the beginning a spherical laminar flame with 5 cm radius expands freely outwards, as shown at t = 20.4 ms. As the flame passes crossing the obstacles at t = 48.5 ms, the flame front starts to wrinkling and the propagation speed is accelerated due to the increasing flame front area and thus the turbulent burning velocity.

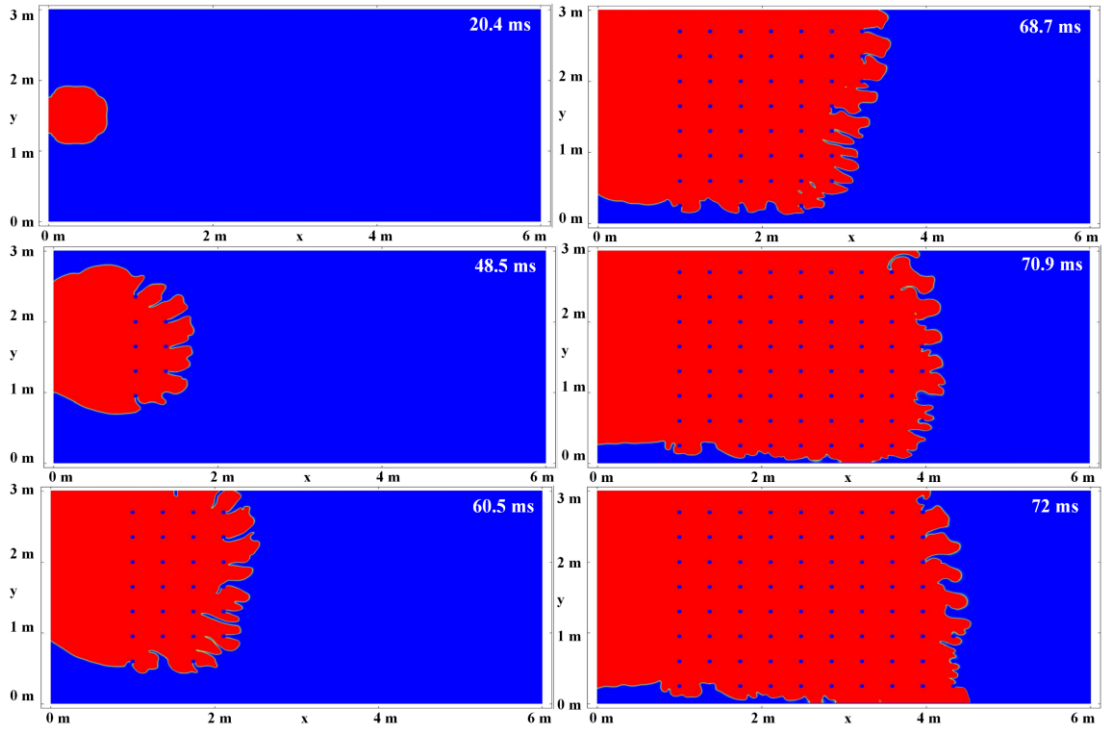


Figure 6.6. Time-sequence of progress variable filed (red burned gases, blue unburned gases) demonstrating the turbulent flame acceleration and its interaction with the cylindrical obstacle rows.

Figure 6.7 shows the flame front speed in relation to the flame front position (a), and both the flame front speed and position against with time (b). It is observed that during the initial phase of laminar flame propagation, the acceleration remains relatively slow, maintaining a low speed of approximately 30 m/s. This is explained by [217, 218] in the early flame acceleration stage of laminar flame in a channel mainly originates from the thermal expansion of hot products of combustion. Once the flame starts to entrain the obstacles region at position of 1 m, a rapid acceleration of the flame front speed is observed. This speed increases from 40 m/s to approximately 600 m/s at a position of 6.2 m, marking almost the end of the obstacle's region. DDT occurs when the flame reaches 7 meters, approximately 75 ms after ignition, and this phenomenon will be further discussed in Section 6.3.2. This observed acceleration of the flame through the obstacles within the channel aligns with the findings from experimental studies [15, 219] and simulation research [155-157].

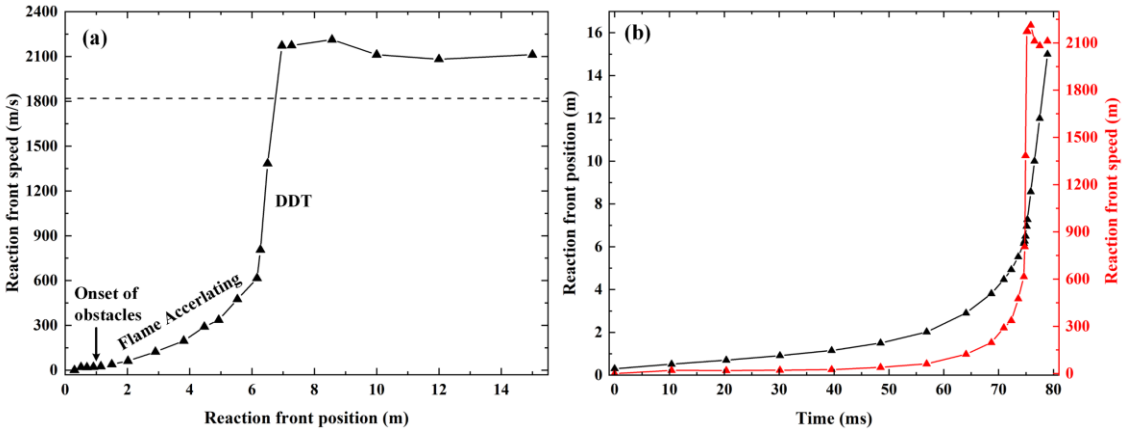


Figure 6.7. Reaction front speed as a function of reaction front position (a) and reaction front position/speed with time.

Figure 6.8 offers further insights into flame acceleration across obstacles by illustrating the temperature field (left column) and the turbulent kinetic energy field (right column) at t = 48.5, 68.7, and 70.9 ms. For the turbulent kinetic energy field, *k*, the scale ranges from 0 (represented in blue) to a maximum of 4245 $m^2/s^2$ (indicated in red). At t = 48.5 ms in Fig. 6.8, only a small red vortex area with which represents high value of *k* emerges exclusively around the obstacles situated ahead of flame. This localized turbulence is primarily generated due to the dynamic interaction between the flame front and the obstacles. As the flame continues propagating across the numerous obstacles, there is a conspicuous amplification in vortex characteristics, including an escalation in size, a proliferation in quantity, and a surge in strength, observable within the timeframe from t = 68.7 ms to t = 70.9 ms.

The generation of turbulent vortex ahead of flame play a key role in flame acceleration in the channel and this is supported with the numerical study of [1, 6, 16, 156] and experimental study of [220]. Sarli et al. [220] employed particle image velocimetry (PIV) techniques in the channel with baffles to examine the interaction between the flame and turbulent vortex. Their result showed that the turbulent vortex wrinkling the flame surface and accelerate the flame propagation speed. Bradley et al. [16] in the numerical study emphasized the role of turbulence accelerating the flame in the channel due to the increasing of turbulent burning velocity. In the present simulation, it is observed that the dynamic interaction between flame and obstacles accelerates the generation of turbulence

vortex with substantial turbulent kinetics energy. As the Eq. 6.1 suggests, an increase in turbulent kinetics energy results in a corresponding rise in $u'$, consequently boosting the value of $u_t$ and flame propagation speed. Such rising further enhance the interaction between the flame and obstacles, resulting in a greater quantity of turbulent vortices with heightened kinetic energy, thereby further increasing the value of $u_t$. This is the first feedback mechanism leading to the high flame speed.

The left column in Fig. 6.8 displays the temperature filed at t = 48.5, 68.7, and 70.9 ms with x axle domain from 0 to 6 m. To clearly illustrate the compression effects on the flow ahead of flame, the temperature scale is set from 300 K to 500 K. At t = 48.5 ms, the compression effects on the gas are minimal due to the low velocity of the gas in front of the flame, as evidenced by the temperature staying roughly 350 K ahead of the flame front. However, as the flame accelerating, the rising of gas velocity ahead of the flame enhances the compression effects. By t = 70.9 ms, these enhanced compression effects elevate the unburned gas temperature to around 450 K. This phenomenon serves as the second feedback mechanism that leads to high flame speed. As proposed by Bradley et al. [16], during flame acceleration, a shock wave forms ahead of the flame, compressing the unburned mixtures to higher temperature and pressure. As indicated by Eq. 6.1, increases in both temperature and pressure raise the value of $u_t$, consequently increasing the speed of flame propagation.

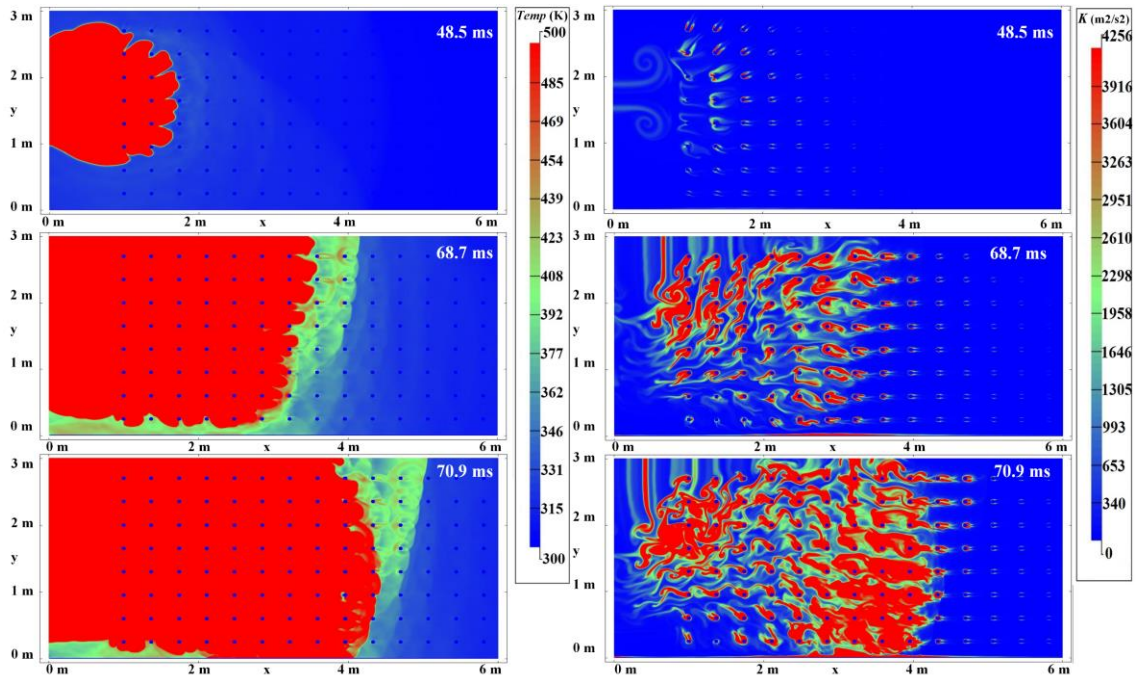


Figure 6.8. Time-sequence of temperature (left) and turbulent kinetic energy filed (right) as reaction wave crossing the obstacles region.

### 6.3.2 Deflagration to Detonation

In this simulation, the DDT was observed once the flame had exited the obstacle region. This phenomenon is evidenced through the measured parameters of density (left column), temperature (center column), and pressure (right column) recorded at timestamps of t = 74.9, 75.3, and 75.6 ms across the x-axis domain ranging from 6 to 9 meters in Fig. 6.9. At t = 74.9 ms, the strong shock wave is generated ahead of the reaction front. This wave proceeds to compress the unburned mixture to a maximum of 1250 K in temperature, 3 MPa in pressure, and a density of 12.9 kg/m$^3$, primarily around the lower column baffle. Under these conditions, autoignition could occur, leading to a transition to detonation. Subsequently, the occurrence of the DDT at t = 75.3 ms is evidenced by the coupling of the reaction front with the shock wave around the coordinates x = 7.3 m and y = 0.5 m. This coupling is indicated by an enhancement of temperature and pressure at the reaction front, serving as a primary indicator of DDT, as referenced in [221].

Combining the reaction front speed as a function of position (a) and time (b) in Fig. 6.7, from t = 74.9 to 75.3 ms, the reaction front speed rapidly rising from 750 m/s up to 2150 m/s beyond the Chapman-Jouguet (CJ) detonation speed. The successfully DDT is the

reaction front speed beyond the C-J detonation speed [10, 154, 156, 222]. Following this, a steady detonation wave is formed by t = 75.6 ms, as visualized in Fig. 6.9. This wave maintains a nearly consistent speed of around 2100 m/s as it propagating towards the right end of the channel. Moreover, the pressure profile traced ahead of the reaction front along the axle y = 1.5, as illustrated in Fig. 6.10, demonstrates the strength of shock wave. In the obstacle region, an incremental increase in pressure illustrates the developing strength of the shock wave. Simultaneously, a sudden surge to a peak value of 3.3 MPa in pressure corresponds with the occurrence of the DDT. Post this surge, the shock wave, in tandem with the detonation wave, sustains a steady pressure of around 3.3 MPa, indicative of steady-state detonation.

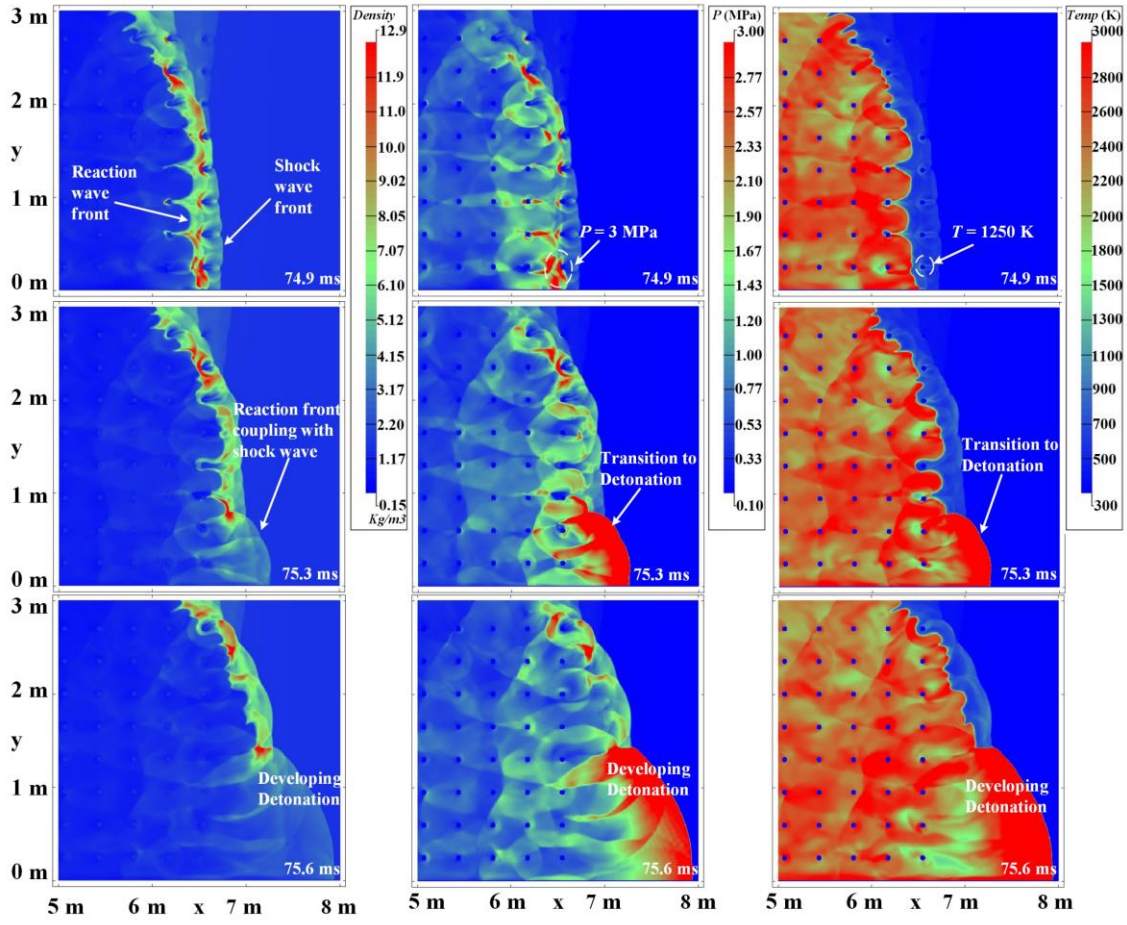


Figure 6.9. Time-sequence of density (left), pressure (mid) and temperature (right) filed showing the transition to detonation.

In this simulation, it is noteworthy that DDT occurs in a localized area near the bottom solid wall. This observation aligns with the findings of Oran et al. [1], which suggested

that DDT occurs when temperature and pressure reach sufficiently high levels in a localized area. Considering the conditions at t = 74.9 ms, both temperature and pressure seem adequately high to initiate the transition to detonation. Moreover, Bradley et al. [16] reported that the trigger for the transition to detonation is severe auto-ignition, occurring when a strong shock wave compresses the unburned mixtures into a state of severe auto-ignition. However, the current simulation is not equipped with the auto-ignition model. Instead, the Detonation Peninsula with two parameters characterized by two parameters, $\xi$ and $\varepsilon$ is implemented in Section 5.3.4. This framework allows for a mathematical analysis of whether the conditions at t = 74.9 ms could potentially trigger auto-ignition leading to detonation.

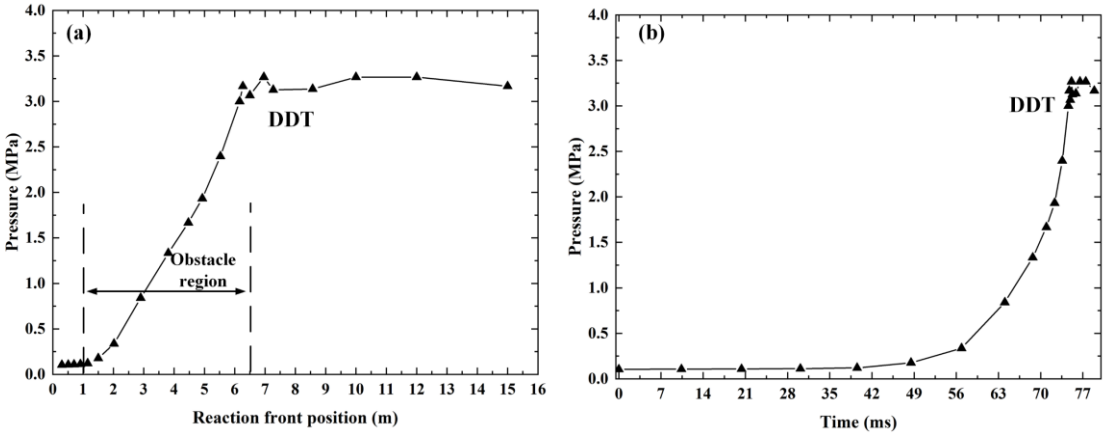


Figure 6.10. Reaction front pressure as a function of reaction front position (a) and time (b).

### 6.3.3 Mesh Refinement Test and Validated with Experimental Results.

This study conducted a numerical mesh resolution test, using three distinct grid resolution levels, to validate simulation accuracy and enhance computational efficiency. Fig. 6.11 (a) shows the reaction front speed histories for the flame propagating in the channel with three different level AMR resolutions. Within the obstacle region, level 1 AMR exhibits the highest propagation speed in comparison to other levels. As mesh resolution intensifies, a corresponding decrease and convergence in speed are observed. This tendency underscores the influence of mesh cell quantity in resolving flame thickness on flame propagation speed. A noteworthy increase in mesh resolution results in a decrease

and subsequent convergence in propagation speed. For the level 3 AMR, a minimum of 8 mesh cells are provided to resolve the integral length scale.

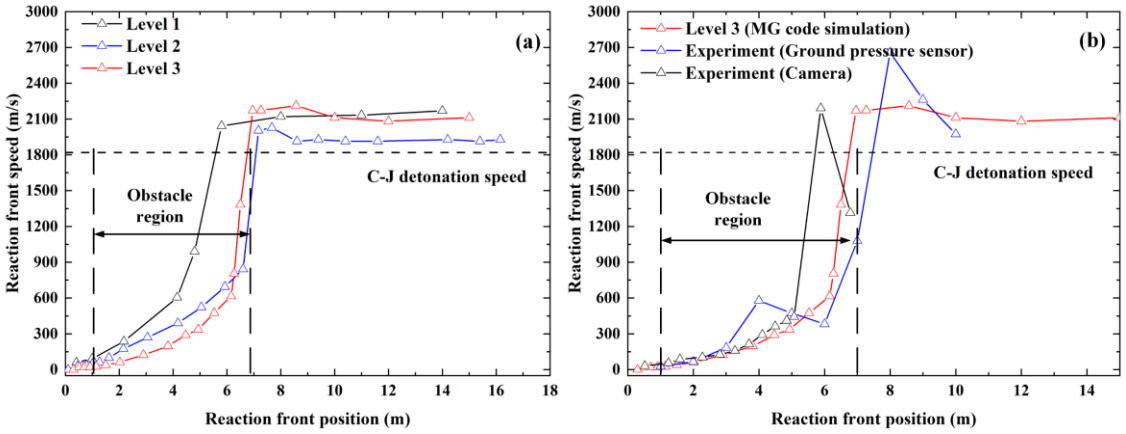


Figure 6.11. Reaction front speed against with reaction front position for level 1, 2 and 3 AMR (a) and simulation speed compared with the experimental speeds (b).

DDT occurred at varying x-axis positions across different AMR levels. Specifically, for Level 1 AMR, the reaction wave reached the x-axis position of 5.5 m, whereas for Levels 2 and 3 AMR, it occurred at 7 m. Following the DDT, all three AMR levels maintained a consistent detonation propagation speed, approximately around 2100 m/s. Although Level 4 AMR warrants further analysis, the computational capacity poses a significant limitation. To illustrate, the complete simulation at Level 3 AMR alone required 400 hours of runtime. Extrapolating from this, Level 4 AMR is estimated to necessitate around 1000 hours, a timeframe that is not feasible for completion within the scope of the current study. Figure 6.11 (b) compares the reaction front speed measured in study [21] with the reaction front speed from the Level 3 AMR simulation. The comparison involves the measured data gathered from both a high-speed camera and a pressure sensor, each compared with the simulation results. As the flame advances through the obstacle region, the simulation results display a reaction front speed that is similar to, but slightly lower than, the measured data. From the high-speed camera measurements, the transition to DDT takes place at an x-axis position of 6 m, reaching a maximum speed of 2100 m/s. This contrasts with the simulated DDT occurring at an x-axis position of 7 m, where it achieves a maximum speed of 2100 m/s. Overall, the reaction front propagation speed observed in

this simulation closely aligns and matches with the experimental data.

### 6.3.4 Detonation Peninsula, $\xi$ and $\varepsilon$ for Ethane-Air Mixtures

The study of Bradley et al. [16] reported that the transition to detonation occurs when a shock wave compresses the unburned mixture, triggering autoignition and if the autoignition is strong, it can develop into detonation. However, since the current version of the MG code does not include the autoignition model, it would be beneficial to implement the detonation peninsula to estimate at which temperature and pressure the DDT will occur and also help to ascertain whether the post-shock conditions depicted in Fig. 6.9 at t = 74.9 ms could trigger a detonation. The detailed explanation of $\xi$ and $\varepsilon$ can be found in Section 2.3.5 and for details on their implementation, refer to Section 4.3.4. The ethane oxidation kinetics embedded in the detailed AramcoMECH 1.3 [202] was employed here to calculate the ignition delay time, $\tau_i$, and excitation time, $\tau_e$ under closed homogeneous batch reactor conditions using the CHEMKIN-PRO software [194]. This kinetics has been validated using the ignition delay time of ethane-air mixtures from shock tube experiments conducted over a wide range of temperatures (833 - 2500 K), pressures (0.06 to 26 MPa), and equivalence ratios (0.06 to 6).

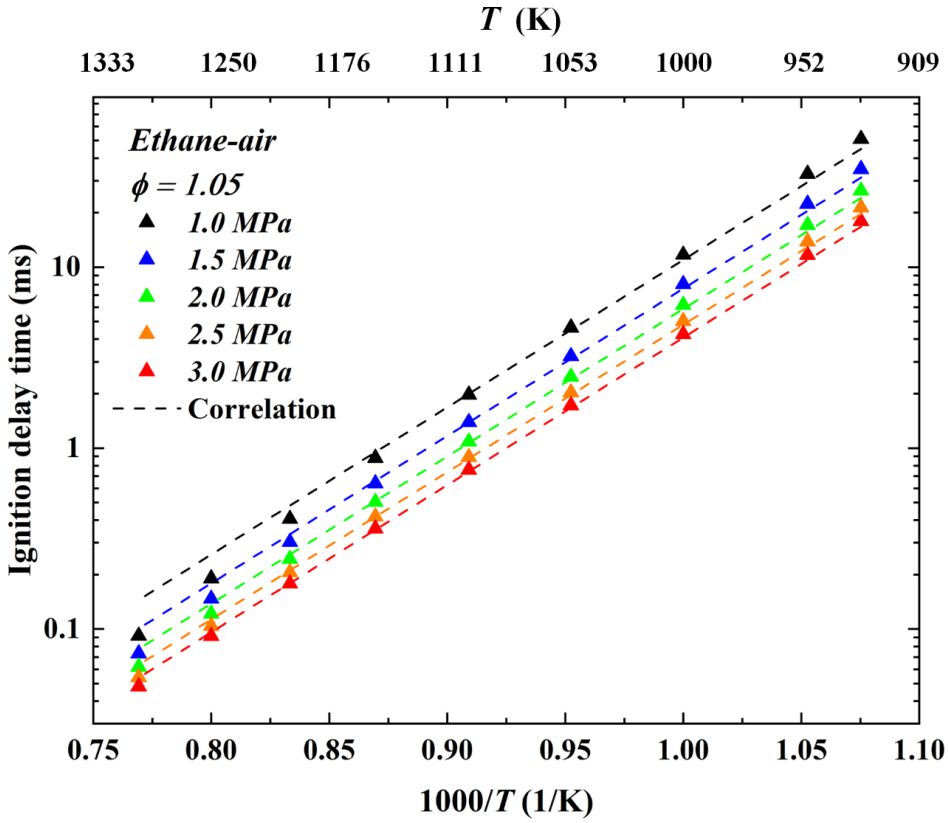


Figure 6.12. Chemical kinetic (symbols) and correlation values (dashed line) of ignition delay time for ethane-air with $\phi$=1.05 at pressure from 1.0 to 3.0 MPa.

The predicted $\tau_i$ and $\tau_e$ of ethane-air with $\phi$=1.05 as a function of the inverse temperature 1000/$T$, at pressure 1 - 3 MPa for ethane-air are presented in Fig. 6.12. A correlation of $\tau_i$ and $\tau_e$ for ethane-air as a function of $T$ and $P$ proposed by Kalghatgi et al. [46] is adopted here:

$$\tau_i, \tau_e = A \times e^{(B/T)} \times (P)^C. \quad (6.7)$$

Where, $\tau_i$ in ms, $\tau_e$ in $T$ is in K and $P$ is in MPa

The partial derivative of Eq. 17 with respect to temperature yields Eq.18:

$$\partial\tau_i/\partial T = B \times \tau_i/T^2, \quad (6.8)$$

In order to match the computed $\tau_i$ and $\tau_e$ in Fig. 6.12 & 6.13, the multiple-regression method is used to determine the constants A, B and C in Eqs. 6.7&6.8. For a thorough investigation of the impact of temperature and pressure on the transition of ethane-air to detonation in open space, the temperature and pressure scales extend up to 1300 K and 3 MPa, respectively.

Table 6.2. Constants A, B and C for $\tau_i$ and $\tau_e$ in ethane-air with $\phi$=1.05.

| | $\tau_i$ | $\tau_e$ |
|---|---|---|
| A | $7.8 \times 10^{-8}$ | 0.29 |
| B | 18740 | 3414 |
| C | -0.9 | -0.66 |

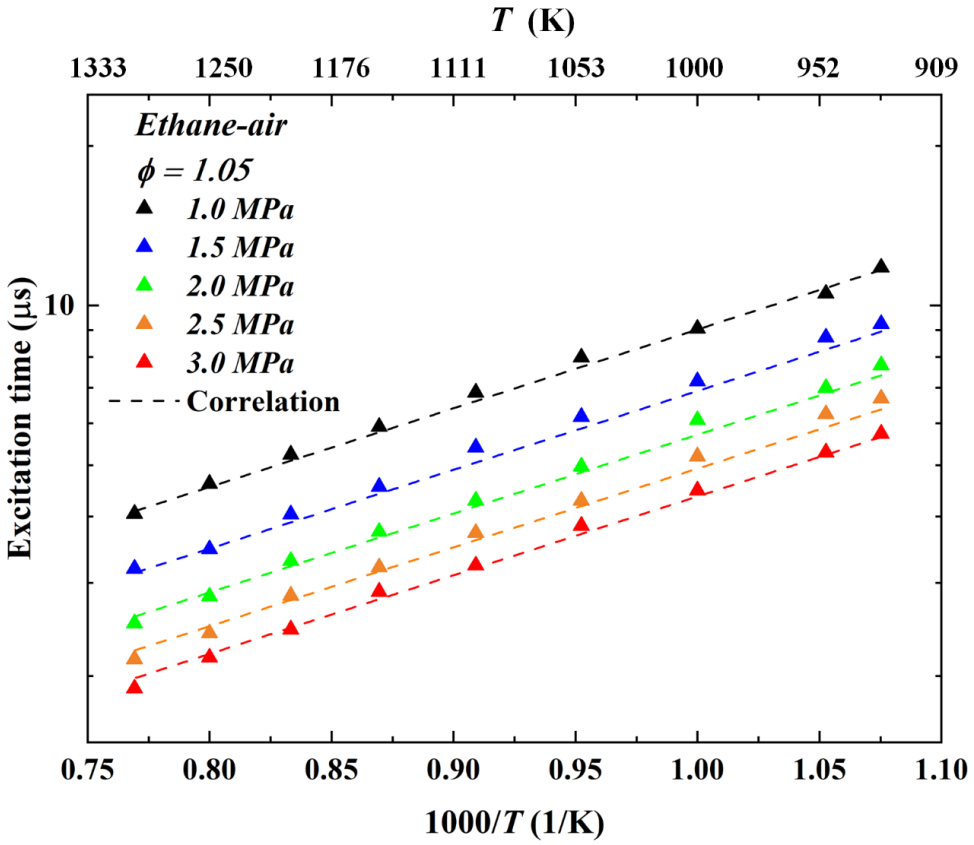


Figure 6.13. Chemical kinetic and correlation values of excitation time for ethane-air with $\phi$=1.05 at pressure from 1.0 to 3.0 MPa.

As seen in Fig. 6.14, the impacts of temperature (ranging from 930 to 1300 K) and pressure (varying between 1 and 3 MPa) on the values of $\xi$ and $\varepsilon$ are depicted. It is observed that temperature significantly influences the decline in $\xi$, while pressure dominates the increase in $\varepsilon$. Both increasing in temperature and pressure will lead to the decreasing $\xi$ of and increasing of $\varepsilon$ indicating the increasing heat release rate from hot spot. For an ethane-air mixture with $\phi$=1.05, the conditions for entering the detonation peninsula are marked by specific temperature and pressure thresholds. At 1 MPa, the

temperature required is 1250 K, while at higher pressures of 2 and 3 MPa, the temperature threshold decreases to 1200 K. This suggests an inverse relationship between pressure and the requisite temperature for entering the detonation peninsula: as pressure increases, the necessary temperature correspondingly decreases. The post-shock conditions represented in Fig. 6.9 at t = 74.9 ms, which correspond to a temperature of 1200 K and a pressure of 3 MPa, are located in the developing detonation regime. This suggests that under such conditions, the triggering of a detonation becomes feasible.

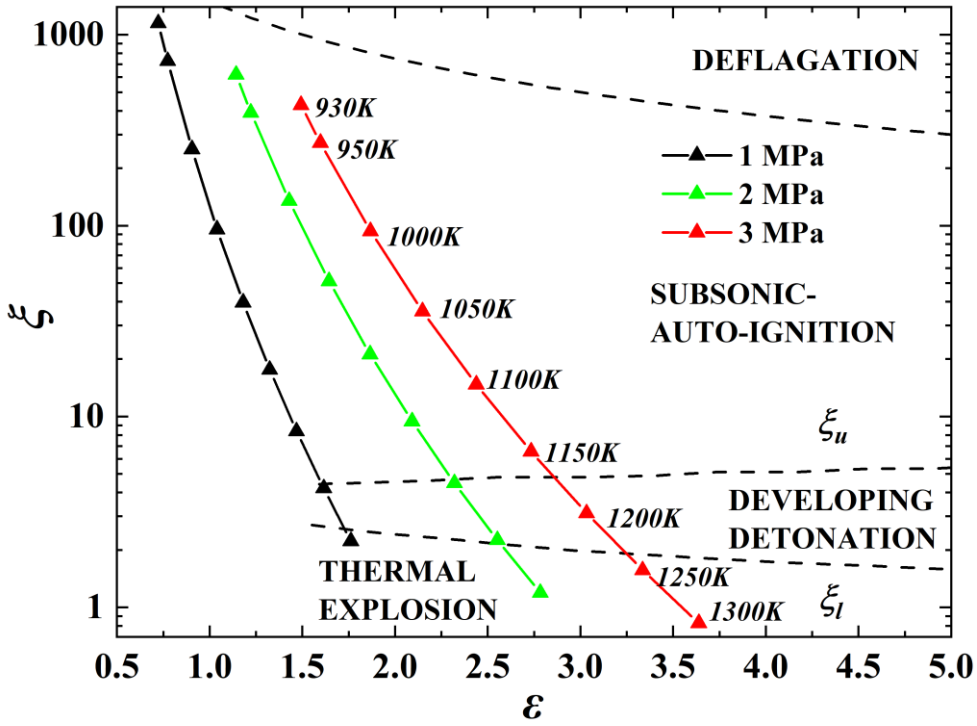


Figure 6.14. Detonation peninsulas $\xi$-$\varepsilon$ diagram for ethane-air with $\phi$=1.05 at pressure of 1, 2 and 3 MPa, temperature from 930 to 1300 K.

## 6.4 Conclusions

In this chapter, the development of a finite volume MG code has been presented, integrating both the reaction progress variable and the $k-\varepsilon$ turbulent model, along with a correlation for measured turbulent burning velocity. Using this framework, large-scale simulations of turbulent flame and DDT in ethane-air mixtures with $\phi$=1.05 were conducted and subsequently compared with experimental results. Overall, the entire simulation can be categorized into four distinct stages: (i) Prior to the flame entering the

obstacle region, laminar flame propagation is observed with speeds below 30 m/s. (ii) When the flame interacts with the obstacles, turbulence is generated, which wrinkles the flame front area. This increase in turbulent kinetic energy leads to an enhanced turbulent burning velocity, causing the flame propagation speed to rise from 30 m/s to 600 m/s. (iii) As the turbulent flame exits the obstacle region, a strong shock wave form ahead of it. This wave compresses the unburned mixtures, elevating their temperature and pressure, which results in a transition to detonation. Consequently, the speed surges from 600 m/s to 2100 m/s, surpassing the C-J detonation speed. (iv) Following this transition to detonation, a stable detonation wave establishes itself with a consistent propagation speed of 2100 m/s. It is observed that the simulated turbulent flame propagation speed is influenced by the level of AMR. Enhancing the AMR correspondingly decreased the turbulent flame speed, especially in the vicinity of the obstacle region.

The dimensionless $\xi$ and $\varepsilon$ diagram, in conjunction with Aramco MECH 1.3 chemical kinetics, was utilized to determine under which conditions (pressure ranging from 1 to 3 MPa, temperature spanning from 930 to 1300 K) DDT would transpire for ethane-air mixture with $\phi$=1.05. It is evident that the post-shock conditions in the current simulation, with a pressure of 3 MPa and temperature of 1250 K, are squarely within the detonation peninsula, signifying the occurrence of DDT. Looking ahead, future simulations will benefit from heightened mesh resolution to ensure results that are free from mesh resolution effects.

# 7. Conclusions and Future Research

## 7.1 Summary of Conclusions

### 7.1.1 Reaction Propagation Prior to Developing Detonation in a Rapid Compression Machine

- Pressures, reaction propagation speeds, and transitions to detonation of the stoichiometric mixture of *i*-octane-oxygen, with variable proportions of inert gases

has been studied in an optical RCM. The $T_c$ varying from 640 K to 930 K at constant pressure 2 MPa. Several propagation modes were observed: the laminar propagation was observed at the lowest compression temperature, $T_c$ = 640 K, a significant reaction propagation speed displayed characteristics of a slightly wrinkled laminar flame; A transition to the detonation occurred at $T_c$ =790 K, marked by a big amplitude of pressure oscillation.

- Upon entering the NTC regime, there is a significant increase in the measured propagation speed. At approximately $T_c$ = 740 K, the measured propagation speed attained a peak value of 323 m/s. This behaviour might be attributed to the speed being inversely proportional to $\frac{\partial \tau_i}{\partial T}$. Although in the NTC regime, the value of $\frac{\partial \tau_i}{\partial T}$ can significantly increase autoignitive speeds, it does not directly induce detonation.
- The transition to detonation was traced through the changes in $\xi$, the chemical kinetically derived $\varepsilon$, and the Detonation Peninsulas. The mixture entered the detonation peninsula occurred at $T_c$ =790 K, leading a mild detonation with $\xi$ = 2.4 and $\varepsilon$ = 3.5. The normalized amplitude of the pressure oscillations, $\Delta P/P$, shoed an increased correlated with a proposed Detonation Parameter, defined by ($\varepsilon/\xi$).
- The pressure traces and explosion image evolution indicate that the transition to detonation arises from a new AI spot ahead of the reaction wave. This is due to the compression effect of the reaction wave on the unburned gas situated at the cylinder wall's corner. The transition to detonation is following with super-knock with big amplitude of pressure oscillation.
- This chapter offers insights into the conditions under which the transition to detonation and super-knock occur in engine. The pressure oscillation diagram serves as a convenient tool for diagnosing ignition modes in engine conditions, based on the amplitude of pressure oscillations.

### 7.1.2 The Measurements of Laminar and Turbulent Characteristics of Ethane-Hydrogen-Air Mixtures

- The premixed laminar flames measurements of ethane-hydrogen-air mixtures, with

hydrogen concentrations ($X_{H_2}$ = 25%, 50%, 75% and 100%), were measured in a combustion vessel. The range of equivalence ratio varied from 0.7 to 1.3 and pressure from 0.1 MPa to 0.5 MPa, temperature from 300 K to 360 K.

- The measured laminar burning velocities of ethane-hydrogen-air in current study were compared with the predictions value from Aramco Mech 1.3 and USC Mech II chemical mechanisms showed agreement with measurements under temperature of 300 K. However, both mechanisms overpredicted the laminar burning velocity at an initial temperature of 360 K.
- The measured Markstein length of ethane-hydrogen-air decreases with the increasing pressure and $X_{H_2}$ primarily due to reductions in flame thickness and effective Lewis number, amplifying the effects of hydrodynamic and thermal-diffusivity instability.
- The measured critical $Pe_{cl}$ has been correlated with the $Ma_b$ across a range of mixtures, including hydrogen-air, ethane-hydrogen-air and methane-hydrogen-air to define the stable and unstable regime of flame propagation. This correlation reveals that flame stability tends to increase with the rise of $Ma_b$. Furthermore, it highlights that the addition of ethane to hydrogen effectively mitigates the inherent cellular instability, thereby extending the stable propagation regime compared to that of pure hydrogen.
- Turbulent ethane-air premixed flames were measured in a fan-stirred combustion vessel using high-speed schlieren photography to monitor flame development across equivalence ratios from 0.8 to 1.2, under test conditions of pressures (0.1 and 0.5 MPa), temperatures (300 and 360 K), and $u'$ values of 1, 3, and 5 m/s.
- The reference turbulent burning velocity, at the point where $r_{sch}$ = 30 mm, were selected to quantify the effects of equivalence ratio, temperature, pressure and $u'$ on turbulent burning velocities. The current measurements of ethane-air mixture demonstrate that $u'$ is the dominate factor influencing the turbulent burning velocity. Increases in temperature and pressure lead to a rise in turbulent flame speed.
- The non-dimensional parameters *U* and *K* demonstrate a strong correlation with the measured turbulent burning velocity of ethane-air, achieving an $R^2$ value of up to

0.97. These robust correlations provide a pivotal foundation for computational modelling and simulations concerning ethane explosions.

### 7.1.3 Turbulent Flame Acceleration and Deflagration to Detonation Transition in Ethane-Air Mixture Modelling

- A finite volume MG code, was developed, integrating the reaction progress variable, the $k-\varepsilon$ turbulent model, and a highly accurate correlation for the measured turbulent burning velocity. Leveraging this code, detailed simulations of turbulent flame and DDT in stoichiometric ethane-air mixtures were conducted, and the results were compared the Shell large-scale explosion experiment.
- In this simulation, the flame progression unfolds in four key phases: initially, before encountering obstacles, the flame shows laminar propagation with speeds under 20 m/s. As it interacts with obstacles, turbulence forms, wrinkling the flame and elevating speeds to 600 m/s. Upon exiting this region, a shock wave compresses unburned mixtures, escalating their temperature and pressure, and prompting a transition to detonation with speeds soaring to 2100 m/s. This detonative phase then stabilizes with a consistent speed of 2100 m/s.
- The turbulence plays a significant role in accelerating the flame burning velocity. Once it reaches a certain value, the flame front, coupled with acoustic waves, leads to DDT.
- Overall, the flame propagation speed and DDT observed in the current simulation align well with the findings from the Shell large-scale explosion experiment [21].
- Notably, the simulated turbulent flame propagation speed showed a pronounced sensitivity to the level of AMR. An increase in AMR level resulted in a decrease in the turbulent flame speed, especially in the obstacle region. This behaviour can potentially be attributed to the absence of a wall function and adequate boundary treatments.
- The dimensionless $\xi$ and $\varepsilon$, in conjunction with Aramco Mech 1.3 chemical kinetics, was utilized to determine theoretically under which conditions DDT would transpire for a stoichiometric ethane-air mixture. At 1 MPa, the detonation peninsula is entered

at 1250 K, at 2 MPa at 1200 K, and similarly at 3 MPa at 1200 K.

## 7.2 Recommendations for Future Research

### 7.2.1 The Temperature Gradient Along a Hot Spot

Referring to the Eq. 2.43, $u_a = \frac{\partial r}{\partial \tau_i} = \left(\frac{\partial r}{\partial T}\right)\left(\frac{\partial T}{\partial \tau_i}\right)$, both temperature gradient $\frac{\partial r}{\partial T}$ at the hot or cold spot and the gradient of ignition delay time with temperature $\frac{\partial T}{\partial \tau_i}$ play pivotal roles in accurately determining $u_a$. The modelling from chemical kinetics can predict precise value of $\frac{\partial T}{\partial \tau_i}$, as $\tau_i$ frequently serves as a primary metric constraining the error margins in chemical kinetics development. In Chapter 4 and 6, the gradient $\frac{\partial r}{\partial T}$ is given as either -2 K/mm or 2 K/mm in NTC regimes based on empirical assumptions. However, uncertainties associated with this gradient introduce challenges in accurately predicting both $u_a$ and DDT. Owing to the rapid propagation of autoignitive speed, along with variations in temperature, pressure, and hotspot reactivity, directly measuring $\frac{\partial r}{\partial T}$ experimentally is challenging.

Most recently, several simulations have explored the transient autoignition front propagation in a one-dimensional planar hot and cold spot [223-226]. However, these simulations often rely on the critical temperature gradient, which represents the gradient value where the hot spot interacts with the acoustic wave. Notably, such values have yet to be validated experimentally. Li et al. [223] highlighted the difficulties in applying chemical kinetics to predict DDT, especially with reduced mechanisms. Their study compared a detailed mechanism with two reduced mechanisms and found that, even if three mechanisms predicted ignition delays with similar values, each might yield considerably different critical temperature gradient values, crucial for modeling DDT.

In future research endeavors, the current optical RCM equipped with a high-speed camera can be updated to include the PIV technique, offering a more accurate measurement approach for determining the experimental $u_a$ Based on either directly measured values or accurately predicted ones for $\frac{\partial T}{\partial \tau_i}$, the temperature gradient $\frac{\partial r}{\partial T}$ can be indirectly

derived as $\frac{\partial r}{\partial T} = u_a / \left(\frac{\partial T}{\partial \tau_i}\right)$. Looking ahead, there is potential to expand the study by testing various fuels, such as *n*-heptane, Dimethyl Ether (DME), hydrogen, and ammonia, across a diverse range of temperatures, pressures, and within the NTC regime.

### 7.2.2 Boundary Layer Treatment of Turbulent Flame Propagation Simulation

In the large-scale turbulent flame propagation and DDT simulations presented in Chapter 6, the $k-\varepsilon$ model was implemented without a wall function. The boundary layer treatment for the current k-ε model primarily set the boundary condition on $k$, with the value in the first cell adjacent to a solid set to zero. This could potentially result in an overestimation of $k$, causing an acceleration in the turbulent flame propagation and an earlier transition to detonation.

While, the $k-\omega$ model offers a more accurate boundary treatment, where $k$ in the first cell next to a solid is set to zero and $\omega$ is expressed as $\omega = \frac{4\times10^4 v}{k^2}$. However, the $k-\omega$ is developed and and tested briefly towards the end of my PhD research. Due to time constraints and the computational cost of the simulations (estimated at 16,000 CPU hours), it was not feasible to implement the $k-\varepsilon$ model in the same setup as described in Chapter 6. Future research would benefit from the implementation of the k-ω model in tandem with a higher-resolution mesh. Comparing the results with those from the $k-\varepsilon$ model would elucidate the impact of the differing boundary treatments, providing a deeper understanding of turbulent flame propagation and DDT dynamics.

## References

[1] Oran, E. S., Chamberlain, G. and Pekalski, A. Mechanisms and occurrence of detonations in vapor cloud explosions. *Progress in energy and combustion science*. 2020, **77**, article no:100804.

[2] Zhen, X., Wang, Y., Xu, S., Zhu, Y., Tao, C., Xu, T. and Song, M. The engine knock analysis - An overview. *Applied Energy*, 2012, **92**, pp.628-636.

[3] Schwantes, J. M., Orton, C. R. and Clark, R. A. Analysis of a nuclear accident: fission

and activation product releases from the Fukushima Daiichi nuclear facility as remote indicators of source identification, extent of release, and state of damaged spent nuclear fuel. *Environmental science & technology*. 2012, **46**(16), pp.8621-8627.

[4] Kuznetsov, M., Yanez, J., Grune, J., Friedrich, A. and Jordan, T. Hydrogen combustion in a flat semi-confined layer with respect to the Fukushima Daiichi accident. *Nuclear Engineering and Design*. 2015, **286**, pp.36-48.

[5] Cheaito, M. A. and Al-Hajj, S. A brief report on the Beirut port explosion. *Mediterranean Journal of Emergency Medicine & Acute Care*. 2020, **1**(4).

[6] Oran, E. S. and Gamezo, V. N. Origins of the deflagration-to-detonation transition in gas-phase combustion. *Combustion and flame*. 2020, **148**(1-2), pp.4-47.

[7] Brown, S. (2020, August). *Beirut explosion: Huge blast in Lebanon leaves people 'covered in blood and glass' - video*. [Online]. 2020. [Accessed 10 September 2023]. Available from: https://www.express.co.uk/news/world/1318594/beirut-explosion-lebanon-latest-update-video

[8] Liss, W. E., Thrasher, W. H., Steinmetz, G. F., Chowdiah, P. and Attari, A. Variability of natural gas composition in select major metropolitan areas of the United States. final report, august 1990-february 1992. American Gas Association Labs., Cleveland, OH (United States), 1992.

[9] Young, J. U.S. ethane production established a new record in April 2023. 2023. [Accessed 09 September 2023]. Available from: https://www.eia.gov/todayinenergy/detail.php?id=60362.

[10] Brelsford, R. Shell commissions Pennsylvania petrochemical complex. 2022. [Accessed 10 September 2023]. Available from: https://www.ogj.com/refining-processing/petrochemicals/article/14285782/shell-commissions-pennsylvania-petrochemical-complex.

[11] Gassner, G., Cenini, P. and Ulstein, K. “World’s first ethane-powered marine vessels”, Wartsila, 20 September 2016. [Online]. Available: https://www.wartsila.com/insights/article/worlds-first-ethane-powered-marine-vessels. [Accessed 17 December 2023].

[12] Kobashi, Y., Hirako, S., Matsumoto, A. and Naganuma, K. Flash boiling spray of diesel fuel mixed with ethane and its effects on premixed diesel combustion. *Fuel*, 2019, **237**, pp.686-693.

[13] Ahmad, Z. Kaario, O. Cheng, Q and Larmi, M. Impact of ethane enrichment on diesel-methane dual-fuel combustion. *SAE Technical Paper*. 2020, pp.2020-01-0305.

[14] Ahmad, Z. Kaario, O. Karimkashi, S. Qiang, C. Vuorinen, V. and Larmi, M. Effects of ethane addition on diesel-methane dual-fuel combustion in a heavy-duty engine. *Fuel*. 2021, **289**, pp.119834.

[15] Sierens, R. and Rosseel, E. Variable composition hydrogen/natural gas mixtures for increased engine efficiency and decreased emissions. *Journal of Engineering for Gas Turbines and Power*. 2000, **122**(1), pp.135-140.

[16] Bradley, D., Lawes, M. and Liu, K. Turbulent flame speeds in ducts and the deflagration/detonation transition. *Combustion and flame*. 2008, **154**(1-2), pp.96-108.

[17] Ciccarelli, G. and Dorofeev, S. Flame acceleration and transition to detonation in ducts. *Progress in energy and combustion science*. 2008, **34**(4), pp.499-550.

[18] Oran, E. S., Gamezo, V. N. and Zipf Jr, R. K. Large-scale experiments and absolute detonability of methane/air mixtures. *Combustion Science and Technology*. 2015, **187**(1-2), pp.324-341.

[19] Bates, L., Bradley, D., Paczko, G. and Peters, N. Engine hot spots: Modes of auto-ignition and reaction propagation. *Combustion and Flame*. 2016, **166**, pp.80-85.

[20] Bates, L. and Bradley, D. Deflagrative, auto-ignitive, and detonative propagation regimes in engines. *Combustion and Flame*. 2017, **175**, pp.118-122.

[21] Pekalski, A., Puttock, J. and Chynoweth, S. Deflagration to detonation transition in a vapour cloud explosion in open but congested space: Large scale test. *Journal of Loss Prevention in the Process Industries*. 2015, **36**, pp.365-370.

[22] Bradley, D., Gaskell, P. H. and Gu, X. J. Burning velocities, Markstein lengths, and flame quenching for spherical methane-air flames: a computational study. *Combustion and flame*. 1996, **104**(1-2), pp.176-198.

[23] Correa, S. M. A review of NOx formation under gas-turbine combustion conditions.

*Combustion science and technology*. 1993, **87**(1-6), pp.329-362.

[24] Flamme, M. New combustion systems for gas turbines (NGT). *Applied Thermal Engineering*. 2004, **24**(11-12), pp.1551-1559.

[25] Wang, H. and Sheen, D. A. Combustion kinetic model uncertainty quantification, propagation and minimization. *Progress in Energy and Combustion Science*. 2015, **47**, pp.1-31.

[26] Law, C. K. *Combustion physics*. Cambridge: Cambridge university press, 2010.

[27] Wu, F., Liang, W., Chen, Z., Ju, Y. and Law, C. K. Uncertainty in stretch extrapolation of laminar flame speed from expanding spherical flames. *Proceedings of the Combustion Institute*. 2015, **35**(1), pp.663-670.

[28] Dowdy, D. R., Smith, D. B., Taylor, S. C. and Williams, A. The use of expanding spherical flames to determine burning velocities and stretch effects in hydrogen/air mixtures. *Symposium (International) on Combustion*. 1991, **23**(1) pp. 325-332.

[29] Mishra, D. P., Paul, P. J. and Mukunda, H. S. Stretch effects extracted from inwardly and outwardly propagating spherical premixed flames. *Combustion and flame*. 1994, **97**(1), pp.35-47.

[30] Qin, X. and Ju, Y. Measurements of burning velocities of dimethyl ether and air premixed flames at elevated pressures. *Proceedings of the Combustion Institute*. 2005, **30**(1), pp.233-240.

[31] Bonhomme, A., Selle, L. and Poinsot, T. Curvature and confinement effects for flame speed measurements in laminar spherical and cylindrical flames. *Combustion and Flame*. 2013, **160**(7), pp.1208-1214.

[32] Kee, R. J., Miller, J. A., Evans, G. H. and Dixon-Lewis, G. A computational model of the structure and extinction of strained, opposed flow, premixed methane-air flames. *Symposium (International) on Combustion*. 1989, **22**(1), pp.1479-1494.

[33] Wang, Y. L., Holley, A. T., Ji, C., Egolfopoulos, F. N., Tsotsis, T. T. and Curran, H. J. Propagation and extinction of premixed dimethyl-ether/air flames. *Proceedings of the Combustion Institute*. 2009, **32**(1), pp.1035-1042.

[34] Veloo, P. S., Wang, Y. L., Egolfopoulos, F. N. and Westbrook, C. K. A comparative

experimental and computational study of methanol, ethanol, and n-butanol flames. *Combustion and Flame*. 2010, **157**(10), pp.1989-2004.

[35] Ji, C., Wang, Y. L. and Egolfopoulos, F. N. Flame studies of conventional and alternative jet fuels. *Journal of Propulsion and Power*. 2011, **27**(4), pp.856-863.

[36] Van Maaren, A. and De Goey, L. P. H. Laser Doppler thermometry in flat flames. *Combustion Science and Technology*. 1994, **99**(1-3), pp.105-118.

[37] Bosschaart, K. J. and De Goey, L. P. H. The laminar burning velocity of flames propagating in mixtures of hydrocarbons and air measured with the heat flux method. *Combustion and Flame*. 2004, **136**(3), pp.261-269.

[38] Goswami, M., Derks, S. C., Coumans, K., Slikker, W. J., de Andrade Oliveira, M. H., Bastiaans, R. J., Luijten, C.C.M., de Goey, L.P.H. and Konnov, A. A. The effect of elevated pressures on the laminar burning velocity of methane+ air mixtures. *Combustion and Flame*. 2013, **160**(9), pp. 1627-1635.

[39] Goswami, M., Van Griensven, J. G. H., Bastiaans, R. J. M., Konnov, A. A. and De Goey, L. P. H. Experimental and modeling study of the effect of elevated pressure on lean high-hydrogen syngas flames. *Proceedings of the Combustion Institute*. 2015, **35**(1), pp.655-662.

[40] Griffiths, J.F. and Barnard, J.A. *Flame and combustion*. 3rd ed. London: CRC Press, 1995.

[41] Göttgens, J., Mauss, F. and Peters, N. Analytic approximations of burning velocities and flame thicknesses of lean hydrogen, methane, ethylene, ethane, acetylene, and propane flames. *Symposium (International) on Combustion*. 1992, **24**(01) pp.129-135.

[42] Clavin, P. Dynamic behavior of premixed flame fronts in laminar and turbulent flows. *Progress in energy and combustion science*. 1985, **11**(1), pp.1-59.

[43] Abdel-Gayed, R. G., Bradley, D., & Lung, F. K. Combustion regimes and the straining of turbulent premixed flames. *Combustion and Flame*. 1989, **76**(2), pp.213-218.

[44] Bradley, D., Hicks, R. A., Lawes, M., Sheppard, C. G. and Woolley, R. The measurement of laminar burning velocities and Markstein numbers for iso-octane–air and iso-octane–n-heptane–air mixtures at elevated temperatures and pressures in an explosion

bomb. *Combustion and flame*. 1998, **115**(1-2), pp.126-144.

[45] Jomaas, G., Law, C. K. and Bechtold, J. K. On transition to cellularity in expanding spherical flames. *Journal of Fluid Mechanics*. 2007, **583**, pp.1-26.

[46] Bradley, D., Lawes, M., Liu, K., Verhelst, S. and Woolley, R. Laminar burning velocities of lean hydrogen–air mixtures at pressures up to 1.0 MPa. *Combustion and Flame*. 2007, **149**(1-2), pp.162-172.

[47] Li, H., Xiao, H. and Sun, J. Laminar burning velocity, Markstein length, and cellular instability of spherically propagating NH3/H2/Air premixed flames at moderate pressures. *Combustion and Flame*. 2022, **241**, article no:112079.

[48] Morley, C. *GasEq: a chemical equilibrium program for windows*. [Software]. 2005. [Accessed 20 June 2020].

[49] Gu, X. J., Haq, M. Z., Lawes, M. and Woolley, R. Laminar burning velocity and Markstein lengths of methane–air mixtures. *Combustion and Flame*. 2000, **121**(1-2), pp.41-58.

[50] Williams, F. A. Combustion Theory. 2nd ed. California: Addison-Wesley, 1985.

[51] Candel, S. M. and Poinsot, T. J. Flame stretch and the balance equation for the flame area. *Combustion Science and Technology*. 1990, **70**(1-3), pp.1-15.

[52] Konnov, A. A., Mohammad, A., Kishore, V. R., Kim, N. I., Prathap, C. and Kumar, S. A comprehensive review of measurements and data analysis of laminar burning velocities for various fuel + air mixtures. *Progress in Energy and Combustion Science*. 2018, **68**, pp.197-267.

[53] Hu, E., Huang, Z., He, J., Jin, C. and Zheng, J. Experimental and numerical study on laminar burning characteristics of premixed methane–hydrogen–air flames. *international journal of hydrogen energy*. 2009, **34**(11), pp.4876-4888.

[54] Verhelst, S., Woolley, R., Lawes, M. and Sierens, R. Laminar and unstable burning velocities and Markstein lengths of hydrogen–air mixtures at engine-like conditions. *Proceedings of the Combustion Institute*. 2005, **30**(1), pp.209-216.

[55] Xie, Y., Morsy, M. E., Li, J. and Yang, J. Intrinsic cellular instabilities of hydrogen laminar outwardly propagating spherical flames. *Fuel*. 2022, **327**, article no:125149.

[56] Takizawa, K., Takahashi, A., Tokuhashi, K., Kondo, S. and Sekiya, A. Burning velocity measurement of fluorinated compounds by the spherical-vessel method. *Combustion and Flame*. 2005, **141**(3), pp.298-307.

[57] Halter, F., Chauveau, C., Djebaïli-Chaumeix, N. and Gökalp, I. Characterization of the effects of pressure and hydrogen concentration on laminar burning velocities of methane–hydrogen–air mixtures. *Proceedings of the Combustion Institute*. 2005, **30**(1), pp. 201-208.

[58] Lowry, W., de Vries, J., Krejci, M., Petersen, E., Serinyel, Z., Metcalfe, W., Curran, H and Bourque, G. Laminar flame speed measurements and modeling of pure alkanes and alkane blends at elevated pressures. *Journal of Engineering for Gas Turbines and Power*. 2011, **133**(9), article no: 091501.

[59] Mitu, M., Razus, D., Giurcan, V. and Oancea, D. Normal burning velocity and propagation speed of ethane–air: Pressure and temperature dependence. *Fuel*. 2015, **147**, pp.27-34.

[60] Nilsson, E. J., van Sprang, A., Larfeldt, J. and Konnov, A. A. The comparative and combined effects of hydrogen addition on the laminar burning velocities of methane and its blends with ethane and propane. *Fuel*. 2017, **189**, pp.369-376.

[61] Goswami, M., Bastiaans, R. J. M., De Goey, L. P. H. and Konnov, A. A. Experimental and modelling study of the effect of elevated pressure on ethane and propane flames. *Fuel*. 2016, **166**, pp.410-418.

[62] Ravi, S., Sikes, T. G., Morones, A., Keesee, C. L. and Petersen, E. L. Comparative study on the laminar flame speed enhancement of methane with ethane and ethylene addition. *Proceedings of the Combustion Institute*. 2015, **35**(1), pp.679-686.

[63] Zuo, Z., Hu, B., Bao, X., Zhang, S., Fan, L., Deng, L., Xu, Y., Pan, S. and Wu, Y. Self-acceleration characteristics of premixed C1-C3 alkanes-air mixtures in a constant-volume chamber. *Fuel Processing Technology*. 2022, **231**, article no:107252.

[64] Zuo, Z., Hu, B., Bao, X., Zhang, S., Kong, L., Deng, L., Xu, Y., Zhu, Z. and Pan, S. Quantitative research on cellular instabilities of premixed C1–C3 alkane–air mixtures using spherically expanding flames. *Fuel Processing Technology*. 2022, **226**, article

no:107075.

[65] Hassan, M. I., Aung, K. T., Kwon, O. C. and Faeth, G. M. Properties of laminar premixed hydrocarbon/air flames at various pressures. *Journal of Propulsion and Power*. 1998, **14**(4), pp.479-488.

[66] Jomaas, G., Zheng, X. L., Zhu, D. L. and Law, C. K. Experimental determination of counterflow ignition temperatures and laminar flame speeds of C2–C3 hydrocarbons at atmospheric and elevated pressures. *Proceedings of the Combustion Institute*. 2005, **30**(1), pp.193-200.

[67] Kelley, A. P. and Law, C. K. Nonlinear effects in the extraction of laminar flame speeds from expanding spherical flames. *Combustion and Flame*. 2009, **156**(9), pp.1844-1851.

[68] Kim, W., Sato, Y., Johzaki, T., Endo, T., Shimokuri, D. and Miyoshi, A. Experimental study on self-acceleration in expanding spherical hydrogen-air flames. *International Journal of Hydrogen Energy*. 2018, **43**(27), pp.12556-12564.

[69] Darrieus, G. J. L. T. M. Propagation d'un front de flamme. *La Technique Moderne*. 1938, **30**, article no:18.

[70] Landau, L. On the theory of slow combustion. In Dynamics of curved fronts. Academic Press, 1988, pp. 403-411.

[71] Searby, G. Experimental studies of instabilities of laminar premixed flames. *International Conference on Combustion and Detonation, Zel'dovich Memorial II*, 2004, Russia.

[72] Bradley, D. and Harper, C. M. The development of instabilities in laminar explosion flames. *Combustion and Flame*. 1994, **99(**3-4), pp.562-572.

[73] Mallard, E. and H. Le Chatelier, Combustion of explosive gas mixtures. Ann. mines, 1883, **8**, pp. 274.

[74] Damköhler, G. Der einfluss der turbulenz auf die flammengeschwindigkeit in gasgemischen. Zeitschrift für Elektrochemie und angewandte physikalische Chemie. 1940, **46**(11), pp.601-626.

[75] Goulier, J., Comandini, A., Halter, F. and Chaumeix, N. Experimental study on

turbulent expanding flames of lean hydrogen/air mixtures. *Proceedings of the Combustion Institute*. 2017, **36**(2), pp.2823-2832.

[76] Kitagawa, T., Nakahara, T., Maruyama, K., Kado, K., Hayakawa, A. and Kobayashi, S. Turbulent burning velocity of hydrogen–air premixed propagating flames at elevated pressures. *International Journal of Hydrogen Energy*. 2008, **33**(20), pp.5842-5849.

[77] Goulier, J., Chaumeix, N., Halter, F., Meynet, N. and Bentaïb, A. Experimental study of laminar and turbulent flame speed of a spherical flame in a fan-stirred closed vessel for hydrogen safety application. *Nuclear Engineering and Design*. 2017, **312**, pp.214-227.

[78] Burluka, A. A., Gaughan, R. G., Griffiths, J. F., Mandilas, C., Sheppard, C. G. W., and Woolley, R. Experimental observations on the influence of hydrogen atoms diffusion on laminar and turbulent premixed burning velocities. *Fuel*. 2017, **189**, pp.66-78.

[79] Lawes, M., Ormsby, M. P., Sheppard, C. G. W. and Woolley, R. Variation of turbulent burning rate of methane, methanol, and iso-octane air mixtures with equivalence ratio at elevated pressure. *Combustion Science and Technology*. 2005, **177**(7), pp.1273-1289.

[80] Fairweather, M., Ormsby, M. P., Sheppard, C. G. W. and Woolley, R. Turbulent burning rates of methane and methane–hydrogen mixtures. *Combustion and Flame*. 2009, **156**(4), pp.780-790.

[81] Mandilas, C., Ormsby, M. P., Sheppard, C. G. W. and Woolley, R. Effects of hydrogen addition on laminar and turbulent premixed methane and iso-octane–air flames. *Proceedings of the combustion institute*. 2007, **31**(1), pp.1443-1450.

[82] Lawes, M., Ormsby, M. P., Sheppard, C. G. and Woolley, R. The turbulent burning velocity of iso-octane/air mixtures. *Combustion and Flame*. 2012, **159**(5), pp.1949-1959.

[83] Bradley, D., Lawes, M. and Mansour, M. S. Correlation of turbulent burning velocities of ethanol–air, measured in a fan-stirred bomb up to 1.2 MPa. *Combustion and Flame*. 2011, **158**(1), pp.123-138.

[84] Wang, S., Elbaz, A. M., Arab, O. Z. and Roberts, W. L. Turbulent flame speed measurement of NH3/H2/air and CH4/air flames and a numerical case study of NO emission in a constant volume combustion chamber (CVCC). *Fuel*. 2023, **332**, article no:126152.

[85] Tennekes, H. and Lumley, J. A First Course In Turbulence. Massachusetts: MIT Press Design Department, 1972.

[86] Yang, J. *Turbulent Combustion (Laser-based Measurement)*. MATH5453M Foundations of Fluids. University of Leeds, 2019.

[87] Chorin, A. J. *Vorticity and turbulence*. New York: Springer Science & Business Media, 2013.

[88] Turns, S. R. *Introduction to combustion*. New York: McGraw-Hill Companies, 1996.

[89] McComb, W. *The Physics of Fluid Turbulence*. Oxford: Oxford University Press, 1990.

[90] Hjertager, B. *Turbulence theory and modelling*. Lecture notes. University of Stavanger, Stavanger, July 2014.

[91] Gülder, Ö. L. Turbulent premixed flame propagation models for different combustion regimes. *Symposium (International) on Combustion*. 1991, **23**(01), pp.743-750

[92] Abdel-Gayed, R. G., Bradley, D. and Lung, F. K. Combustion regimes and the straining of turbulent premixed flames. *Combustion and Flame*. 1989, **76**(2), pp.213-218.

[93] Borghi, R. and Escudie, D. Assessment of a theoretical model of turbulent combustion by comparison with a simple experiment. *Combustion and flame*. 1984, **56**(2), pp.149-164.

[94] Peters, N. Laminar flamelet concepts in turbulent combustion. *Symposium (International) on Combustion*. 1988, **21**(01), pp.1231-1250.

[95] Poinsot, T., Veynante, D. and Candel, S. Quenching processes and premixed turbulent combustion diagrams. *Journal of Fluid Mechanics*. 1991, **228**, pp.561-606.

[96] Borghi, R. On the structure and morphology of turbulent premixed flames. In: Corrado, C. ed. *Recent Advances in the Aerospace Sciences: In Honor of Luigi Crocco on His Seventy-fifth Birthday. Boston:* Springer, 1985, pp.117-138.

[97] Peters, N. Turbulent combustion. *Measurement Science and Technology*. 2001, **12**(11), pp.2022-2022.

[98] Bradley, D., Haq, M. Z., Hicks, R. A., Kitagawa, T., Lawes, M., Sheppard, C. G. W. and Woolley, R. Turbulent burning velocity, burned gas distribution, and associated flame

surface definition. *Combustion and Flame*. 2003, **133**(4), pp.415-430.

[99] Gillespie, L., Lawes, M., Sheppard, C. G. W. and Woolley, R. Aspects of laminar and turbulent burning velocity relevant to SI engines. *SAE transactions*. 2000, **109**(3), pp.13-33.

[100] Filatyev, S. A., Driscoll, J. F., Carter, C. D. and Donbar, J. M. Measured properties of turbulent premixed flames for model assessment, including burning velocities, stretch rates, and surface densities. *Combustion and Flame*. 2005, **141**(1-2), pp.1-21.

[101] Lawn, C. J. and Schefer, R. W. Scaling of premixed turbulent flames in the corrugated regime. *Combustion and Flame*. 2006, **146**(1-2), pp.180-199.

[102] Abdel-Gayed, R. G., Bradley, D., & Lawes, M. Turbulent burning velocities: a general correlation in terms of straining rates. *Proceedings of the Royal Society of London. Series A: Mathematical and Physical Sciences*. 1987, **414**(1847), pp.389-413.

[103] Bradley, D., Lawes, M. and Mansour, M. S. Flame surface densities during spherical turbulent flame explosions. *Proceedings of the Combustion Institute*. 2009, **32**(1), pp.1587-1593.

[104] Kobayashi, H., Kawabata, Y. and Maruta, K. Experimental study on general correlation of turbulent burning velocity at high pressure. Symposium (International) on Combustion. 1998, **27**(1), pp. 941-948.

[105] Clavin, P. and Williams, F. A. Theory of premixed-flame propagation in large-scale turbulence. *Journal of Fluid Mechanics*. 1979, **90**(3), pp.589-604.

[106] Bray, K. N. C. Studies of the turbulent burning velocity. *Proceedings of the Royal Society of London. Series A: Mathematical and Physical Sciences*. 1990, **431**(1882), pp.315-335.

[107] Bradley, D., Lawes, M., Liu, K. and Mansour, M. S. Measurements and correlations of turbulent burning velocities over wide ranges of fuels and elevated pressures. *Proceedings of the Combustion Institute*. 2013, **34**(1), pp.1519-1526.

[108] Bradley, D., Lawes, M. and Morsy, M. E. Measurement of turbulence characteristics in a large scale fan-stirred spherical vessel. *Journal of Turbulence*. 2019, **20**(3), pp.195-213.

[109] Bradley, D. Autoignitions and detonations in engines and ducts. *Philosophical Transactions of the Royal Society A: Mathematical, Physical and Engineering Sciences*. 2012, **370**(1960), pp.689-714.

[110] Wang, Z., Liu, H. and Reitz, R. D. Knocking combustion in spark-ignition engines. *Progress in Energy and Combustion Science*. 2017, **61**, pp.78-112.

[111] Hirst, S. L. and Kirsch, L. J. The application of a hydrocarbon autoignition model in simulating knock and other engine combustion phenomena. *Combustion Modeling in Reciprocating Engines*. 1980, 193.

[112] Moses, E., Yarin, A. L., & Bar-Yoseph, P. (1995). On knocking prediction in spark ignition engines. *Combustion and Flame*, **101**(3), pp.239-261.

[113] Zhen, X., Wang, Y., Xu, S., Zhu, Y., Tao, C., Xu, T. and Song, M. The engine knock analysis–An overview. *Applied Energy*. 2012, **92**, pp.628-636.

[114] Wang, Z., Qi, Y., He, X., Wang, J., Shuai, S. and Law, C. K. Analysis of pre-ignition to super-knock: Hotspot-induced deflagration to detonation. *Fuel*. 2015, **144**, pp.222-227.

[115] Pan, J., Hu, Z., Wei, H., Pan, M., Liang, X., Shu, G. and Zhou, L. Understanding strong knocking mechanism through high-strength optical rapid compression machines. *Combustion and Flame*. 2019, **202**, pp.1-15.

[116] Liu, W., Qi, Y., Zhang, R. and Wang, Z. Flame propagation and auto-ignition behavior of iso-octane across the negative temperature coefficient (NTC) region on a rapid compression machine. *Combustion and Flame*. 2022, **235**, article no:111688.

[117] Dagaut, P., Voisin, D., Cathonnet, M., Mcguinness, M. and Simmie, J. M. The oxidation of ethylene oxide in a jet-stirred reactor and its ignition in shock waves. *Combustion and flame*. 1996, **106**(1-2), pp.62-68.

[118] Burke, U., Metcalfe, W. K., Burke, S. M., Heufer, K. A., Dagaut, P. and Curran, H. J. A detailed chemical kinetic modeling, ignition delay time and jet-stirred reactor study of methanol oxidation. *Combustion and Flame*. 2016, **165**, pp.125-136.

[119] Pelucchi, M., Namysl, S., Ranzi, E., Rodriguez, A., Rizzo, C., Somers, K. P., Zhang, Y., Herbinet, O., Curran, H.J., Battin-Leclerc, F. and Faravelli, T. Combustion of n-C3–C6 linear alcohols: an experimental and kinetic modeling study. Part II: Speciation

measurements in a jet-stirred reactor, ignition delay time measurements in a rapid compression machine, model validation, and kinetic analysis. *Energy & Fuels*. 2020, **34**(11), pp.4708-14725.

[120] Gauthier, B. M., Davidson, D. F. and Hanson, R. K. Shock tube determination of ignition delay times in full-blend and surrogate fuel mixtures. *Combustion and Flame*. 2004, **139**(4), pp.300-311.

[121] Würmel, J., Silke, E. J., Curran, H. J., Conaire, M. Ó. and Simmie, J. M. The effect of diluent gases on ignition delay times in the shock tube and in the rapid compression machine. *Combustion and Flame*. 2007, **151**(1-2), pp.289-302.

[122] Saxena, S., Kahandawala, M. S. P. and Sidhu, S. S. A shock tube study of ignition delay in the combustion of ethylene. *Combustion and Flame*. 2011, **158**(6), 1019-1031.

[123] Cook, R. D., Davidson, D. F., & Hanson, R. K. Shock tube measurements of ignition delay times and OH time-histories in dimethyl ether oxidation. *Proceedings of the Combustion Institute*. 2009, **32**(1), pp.189-196.

[124] Das, A. K., Sung, C. J., Zhang, Y. and Mittal, G. Ignition delay study of moist hydrogen/oxidizer mixtures using a rapid compression machine. *International Journal of Hydrogen Energy*. 2012, **37**(8), pp.6901-6911.

[125] Gersen, S., Anikin, N. B., Mokhov, A. V. and Levinsky, H. B. Ignition properties of methane/hydrogen mixtures in a rapid compression machine. *International Journal of Hydrogen Energy*. 2008, **33**(7), pp.1957-1964.

[126] Xu, N., Wu, Y., Tang, C., Zhang, P., He, X., Wang, Z. and Huang, Z. Ignition delay times of low alkylfurans at high pressures using a rapid compression machine. *Proceedings of the Combustion Institute*. 2017, **36**(1), pp.323-332.

[127] Goldsborough, S. S., Hochgreb, S., Vanhove, G., Wooldridge, M. S., Curran, H. J., and Sung, C. J. (2017). Advances in rapid compression machine studies of low-and intermediate-temperature autoignition phenomena. *Progress in Energy and Combustion Science*, **63**, pp.1-78.

[128] Vasu, S. S., Davidson, D. F., Hong, Z., Vasudevan, V. and Hanson, R. K. n-Dodecane oxidation at high-pressures: Measurements of ignition delay times and OH

concentration time-histories. *Proceedings of the Combustion Institute*. 2009, **32**(1), pp.173-180.

[129] AlAbbad, M., Javed, T., Khaled, F., Badra, J. and Farooq, A. Ignition delay time measurements of primary reference fuel blends. *Combustion and Flame*. 2017, **178**, pp.205-216.

[130] Sung, C. J. and Curran, H. J. Using rapid compression machines for chemical kinetics studies. *Progress in Energy and Combustion Science*. 2014, **44**, pp.1-18.

[131] Michelbach, C. and Tomlin, A. An experimental and kinetic modeling study of the ignition delay and heat release characteristics of a five component gasoline surrogate and its blends with iso-butanol within a rapid compression machine. *International Journal of Chemical Kinetics*. 2021, **53**(6), pp.787-808.

[132] Gorbatenko, I., Tomlin, A. S., Lawes, M. and Cracknell, R. F. Experimental and modelling study of the impacts of n-butanol blending on the auto-ignition behaviour of gasoline and its surrogate at low temperatures. *Proceedings of the Combustion Institute*. 2019, **37**(1), pp.501-509.

[133] Gorbatenko, I., Bradley, D. and Tomlin, A. S. Auto-ignition and detonation of n-butanol and toluene reference fuel blends (TRF). *Combustion and Flame*. 2021, **229**, article no: 111378.

[134] Gorbatenko, I. *Auto-ignition and heat release of alternative engine fuels*. Ph.D. thesis, University of Leeds, 2019.

[135] Battin-Leclerc, F., Blurock, E., Bounaceur, R., Fournet, R., Glaude, P. A., Herbinet, O. Sirjean, B. and Warth, V. Towards cleaner combustion engines through groundbreaking detailed chemical kinetic models. *Chemical Society Reviews*. 2011 **40**(9), pp.4762-4782.

[136] Radulescu, M. I., Sharpe, G. J., Law, C. K. and Lee, J. H. The hydrodynamic structure of unstable cellular detonations. *Journal of Fluid Mechanics*. 2007, **580**, pp.31-81.

[137] Merzhanov, A. G. On critical conditions for thermal explosion of a hot spot. *Combustion and Flame*. 1966, **10**(4), pp.341-348.

[138] Borisov, A. A. On the origin of exothermic centers in gaseous mixtures. *Acta*

*Astronautica*. 1974, **1**(7-8), pp.909-920.

[139] Zeldovich, Y. B. Regime classification of an exothermic reaction with nonuniform initial conditions. *Combustion and Flame*.1980, **39**(2), pp.211-214.

[140] Gu, X. J., Emerson, D. R. and Bradley, D. Modes of reaction front propagation from hot spots. *Combustion and Flame*. 2003, **133**(1-2), pp.63-74.

[141] Kalghatgi, G. T. and Bradley, D. Pre-ignition and 'super-knock' in turbo-charged spark-ignition engines. *International Journal of Engine Research*. 2012, **13**(4), pp.399-414.

[142] Robert, A., Richard, S., Colin, O. and Poinsot, T. LES study of deflagration to detonation mechanisms in a downsized spark ignition engine. *Combustion and Flame*. 2015, **162**(7), pp.2788-2807.

[143] Pan, J., Dong, S., Wei, H., Li, T., Shu, G. and Zhou, L. Temperature gradient induced detonation development inside and outside a hotspot for different fuels. *Combustion and Flame*. 2019, **205**, pp.269-277.

[144] Dai, P., Qi, C. and Chen, Z. Effects of initial temperature on autoignition and detonation development in dimethyl ether/air mixtures with temperature gradient. *Proceedings of the Combustion Institute*. 2017, **36**(3), pp.3643-3650.

[145] Pan, J., Wang, L., He, Y., Wei, H., Shu, G. and Li, T. Hotspot auto-ignition induced detonation development: emphasis on energy density and chemical reactivity. *Combustion Theory and Modelling*. 2022, **26**(1), pp.179-200.

[146] Lutz, A. E., Kee, R. J., Miller, J. A., Dwyer, H. A. and Oppenheim, A. K. Dynamic effects of autoignition centers for hydrogen and C1, 2-hydrocarbon fuels. *Symposium (International) on Combustion*. 1989, **22**(1), pp.1683-1693.

[147] Davis, S., Merilo, E., Engel, D., Ziemba, A., Pinto, M. and van Wingerden, K. Large scale detonation testing: New findings in the prediction of DDTs at large scales. *Journal of Loss Prevention in the Process Industries*. 2017, **48**, pp.345-357.

[148] Skjold, T., Souprayen, C. and Dorofeev, S. Fires and explosions. *Progress in Energy and Combustion Science*. 2018, **64**, pp.2-3.

[149] Bradley, D., Chamberlain, G. A. and Drysdale, D. D. Large vapour cloud explosions,

with particular reference to that at Buncefield. *Philosophical Transactions of the Royal Society A: Mathematical, Physical and Engineering Sciences*. 2012, **370**(1960), pp.544-566.

[150] Sherman, M. P., Tiezsen, S. R., Benedick, W. B., Fisk, J. W. and Carcassi, M. Effect of transverse venting on flame acceleration and transition to detonation in a large channel. *Sandia National Labs*. 1985, article no: SAND--85-1386C.

[151] Harris, R. J. and Wickens, M. J. Understanding vapour cloud explosions: an experimental study. *London: Institution of Gas Engineers*, 1989.

[152] Lowesmith, B. J., Hankinson, G. and Johnson, D. M. Vapour cloud explosions in a long congested region involving methane/hydrogen mixtures. *Process Safety and Environmental Protection*. 2011, **89**(4), pp.234-247.

[153] Maxwell, B., Pekalski, A. and Radulescu, M. Modelling of the transition of a turbulent shock-flame complex to detonation using the linear eddy model. *Combustion and Flame*. 2018, **192**, pp.340-357.

[154] Coates, A. M., Mathias, D. L. and Cantwell, B. J. Numerical investigation of the effect of obstacle shape on deflagration to detonation transition in a hydrogen–air mixture. *Combustion and Flame*. 2019, **209**, pp.278-290.

[155] Woolley, R. M., Fairweather, M., Falle, S. A. E. G. and Giddings, J. R. Prediction of confined, vented methane-hydrogen explosions using a computational fluid dynamic approach. *International Journal of Hydrogen Energy*. 2013, **38**(16), pp.6904-6914.

[156] Kessler, D. A., Gamezo, V. N. and Oran, E. S. Simulations of flame acceleration and deflagration-to-detonation transitions in methane–air systems. *Combustion and Flame*. 2010, **157**(11), pp.2063-2077.

[157] Xiao, H. and Oran, E. S. Flame acceleration and deflagration-to-detonation transition in hydrogen-air mixture in a channel with an array of obstacles of different shapes. *Combustion and Flame*. 2020, **220**, pp.378-393.

[158] Al-Shahrany, A. S., Bradley, D., Lawes, M. and Woolley, R. Measurement of unstable burning velocities of iso-octane–air mixtures at high pressure and the derivation of laminar burning velocities. *Proceedings of the Combustion Institute*. 2005, **30**(1),

pp.225-232.

[159] Al-Shahrany, A. S., Bradley, D., Lawes, M., Liu, K. and Woolley, R. Darrieus–Landau and thermo-acoustic instabilities in closed vessel explosions. *Combustion Science and Technology*. 2006, **178**(10-11), pp.1771-1802.

[160] Bradley, D., Lawes, M., Liu, K. and Woolley, R. The quenching of premixed turbulent flames of iso-octane, methane and hydrogen at high pressures. *Proceedings of the Combustion Institute*. 2007, **31**(1), pp.1393-1400.

[161] Bradley, D., Lawes, M. and Mansour, M. S. Explosion bomb measurements of ethanol–air laminar gaseous flame characteristics at pressures up to 1.4 MPa. *Combustion and Flame*. 2009, **156**(7), pp.1462-1470.

[162] Bradley, D., Lawes, M. and Mansour, M. S. Measurement of turbulent burning velocities in implosions at high pressures. *Proceedings of the Combustion Institute*. 2011, **33**(1), pp.1269-1275.

[163] Marwaan, A. K., Yang, J., Tomlin, A. S., Thompson, H. M., de Boer, G., Liu, K., and Morsy, M. E. Laminar burning velocities and Markstein numbers for pure hydrogen and methane/hydrogen/air mixtures at elevated pressures. *Fuel*. 2023, **354**, article no:129331.

[164] Xie, Y., Lu, A., Li, J., Yang, J., Zhang, C. and Morsy, M. E. Laminar burning characteristics of coal-based naphtha. *Combustion and Flame*. 2023, **249**, article no:112625.

[165] Morsy, M. E. *Studies of Laminar and Turbulent Combustion Using Particle Image Velocimetry*. Ph.D. thesis, University of Leeds, 2019.

[166] Mumby, R. D. *Experimental Characterisation of Fuel Blends*. Ph.D. thesis, University of Leeds, 2017.

[167] Sharpe, G. 2011. Private Communications, cited in Mumby, R. D. [166]

[168] Otsu, N. A threshold selection method from gray-level histograms. *IEEE transactions on systems, man, and cybernetics*. 1979, **9**(1), pp.62-66.

[169] Dai, H., Wang, J., Su, S., Su, L., Cai, X. and Huang, Z. Turbulent burning velocity of hydrogen/n-heptane/air propagating spherical flames: Effects of hydrogen content.

*Combustion and Flame*. 2024, **260**, article no:113248.

[170] Wang, S., Elbaz, A. M., Wang, G., Wang, Z. and Roberts, W. L. Turbulent flame speed of NH3/CH4/H2/H2O/air-mixtures: Effects of elevated pressure and Lewis number. *Combustion and Flame*. 2023, **247**, article no:112488.

[171] Zhao, H., Li, G., Wang, J. and Huang, Z. Experimental study of H2/air turbulent expanding flames over wide equivalence ratios: Effects of molecular transport. *Fuel*. 2023, **341**, article no:127652.

[172] Affleck, W. S. and Thomas, A. An opposed piston rapid compression machine for preflame reaction studies. *Proceedings of the Institution of Mechanical Engineers*. 1968, **183**(1), pp.365-387.

[173] Brindley, J., Griffiths, J. F. and McIntosh, A. C. Ignition phenomenology and criteria associated with hotspots embedded in a reactive material. *Chemical Engineering Science*. 2001, **56**(6), pp.2037-2046.

[174] Griffiths, J. F., MacNamara, J. P., Sheppard, C. G. W., Turton, D. A. and Whitaker, B. J. The relationship of knock during controlled autoignition to temperature inhomogeneities and fuel reactivity. *Fuel*. 2002, **81**(17), pp.2219-2225.

[175] Michelbach, C. A. and Tomlin, A. S. Influence of iso-butanol blending with a reference gasoline and its surrogate on spark-ignition engine performance. *Energy & Fuels*. 2021, **35**(23), pp.19665-19688.

[176] Michelbach, C. A. and Tomlin, A. An experimental and kinetic modeling study of the ignition delay and heat release characteristics of a five component gasoline surrogate and its blends with iso - butanol within a rapid compression machine. *International Journal of Chemical Kinetics*. 2021, **53**(6), pp.787-808.

[177] Materego, M. *Auto-ignition characterisation of synthetic fuels via Rapid Compression Machine*. Ph.D. thesis, University of Leeds, 2015.

[178] Bates, L. R. Characterisation of reaction propagation from auto-ignition. Ph.D. thesis, University of Leeds, 2016.

[179] Michelbach, C. A. *Ignition and Heat Release Behaviour of iso-Butanol and Gasoline Blended Fuels: An Experimental and Kinetic Modelling Study*. Ph.D. thesis,

University of Leeds, 2020.

[180] Mittal, G. *A rapid compression machine–design, characterization, and autoignition investigations*. Ph.D. thesis, Case Western Reserve University, 2006

[181] Desgroux, P., Gasnot, L. and Sochet, L. R. Instantaneous temperature measurement in a rapid-compression machine using laser Rayleigh scattering. *Applied Physics B*. 1995, **61**, pp.69-72.

[182] Griffiths, J. F., Jiao, Q., Kordylewski, W., Schreiber, M., Meyer, J. and Knoche, K. F. Experimental and numerical studies of ditertiary butyl peroxide combustion at high pressures in a rapid compression machine. *Combustion and Flame*. 1993, **93**(3), pp.303-315.

[183] The MathWorks Inc. *MATLAB* (2021b). [Software]. 2021. [Accessed 20 April 2021].

[184] Wang, Y., Qi, Y., Liu, W. and Wang, Z. Investigation of methanol ignition phenomena using a rapid compression machine. *Combustion and Flame*. 2020, **211**, pp.147-157.

[185] Pan, J., Zheng, Z., Wei, H., Pan, M., Shu, G. and Liang, X. An experimental investigation on pre-ignition phenomena: Emphasis on the role of turbulence. *Proceedings of the Combustion Institute*. 2021, **38**(4), pp.5801-5810.

[186] Falle, S. A. E. G. Self-similar jets. *Monthly Notices of the Royal Astronomical Society*. 1991, **250**(3), pp.581-596.

[187] Jones, W. P. and Launder, B. E. The prediction of laminarization with a two-equation model of turbulence. *International Journal of Heat and Mass Transfer*. 1972, **15**(2), pp.301-314.

[188] Catlin, C. A., Fairweather, M. and Ibrahim, S. S. Predictions of turbulent, premixed flame propagation in explosion tubes. *Combustion and Flame*. 1995, **102**(1-2), pp.115-128.

[189] Joshua, K. A. *Understanding the Generation of Hot Spots in the Rapid Compression Machine*. MSC thesis, University of Leeds, 2019.

[190] University of Leeds Research Computing Team. Getting started with ARC. [Online].

2023. [Accessed 05 August 2023]. Available from : https://arcdocs.leeds.ac.uk/getting_started/start.html.

[191] Mobatek. *MobaXterm Personal Edition* (v21.4). [Software]. 2020. [Accessed 21 May 2020].

[192] Bradley, D., Lawes, M. and Materego, M. Interpretation of auto-ignition delay times measured in different rapid compression machines. In: *25th International Colloquium on the Dynamics of Explosions and Reactive systems*. April 2015, Leeds.

[193] Kalghatgi, G. T., Bradley, D., Andrae, J. and Harrison, A. J. The nature of 'superknock'and its origins in SI engines. In: *IMechE conference on internal combustion engines: performance fuel economy and emissions*. December 2009, pp. 8-9.

[194] Reaction Design. *CHEMKIN-Pro* (19.2). [Software]. 2017. [Accessed 20 April 2020].

[195] Mehl, M., Pitz, W. J., Westbrook, C. K. and Curran, H. J. Kinetic modeling of gasoline surrogate components and mixtures under engine conditions. *Proceedings of the Combustion Institute*. 2011, **33**(1), pp.193-200.

[196] Bannister, R. L., Newby, R. A. and Yang, W. C. Final report on the development of a hydrogen-fueled combustion turbine cycle for power generation. *Journal of Engineering for Gas Turbines and Power*. 1999, **121**(1), pp.38-45.

[197] Morris, J. D., Symonds, R. A., Ballard, F. L. and Banti, A. Combustion aspects of application of hydrogen and natural gas fuel mixtures to MS9001E DLN-1 gas turbines at Elsta Plant, Terneuzen, The Netherlands. *American Society of Mechanical Engineers*. 1998, **78644**, article no: V003T05A033.

[198] Bell, S. R. and Gupta, M. Extension of the lean operating limit for natural gas fueling of a spark ignited engine using hydrogen blending. *Combustion Science and Technology*. 1997, **123**(1-6), pp.23-48.

[199] Sierens, R. and Rosseel, E. Variable composition hydrogen/natural gas mixtures for increased engine efficiency and decreased emissions. *Journal of Engineering for Gas Turbines and Power*. 2000, **122**(1), pp.135-140.

[200] Bradley, D., Sheppard, C. G. W., Suardjaja, I. M. and Woolley, R. Fundamentals of

high-energy spark ignition with lasers. *Combustion and Flame*. 2004, **138**(1-2), pp.55-77.

[201] Morsy, M. E. and Yang, J. The instability of laminar methane/hydrogen/air flames: correlation between small and large-scale explosions. *International Journal of Hydrogen Energy*. 2022, **47**(69), pp.29959-29970.

[202] Metcalfe, W. K., Burke, S. M., Ahmed, S. S. and Curran, H. J. A hierarchical and comparative kinetic modeling study of C1− C2 hydrocarbon and oxygenated fuels. *International Journal of Chemical Kinetics*. 2013, **45**(10), pp.638-675.

[203] Smith, G. P., Golden, D. M., Frenklach, M., Moriarty, N. W., Eiteneer, B., Goldenberg, M., Bowman, C. T., Hanson, R. K., Song, S., Gardiner, W. C. Jr., Lissianski, V. V., and Qin, Z. GRI-Mech 3.0 detailed mechanism. http://www.me.berkeley.edu/gri_mech/.

[204] Chemical-Kinetic Mechanisms for Combustion Applications. San Diego Mechanism web page. Mechanical and Aerospace Engineering (Combustion Research). University of California at San Diego. http://combustion.ucsd.edu.

[205] Wang, H., You, X., Joshi, A. V., Davis, S. G., Laskin, A., Egolfopoulos, F and Law, C.K. USC Mech Version II. High-Temperature Combustion Reaction Model of H2/CO/C1-C4 Compounds. 2007. http://ignis.usc.edu/USC_Mech_II.htm.

[206] Dayma, G., Halter, F. and Dagaut, P. New insights into the peculiar behavior of laminar burning velocities of hydrogen–air flames according to pressure and equivalence ratio. *Combustion and Flame*. 2014, **161**(9), pp.2235-2241.

[207] Metghalchi, M. and Keck, J. C. Burning velocities of mixtures of air with methanol, isooctane, and indolene at high pressure and temperature. *Combustion and Flame*. 1982, **48**, pp.191-210.

[208] Van Lipzig, J. P. J., Nilsson, E. J. K., De Goey, L. P. and Konnov, A. A. Laminar burning velocities of n-heptane, iso-octane, ethanol and their binary and tertiary mixtures. *Fuel*. 2011, **90**(8), pp.2773-2781.

[209] Chen, Z., Tang, C., Fu, J., Jiang, X., Li, Q., Wei, L. and Huang, Z.H. Experimental and numerical investigation on diluted DME flames: Thermal and chemical kinetic effects on laminar flame speeds. *Fuel*. 2012, **102**, pp.567-573.

[210] Okafor, E.C., Naito, Y., Colson, S., Ichikawa, A., Kudo, T., Hayakawa, A. and Kobayashi, H. Measurement and modelling of the laminar burning velocity of methane-ammonia-air flames at high pressures using a reduced reaction mechanism. *Combustion and Flame*. 2019, **204**, pp.162-175.

[211] Bouvet, N., Halter, F., Chauveau, C. and Yoon, Y. On the effective Lewis number formulations for lean hydrogen/hydrocarbon/air mixtures. *International Journal of Hydrogen Energy*. 2013, **38**, pp.5949-5960.

[212] Law, C. K., Jomaas, G. and Bechtold, J. K. Cellular instabilities of expanding hydrogen/propane spherical flames at elevated pressures: theory and experiment. *Proceedings of the Combustion Institute*. 2005, **30**(1), pp.159-167.

[213] Oppong, F., Zhongyang, L., Li, X. and Xu, C. Inherent instabilities in ethyl acetate premixed flames. *Fuel*. 2021, **290**, article no:120000.

[214] Mannaa, O., Mansour, M.S., Roberts, W.L. and Chung, S.H. Laminar burning velocities at elevated pressures for gasoline and gasoline surrogates associated with RON. *Combustion and Flame*. 2015, **162** pp.2311-2321.

[215] Wu, F., Saha, A., Chaudhuri, S. and Law, C. K. Propagation speeds of expanding turbulent flames of C4 to C8 n-alkanes at elevated pressures: Experimental determination, fuel similarity, and stretch-affected local extinction. *Proceedings of the Combustion Institute*. 2015, **35**(2), pp.1501-1508.

[216] Bradley, D., Lawes, M. and Morsy, M. E. Combustion-induced turbulent flow fields in premixed flames. *Fuel*. 2021, **290**, article no:119972.

[217] Xiao, H., Makarov, D., Sun, J. and Molkov, V. Experimental and numerical investigation of premixed flame propagation with distorted tulip shape in a closed duct. *Combustion and Flame*. 2012, **159**(4), pp.1523-1538.

[218] Bychkov, V., Akkerman, V. Y., Fru, G., Petchenko, A. and Eriksson, L. E. Flame acceleration in the early stages of burning in tubes. *Combustion and Flame*. 2007, **150**(4), pp.263-276.

[219] Pinos, T. and Ciccarelli, G. Combustion wave propagation through a bank of cross-flow cylinders. *Combustion and Flame*. 2015, **162**(9), pp.3254-3262.

[220] Di Sarli, V., Di Benedetto, A., Russo, G., Jarvis, S., Long, E. J. and Hargrave, G. K. Large eddy simulation and PIV measurements of unsteady premixed flames accelerated by obstacles. *Flow, Turbulence and Combustion*. 2009, **83**, pp.227-250.

[221] Yanez, J., Kuznetsov, M. and Souto-Iglesias, A. An analysis of the hydrogen explosion in the Fukushima-Daiichi accident. *International Journal of Hydrogen Energy*. 2015, **40**(25), pp.8261-8280.

[222] Wang, L. Q., Ma, H. H., Shen, Z. W. and Chen, D. G. Experimental study of DDT in hydrogen-methane-air mixtures in a tube filled with square orifice plates. *Process Safety and Environmental Protection*. 2018, **116**, pp.228-234.

[223] Li, H., Zhang, T. and Chen, Z. X. Effect of Chemical Mechanisms on Deflagration to Detonation Transition and Its Application to Mechanism Reduction. In: *29th International Colloquium on the Dynamics of Explosions and Reactive Systems, July 2023, Siheung.*

[224] Luong, M. B. and Im, H. G. Prediction of the developing detonation regime in a NTC-fuel/air mixture with temperature inhomogeneities under engine conditions. *Proceedings of the Combustion Institute*. 2023, **39**(4), pp. 4979-4988.

[225] Dai, P., Chen, Z., Gan, X. and Liberman, M. A. Autoignition and detonation development from a hot spot inside a closed chamber: Effects of end wall reflection. *Proceedings of the Combustion Institute*. 2021, **38**(4), pp.5905-5913.

[226] Li, H., Liang, W. and Law, C. K. Effects of Ozone Addition on Direct Initiation of Detonation in Hydrogen/Oxygen Mixtures. In: *29th International Colloquium on the Dynamics of Explosions and Reactive Systems, July 2023, Siheung.*

# Appendix A .

The measured data of laminar and turbulent flame characteristics of ethane-hydrogen-air flame.

Table A.1: Experimental data of ethane-air at 300 K, 0.1 MPa.

| $\phi$ | $\rho_u/\rho_b$ | $Ss$ (m/s) | $u_l$ (m/s) | $\delta_l$ (mm) | $L_b$ (mm) | $Ma_b$ |
|---|---|---|---|---|---|---|
| 0.7 | 6.371 | 1.469 | 0.231 | 0.0829 | 0.972 | 11.7 |
| 0.8 | 6.946 | 2.063 | 0.297 | 0.0640 | 0.941 | 14.7 |
| 0.9 | 7.450 | 2.714 | 0.364 | 0.0516 | 0.792 | 15.3 |
| 1.0 | 7.817 | 3.140 | 0.402 | 0.0466 | 0.802 | 16.9 |
| 1.1 | 7.922 | 3.274 | 0.413 | 0.0450 | 0.807 | 17.9 |
| 1.2 | 7.841 | 3.097 | 0.395 | 0.0468 | 0.679 | 14.5 |
| 1.3 | 7.718 | 2.634 | 0.341 | 0.0539 | 0.641 | 11.9 |

Table A.2: Experimental data of ethane-air at 360 K, 0.1 MPa.

| $\phi$ | $\rho_u/\rho_b$ | $Ss$ (m/s) | $u_l$ (m/s) | $\delta_l$ (mm) | $L_b$ (mm) | $Ma_b$ |
|---|---|---|---|---|---|---|
| 0.7 | 5.431 | 1.651 | 0.304 | 0.0865 | 0.934 | 10.8 |
| 0.8 | 5.902 | 2.250 | 0.381 | 0.0684 | 0.856 | 12.5 |
| 0.9 | 6.308 | 2.986 | 0.473 | 0.0547 | 0.882 | 16.1 |
| 1.0 | 6.606 | 3.534 | 0.535 | 0.0482 | 0.846 | 17.6 |
| 1.1 | 6.702 | 3.684 | 0.550 | 0.0466 | 0.904 | 19.4 |
| 1.2 | 6.649 | 3.549 | 0.534 | 0.0476 | 0.538 | 11.3 |
| 1.3 | 6.554 | 3.240 | 0.494 | 0.0512 | 0.412 | 8.1 |

Table A.3: Experimental data of ethane-air at 300 K, 0.5 MPa.

| $\phi$ | $\rho_u/\rho_b$ | $Ss$ (m/s) | $u_l$ (m/s) | $\delta_l$ (mm) | $L_b$ (mm) | $Ma_b$ | $r_{cl}$ (mm) | $Pe_{cl}$ |
|---|---|---|---|---|---|---|---|---|
| 0.7 | 6.378 | 0.774 | 0.121 | 0.0314 | 0.415 | 13.2 | | |
| 0.8 | 6.965 | 1.282 | 0.184 | 0.0224 | 0.337 | 16.4 | | |
| 0.9 | 7.505 | 1.831 | 0.244 | 0.0155 | 0.285 | 18.5 | 47 | 3040 |
| 1.0 | 7.922 | 2.179 | 0.275 | 0.0136 | 0.342 | 25.1 | 37.4 | 2750 |
| 1.1 | 7.977 | 2.526 | 0.317 | 0.0118 | 0.331 | 28.1 | 28.7 | 2440 |
| 1.2 | 7.863 | 2.372 | 0.302 | 0.0123 | 0.251 | 20.4 | 25.2 | 2050 |

| | | | | | | | | |
|---|---|---|---|---|---|---|---|---|
| 1.3 | 7.729 | 1.912 | 0.247 | 0.0149 | 0.222 | 14.9 | 20.2 | 1360 |

Table A.4: Experimental data of ethane-air at 360 K, 0.5 MPa.

| $\phi$ | $\rho_u/\rho_b$ | $Ss$ (m/s) | $u_l$ (m/s) | $\delta_l$ (mm) | $L_b$ (mm) | $Ma_b$ | $r_{cl}$ (mm) | $Pe_{cl}$ |
|---|---|---|---|---|---|---|---|---|
| 0.7 | 5.438 | 0.910 | 0.167 | 0.0314 | 0.380 | 12.1 | | |
| 0.8 | 5.922 | 1.378 | 0.233 | 0.0224 | 0.325 | 14.5 | | |
| 0.9 | 6.362 | 1.961 | 0.308 | 0.0168 | 0.297 | 17.7 | 49.2 | 2930 |
| 1.0 | 6.697 | 2.507 | 0.374 | 0.0138 | 0.315 | 22.9 | 39.0 | 2830 |
| 1.1 | 6.759 | 2.762 | 0.409 | 0.0125 | 0.315 | 25.1 | 32.1 | 2560 |
| 1.2 | 6.674 | 2.669 | 0.401 | 0.0127 | 0.208 | 16.3 | 29.2 | 2290 |
| 1.3 | 6.567 | 2.379 | 0.362 | 0.0141 | 0.155 | 11.1 | 24.0 | 1720 |

Table A.5: Experimental data of ethane-hydrogen-air ($X_{H_2}$= 50%) at 300 K, 0.1 MPa.

| $\phi$ | $\rho_u/\rho_b$ | $Ss$ (m/s) | $u_l$ (m/s) | $\delta_l$ (mm) | $L_b$ (mm) | $Ma_b$ |
|---|---|---|---|---|---|---|
| 0.7 | 6.316 | 1.842 | 0.292 | 0.0741 | 0.190 | 2.6 |
| 0.8 | 6.863 | 2.741 | 0.399 | 0.0546 | 0.359 | 6.6 |
| 0.9 | 7.326 | 3.407 | 0.465 | 0.0473 | 0.493 | 10.4 |
| 1.0 | 7.658 | 3.980 | 0.520 | 0.0427 | 0.555 | 13.0 |
| 1.1 | 7.751 | 4.315 | 0.557 | 0.0402 | 0.568 | 14.1 |
| 1.2 | 7.673 | 4.087 | 0.533 | 0.0424 | 0.501 | 11.8 |
| 1.3 | 7.555 | 3.544 | 0.469 | 0.0486 | 0.451 | 9.3 |

Table A.6: Experimental data of ethane-hydrogen-air ($X_{H_2}$= 50%) at 360 K, 0.1 MPa.

| $\phi$ | $\rho_u/\rho_b$ | $Ss$ (m/s) | $u_l$ (m/s) | $\delta_l$ (mm) | $L_b$ (mm) | $Ma_b$ |
|---|---|---|---|---|---|---|
| 0.7 | 5.401 | 2.036 | 0.377 | 0.0788 | 0.108 | 1.4 |
| 0.8 | 5.823 | 3.018 | 0.518 | 0.0577 | 0.326 | 5.7 |
| 0.9 | 6.203 | 3.796 | 0.612 | 0.0493 | 0.438 | 8.9 |

| | | | | | | |
|---|---|---|---|---|---|---|
| 1.0 | 6.468 | 4.547 | 0.703 | 0.0432 | 0.605 | 14.0 |
| 1.1 | 6.556 | 4.668 | 0.712 | 0.0431 | 0.640 | 14.9 |
| 1.2 | 6.507 | 4.548 | 0.699 | 0.0442 | 0.510 | 11.5 |
| 1.3 | 6.415 | 3.918 | 0.611 | 0.0509 | 0.492 | 9.7 |

Table A.7: Experimental data of ethane-hydrogen-air ($X_{H_2}$= 50%) at 300 K, 0.5 MPa.

| $\phi$ | $\rho_u/\rho_b$ | $Ss$ (m/s) | $u_l$ (m/s) | $\delta_l$ (mm) | $L_b$ (mm) | $Ma_b$ | $r_{cl}$ (mm) | $Pe_{cl}$ |
|---|---|---|---|---|---|---|---|---|
| 0.7 | 6.323 | 1.1895 | 0.188 | 0.0230 | -0.208 | -9.1 | 34.5 | 1500 |
| 0.8 | 6.874 | 1.730 | 0.252 | 0.0173 | -0.033 | -1.9 | 22.9 | 1320 |
| 0.9 | 7.374 | 2.328 | 0.316 | 0.0139 | 0.074 | 5.3 | 19.1 | 1370 |
| 1.0 | 7.763 | 2.771 | 0.357 | 0.0125 | 0.155 | 12.5 | 17.3 | 1390 |
| 1.1 | 7.810 | 3.012 | 0.386 | 0.0116 | 0.178 | 15.3 | 19.3 | 1660 |
| 1.2 | 7.698 | 2.789 | 0.362 | 0.0125 | 0.182 | 14.5 | 23.3 | 1870 |
| 1.3 | 7.570 | 2.263 | 0.299 | 0.0153 | 0.194 | 12.7 | 29.7 | 1950 |

Table A.8: Experimental data of ethane-hydrogen-air ($X_{H_2}$= 50%) at 360 K, 0.5 MPa.

| $\phi$ | $\rho_u/\rho_b$ | $Ss$ (m/s) | $u_l$ (m/s) | $\delta_l$ (mm) | $L_b$ (mm) | $Ma_b$ | $r_{cl}$ (mm) | $Pe_{cl}$ |
|---|---|---|---|---|---|---|---|---|
| 0.7 | 5.390 | 1.297 | 0.241 | 0.0246 | -0.301 | -12 | 35.8 | 1450 |
| 0.8 | 5.844 | 2.0041 | 0.343 | 0.0174 | -0.033 | -1.9 | 26.2 | 1500 |
| 0.9 | 6.251 | 2.667 | 0.427 | 0.0141 | 0.025 | 1.8 | 21.7 | 1540 |
| 1.0 | 6.563 | 3.157 | 0.481 | 0.0127 | 0.120 | 9.5 | 20.0 | 1580 |
| 1.1 | 6.617 | 3.403 | 0.514 | 0.0119 | 0.192 | 16.1 | 21.5 | 1800 |
| 1.2 | 6.534 | 3.322 | 0.508 | 0.0122 | 0.180 | 14.8 | 23.3 | 1920 |
| 1.3 | 6.431 | 2.896 | 0.450 | 0.0139 | 0.155 | 11.2 | 28.1 | 2030 |

Table A.9: Experimental data of ethane-hydrogen-air ($X_{H_2}$= 25%) at 300 K, 0.1 MPa.

| $\phi$ | $\rho_u/\rho_b$ | $Ss$ (m/s) | $u_l$ (m/s) | $\delta_l$ (mm) | $L_b$ (mm) | $Ma_b$ |
|---|---|---|---|---|---|---|
| 0.7 | 6.335 | 1.493 | 0.236 | 0.0912 | 0.683 | 7.5 |

| | | | | | | |
|---|---|---|---|---|---|---|
| 0.8 | 6.929 | 2.155 | 0.311 | 0.0698 | 0.699 | 10.0 |
| 0.9 | 7.400 | 2.829 | 0.382 | 0.0573 | 0.743 | 13.0 |
| 1.0 | 7.763 | 3.366 | 0.434 | 0.0510 | 0.736 | 14.4 |
| 1.1 | 7.855 | 3.564 | 0.454 | 0.0489 | 0.746 | 15.2 |
| 1.2 | 7.773 | 3.412 | 0.439 | 0.0513 | 0.639 | 12.5 |
| 1.3 | 7.656 | 2.909 | 0.380 | 0.0595 | 0.605 | 10.2 |

Table A.10: Experimental data of ethane-hydrogen-air ($X_{H_2}$= 75%) at 300 K, 0.1 MPa.

| $\phi$ | $\rho_u/\rho_b$ | *Ss* (m/s) | $u_l$ (m/s) | $\delta_l$ (mm) | $L_b$ (mm) | $Ma_b$ |
|---|---|---|---|---|---|---|
| 0.7 | 6.190 | 2.592 | 0.419 | 0.0664 | -0.287 | -4.3 |
| 0.8 | 6.767 | 3.900 | 0.576 | 0.0498 | 0.109 | 2.2 |
| 0.9 | 7.151 | 4.782 | 0.669 | 0.0444 | 0.211 | 4.7 |
| 1.0 | 7.456 | 5.630 | 0.755 | 0.0404 | 0.426 | 10.6 |
| 1.1 | 7.531 | 5.940 | 0.789 | 0.0397 | 0.465 | 11.7 |
| 1.2 | 7.453 | 5.736 | 0.770 | 0.0418 | 0.386 | 9.2 |
| 1.3 | 7.343 | 5.132 | 0.699 | 0.0472 | 0.332 | 7.0 |

Table A.11: Experimental data of hydrogen-air at 300 K, 0.1 MPa.

| $\phi$ | $\rho_u/\rho_b$ | *Ss* (m/s) | $u_l$ (m/s) | $\delta_l$ (mm) | $L_b$ (mm) | $Ma_b$ |
|---|---|---|---|---|---|---|
| 0.7 | 5.981 | 8.592 | 1.437 | 0.0441 | -0.314 | -7.1 |
| 0.8 | 6.361 | 11.484 | 1.805 | 0.0357 | -0.035 | -1.0 |
| 0.9 | 6.666 | 13.736 | 2.061 | 0.0341 | 0.119 | 3.5 |
| 1.0 | 6.863 | 15.272 | 2.225 | 0.0301 | 0.201 | 6.7 |
| 1.1 | 6.893 | 16.899 | 2.452 | 0.0291 | 0.261 | 9.0 |
| 1.2 | 6.824 | 18.028 | 2.642 | 0.0283 | 0.346 | 12.2 |
| 1.3 | 6.733 | 18.699 | 2.777 | 0.0272 | 0.385 | 14.3 |

Table A.12. The turbulent flames parameters for ethane-air at 300 K, 0.1 MPa.

| | $u'$ = 1 m/s | | | $u'$ = 3 m/s | | | $u'$ = 5 m/s | | |
|---|---|---|---|---|---|---|---|---|---|
| $\phi$ | $U$ | $K$ | $u_{tr}$ | $U$ | $K$ | $u_{tr}$ | $U$ | $K$ | $u_{tr}$ |
| 0.8 | 0.78 | 0.078 | 0.55 | 0.48 | 0.407 | 1.01 | 0.36 | 0.876 | 1.27 |
| 0.9 | 0.85 | 0.052 | 0.59 | 0.50 | 0.270 | 1.06 | 0.41 | 0.582 | 1.43 |
| 1.0 | 0.91 | 0.043 | 0.64 | 0.57 | 0.222 | 1.20 | 0.44 | 0.477 | 1.53 |
| 1.1 | 1.02 | 0.040 | 0.71 | 0.56 | 0.209 | 1.18 | 0.41 | 0.450 | 1.42 |
| 1.2 | 0.87 | 0.044 | 0.61 | 0.51 | 0.228 | 1.08 | 0.38 | 0.491 | 1.35 |

Table A.13. The turbulent flames parameters for ethane-air at 360 K, 0.1 MPa.

| | $u'$ = 1 m/s | | | $u'$ = 3 m/s | | | $u'$ = 5 m/s | | |
|---|---|---|---|---|---|---|---|---|---|
| $\phi$ | $U$ | $K$ | $u_{tr}$ | $U$ | $K$ | $u_{tr}$ | $U$ | $K$ | $u_{tr}$ |
| 0.8 | 0.97 | 0.056 | 0.68 | 0.49 | 0.293 | 1.02 | 0.44 | 0.631 | 1.54 |
| 0.9 | 1.09 | 0.036 | 0.76 | 0.59 | 0.188 | 1.25 | 0.49 | 0.404 | 1.72 |
| 1.0 | 1.13 | 0.028 | 0.79 | 0.67 | 0.147 | 1.41 | 0.56 | 0.316 | 1.97 |
| 1.1 | 1.17 | 0.027 | 0.82 | 0.70 | 0.139 | 1.47 | 0.59 | 0.298 | 2.05 |
| 1.2 | 1.05 | 0.028 | 0.74 | 0.67 | 0.147 | 1.42 | 0.56 | 0.316 | 1.97 |

Table A.14. The turbulent flames parameters for ethane-air at 300 K, 0.5 MPa

| | $u'$ = 1 m/s | | | $u'$ = 3 m/s | | | $u'$ = 5 m/s | | |
|---|---|---|---|---|---|---|---|---|---|
| $\phi$ | $U$ | $K$ | $u_{tr}$ | $U$ | $K$ | $u_{tr}$ | $U$ | $K$ | $u_{tr}$ |
| 0.8 | 0.93 | 0.091 | 0.65 | 0.64 | 0.475 | 1.34 | 0.470 | 1.021 | 1.64 |
| 0.9 | 1.01 | 0.053 | 0.71 | 0.72 | 0.275 | 1.51 | 0.568 | 0.591 | 1.99 |
| 1.0 | 1.17 | 0.042 | 0.82 | 0.77 | 0.217 | 1.61 | 0.625 | 0.466 | 2.19 |
| 1.1 | 1.23 | 0.030 | 0.86 | 0.79 | 0.157 | 1.67 | 0.677 | 0.338 | 2.37 |
| 1.2 | 1.11 | 0.032 | 0.77 | 0.78 | 0.164 | 1.64 | 0.604 | 0.352 | 2.11 |

Table A.15. The turbulent flames parameters for ethane-air at 360 K, 0.5 MPa.

| | $u'$ = 1 m/s | | | $u'$ = 3 m/s | | | $u'$ = 5 m/s | | |
|---|---|---|---|---|---|---|---|---|---|

| $\phi$ | $U$ | $K$ | $u_{tr}$ | $U$ | $K$ | $u_{tr}$ | $U$ | $K$ | $u_{tr}$ |
|---|---|---|---|---|---|---|---|---|---|
| 0.8 | 1.11 | 0.067 | 0.77 | 0.70 | 0.349 | 1.48 | 0.64 | 0.750 | 2.24 |
| 0.9 | 1.19 | 0.039 | 0.83 | 0.78 | 0.200 | 1.64 | 0.68 | 0.431 | 2.39 |
| 1.0 | 1.28 | 0.026 | 0.89 | 0.89 | 0.137 | 1.88 | 0.75 | 0.295 | 2.61 |
| 1.1 | 1.44 | 0.023 | 1.01 | 0.94 | 0.119 | 1.98 | 0.78 | 0.256 | 2.74 |
| 1.2 | 1.26 | 0.023 | 0.88 | 0.89 | 0.122 | 1.87 | 0.74 | 0.262 | 2.58 |

## Appendix B.

The MATLAB Code developed to post process the autoignitive propagation wave in optical RCM.

```
clear all
close all
%the diameter for the optical verision range is 45mm.
% generate the cycle matrix
m=244;
n=244; %the domain
r=122;  %the radius for cycle
m1=-m/2:m/2-1;   % transform the center of cycle into the center of matrix
n1=-n/2:n/2-1;
[x,y]=meshgrid(m1,n1);
circle=x.^2+y.^2;
circ_mask=zeros(m,n);
circ_mask(find(circle<=r*r))=1;  %in cycle 1
circ_mask(find(circle>r*r))=0;   %out cycle 0
K1=find(~circ_mask); % the position of zero in the matrix circ_mask
K2=find(circ_mask); % number of 1 in the combustion chamber

% calculate the images time corresponding with time
framerate=67500;
Images_interval=(1/67500)*1000; %time interval for each image
Images_gap=(19227-19085)*67500/100000;
time=(1173-Images_gap)/67500*1000;

diameter=45; %45mm for the version
pixel=45/244; %each resolution with 0.1844mm
area=pixel^2; %the area for each images in mm^2
```

```
imgPath = 'D:\RCM publication\Optical ER1 770K 25.11.2021\67500fps_run770K
iso-octane test4 2.8aperture _C001H001S0001\Select_images\';       % the fold
of images position
imgDir  = dir([imgPath '*.jpg']); % reading through all jpg images

for i = 1:length(imgDir)         % the length of imgdir
    img = imread([imgPath imgDir(i).name]); %read each images
    name_string = ['img' num2str(i) '=img']; %the variable will change with
loop.
    eval(name_string)
    I = imcrop(img,[167 117 243 243]); %select the range of images original
[160,112,256,256]
%     level(1,i) = graythresh(I);
    level(1,i)=0.13;
    BW = imbinarize(I, level(1,i));
    BW(K1)=0;  %the area out of combustion chamber will treat as zero
    burned=find(BW); %burned combustion chamber
    radius(1,i)=((length(burned)*area)/pi)^(0.5); %the cycle with same area
    BMF(1,i)=length(burned(:))/length(K2(:)); %burned mass fraction
    contour = bwperim(BW);
    brightness(1,i)=(sum(I,'all'));
    [row,col] = find(contour);
    distance=(((row-9).^2+(col-106).^2).^0.5)*pixel;
    distance_average(1,i)=(sum(distance,'all')./length(distance));

%select the range of distance voctor
%     distance_sort=sort(distance);
%     if (900<length(distance_sort))&&(length(distance_sort)<1000)
%     distance_range=distance_sort(end-400:end);
%     elseif  (1000<length(distance_sort))&&(length(distance_sort)<1500)
%     distance_range=distance_sort(end-450:end);
%     elseif  (700<length(distance_sort))&&(length(distance_sort)<900)
%     distance_range=distance_sort(end-350:end);
%     elseif  (500<length(distance_sort))&&(length(distance_sort)<700)
%     distance_range=distance_sort(end-250:end);
%     elseif  (300<length(distance_sort))&&(length(distance_sort)<500)
%     distance_range=distance_sort(end-150:end);
%     else
%     distance_range=distance_sort(end-100:end);
%     end
%
distance_average(1,i)=(sum(distance_range,'all')./length(distance_range));
```

```
    name_string = ['I' num2str(i) '=I'];
    eval(name_string)
    name_string = ['BW' num2str(i) '=BW'];
    eval(name_string)
    name_string = ['burned' num2str(i) '=burned'];
    eval(name_string)
    name_string = ['contour' num2str(i) '=contour'];
    eval(name_string)
    name_string = ['col' num2str(i) '=col'];
    eval(name_string)
    name_string = ['row' num2str(i) '=row'];
    eval(name_string)
    name_string = ['distance' num2str(i) '=distance'];
    eval(name_string)
%     name_string = ['distance_sort' num2str(i) '=distance_sort'];
%     eval(name_string)
%     name_string = ['distance_range' num2str(i) '=distance_range'];
%     eval(name_string)


    T(1,i)=Images_interval*i+time; %x axel for time
    % write the images
    path = 'D:\RCM publication\Optical ER1 770K 25.11.2021\67500fps_run770K
iso-octane test4 2.8aperture
_C001H001S0001\Select_images\Post_process\'; %path to save the images
    prefix = 'image_'; %name for binary images
    prefix2 = 'contour_'; %name for binary images
    format = 'jpg'; %format for binary images
    suffix = strcat('.',format); % 文件后缀
    imwrite(BW,strcat(path, prefix, num2str(i), suffix), format);
    imwrite(contour,strcat(path, prefix2, num2str(i), suffix), format);


    end


for z= 1:(length(distance_average)-1)
    speed_length(1,z)=((distance_average(1,z+1)-
distance_average(1,z))/1000)/(1/67500);
    T2(1,z)=Images_interval*z+time; %x axel for time
    speed_area(1,z)=((radius(1,z+1)-radius(1,z))/1000)/(1/67500);
```

```
end

figure(1)
plot(T,BMF,'k','linewidth',1);
ylabel('burned mass fraction');
set(gca,'ycolor','k');
hold on
yyaxis right
plot(T,brightness,'r','linewidth',1);
set(gca,'ycolor','r');
set(gca,'FontSize',16);
xlabel('Time - ms');
ylabel('brightness');

figure(2)
plot(T2,speed_length,'k','linewidth',1);
ylabel('speed -m/s');
hold on
yyaxis right %right y axis for displacement
plot(T,distance_average,'r','linewidth',1);
set(gca,'FontSize',16);
set(gca,'ycolor','r');
xlabel('Time - ms');
ylabel('length - mm');

figure(3)
plot(T2,speed_area,'k','linewidth',1);
ylabel('speed -m/s');
hold on
yyaxis right %right y axis for displacement
plot(T,radius,'r','linewidth',1);
% xlim([10.8 12]);
set(gca,'FontSize',16);
set(gca,'ycolor','r');
xlabel('Time - ms');
ylabel('radius - mm');
```

# Appendix C.

1. Data file, used to input the physical and combustion parameter of ethane-air, also set up the domain and mesh information:

```
diffbad 50
heun
solid
keps
rat 5.0
combustion
vis 1.52e-1
prandtl 0.813
ulburning 40.2
udensity 1.1748e-3
bdensity 0.15028e-3
alphaut 0.36
betaut 0.29
tcond 1.87e-1
sdiff 1.87e-1
rtol 5.0e-5
START " "
  LEVELS 3
     XYZ 2
        X 2100 0 2100 FREE
        Y 300 0 300 FREE
  CASE ETHANEOPENTEST
END
kt
split
idumpdt 0.1
cn 0.3
dump
```

2. usrqis.c file of ethaneopentest model: used to set up the dimensionless scale, initial temperature, pressure and density, turbulent intensity and dissipation rate, also build the wall, baffles boundary condition.

```
//li added: ethane large scale explosion test
   else if (strcmp(cas, "ETHANEOPENTEST") == 0){
      float mass;
      //g = 1.401; //gamma value hydrogen 1.401
      g = 1.375;
      mass = udensity*kboltz*300.0/(1.0e6*massh);
      rhoscale = 1e6/(kboltz/(mass*massh)*300.0); /*pa*/
      pscale = rhoscale*kboltz/(mass*massh);
      vscale = sqrt(pscale/rhoscale);
      lscale = 1;    //length scale with 1 cm meter in one unit
      pa[iqd] = 1;/*g/cm^3*/
      pa[iqe] = 300.0; /*cgs unit the pressure in ba*/
      pa[iqu0+1] = 0.0;

        //WALL
       if ((mabs(xc[0]) <= 1)&&(mabs(xc[1]) >= 0)){
        pa[iqss] = 1.0;
        pa[iqsm] = 0.0;
      }
      if ((mabs(xc[0]) > 1)&&(mabs(xc[1]) < 1)){
        pa[iqss] = 1.0;
        pa[iqsm] = 0.0;
      }
```

```
        if ((mabs(xc[0]) > 1)&&(mabs(xc[1]) > 299)){
        pa[iqss] = 1.0;
        pa[iqsm] = 0.0;
      }
//bufffles
//first colume    original is 5
  if (((xc[0]-100)*(xc[0]-100) + (xc[1]-25)*(xc[1]-25)) <= 7){
        pa[iqss] = 1.0;
        pa[iqsm] = 0.0;
      }

      if (((xc[0]-100)*(xc[0]-100) + (xc[1]-60)*(xc[1]-60)) <= 7){
        pa[iqss] = 1.0;
        pa[iqsm] = 0.0;
      }

       if (((xc[0]-100)*(xc[0]-100) + (xc[1]-95)*(xc[1]-95)) <= 7){
        pa[iqss] = 1.0;
        pa[iqsm] = 0.0;
      }

      if (((xc[0]-100)*(xc[0]-100) + (xc[1]-130)*(xc[1]-130)) <= 7){
        pa[iqss] = 1.0;
        pa[iqsm] = 0.0;
      }
      if (((xc[0]-100)*(xc[0]-100) + (xc[1]-165)*(xc[1]-165)) <= 7){
        pa[iqss] = 1.0;
        pa[iqsm] = 0.0;
      }
```

```
if (((xc[0]-100)*(xc[0]-100) + (xc[1]-200)*(xc[1]-200)) <= 7){
   pa[iqss] = 1.0;
   pa[iqsm] = 0.0;
}
if (((xc[0]-100)*(xc[0]-100) + (xc[1]-235)*(xc[1]-235)) <= 7){
   pa[iqss] = 1.0;
   pa[iqsm] = 0.0;
}
if (((xc[0]-100)*(xc[0]-100) + (xc[1]-270)*(xc[1]-270)) <= 7){
   pa[iqss] = 1.0;
   pa[iqsm] = 0.0;
}
//second

if (((xc[0]-137)*(xc[0]-137) + (xc[1]-25)*(xc[1]-25)) <= 7){
   pa[iqss] = 1.0;
   pa[iqsm] = 0.0;
}

if (((xc[0]-137)*(xc[0]-137) + (xc[1]-60)*(xc[1]-60)) <= 7){
   pa[iqss] = 1.0;
   pa[iqsm] = 0.0;
}

  if (((xc[0]-137)*(xc[0]-137) + (xc[1]-95)*(xc[1]-95)) <= 7){
   pa[iqss] = 1.0;
   pa[iqsm] = 0.0;
}
```

```
    if (((xc[0]-137)*(xc[0]-137) + (xc[1]-130)*(xc[1]-130)) <= 7){
       pa[iqss] = 1.0;
       pa[iqsm] = 0.0;
    }
    if (((xc[0]-137)*(xc[0]-137) + (xc[1]-165)*(xc[1]-165)) <= 7){
       pa[iqss] = 1.0;
       pa[iqsm] = 0.0;
    }
    if (((xc[0]-137)*(xc[0]-137) + (xc[1]-200)*(xc[1]-200)) <= 7){
       pa[iqss] = 1.0;
       pa[iqsm] = 0.0;
    }
    if (((xc[0]-137)*(xc[0]-137) + (xc[1]-235)*(xc[1]-235)) <= 7){
       pa[iqss] = 1.0;
       pa[iqsm] = 0.0;
    }
    if (((xc[0]-137)*(xc[0]-137) + (xc[1]-270)*(xc[1]-270)) <= 7){
       pa[iqss] = 1.0;
       pa[iqsm] = 0.0;
    }

    //third colume
if (((xc[0]-174)*(xc[0]-174) + (xc[1]-25)*(xc[1]-25)) <= 7){
       pa[iqss] = 1.0;
       pa[iqsm] = 0.0;
    }

    if (((xc[0]-174)*(xc[0]-174) + (xc[1]-60)*(xc[1]-60)) <= 7){
       pa[iqss] = 1.0;
```

```
    pa[iqsm] = 0.0;
}

  if (((xc[0]-174)*(xc[0]-174) + (xc[1]-95)*(xc[1]-95)) <= 7){
    pa[iqss] = 1.0;
    pa[iqsm] = 0.0;
}

if (((xc[0]-174)*(xc[0]-174) + (xc[1]-130)*(xc[1]-130)) <= 7){
    pa[iqss] = 1.0;
    pa[iqsm] = 0.0;
}
if (((xc[0]-174)*(xc[0]-174) + (xc[1]-165)*(xc[1]-165)) <= 7){
    pa[iqss] = 1.0;
    pa[iqsm] = 0.0;
}
if (((xc[0]-174)*(xc[0]-174) + (xc[1]-200)*(xc[1]-200)) <= 7){
    pa[iqss] = 1.0;
    pa[iqsm] = 0.0;
}
if (((xc[0]-174)*(xc[0]-174) + (xc[1]-235)*(xc[1]-235)) <= 7){
    pa[iqss] = 1.0;
    pa[iqsm] = 0.0;
}
if (((xc[0]-174)*(xc[0]-174) + (xc[1]-270)*(xc[1]-270)) <= 7){
    pa[iqss] = 1.0;
    pa[iqsm] = 0.0;
}
```

```
            //four colume
if (((xc[0]- 211)*(xc[0]-211) + (xc[1]-25)*(xc[1]-25)) <= 7){
        pa[iqss] = 1.0;
        pa[iqsm] = 0.0;
    }

    if (((xc[0]-211)*(xc[0]-211) + (xc[1]-60)*(xc[1]-60)) <= 7){
        pa[iqss] = 1.0;
        pa[iqsm] = 0.0;
    }

     if (((xc[0]-211)*(xc[0]-211) + (xc[1]-95)*(xc[1]-95)) <= 7){
        pa[iqss] = 1.0;
        pa[iqsm] = 0.0;
    }

    if (((xc[0]-211)*(xc[0]-211) + (xc[1]-130)*(xc[1]-130)) <= 7){
        pa[iqss] = 1.0;
        pa[iqsm] = 0.0;
    }
    if (((xc[0]-211)*(xc[0]-211) + (xc[1]-165)*(xc[1]-165)) <= 7){
        pa[iqss] = 1.0;
        pa[iqsm] = 0.0;
    }
    if (((xc[0]-211)*(xc[0]-211) + (xc[1]-200)*(xc[1]-200)) <= 7){
        pa[iqss] = 1.0;
        pa[iqsm] = 0.0;
    }
    if (((xc[0]-211)*(xc[0]-211) + (xc[1]-235)*(xc[1]-235)) <= 7){
```

```
        pa[iqss] = 1.0;
        pa[iqsm] = 0.0;
    }
    if (((xc[0]-211)*(xc[0]-211) + (xc[1]-270)*(xc[1]-270)) <= 7){
        pa[iqss] = 1.0;
        pa[iqsm] = 0.0;
    }

        //five colume
if (((xc[0]-248)*(xc[0]-248) + (xc[1]-25)*(xc[1]-25)) <= 7){
        pa[iqss] = 1.0;
        pa[iqsm] = 0.0;
    }

    if (((xc[0]-248)*(xc[0]-248) + (xc[1]-60)*(xc[1]-60)) <= 7){
        pa[iqss] = 1.0;
        pa[iqsm] = 0.0;
    }

     if (((xc[0]-248)*(xc[0]-248) + (xc[1]-95)*(xc[1]-95)) <= 7){
        pa[iqss] = 1.0;
        pa[iqsm] = 0.0;
    }

    if (((xc[0]-248)*(xc[0]-248) + (xc[1]-130)*(xc[1]-130)) <= 7){
        pa[iqss] = 1.0;
        pa[iqsm] = 0.0;
    }
    if (((xc[0]-248)*(xc[0]-248) + (xc[1]-165)*(xc[1]-165)) <= 7){
```

```
        pa[iqss] = 1.0;
        pa[iqsm] = 0.0;
    }
    if (((xc[0]-248)*(xc[0]-248) + (xc[1]-200)*(xc[1]-200)) <= 7){
        pa[iqss] = 1.0;
        pa[iqsm] = 0.0;
    }
    if (((xc[0]-248)*(xc[0]-248) + (xc[1]-235)*(xc[1]-235)) <= 7){
        pa[iqss] = 1.0;
        pa[iqsm] = 0.0;
    }
    if (((xc[0]-248)*(xc[0]-248) + (xc[1]-270)*(xc[1]-270)) <= 7){
        pa[iqss] = 1.0;
        pa[iqsm] = 0.0;
    }

        //six colume
if (((xc[0]-285)*(xc[0]-285) + (xc[1]-25)*(xc[1]-25)) <= 7){
        pa[iqss] = 1.0;
        pa[iqsm] = 0.0;
    }

    if (((xc[0]-285)*(xc[0]-285) + (xc[1]-60)*(xc[1]-60)) <= 7){
        pa[iqss] = 1.0;
        pa[iqsm] = 0.0;
    }

     if (((xc[0]-285)*(xc[0]-285) + (xc[1]-95)*(xc[1]-95)) <= 7){
        pa[iqss] = 1.0;
```

```
        pa[iqsm] = 0.0;
    }

    if (((xc[0]-285)*(xc[0]-285) + (xc[1]-130)*(xc[1]-130)) <= 7){
        pa[iqss] = 1.0;
        pa[iqsm] = 0.0;
    }
    if (((xc[0]-285)*(xc[0]-285) + (xc[1]-165)*(xc[1]-165)) <= 7){
        pa[iqss] = 1.0;
        pa[iqsm] = 0.0;
    }
    if (((xc[0]-285)*(xc[0]-285) + (xc[1]-200)*(xc[1]-200)) <= 7){
        pa[iqss] = 1.0;
        pa[iqsm] = 0.0;
    }
    if (((xc[0]-285)*(xc[0]-285) + (xc[1]-235)*(xc[1]-235)) <= 7){
        pa[iqss] = 1.0;
        pa[iqsm] = 0.0;
    }
    if (((xc[0]-285)*(xc[0]-285) + (xc[1]-270)*(xc[1]-270)) <= 7){
        pa[iqss] = 1.0;
        pa[iqsm] = 0.0;
    }


   //seven colume
if (((xc[0]-322)*(xc[0]-322) + (xc[1]-25)*(xc[1]-25)) <= 7){
        pa[iqss] = 1.0;
        pa[iqsm] = 0.0;
```

```
}

if (((xc[0]-322)*(xc[0]-322) + (xc[1]-60)*(xc[1]-60)) <= 7){
   pa[iqss] = 1.0;
   pa[iqsm] = 0.0;
}

  if (((xc[0]-322)*(xc[0]-322) + (xc[1]-95)*(xc[1]-95)) <= 7){
   pa[iqss] = 1.0;
   pa[iqsm] = 0.0;
}

if (((xc[0]-322)*(xc[0]-322) + (xc[1]-130)*(xc[1]-130)) <= 7){
   pa[iqss] = 1.0;
   pa[iqsm] = 0.0;
}
if (((xc[0]-322)*(xc[0]-322) + (xc[1]-165)*(xc[1]-165)) <= 7){
   pa[iqss] = 1.0;
   pa[iqsm] = 0.0;
}
if (((xc[0]-322)*(xc[0]-322) + (xc[1]-200)*(xc[1]-200)) <= 7){
   pa[iqss] = 1.0;
   pa[iqsm] = 0.0;
}
if (((xc[0]-322)*(xc[0]-322) + (xc[1]-235)*(xc[1]-235)) <= 7){
   pa[iqss] = 1.0;
   pa[iqsm] = 0.0;
}
if (((xc[0]-322)*(xc[0]-322) + (xc[1]-270)*(xc[1]-270)) <= 7){
```

```
        pa[iqss] = 1.0;
        pa[iqsm] = 0.0;
    }
        //eight colume
if (((xc[0]-359)*(xc[0]-359) + (xc[1]-25)*(xc[1]-25)) <= 7){
        pa[iqss] = 1.0;
        pa[iqsm] = 0.0;
    }

    if (((xc[0]-359)*(xc[0]-359) + (xc[1]-60)*(xc[1]-60)) <= 7){
        pa[iqss] = 1.0;
        pa[iqsm] = 0.0;
    }

     if (((xc[0]-359)*(xc[0]-359) + (xc[1]-95)*(xc[1]-95)) <= 7){
        pa[iqss] = 1.0;
        pa[iqsm] = 0.0;
    }

    if (((xc[0]-359)*(xc[0]-359) + (xc[1]-130)*(xc[1]-130)) <= 7){
        pa[iqss] = 1.0;
        pa[iqsm] = 0.0;
    }
    if (((xc[0]-359)*(xc[0]-359) + (xc[1]-165)*(xc[1]-165)) <= 7){
        pa[iqss] = 1.0;
        pa[iqsm] = 0.0;
    }
    if (((xc[0]-359)*(xc[0]-359) + (xc[1]-200)*(xc[1]-200)) <= 7){
        pa[iqss] = 1.0;
```

```
        pa[iqsm] = 0.0;
    }
    if (((xc[0]-359)*(xc[0]-359) + (xc[1]-235)*(xc[1]-235)) <= 7){
        pa[iqss] = 1.0;
        pa[iqsm] = 0.0;
    }
    if (((xc[0]-359)*(xc[0]-359) + (xc[1]-270)*(xc[1]-270)) <= 7){
        pa[iqss] = 1.0;
        pa[iqsm] = 0.0;
    }
        //nine colume
if (((xc[0]-396)*(xc[0]-396) + (xc[1]-25)*(xc[1]-25)) <= 7){
        pa[iqss] = 1.0;
        pa[iqsm] = 0.0;
    }

    if (((xc[0]-396)*(xc[0]-396) + (xc[1]-60)*(xc[1]-60)) <= 7){
        pa[iqss] = 1.0;
        pa[iqsm] = 0.0;
    }

     if (((xc[0]-396)*(xc[0]-396) + (xc[1]-95)*(xc[1]-95)) <= 7){
        pa[iqss] = 1.0;
        pa[iqsm] = 0.0;
    }

    if (((xc[0]-396)*(xc[0]-396) + (xc[1]-130)*(xc[1]-130)) <= 7){
        pa[iqss] = 1.0;
        pa[iqsm] = 0.0;
```

```
    }
    if (((xc[0]-396)*(xc[0]-396) + (xc[1]-165)*(xc[1]-165)) <= 7){
       pa[iqss] = 1.0;
       pa[iqsm] = 0.0;
    }
    if (((xc[0]-396)*(xc[0]-396) + (xc[1]-200)*(xc[1]-200)) <= 7){
       pa[iqss] = 1.0;
       pa[iqsm] = 0.0;
    }
    if (((xc[0]-396)*(xc[0]-396) + (xc[1]-235)*(xc[1]-235)) <= 7){
       pa[iqss] = 1.0;
       pa[iqsm] = 0.0;
    }
    if (((xc[0]-396)*(xc[0]-396) + (xc[1]-270)*(xc[1]-270)) <= 7){
       pa[iqss] = 1.0;
       pa[iqsm] = 0.0;
    }

    // ten colume
if (((xc[0]- 433)*(xc[0]-433) + (xc[1]-25)*(xc[1]-25)) <= 7){
       pa[iqss] = 1.0;
       pa[iqsm] = 0.0;
    }

    if (((xc[0]-433)*(xc[0]-433) + (xc[1]-60)*(xc[1]-60)) <= 7){
       pa[iqss] = 1.0;
       pa[iqsm] = 0.0;
    }
```

```
  if (((xc[0]-433)*(xc[0]-433) + (xc[1]-95)*(xc[1]-95)) <= 7){
    pa[iqss] = 1.0;
    pa[iqsm] = 0.0;
  }

  if (((xc[0]-433)*(xc[0]-433) + (xc[1]-130)*(xc[1]-130)) <= 7){
    pa[iqss] = 1.0;
    pa[iqsm] = 0.0;
  }
  if (((xc[0]-433)*(xc[0]-433) + (xc[1]-165)*(xc[1]-165)) <= 7){
    pa[iqss] = 1.0;
    pa[iqsm] = 0.0;
  }
  if (((xc[0]-433)*(xc[0]-433) + (xc[1]-200)*(xc[1]-200)) <= 7){
    pa[iqss] = 1.0;
    pa[iqsm] = 0.0;
  }
  if (((xc[0]-433)*(xc[0]-433) + (xc[1]-235)*(xc[1]-235)) <= 7){
    pa[iqss] = 1.0;
    pa[iqsm] = 0.0;
  }
  if (((xc[0]-433)*(xc[0]-433) + (xc[1]-270)*(xc[1]-270)) <= 7){
    pa[iqss] = 1.0;
    pa[iqsm] = 0.0;
  }

  //eleven colume
if (((xc[0]-470)*(xc[0]-470) + (xc[1]-25)*(xc[1]-25)) <= 7){
    pa[iqss] = 1.0;
```

```
    pa[iqsm] = 0.0;
}

if (((xc[0]-470)*(xc[0]-470) + (xc[1]-60)*(xc[1]-60)) <= 7){
    pa[iqss] = 1.0;
    pa[iqsm] = 0.0;
}

  if (((xc[0]-470)*(xc[0]-470) + (xc[1]-95)*(xc[1]-95)) <= 7){
    pa[iqss] = 1.0;
    pa[iqsm] = 0.0;
}

if (((xc[0]-470)*(xc[0]-470) + (xc[1]-130)*(xc[1]-130)) <= 7){
    pa[iqss] = 1.0;
    pa[iqsm] = 0.0;
}
if (((xc[0]-470)*(xc[0]-470) + (xc[1]-165)*(xc[1]-165)) <= 7){
    pa[iqss] = 1.0;
    pa[iqsm] = 0.0;
}
if (((xc[0]-470)*(xc[0]-470) + (xc[1]-200)*(xc[1]-200)) <= 7){
    pa[iqss] = 1.0;
    pa[iqsm] = 0.0;
}
if (((xc[0]-470)*(xc[0]-470) + (xc[1]-235)*(xc[1]-235)) <= 7){
    pa[iqss] = 1.0;
    pa[iqsm] = 0.0;
}
```

```
if (((xc[0]-470)*(xc[0]-470) + (xc[1]-270)*(xc[1]-270)) <= 7){
   pa[iqss] = 1.0;
   pa[iqsm] = 0.0;
}

//12 colume
  if (((xc[0]-507)*(xc[0]-507) + (xc[1]-25)*(xc[1]-25)) <= 7){
   pa[iqss] = 1.0;
   pa[iqsm] = 0.0;
}

if (((xc[0]-507)*(xc[0]-507) + (xc[1]-60)*(xc[1]-60)) <= 7){
   pa[iqss] = 1.0;
   pa[iqsm] = 0.0;
}

  if (((xc[0]-507)*(xc[0]-507) + (xc[1]-95)*(xc[1]-95)) <= 7){
   pa[iqss] = 1.0;
   pa[iqsm] = 0.0;
}

if (((xc[0]-507)*(xc[0]-507) + (xc[1]-130)*(xc[1]-130)) <= 7){
   pa[iqss] = 1.0;
   pa[iqsm] = 0.0;
}
if (((xc[0]-507)*(xc[0]-507) + (xc[1]-165)*(xc[1]-165)) <= 7){
   pa[iqss] = 1.0;
   pa[iqsm] = 0.0;
}
```

```
if (((xc[0]-507)*(xc[0]-507) + (xc[1]-200)*(xc[1]-200)) <= 7){
   pa[iqss] = 1.0;
   pa[iqsm] = 0.0;
}
if (((xc[0]-507)*(xc[0]-507) + (xc[1]-235)*(xc[1]-235)) <= 7){
   pa[iqss] = 1.0;
   pa[iqsm] = 0.0;
}
if (((xc[0]-507)*(xc[0]-507) + (xc[1]-270)*(xc[1]-270)) <= 7){
   pa[iqss] = 1.0;
   pa[iqsm] = 0.0;
}



//13 colume
  if (((xc[0]-544)*(xc[0]-544) + (xc[1]-25)*(xc[1]-25)) <= 7){
   pa[iqss] = 1.0;
   pa[iqsm] = 0.0;
}

if (((xc[0]-544)*(xc[0]-544) + (xc[1]-60)*(xc[1]-60)) <= 7){
   pa[iqss] = 1.0;
   pa[iqsm] = 0.0;
}

  if (((xc[0]-544)*(xc[0]-544) + (xc[1]-95)*(xc[1]-95)) <= 7){
   pa[iqss] = 1.0;
   pa[iqsm] = 0.0;
}
```

```
if (((xc[0]-544)*(xc[0]-544) + (xc[1]-130)*(xc[1]-130)) <= 7){
   pa[iqss] = 1.0;
   pa[iqsm] = 0.0;
}
if (((xc[0]-544)*(xc[0]-544) + (xc[1]-165)*(xc[1]-165)) <= 7){
   pa[iqss] = 1.0;
   pa[iqsm] = 0.0;
}
if (((xc[0]-544)*(xc[0]-544) + (xc[1]-200)*(xc[1]-200)) <= 7){
   pa[iqss] = 1.0;
   pa[iqsm] = 0.0;
}
if (((xc[0]-544)*(xc[0]-544) + (xc[1]-235)*(xc[1]-235)) <= 7){
   pa[iqss] = 1.0;
   pa[iqsm] = 0.0;
}
if (((xc[0]-544)*(xc[0]-544) + (xc[1]-270)*(xc[1]-270)) <= 7){
   pa[iqss] = 1.0;
   pa[iqsm] = 0.0;
}

      //14 colume
  if (((xc[0]-581)*(xc[0]-581) + (xc[1]-25)*(xc[1]-25)) <= 7){
   pa[iqss] = 1.0;
   pa[iqsm] = 0.0;
}

if (((xc[0]-581)*(xc[0]-581) + (xc[1]-60)*(xc[1]-60)) <= 7){
```

```
    pa[iqss] = 1.0;
    pa[iqsm] = 0.0;
}

  if (((xc[0]-581)*(xc[0]-581) + (xc[1]-95)*(xc[1]-95)) <= 7){
    pa[iqss] = 1.0;
    pa[iqsm] = 0.0;
}

if (((xc[0]-581)*(xc[0]-581) + (xc[1]-130)*(xc[1]-130)) <= 7){
    pa[iqss] = 1.0;
    pa[iqsm] = 0.0;
}
if (((xc[0]-581)*(xc[0]-581) + (xc[1]-165)*(xc[1]-165)) <= 7){
    pa[iqss] = 1.0;
    pa[iqsm] = 0.0;
}
if (((xc[0]-581)*(xc[0]-581) + (xc[1]-200)*(xc[1]-200)) <= 7){
    pa[iqss] = 1.0;
    pa[iqsm] = 0.0;
}
if (((xc[0]-581)*(xc[0]-581) + (xc[1]-235)*(xc[1]-235)) <= 7){
    pa[iqss] = 1.0;
    pa[iqsm] = 0.0;
}
if (((xc[0]-581)*(xc[0]-581) + (xc[1]-270)*(xc[1]-270)) <= 7){
    pa[iqss] = 1.0;
    pa[iqsm] = 0.0;
}
```

```
  //15 colume
  if (((xc[0]-618)*(xc[0]-618) + (xc[1]-25)*(xc[1]-25)) <= 7){
    pa[iqss] = 1.0;
    pa[iqsm] = 0.0;
}

if (((xc[0]-618)*(xc[0]-618) + (xc[1]-60)*(xc[1]-60)) <= 7){
    pa[iqss] = 1.0;
    pa[iqsm] = 0.0;
}

  if (((xc[0]-618)*(xc[0]-618) + (xc[1]-95)*(xc[1]-95)) <= 7){
    pa[iqss] = 1.0;
    pa[iqsm] = 0.0;
}

if (((xc[0]-618)*(xc[0]-618) + (xc[1]-130)*(xc[1]-130)) <= 7){
    pa[iqss] = 1.0;
    pa[iqsm] = 0.0;
}
if (((xc[0]-618)*(xc[0]-618) + (xc[1]-165)*(xc[1]-165)) <= 7){
    pa[iqss] = 1.0;
    pa[iqsm] = 0.0;
}
if (((xc[0]-618)*(xc[0]-618) + (xc[1]-200)*(xc[1]-200)) <= 7){
    pa[iqss] = 1.0;
    pa[iqsm] = 0.0;
}
```

```
if (((xc[0]-618)*(xc[0]-618) + (xc[1]-235)*(xc[1]-235)) <= 7){
   pa[iqss] = 1.0;
   pa[iqsm] = 0.0;
}
if (((xc[0]-618)*(xc[0]-618) + (xc[1]-270)*(xc[1]-270)) <= 7){
   pa[iqss] = 1.0;
   pa[iqsm] = 0.0;
}

//16 colume
  if (((xc[0]-655)*(xc[0]-655) + (xc[1]-25)*(xc[1]-25)) <= 7){
   pa[iqss] = 1.0;
   pa[iqsm] = 0.0;
}

if (((xc[0]-655)*(xc[0]-655) + (xc[1]-60)*(xc[1]-60)) <= 7){
   pa[iqss] = 1.0;
   pa[iqsm] = 0.0;
}

  if (((xc[0]-655)*(xc[0]-655) + (xc[1]-95)*(xc[1]-95)) <= 7){
   pa[iqss] = 1.0;
   pa[iqsm] = 0.0;
}

if (((xc[0]-655)*(xc[0]-655) + (xc[1]-130)*(xc[1]-130)) <= 7){
   pa[iqss] = 1.0;
   pa[iqsm] = 0.0;
}
```

```
if (((xc[0]-655)*(xc[0]-655) + (xc[1]-165)*(xc[1]-165)) <= 7){
   pa[iqss] = 1.0;
   pa[iqsm] = 0.0;
}
if (((xc[0]-655)*(xc[0]-655) + (xc[1]-200)*(xc[1]-200)) <= 7){
   pa[iqss] = 1.0;
   pa[iqsm] = 0.0;
}
if (((xc[0]-655)*(xc[0]-655) + (xc[1]-235)*(xc[1]-235)) <= 7){
   pa[iqss] = 1.0;
   pa[iqsm] = 0.0;
}
if (((xc[0]-655)*(xc[0]-655) + (xc[1]-270)*(xc[1]-270)) <= 7){
   pa[iqss] = 1.0;
   pa[iqsm] = 0.0;
}



if (strcmp(geom,"RZP")==0)
   tv = xc[ipr-1]*xc[ipr-1] + xc[ipz-1]*xc[ipz-1];
else
   tv = (xc[1]-150)*(xc[1]-150) + (xc[0]-30)*(xc[0]-30);
if (tv <= rat*rat){
   pa[iqc] = 1.0;
   tv1 = udensity/bdensity;    // unburnt/burnt density ratio
//    tv1 = 1.0;
   pa[iqd] /= tv1; //burned density
}else{
```

```
        pa[iqc] = 0.0;
      }
      if (keps){
        //pa[iqk] = 1.0e-4*pa[iqe]/(g-1);
        pa[iqk] = (100.0*100.0)/(0.8165*0.8165)/(vscale*vscale); // the intial u' is 1m/s
        tv = pa[iqk];
        //pa[iqeps] = pa[iqk]*pa[iqk]/(vis/(vscale*lscale));//initial turbulent length is Kolmogorov length scale
        //pa[iqeps] = 0.5*pow(0.09,3/4)*lscale*(15000/(vscale*vscale))*sqrt(15000/(vscale*vscale));
        pa[iqeps] = pow(cs,0.75)*pow(tv,1.5)/2.0/lscale;

      }
    }
```

Usrsaf.c: The source terms of progress variable is added and developed here:

```
//Li and sven added: progress variable
      if ((combustion)&&(!splitcool)){
        float R, rhou, rhob, ul, v, q, P0, T0;
        float temp = usrte(pa);
        P0 = 300.0;
        T0 = 300.0;
        v = (vis /prandtl)/(lscale*vscale);     // v is thermal diffusivity 0.513 is prandtl number
        //A = 0.4; //constant for reaction rate
       // A = 4.133; //A = 4.133; for hydrogen 0.1 length scale
        A = 2.0;    //ethane
        //v=2.16e-1;
```

```
        ul = ulburning/vscale;//*(temp/T0)*(temp/T0)/sqrt(pa[iqe]/P0);      // laminar
burning velocity
        //ul = 1.81e2;
        tv = v/ul;          // laminar flame thickness
        //rhou = 0.8496e-3*pow(pa[iqe]/P0, 1.0/g)/rhoscale;    // unburnt density
        rhou = udensity/rhoscale;
        rhob = bdensity/rhoscale;    // burnt density
        //R = A*ul/tv*0.346)*lscale/vscale; // laminar reaction rate
        //R =A*(ul/tv)*lscale/vscale;
        R =A*(ul/tv);
        tv = (1.0 - pa[iqc])*pa[iqc]*pa[iqc]*pa[iqc]*pa[iqc];
        tv *= pa[iqd]*R*(rhou/rhob)*(rhou/rhob);
        so[iqc] += tv;      //source term for progress variable
        //tv *=    (P0/rhou) * (rhou/rhob - 1.0) * (g/(g-1.0))/(vscale*vscale);
        tv *=    (P0/rhou) * (rhou/rhob - 1.0) * (g/(g-1.0));
        so[iqe] += tv;    //source term for energy equation
      }
      //LI added: turbulent burning velocity case
        if ((combustion)&&(!splitcool)&&(keps)){
        float R, rhou, rhob, ult, v, q, Masr, alpha, beta, tl, uprime, K, ut,    P0, T0, tvt, tvp,
tv1, A, ul, B, ul2, v2, Rl, temp2;
        float temp = usrte(pa);
       // B = 1.12; // 1.12 for hydrogen facter for reaction constatn
        B = 0.8;    //0.8 for ethane
        P0 = 300.0;
        T0 = 300.0;
        ul = ulburning/vscale; //lamianr ulburning velocity after scale
        //rhou = 0.8496e-3*pow(pa[iqe]/P0, 1.0/g)/rhoscale;    // unburnt density
        rhou = udensity/rhoscale;
```

```
rhob = bdensity/rhoscale;    // burnt density
v = vis/(lscale*vscale);    // kinematic viscosity
//turbulent case
//Masr = 8.8; //markstein number
//alpha = 0.023*(30-Masr); //constant
//beta = 0.0103*(Masr-30);    //constant
alpha = alphaut;
beta = 0.0-betaut;
tv = max(pa[iqk], kmin);
tv1 = sqrt(tv);
uprime = 0.8165*tv1;      //rms turbulent speed
//uprime = 0.8165*tv1*100/vscale;
//turbulent intergral length scale
tl = pow(cs, 0.75)*tv*tv1/max(pa[iqeps], epsmin);
tl = min(tl, mtl);
temp2 =    temp/(1.0 + pa[iqc]*(rhou/rhob-1.0)); //temperature ahead of flame
//tl = 2/lscale;    //asume the constant length scale with 2cm;

tvt = temp2/T0;
tvp = pa[iqe]/P0;
ul2 = ul*pow(tvt,1.55)*pow(tvp,-0.24); //post shock lamianr burning velocity
v2 = v*pow(tvt,1.74)*pow(tvp,-1.0); //post shock kinematic viscosity
Rl = uprime*tl/v2;
K = 0.25*(uprime/ul2)*(uprime/ul2)/sqrt(Rl); //post shock kalovitiz number
ut = uprime*alpha*pow(K,beta)*pow(tvt,0.5)*pow(tvp,0.2); //ut as function of
temperature and pressure

R = B*(ut*3.575)/(tl*0.346); // reaction rate
tv = (1.0 - pa[iqc])*pa[iqc]*pa[iqc]*pa[iqc]*pa[iqc];
```

```
    tv *= pa[iqd]*R*(rhou/rhob)*(rhou/rhob);
    so[iqc] += tv;
    tv *=    (P0/rhou) * (rhou/rhob - 1.0) * (g/(g-1.0));
    so[iqe] += tv;
}
```